Computational Intelligence & Neuroscience

Neuromath: Advanced Methods for the Estimation of Human Brain Activity and Connectivity

Guest Editors: Fabio Babiloni, Laura Astolfi, and Andrzej Cichocki

Neuromath: Advanced Methods for the Estimation of Human Brain Activity and Connectivity

Neuromath: Advanced Methods for the Estimation of Human Brain Activity and Connectivity

Guest Editors: Fabio Babiloni, Laura Astolfi, and Andrzej Cichocki

Contents

Hindawi Publishing Corporation
Computational Intelligence and Neuroscience
Volume 2009, Article ID 275638, 2 pages
doi:10.1155/2009/275638

Editorial

NeuroMath: Advanced Methods for the Estimation of Human Brain Activity and Connectivity

Laura Astolfi,[1] Andrzej Cichocki,[2] and Fabio Babiloni[3]

[1] *Department of Informatic and Systems, Faculty of Engineering, University of Rome "Sapienza", Via Ariosto 25, 00185 Rome, Italy*
[2] *Laboratory for Advanced Brain Signal Processing (ABSP), RIKEN Brain Science Institute, 2-1 Hirosawa, Wako-shi, Saitama 351-0198, Japan*
[3] *Department of Physiology and Pharmacology, School of Medicine, University of Rome "Sapienza", 00185 Rome, Italy*

Correspondence should be addressed to Laura Astolfi, laura.astolfi@uniroma1.it

Received 13 August 2009; Accepted 13 August 2009

It is well known that the electroencephalography (EEG) and magnetoencephalography (MEG) are useful techniques for the study of brain dynamics, due to their high temporal resolution. However, it is known that the spatial resolution of the standard EEG is rather low, due to the different electrical conductivities of brain, skull, and scalp that markedly blur the EEG potential distributions, making the localization of the underlying cortical generators problematic. In the last ten years, a body of mathematical techniques, known as high-resolution EEG, was developed to estimate more precisely the cortical activity from non-invasive EEG measurements. Such techniques include the use of a large number of scalp electrodes, realistic models of the head derived from magnetic resonance images (MRIs), and advanced processing methodologies related to the solution of the so-called "inverse problem," that is, the estimation of the brain activity (i.e., electromagnetic generators) from the EEG/MEG measurements. The approach implies both the use of thousands of equivalent current dipoles as a source model and the realistic head models, reconstructed from magnetic resonance images, as the volume conductor medium. The use of geometrical constraints on the position of the neural source or sources within the head model generally reduces the solution space (i.e., the set of all possible combinations of the cortical dipoles strengths). An additional constraint is to force the dipoles to explain the recorded data with a minimum or a low amount of energy (minimum-norm solutions). The solution space can be further reduced by using information derived from hemodynamic measures (i.e., fMRI-BOLD phenomena) recorded during the same task. The rationale of a multimodal approach is that neural activity, modulating neuronal firing and generating EEG/MEG potentials, increases glucose and oxygen demands. This results in an increase in the local hemodynamic response that can be measured by functional magnetic resonance images (fMRIs). Hence, fMRI responses and cortical sources of EEG/MEG data can be spatially related, and the fMRI information can be used as a priori in the solution of the inverse problem**.** As a result of all these computational approaches, it is possible to estimate the cortical activity with a spatial resolution of few millimeters and with a temporal resolution of milliseconds from non-invasive EEG measurements.

However, static images of brain regions activated during particular tasks do not convey the information of how these regions communicate to each other. The concept of brain connectivity is viewed as central for the understanding of the organized behavior of cortical regions beyond the simple mapping of their activity. This organization is thought to be based on the interaction between different and differently specialized cortical sites. Cortical connectivity estimation aims at describing these interactions as connectivity patterns which hold the direction and strength of the information flow between cortical areas. To achieve this, several computational methods have been already applied on data gathered from both hemodynamic and electromagnetic techniques. By using such methods, it is possible to infer the information flows between the cortical areas in human during particular motor and cognitive tasks. Possible applications of this promising technology are in the fields of the study of human

behavior and cognition and in the brain computer interface area. Methods for the estimation of brain connectivity have been scattered proposed in literature related to the fMRI, NIRS, and EEG or MEG technologies.

Hence, the main objective of this special issue is to increase the knowledge on the mathematical methods able to estimate the cortical activity and connectivity in the human brain from non-invasive neuroelectric and hemodynamic measurements. Such special issue includes both the state-of-technique review articles on the EEG and MEG methodologies written by world-class scientists, as well as the description of particular cortical models that can be used to generate cortico-cortical connectivity.

Several papers of this special issue are devoted to the theme of brain-machine interfaces, treating the collection and the analysis of brain signals related to the imagination of motor acts, in the context of brain-computer interface. Applications of the techniques of source estimations were provided also in the field of neuroeconomics, with an example of the track of the brain activity with the EEG during the observation of TV clips, or even during the car driving, by using NIRS device, or in the study of emotional processing with the ERD/ERS techniques. Other papers in this special issue are related to the use of different advanced methodologies for the analysis of brain signals in psychiatric patients, and one is devoted to the description of a possible WEB structure for data sharing in the field of neuroscience.

In summary, this special issue conveys interesting information about the state-of-the-art methodologies able to track the brain activity and connectivity during different tasks in the healthy subjects as well as in the psychiatric patients. We hope that the readership of CIN could appreciate this special issue as we appreciated it during its composition.

Laura Astolfi
Andrzej Cichocki
Fabio Babiloni

Hindawi Publishing Corporation
Computational Intelligence and Neuroscience
Volume 2009, Article ID 656092, 12 pages
doi:10.1155/2009/656092

Review Article

EEG/MEG Source Imaging: Methods, Challenges, and Open Issues

Katrina Wendel,[1] Outi Väisänen,[1] Jaakko Malmivuo,[1] Nevzat G. Gencer,[2] Bart Vanrumste,[3,4] Piotr Durka,[5] Ratko Magjarević,[6] Selma Supek,[7] Mihail Lucian Pascu,[8] Hugues Fontenelle,[9] and Rolando Grave de Peralta Menendez[10,11]

[1] *Department of Biomedical Engineering, Tampere University of Technology, 33101 Tampere, Finland*
[2] *Department of Electrical and Electronics Engineering, Middle East Technical University, 06531 Ankara, Turkey*
[3] *SCD, Department of Electrical Engineering (ESAT), Katholieke Universiteit Leuven, Kasteelpark Arenberg 10, B-3001 Leuven, Belgium*
[4] *MOBILAB, Biosciences and Technology Department, Katholieke Hogeschool Kempen, Kleinhoefstraat 4, B-2440 Geel, Belgium*
[5] *Department of Biomedical Physics, University of Warsaw ul. Hoża 69, 00-681 Warszawa, Poland*
[6] *Faculty of Electrical Engineering and Computing, University of Zagreb, 10000 Zagreb, Croatia*
[7] *Department of Physics, Faculty of Science, University of Zagreb, 10000 Zagreb, Croatia*
[8] *National Institute for Laser, Plasma and Radiation Physics, Laser Department, 077125 Bucharest, Romania*
[9] *Department of Medical Physics, School of Medicine, University of Patras, 26504 Patras, Greece*
[10] *Electrical Neuroimaging Group, Department of Clinical Neurosciences, Geneva University Hospital, 1211 Geneva, Switzerland*
[11] *Neurodynamics Laboratory, Department of Psychiatry and Clinical Psychobiology, University of Barcelona, 08035 Barcelona, Catalonia, Spain*

Correspondence should be addressed to Katrina Wendel, katrina.wendel@tut.fi and
Rolando Grave de Peralta Menendez, rolando.grave@hcuge.ch

Received 25 November 2008; Revised 31 March 2009; Accepted 29 April 2009

Recommended by Laura Astolfi

We present the four key areas of research—preprocessing, the volume conductor, the forward problem, and the inverse problem—that affect the performance of EEG and MEG source imaging. In each key area we identify prominent approaches and methodologies that have open issues warranting further investigation within the community, challenges associated with certain techniques, and algorithms necessitating clarification of their implications. More than providing definitive answers we aim to identify important open issues in the quest of source localization.

1. Introduction

Electroencephalography (EEG) and magnetoencephalography (MEG) represent two noninvasive functional brain imaging methods, whose extracranial recordings measure electric potential differences and extremely weak magnetic fields generated by the electric activity of the neural cells, respectively. These recordings offer direct, real time, monitoring of spontaneous and evoked brain activity and allow for spatiotemporal localization of underlying neuronal generators. EEG and MEG share the following characteristics: (1) they have a millisecond temporal resolution; (2) potential differences and magnetic fields are linear functions of source strengths and nonlinear functions of the source support (e.g., dipole locations); (3) they are caused by the same neurophysiological events, that is, currents from synchronously activated neuronal tissue often referred to as the primary or impressed current source density, and thus both can be used equivalently for the localization of neuronal generators.

The three-dimensional reconstruction of neural activity is commonly misconstrued as *tomography*, which is defined [1] as "*any technique that makes detailed predetermined plane sections of an object while blurring out the images of other planes*." The physics governing the propagation of the electromagnetic fields depends on the composition of the volume conductor, which means that the source activity outside the predetermined plane also influences the readings

of the sensors lying in the plane. So, actually the procedures applied in tomography and inverse solutions are somehow reversed: in tomography we reconstruct a 3D image by combining separately obtained slices, whereas, inverse solutions calculate the whole 3D distribution, which can be later presented as slices. While tomographic techniques (e.g., CT, PET, MRI, etc.) are associated with well-posed mathematical problems, the noninvasive estimation of the brain activity is essentially an ill-posed problem due to the infinite number of solutions.

In the subsequent sections we remark about some important issues for the understanding, selection, and evaluation of source imaging methods; hence our emphasis is on general approaches rather than particular solutions. These sections reflect upon our group discussion held at a NeuroMath workshop. As a group we acknowledge that we have differences of opinion regarding the selection of methods, we face various challenges as separate research centers, and we differ on what are the key open issues due to our different interests. Therefore, we have attempted to write an article that benefits the novice, aligns disparate parts of the source imaging community, and focuses much needed attention to several open issues.

1.1. Theory. The relationship between the sources inside the head and the external measurements d is described as

$$d = Lj, \tag{1}$$

where L is the linear operator representing the lead field (also known as the gain model or the direct model), and j represents the sources. The two mathematical properties of (1) reflect the attributes of the physical magnitudes involved. Firstly, the homogeneity property states that the image of an amplified source $k * j$ is an amplified measurement $k * d$, and secondly, the additive property states that the sum of the two sources $j = j_1 + j_2$ produces a measurement equal to the sum of each measurement alone $d = d_1 + d_2$. Together these two properties follow the superposition principle, that is, $L(k_1 * j_1 + k_2 * j_2) = k_1 * d_1 + k_2 * d_2$, where $d_1 = Lj_1$ and $d_2 = Lj_2$.

The ill-posed nature of this problem arises from the fact that two different sources j_1 and j_2 might produce the same measurement d, that is, $d = Lj_1 = Lj_2$, which is trivially equivalent to say that there exists a "silent" source h such that $Lh = 0$. In order to see the equivalence, note that if $d = Lj_1 = Lj_2$, therefore, the silent source $h = j_1 - j_2$ fulfils $Lh = Lj_1 - Lj_2 = d - d = 0$. In the other direction, if we assume that $Lh = 0$ and the existence of source j_1 such that $Lj_1 = d$, we can always build a new source $j_2 = j_1 + h$ that yields the same data, that is, $Lj_2 = L(j_1 + h) = Lj_1 + Lh = Lj_1 = d$.

That being said, we can establish one of the main properties of EEG/MEG scalp distributions (maps). While similar scalp maps cannot rule out the possibility of different subjacent source distributions, different maps are necessarily due to different source distributions. Importantly, we do not need to resort to any inverse method to conclude that.

Building on linearity and in the absence of a priori information to justify otherwise, we can represent the solution of (1) with a linear operator G that "estimates" j as follows:

$$j_{\text{est}} = G * d. \tag{2}$$

Substituting d by its value defined in (1) yields a fundamental equation of linear operators relating to the estimated and the original source distribution

$$j_{\text{est}} = G * L * j \ = R * j, \tag{3}$$

where $R = G * L$ is the resolution operator [2, 3]. In practice both the sensors and the geometry are made of discrete measurements, and thus it can be assumed that L, G, and R are finite dimensional matrices approximating the continuous (integral) operators.

2. Preprocessing

In this section, we discuss some relevant issues related to the preparation of the data identifying some useful preprocessing and things to avoid. In general, the philosophy of preprocessing is to prepare the signal for solving. Typically, these steps decompose complex signals and reduce the noise from the sensors as well as other undesirable sources.

The EEG and MEG inverse problems (Figure 1, green arrow) start with the time series (Figure 1) recorded at the scalp sensors. Therefore, the localizations based on the distribution of scalp amplitudes in single time instants might be improved by the application of signal processing techniques to the measured time series (Figure 1, blue arrow). In particular the input noise can be reduced by selective and sensitive extraction of relevant activities from the EEG/MEG data. This can be achieved by localizing signal components extracted by a blind source separation (e.g., ICA [4]). Other approaches rely on the information derived from the time-frequency representations, corresponding to the relevant phenomena we want to localize (e.g., sleep spindles [5]). A similar but more sensitive and selective preprocessing was proposed in [6] using the multichannel matching pursuit algorithm. Overall, most preprocessing algorithms are expected to benefit the quality and accuracy of the inverse solution.

2.1. Epochs. We should weigh the advantages and disadvantages of the role epochs play in the recordings of event-related potentials. So far there has been no standard on the number of trials, jitter, averaging amplitudes, or the appropriateness of single trial analysis. For instance, the signal-to-noise ratio (SNR) increases with the number of trials, that is, the number of epochs; however, habituation can affect the results of some studies. We propose that a document outlining these categories would benefit future studies in terms of comparison and regularization.

The neuroelectric signals are buried in spontaneous EEGs with signal-to-noise ratios as low as 5 dB. In order to decrease the noise level and find a *template* Evoked Potential (EP) signal, an ensemble-average (EA) is obtained using a large number of repetitive measurements [7]. This approach

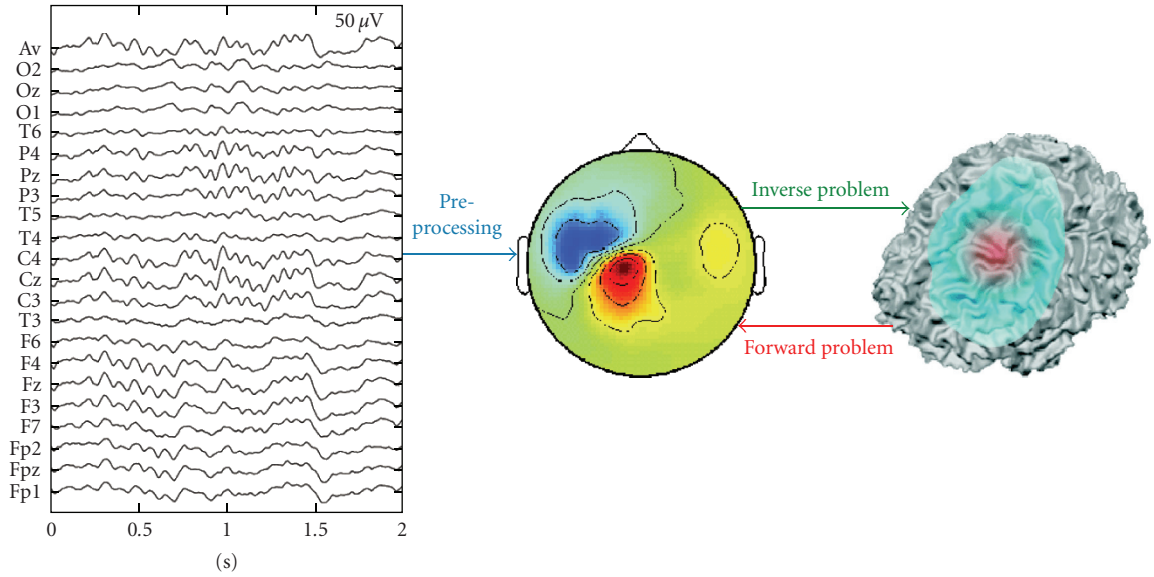

Figure 1: Key parts of source imaging. Preprocessing prepares the recorded signals for solving the inverse problem. The inverse problem attempts to locate the sources from recorded measurements, whereas the forward problem assumes a source definition in order to calculate a potential distribution map.

[8] treats the background EEG as additive noise and the EP as an uncorrelated signal. The magnitudes and latencies of EP waveforms display large interindividual differences and changes depending on the psychophysiological factors for a given individual [9]. Consequently, one goal in the methodological EP research is to develop techniques to extract the true EP waveform from a *single sweep*.

For clinical evaluations, either the template EP signal or possible amplitude and/or latency variations on single sweeps are used [9]. To observe such variations, the specific features are identified from a reference/template EP based on various estimation approaches. Since there are relatively tight constraints related to the available recording time or cooperativeness of the subject, the use of EA (as a reference EP signal) is usually impractical. This has led to the development of the alternative SNR improvement methods based on the additive model. Some of these algorithms are the weighted averaging approach, the subspace averaging method, the parametric filtering, the adaptive filtering, and Wiener filtering. In all these methods, it is assumed that the EP (i.e., signal) is stationary throughout the experiment. However, such assumptions are also questioned in some reports describing the event related potentials as superposition of some phase modulated rhythmic activities which may be related to different cognitive processes of the brain [10].

2.2. Things to Avoid. Contrary to the benefits of most preprocessing algorithms, there are certain algorithms that we should avoid before the application of source localization algorithms. In particular, the following choices threaten the integrity of the inverse solution.

(1) Baseline correction. Varying the values of individual electrodes either by "arbitrary" baseline shifting or by scaling factors changes the surface maps and thus the estimated sources. Although linear inverse solutions are rather stable (continuity with respect to the data), the application of base line correction to two conditions (that will be compared on the basis of their sources) can produce artificial differences induced by the correction and not by the real sources.

(2) Artificial maps produced by grand mean data or segmentation algorithms. Statistical averages (e.g., mean) yield values that are usually not present in the original data. It would not be surprising if the average maps are not present in any of the subject averages. Furthermore, this effect can be amplified by the differences in latencies of the subjects.

(3) The use of very high density of sensors might also jeopardize the source analysis due to different kinds of noise at different sensors. Moreover, no significant information is added after approximately 128 electrodes due to the noise levels. Lastly, some sensors might measure more artifacts than others due to their location near active muscles.

3. Volume Conductor

The head model as a volume conductor is a key element in source localization. The configuration of the volume conductor directly affects the solutions to the forward and inverse solutions. The three nearly equally important areas are head geometry, tissue conductivities, and electrode placement.

3.1. Geometry and Segmentation. The seminal study by Rush and Driscoll [11] used three concentric spheres, whereas, contemporary studies implement realistic models. We find that the differing models within the community are necessary, but how does each type of geometrical model contribute to the goal of source localization? The spherical models answer general questions of theory providing EEG

localization accuracy of a few centimeters, while the realistic models attempt to pinpoint exact locations but actually improve dipole localization by a few centimeters [12–14]. On the other hand, the spherical geometry is sufficient for most MEG-based numerical simulations. Only the localization of the deep sources near the bottom of the skull in the frontotemporal and the frontal areas requires a realistically-shaped-head-volume conductor model for MEG-based simulations [15].

The geometry is directly related to the imaging modality, computed tomography (CT) or magnetic resonance imaging (MRI), and the quality of the segmentation. Naturally, we will question which modality to segment—CT, MRI, or fused CT-MRI images [16]. We are encouraging the modelers to understand the significance of the boundaries defined by a particular modality and are not in any way suggesting the medical community to provide any unsafe and unnecessary radiation to any patient. We must remember that the modality we select influences the segmentation due to its sensitivity to hard or soft tissues accordingly. Furthermore, how many tissues, which tissues, and which cavities should the models include? We foresee that we are nearing a plateau to the improvement in localization accuracy as our segmentation resolution increases along with the inclusion of too many small tissue regions. One avenue of research that could plausibly benefit from the development of the head-model geometry is the integration of anthropometric and craniometric data [17]. This path could justify individual models that claim to represent a subpopulation and repudiate studies that misrepresent an identified subpopulation beyond statistical significance. Moreover, it could lead us to establishing the statistical significance of the shape and size of the geometrical features within individual and groups of models.

3.2. Conductivity Values. The electrical characteristics of many biological tissues are inhomogeneous, anisotropic, dispersive, and nonlinear. Head tissues such as the skull, scalp, muscles, cerebrospinal fluid, and gray and white matter have different conductivities σ, permittivities ε, and magnetic permeabilities μ (in most cases it is considered equal to the permeability of water, which is in turn close to the permeability of free space μ_o). The skull as well as the scalp has a multilayer structure, with each layer possessing different electrical properties. This fact leads either to multilayer modeling of the geometry of the tissue [18] or to attributing inhomogeneous properties to the tissue, that is, assigning tensors for $\sigma = \sigma(x, y, z)$ and $\varepsilon = \varepsilon(x, y, z)$. The values and distributions of inhomogeneities are an even more acute problem in patient populations where pathological processes are likely to significantly influence conductivities in affected brain regions. Could there exist an equivalent hybrid isotropic model that represents multiple anisotropy layers? How significantly would such approximations affect source localization within healthy individuals compared with patients with head pathologies?

The conductivity values of any model influence the lead fields of forward problems and the solutions of the inverse problems. Consequently, it is critical that we must assign as accurate conductivity values as reported from previous literature studies and extrapolate and interpolate the rest. As a community we have established electrical-property ranges for most head tissues in terms of conductivity σ and permittivity ε; however, we have to determine the actual electrical-conductivity distribution of an individual's head. As a result of these ranges, many historical studies assign average values to their tissues [15, 18–26]. Using an average value may not be appropriate for individualized models since those models may result in inaccurate solutions due to a function of position [27] or of age [28, 29]. Nevertheless, studies with patients [30, 31] have shown that using approximate conductivities ratios with an accurate geometrical description of the head (i.e., based on a subject's MRI) might yield reasonable, verifiable results for both cortical and deep EEG sources. Still, future models could benefit from using age-specific conductivities. We speculate that the application of age-based conductivity values applied to the skull tissues—most especially the trilayer skull tissue—would mostly benefit the models of youth, whose ossification centers change rapidly in the first two years and plateau in conductivity value around 18 to 20 years of age when the calvarial ossification process is completed [32].

In order to solidify our motivation for highlighting the significance of the skull conductivity, we must briefly delve into its history. The pioneering work [11] introduced a standard conductivity ratio for the brain-to-skull-to-scalp of 1:80:1, which is a historical value still used by some researchers over four decades later. In [33] are reported measurements on postmortem cadavers yielding a ratio of brain-to-skull conductivity values of 15:1. Three years later [28] presented conductivity values on live tissue as low as a ratio of 4:1. Subsequently, Wendel and Malmivuo [29] correlated *postmortem* to live tissue measurements as a way to incorporate and evaluate past data due to the lack in live tissue measurements. Their previous work used a scaling ratio of 0.33 to 0.4 to accommodate the change in conductivity from living to *postmortem* tissue based upon the conductivity recordings of dying tissue samples [34, 35]. In that previous paper they presented an open issue to the community to make more measurements on live tissue samples—most especially live skull samples—at normal body temperature and moisture, which still remains as an open issue today. Therefore, it is pertinent that we discriminate the conditions under which tissue conductivity and permittivity values were and will be acquired. Values obtained by in vivo or living in vitro measurements should be preferred over *postmortem* measurements. In the case of *postmortem* measurements, the time and temperature of acquisition should be specified since tissue properties change rapidly after cellular death.

3.3. Acquisition of Conductivity Values. In the last two decades, a number of approaches have been proposed to image the electrical conductivity of the human body. In conventional Applied Current Electrical Impedance Tomography (ACEIT) low-frequency-sinusoidal currents are applied

via electrodes attached to the body surface [36]. In Induced Current Electrical Impedance Tomography (ICEIT), time-varying magnetic fields with different spatial-field patterns are applied to induce current in the body. In both cases, surface electrodes are used to make voltage measurements.

Recently, two new approaches were proposed that utilize magnetic measurements in determining the conductivity distribution. In Magnetic Induction Imaging (MII), a transmitter coil is driven by a sinusoidal current to provide time varying magnetic fields [37, 38]. When a body is brought nearby these coils, eddy currents are induced in the body. The distribution of these currents is a function of the body's conductivity distribution. These currents create secondary magnetic fields, and the electromotive force induced in a receiver coil is measured. In Magnetic Resonance Electrical Impedance Tomography (MR EIT), low-frequency currents are applied from the body surface, and the resulting magnetic fields are measured using an MR system [39, 40]. Since magnetic fields are measured inside the body, high-resolution images can be measured. Note that all methods are still in the investigation phase, and none of them can provide the requirements of high-resolution conductivity information required for source localization.

3.4. Electrode Montages. EEG has been traditionally measured using the standard 10–20 electrode system including only 21 measurement electrodes. It has been widely acknowledged that the spatial resolution of the 10–20 system is not sufficient for modern brain research [41–44]. The first step in improving the spatial resolution of EEG is to increase the number of EEG electrodes, which the market has responded to with commercially available systems including up to 256 electrodes.

During the last two decades several studies have investigated the benefits of increasing the number of EEG electrodes. The effect on the accuracy of both the forward solutions and inverse solutions has been evaluated. In several articles, an increase in the number of electrodes to at least 128 has been shown to improve the accuracy of the results [45–50].

Different factors affect the appropriate number of electrodes. These include, for example, the widely debated value of the skull's relative conductivity, which has a great impact on the accuracy of inverse solutions. Additionally, the spatial resolution of especially the dense EEG systems (128–512 electrodes) is extremely sensitive to measurement noise. Thus, for different EEG measurements conducted in different environments, the appropriate number of electrodes may vary considerably [48]. Using active electrodes will reduce the noise.

4. Forward Problem

The 1969 study by Rush and Driscoll [11] on EEG electrode sensitivity ushered in the new era of source localization. Their work analytically solved Maxwell's equations to map the lead field, which is only possible with at least elliptical symmetry. Contemporary models consist of a combination of complex geometry and/or electrical parameters, thus necessitating numerical solutions such as the boundary element method (BEM), finite element method (FEM), and the finite difference method (FDM) (Table 1). In this section we aim to identify some of the complications, advantages, and disadvantages of these numerical methods. Through the following explanations we hope the reader gains an understanding of the differences presented, adopts one or more appropriate methods specific to his/her requirements, and refers to the references for specific information.

Most models are unable to obtain the direct solution so they rely upon iterative solvers such as the successive over-relaxation (SOR), conjugate gradients (CG), preconditioned conjugate gradient method (PCG), and algebraic multigrid (AMG) solvers. While these methods have been developed for regular linear systems, they can also be applied in our semidefinite case. In the case of a consistent right-hand side, semiconvergence can be guaranteed for SOR and (P)CG, while the AMG theoretical results are more complicated [51]. A summary of each method is given based on [52] for the first three methods and [53, 54] for the last method.

A first difference between BEM and FEM or FDM is the domain in which the solutions are calculated. In the BEM the solutions are calculated on the boundaries between the homogeneous isotropic compartments while in the FEM and FDM the solution of the forward problem is calculated in the entire volume. Subsequently, the FEM and FDM lead to a larger number of computational points than the BEM. On the other hand, the potential at an arbitrary point can be determined with FEM and FDM by interpolation of computational points in its vicinity, while for the BEM it is necessary to reapply the Barnard formula [55] and numerical integration.

Another important aspect is the computational efficiency. In the BEM, a full matrix $(\mathbf{I} - \mathbf{C})$, represented in

$$V = CV + \mathbf{V}_0, \tag{4}$$

needs to be inverted. When the scalp potentials need to be known for another dipole, $\mathbf{V}_0$ in (4) needs to be recalculated and multiplied with the already available $(\mathbf{I} - \mathbf{C})^{-1}$. Hence once the matrix is inverted, only a matrix multiplication is needed to obtain the scalp potentials. This limited computational load is an attractive feature when solving the inverse problem, where a large number of forward evaluations need to be performed. Alternatively, an accelerated BEM approach increases the speed considerably by calculating only m (i.e., the number of electrodes) rows of the corresponding inverse, whereas, the normal inversion process requires a lot more time due to the dimensionality of the matrix as $n \times n$ (i.e., n equals the number of nodes) [56, 57]. Projective methods [58] based on the parametric representation of the surfaces also allow for a drastic reduction of the computational load.

For the FEM and the FDM, a direct inversion of the large sparse matrices is not possible due to the dimension of the matrices. Typically at least 500 000 computational points are considered thus leading to system matrices of 500 000 equations with 500 000 unknowns, which cannot be solved in a direct manner with the computers currently

Table 1: A comparison of the four methods for solving Poisson's equation in a realistic head model is presented: boundary element method (BEM), finite element method (FEM), isotropic finite difference method (iFDM), and anisotropic finite difference method (aFDM).

	BEM	FEM	iFDM	aFDM
Position of computational points	Surface	Volume	Volume	Volume
Free choice of computational points	Yes	Yes	No	No
System matrix	Full	Sparse	Sparse	Sparse
Solvers	Direct/iterative	Iterative	Iterative	Iterative
Number of compartments	Small	Large	Large	Large
Requires tessellation	Yes	Yes	No	No
Handles anisotropy	No	Yes	No	Yes

available. However, matrices found in FEM and FDM can be inverted for a given source configuration or right-hand side term, utilizing iterative solvers such as the successive over-relaxation method (SSOR), the conjugate gradient (CG) method [59], or algebraic multigrid (AMG) methods [60, 61]. A disadvantage of the iterative solvers is that for each source configuration the solver has to be reapplied. The FEM and FDM would be computationally inefficient when an iterative solver would need to be used for each dipole. To overcome this inefficiency the reciprocity theorem is used [62].

When a large number of conducting compartments are introduced, a large number of boundaries need to be sampled for the BEM. This leads to a large full system matrix, thus lower numerical efficiency. In FEM and FDM modeling, the heterogeneous nature of realistic head models will make the stiffness matrix less sparse and badly conditioned. Moreover, the incorporation of anisotropic conductivities will decrease the sparseness of the stiffness matrix. This can lead to an unstable system or very slow convergence if iterative methods are used. To obtain a fast convergence or a stable system, preconditioning should be used. Preconditioning transforms the system of equations $Ax = b$ into a preconditioned system $M^{-1}Ax = M^{-1}b$, which has the same solution as the orignal system. M is a preconditioning matrix or a preconditioner, and its goal is to reduce the condition number (ratio of the largest eigenvalue to the smallest eigenvalue) of the stiffness matrix toward the optimal value of 1. Basic preconditioning can be used in the form of Jacobi, Gauss-Seidel, Successive Over-Relaxation (SOR), and Symmetric Successive Over-Relaxation (SSOR). These are easily implemented [63]. More advanced methods use incomplete LU factorization and polynomial preconditioning [63, 64].

For the FDM in contrast with the BEM and FEM, the computational points lie fixed in the cube centers for the isotropic approach and at the cube corners for the anisotropic approach. In the FEM and BEM, the computational points, the vertices of the tetrahedrons and triangles, respectively, can be chosen more freely. Therefore, the FEM can better represent the irregular interfaces between the different compartments than the FDM, for the same amount of nodes. However, the segmented medical images used to obtain the realistic volume conductor model are constructed out of cubic voxels. It is straightforward to generate a structured grid used in FDM from these segmented images. In the FEM and the BEM, additional tessellation algorithms [65] need to be used to obtain the tetrahedron elements and the surface triangles, respectively, although cubic and rectangular prism elements are possible in FEM like FDM.

Finally, it is known that the conductivities of some tissues in the human head are anisotropic such as the skull and the white matter tissue. Anisotropy can be introduced in the FEM [66] and in the FDM [67], but not in the BEM.

5. Inverse Problem

While previous sections focused on the different steps preceding the application of inverse procedures, that is, head geometry approximations, conductivity, geometry profile, accuracy of conductivity values, and so forth, this section discusses some open issues including the selection of the recording modality, the source model, and possible post processing to improve the robustness of the inverse solution estimates.

5.1. Recording Modality: MEG versus EEG. The introduction of the Superconducting Quantum Interference Device (SQUID) made it possible to measure the very low magnetic fields induced by the electric activity of the brain, called magnetoencephalography, MEG.

In the beginning of biomagnetic research, there was a lot of hope that biomagnetic signals would include information independent on the bioelectric signals. As described by Plonsey [68], the fact that according to the Helmholtz theorem the scalar and the vector potential fields could be selected independently was considered as evidence for the independence of the electric and magnetic measurements. On the other side, considering the origin of the bioelectric currents it is concluded that the divergence and the curl of the primary current could not be really arbitrarily assigned. Further experiments described in [68] pointed to the relevant contribution of the secondary sources to both electric and magnetic fields. Thus, while we cannot claim that measures of bioelectric or biomagnetic fields alone are enough to define the other [69], we should not expect important differences on the information recorded by them.

The conclusion that electric and magnetic measurements provide comparable information has been confirmed on theoretical and simulation grounds. Using the novel concept

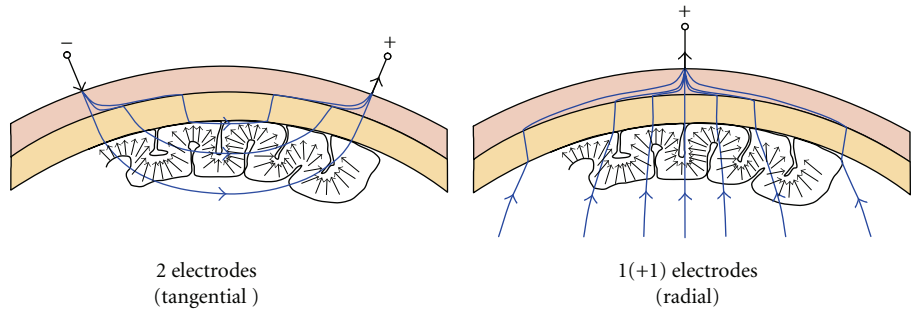

Figure 2: The Sensitivity Distributions of EEG. (Left) An EEG setup measuring the tangential components of neuroelectrical activity, where each bipolar lead is located relatively close to each other. (Right) An EEG setup measuring the radial components of neuroelectric activity, where the measuring electrode is located far from the reference electrode. The arrows in both figures represent macrocolumns of cellular architecture not dipolar sources.

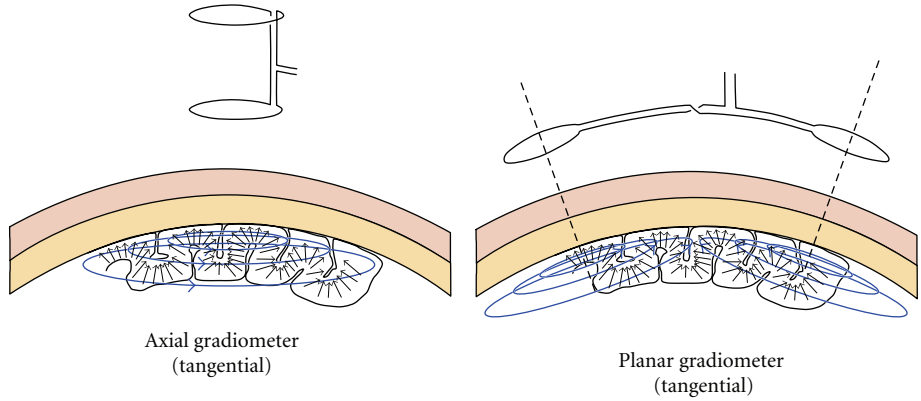

Figure 3: The Sensitivity Distributions of MEG. (Left) An MEG setup measuring the tangential components of neuroelectrical activity, using an axial gradiometer. (Right) An MEG setup measuring the tangential components of neuroelectric activity, using a planar gradiometer. The arrows in both figures represent macrocolumns of cellular architecture not dipolar sources.

of the half sensitivity volume, Malmivuo et al. [70] demonstrated that EEG and MEG record the electric activity in a very similar way, that is, the differences between the EEG and the MEG in the size of the half sensitivity volumes and the form of the sensitivity distributions are very small. Further evaluations of the spatial resolution for cortical sources in the spherical model led to better results for the EEG [71]. Using simulations [72] confirmed also a slight advantage of the EEG over many source locations and orientations with best results for the combined EEG/MEG measurements. More recently [73] applied pattern recognition techniques to decode hand movement directions from simultaneous EEG/MEG measurements, concluding that the inference of movement direction works equally well for both techniques.

Therefore, it may be beneficial to consider also the cost effect of the recording modality. The MEG instrumentation costs about 20 times more than the EEG instrumentation with the same number of channels. Thus, for improving the accuracy of the inverse solution it might be beneficial to first improve all aspects of the EEG technology, that is, number of channels, electrode location accuracy, head model geometry, and tissue resistivity accuracy, and so forth, because improving all these cost much less than the MEG instrumentation.

In summary we can confirm to the reader that besides the cost differences, these two techniques offer similar information about brain sources in what concerns accuracy of source localization, spatiotemporal resolution, and decoding or predictive power. We would like to highlight that although similar information is detected, the EEG and MEG measurement sensitivities are orthogonal. The EEG primarily detects electric sources that are radial to the scalp surface with sufficiently distant electrodes and tangential components when the leads are located near to each other (Figure 2); however, the MEG primarily senses magnetic currents generated by electric sources in the radial direction (Figure 3).

5.2. Source Models. There is vast literature reviewing the arsenal of methods available for the solution of the so-called bioelectromagnetic-inverse problem dealing with the estimation of the electrical activity (i.e., the distribution of sources) inside the head given external measurements of the electric and magnetic fields, for example, [44, 74, 75]. Nevertheless, before applying an inverse solution we must decide about the type of sources and their possible distribution (i.e., locations) inside the head.

The inverse solution estimators differ in source modeling assumptions. By comparing the number of unknowns of the source model with the amount of data, we can differentiate two main type of problems (i.e., of solutions). Firstly, overdetermined problems (e.g., dipolar solutions) with more data than unknowns can differ in minimization algorithms and their efficiency to escape local minima, measures of goodness of fit as well as the use of physiological and/or mathematical constraints often required in the solution estimation/selection process. These models require assumptions regarding the number and location of the brain sources modeled as point-current dipoles giving a unique solution provided that the global minimum is identified. Such approaches require a model order search in addition to a source parameter optimization [76]. Numerical simulation studies have demonstrated that an accurate estimation of the temporal dynamics of dipolar models is critically dependent on the ability to resolve and accurately localize all active brain regions [77]. While there is a range of physiological and anatomical reasons, animal studies as well as already converging evidence from the human hemodynamic and/or metabolic fMRI and PET studies suggest that the sensory and cognitive process can be considered as a network of distributed focal activity; possibility of extended activations of neuronal tissue in some conditions cannot be disregarded. In-depth electrode recordings used to be the primary evidence for the latter assumption, demonstrating activity over wide brain regions. However, even with such recordings, the summed contributions of the primary source contributions and volume currents are to be expected, and inverse models should be considered instead of taking such measures as strong evidence for extended brain activations.

On the other hand, we have the underdetermined problems (e.g., distributed inverse solutions) with more unknowns than data associated with the linear-minimum-norm approaches that is suggested [75, 78, 79] for cases when focal source assumptions are not justified. Such an approach is challenging as it might require further weighting and regularization to compensate for depth bias, selected by imposing mathematical criteria or physiological ones.

In order to help the reader make the correct choice, we describe four primary source models obtained by restriction on the source type and/or their location together with their main assumptions.

(1) *The equivalent-current dipole model.* It assumes that measurements are due to a single concentrated source. It is primarily valid for strong and spatially limited sources (e.g., some focal epilepsy) or sources observed from a far away measurement surface. It is probably more useful to summarize the measured field than the source itself, which is a particular case of the following source model.

(2) *Dipolar models as used in overdetermined problems.* These models consider that the measured fields are due to a small number of sources with unknown locations and orientations. They are very well suited for low-rank data as produced by filtered and averaged-evoked responses [80, 81].

(3) *Cortical model.* Under the extreme assumption that deep sources do not contribute to the external fields of the head, it assumes that the primary sources are located only in the cortical mantel with a direction constraint. It is probably very well suited for the analysis of measurements associated with the activation of some primary cortical areas [82].

Previous models can be considered as data driven in the sense that they can be only used under very specific and restrictive experimental conditions that will not be acceptable as a general model for the EEG and MEG sources. Furthermore, there is scarce experimental evidence in favor of the dipole. In fact a dipole would imply an indefinitely increasing potential when we approach its location. Hopefully, this has never been reported because that would correspond to an undefined potential at that location. Nevertheless, a more complete source model must contain, as a particular case, previous source models while incorporating those elements that are out of discussion so far, that is as follows.

(4) *Potential distribution inside the head.* The electromagnetic measurements at/near the scalp are due to the potential distribution inside the brain. These (intracranial) potentials that represent the primary source are generated in at, at least, the entire gray matter and not only at the cortex. This source model is compatible with all previous geometrical constraints while including the dipoles as a particular case. Importantly, this source model implies significant theoretical and numerical simplifications, solving also the issue of focal versus extended sources, since the potential is always a continuous function defined at all points of the head.

After defining the adequate preprocessing and source model for our data, we face the problem of the inverse procedure selection. The following issues might be relevant at this stage.

5.3. The Dipole Localization Error. The evaluation of the overdetermined-dipolar models seems to have a straightforward solution by comparing target and estimated sources with measures as the dipole localization error. Unfortunately, these measures cannot be directly extrapolated to underdetermined distributed solutions. This is probably why the evaluation of the distributed solutions remains as an open issue in this field. Obviously, this might influence the selection of the inverse solution. While we do not want to tell the reader what he/she should do/use, we would like to discuss some things to avoid.

It has been suggested that the zero dipole localization might be the way to select the inverse solution. This is likely motivated by genuine applications where the data is dominated by single focal sources (e.g., epilepsy focus localization) as well as by the long experience accumulated from overdetermined (dipolar) models. It is probably an abuse of language, which brings people to believe that "if we correctly localize each single source alone, then by the principle of superposition we should correctly localize any combination of sources". There are two clear inaccuracies with this statement.

(1) In this case, correct localization only means that the maximum of the modulus of the current source density coincides with the target site. This ignores that the amplitude will be, as is almost always the case for linear methods and multiple sources, misestimated due to the unavoidable off-diagonal elements on the resolution matrix (3).

(2) As the definition clearly states, the dipole localization error (DLE) is estimated from the modulus of the current source density, which means that the DLE is not a linear function of the data d, and thus the principle of superposition does not hold. Consequently, linear system theory, that characterizes the system by their response to (Delta like) input impulses, cannot be invocated.

Given previous theoretical flaws, it is not surprising that the DLE fails to predict the performance of an inverse solution in the presence of multiple sources. In fact it can be proved that correct localization of single sources is a trivial property of simple yet robust methods (see the work by Grave de Peralta et al. for this issue) that, we insist, are only applicable if the concentrated single source hypothesis holds.

5.4. Inverse Solutions and Spatial Filters. A sound approach for the inverse-problem solution in physical volumes is the estimation of spatial filters, which "filters out" the activity that arises from one special location, while trying to suppress the activity from all others. These methods that have reappeared nowadays under the name "beamformers" are very appreciated, among other things, because the solution can be computed independently for each solution point. Continuing with the original descriptions of these methods [83, 84], it was clear that minimizing crosstalk (i.e., distance to the ideal resolution matrix) between sources does not necessarily imply an optimal resolution kernel. Nevertheless, current applications suggest that the solution provided by these methods is not affected by the crosstalk.

There are very good reasons to select a Backus-Gilbert (i.e., beamformer) method such as its adaptive properties to deal with specific noise structures [85]. However, we cannot emphasize enough that the only way to assess the estimates provided by a linear inversion procedure is to look at the resolution kernels [2, 3, 86]. The fact that we build an independent estimate for each point alone does not mean that this estimate is not contaminated by the effect of simultaneously active sources.

In order to conclude the issue of the inverse procedure selection on a positive note, we mention that there is a sound theoretical way to select, and more importantly, to build an inverse solution. It is enough to note that infinitely-many-linear-inverse methods can be described by the equation $G = C * L' * (L * C * L')^{+}$. The source j_{est} estimated with this method will belong to the space spanned by the columns of $C * L'$ for both the noiseless and the noisy case. On the other hand, it is clear from (3) that the only way to change the rows of the resolution matrix (i.e., the resolution kernels) is by right transformations of the lead field. These two procedures together yield meaningful source estimates, when C is selected according to sound a priori information and when an appropriate right-hand transformation of the lead field is made [87].

5.5. Robust Methods for the Analysis of EEG/MEG Sources. The problem with the estimation of the EEG/MEG sources can be interpreted as follows. The measured data provides precise (up to the noise level) but local information. In order to know more about the whole system (i.e., the brain), we need to ascend to qualitatively higher levels corresponding to the surface maps and the 3D distribution of sources. By doing this we obtain a more complete global descriptor but probably also with a higher incertitude (if compared with the sensor data).

As it is also the case for the fMRI signal [88], in general we cannot rely on the amplitudes provided by the inverse solution to compare the neural activity at two different locations. For the same reason, ghost and lost sources appear in every reconstruction mixed with real sources. Thus, differentiating true sources from artifacts is almost impossible unless we know the real distribution. Consequently, we can say that the source distribution obtained from a single map is probably the most imprecise picture that we can have of brain activation.

What can we do to increase the reliability of these functional images? As for a partial answer, we suggest the following points.

(1) Select your inverse solution keeping in mind the previously discussed points about the spatial filters and the zero dipole localization error and consider with caution source distributions estimated from a single map (as produced, e.g., by segmentation algorithms).

(2) Use source models that reduce the underdetermination of the inverse problem. Give preference to physically sound transformations that reduce the problem to the estimation of scalar fields improving the resolution kernels.

(3) Compute magnitudes or figures of merit based on the temporal course of brain sources instead of the instantaneous local amplitudes and use measures that are independent of the scale factor of the intracranial signals like correlation coefficients.

(4) Evaluate contrasts between experimental conditions or prestimulus versus poststimulus conditions to reduce systematic ghost and lost source effects [31, 89].

(5) Compute correlations between magnitudes derived from the time course of the brain activity and behavioral measurements as reaction times [90].

6. Conclusion

There are many key areas that critically affect the accuracy and precision of source localization. In this paper we discussed the four key areas of EEG/MEG source imaging,

namely, preprocessing, the volume conductor, and the forward and inverse problems. Notwithstanding these wide-ranging components, we emphatically direct the community to allocate attention to these key open issues. Firstly, the conductivity equally affects the forward and inverse solution thus warranting the need for actual conductivity measurements on live tissue to fill the void of these critical parameters. These future studies should accurately document their measurement setups—most especially in terms of moisture and temperature. Secondly, future modeling studies should incorporate how pathologies alter a normal, healthy head model. Lastly, it is critical to select the source model and the inverse procedure based on sound theoretical and experimental basis.

Ultimately, we should make wise decisions to optimize elements of the model that gain the most precision and accuracy in source imaging and suppress those that contribute minimal gains in source localization. After such optimizations, how well do these future models represent their physiological counterpart, that is, the human head? As we proceed forward as a community, we should remember to highlight the shortcomings of future studies reflecting new conductivities, pathologies, source models, and so forth, to prevent any further misinterpretations of those models, while collectively building upon the contributions of past models.

Acknowledgments

This work has been partially supported by the European Project BACS FP6-IST-027140. This paper only reflects the authors' views, and the funding agencies are not liable for any use that may be made of the information contained herein. This work was also supported by the COST Action BM0601 "NeuroMath". Neither the COST Office nor any person acting on its behalf is responsible for the use, which might be made of the information contained in this publication. The COST Office is not responsible for the external websites referred to in this publication.

References

[1] D. Venes, *Taber's Cyclopedic Medical Dictionary*, F. A. Davis Company, Philadelphia, Pa, USA, 20th edition, 2005.

[2] A. M. Dale and M. I. Sereno, "Improved localization of cortical activity by combining EEG and MEG with MRI cortical surface reconstruction: a linear approach," *Journal of Cognitive Neuroscience*, vol. 5, no. 2, pp. 162–176, 1993.

[3] R. Grave de Peralta Menendez, S. L. Gonzalez Andino, and B. Lutkenhoner, "Figures of merit to compare distributed linear inverse solutions," *Brain Topography*, vol. 9, no. 2, pp. 117–124, 1996.

[4] A. J. R. Leal, A. I. Dias, and J. P. Vieira, "Analysis of the EEG dynamics of epileptic activity in gelastic seizures using decomposition in independent components," *Clinical Neurophysiology*, vol. 117, no. 7, pp. 1595–1601, 2006.

[5] P. Anderer, G. Kloesch, G. Gruber, et al., "Low-resolution brain electromagnetic tomography revealed simultaneously active frontal and parietal sleep spindle sources in the human cortex," *Neuroscience*, vol. 103, no. 3, pp. 581–592, 2001.

[6] P. Durka, A. Matysiak, E. M. Montes, P. V. Sosa, and K. J. Blinowska, "Multichannel matching pursuit and EEG inverse solutions," *Journal of Neuroscience Methods*, vol. 148, no. 1, pp. 49–59, 2005.

[7] C. E. Davila and R. Srebro, "Subspace averaging of steady-state visual evoked potentials," *IEEE Transactions on Biomedical Engineering*, vol. 47, no. 6, pp. 720–728, 2000.

[8] O. Bai, M. Nakamura, T. Nagamine, and H. Shibasaki, "Parametric modeling of somatosensory evoked potentials using discrete cosine transform," *IEEE Transactions on Biomedical Engineering*, vol. 48, no. 11, pp. 1347–1351, 2001.

[9] T. W. Picton, *Handbook of Electroencephalography and Clinical Neurophysiology: Human Event-Related Potentials*, Elsevier, Amsterdam, The Netherlands, 1988.

[10] B. H. Jansen, G. Agarwal, A. Hegde, and N. N. Boutros, "Phase synchronization of the ongoing EEG and auditory EP generation," *Clinical Neurophysiology*, vol. 114, no. 1, pp. 79–85, 2003.

[11] S. Rush and D. A. Driscoll, "EEG electrode sensitivity—an application of reciprocity," *IEEE Transactions on Biomedical Engineering*, vol. 16, no. 1, pp. 15–22, 1969.

[12] B. J. Roth, M. Balish, A. Gorbach, and S. Sato, "How well does a three-sphere model predict positions of dipoles in a realistically shaped head?" *Electroencephalography and Clinical Neurophysiology*, vol. 87, no. 4, pp. 175–184, 1993.

[13] A. Crouzeix, B. Yvert, O. Bertrand, and J. Pernier, "An evaluation of dipole reconstruction accuracy with spherical and realistic head models in MEG," *Clinical Neurophysiology*, vol. 110, no. 12, pp. 2176–2188, 1999.

[14] B. N. Cuffin, "EEG localization accuracy improvements using realistically shaped head models," *IEEE Transactions on Biomedical Engineering*, vol. 43, no. 3, pp. 299–303, 1996.

[15] M. S. Hamalainen and J. Sarvas, "Realistic conductivity geometry model of the human head for interpretation of neuromagnetic data," *IEEE Transactions on Biomedical Engineering*, vol. 36, no. 2, pp. 165–171, 1989.

[16] K. Wendel, N. G. Narra, M. Hannula, P. Kauppinen, and J. Malmivuo, "The influence of CSF on EEG sensitivity distributions of multilayered head models," *IEEE Transactions on Biomedical Engineering*, vol. 55, no. 4, pp. 1454–1456, 2008.

[17] K. Wendel, M. Osadebey, and J. Malmivuo, "Incorporating anthropometric and craniometric data into realistically-shaped volume conductor head models," in *Proceedings of the 11th World Congress on Medical Physics and Biomedical Engineering*, Munich, Germany, September 2009.

[18] J. Haueisen, C. Ramon, M. Eiselt, H. Brauer, and H. Nowak, "Influence of tissue resistivities on neuromagnetic fields and electric potentials studied with a finite element model of the head," *IEEE Transactions on Biomedical Engineering*, vol. 44, no. 8, pp. 727–735, 1997.

[19] H. P. Schwan, "Determination of biological impedances," in *Physical Techniques in Biological Research*, W. L. Nastuk, Ed., Academic Press, New York, NY, USA, 1963.

[20] C. Gabriel, S. Gabriel, and E. Corthout, "The dielectric properties of biological tissues—I: literature survey," *Physics in Medicine and Biology*, vol. 41, no. 11, pp. 2231–2249, 1996.

[21] L. A. Geddes and L. E. Baker, "The specific resistance of biological material—a compendium of data for the biomedical engineer and physiologist," *Medical & Biological Engineering*, vol. 5, no. 3, pp. 271–293, 1967.

[22] B. M. Radich and K. M. Buckley, "EEG dipole localization bounds and MAP algorithms for head models with parameter uncertainties," *IEEE Transactions on Biomedical Engineering*, vol. 42, no. 3, pp. 233–241, 1995.

[23] S. P. van den Broek, F. Reinders, M. Donderwinkel, and M. J. Peters, "Volume conduction effects in EEG and MEG," *Electroencephalography and Clinical Neurophysiology*, vol. 106, no. 6, pp. 522–534, 1998.

[24] G. Huiskamp, M. Vroeijenstijn, R. van Dijk, G. Wieneke, and A. C. van Huffelen, "The need for correct realistic geometry in the inverse EEG problem," *IEEE Transactions on Biomedical Engineering*, vol. 46, no. 11, pp. 1281–1287, 1999.

[25] B. Vanrumste, G. Van Hoey, R. Van de Walle, M. D'Havé, I. Lemahieu, and P. Boon, "Dipole location errors in electroencephalogram source analyssis due to volume conductor model errors," *Medical and Biological Engineering and Computing*, vol. 38, no. 5, pp. 528–534, 2000.

[26] N. G. Gencer and C. E. Acar, "Sensitivity of EEG and MEG measurements to tissue conductivity," *Physics in Medicine and Biology*, vol. 49, no. 5, pp. 701–717, 2004.

[27] J. O. Ollikainen, M. Vauhkonen, P. A. Karjalainen, and J. P. Kaipio, "Effects of local skull inhomogeneities on EEG source estimation," *Medical Engineering and Physics*, vol. 21, no. 3, pp. 143–154, 1999.

[28] R. Hoekema, G. H. Wieneke, F. S. S. Leijten, et al., "Measurement of the conductivity of skull, temporarily removed during epilepsy surgery," *Brain Topography*, vol. 16, no. 1, pp. 29–38, 2003.

[29] K. Wendel and J. Malmivuo, "Correlation between live and post mortem skull conductivity measurements," *Proceedings of Annual International Conference of the IEEE Engineering in Medicine and Biology Society*, vol. 1, pp. 4285–4288, 2006.

[30] C. M. Michel, G. Lantz, L. Spinelli, R. Grave de Peralta Menendez, T. Landis, and M. Seeck, "128-channel EEG source imaging in epilepsy: clinical yield and localization precision," *Journal of Clinical Neurophysiology*, vol. 21, no. 2, pp. 71–83, 2004.

[31] S. L. Gonzalez Andino, R. Grave de Peralta Menendez, A. Khateb, T. Landis, and A. J. Pegna, "Electrophysiological correlates of affective blindsight," *NeuroImage*, vol. 44, no. 2, pp. 581–589, 2009.

[32] K. L. Moore and A. F. Dalley, *Clinically Oriented Anatomy*, Lippincott Williams & Wilkins, Philadelphia, Pa, USA, 5th edition, 2005.

[33] T. F. Oostendorp, J. Delbeke, and D. F. Stegeman, "The conductivity of the human skull: results of in vivo and in vitro measurements," *IEEE Transactions on Biomedical Engineering*, vol. 47, no. 11, pp. 1487–1492, 2000.

[34] J. D. Kosterich, K. R. Foster, and S. R. Pollack, "Dielectric permittivity and electrical conductivity of fluid saturated bone," *IEEE Transactions on Biomedical Engineering*, vol. 30, no. 2, pp. 81–86, 1983.

[35] J. D. Kosterich, K. R. Foster, and S. R. Pollack, "Dielectric properties of fluid-saturated bone. The effect of variation in conductivity of immersion fluid," *IEEE Transactions on Biomedical Engineering*, vol. 31, no. 4, pp. 369–374, 1984.

[36] S. I. Goncalves, J. C. de Munck, J. P. A. Verbunt, F. Bijma, R. M. Heethaar, and F. L. da Silva, "In vivo measurement of the brain and skull resistivities using an EIT-based method and realistic models for the head," *IEEE Transactions on Biomedical Engineering*, vol. 50, no. 6, pp. 754–767, 2003.

[37] H. Griffiths, W. R. Stewart, and W. Cough, "Magnetic induction tomography. A measuring system for biological tissues," *Annals of the New York Academy of Sciences*, vol. 873, pp. 335–345, 1999.

[38] N. G. Gencer and M. N. Tek, "Electrical conductivity imaging via contactless measurements," *IEEE Transactions on Medical Imaging*, vol. 18, no. 7, pp. 617–627, 1999.

[39] N. Zhang, *Electrical Impedance Tomography Based on Current Density Imaging*, University of Toronto, Toronto, Canada, 1992.

[40] Y. Z. Ider, S. Onart, and W. R. B. Lionheart, "Uniqueness and reconstruction in magnetic resonance-electrical impedance tomography (MR-EIT)," *Physiological Measurement*, vol. 24, no. 2, pp. 591–604, 2003.

[41] A. Gevins, H. Leong, M. E. Smith, J. Le, and R. Du, "Mapping cognitive brain function with modern high-resolution electroencephalography," *Trends in Neurosciences*, vol. 18, no. 10, pp. 429–436, 1995.

[42] A. Gevins, J. Le, H. Leong, L. K. McEvoy, and M. E. Smith, "Deblurring," *Journal of Clinical Neurophysiology*, vol. 16, no. 3, pp. 204–213, 1999.

[43] F. Babiloni, F. Cincotti, F. Carducci, P. M. Rossini, and C. Babiloni, "Spatial enhancement of EEG data by surface Laplacian estimation: the use of magnetic resonance imaging-based head models," *Clinical Neurophysiology*, vol. 112, no. 5, pp. 724–727, 2001.

[44] C. M. Michel, M. M. Murray, G. Lantz, S. Gonzalez, L. Spinelli, and R. Grave de Peralta Menendez, "EEG source imaging," *Clinical Neurophysiology*, vol. 115, no. 10, pp. 2195–2222, 2004.

[45] A. Gevins, P. Brickett, B. Costales, J. Le, and B. Reutter, "Beyond topographic mapping: towards functional-anatomical imaging with 124-channel EEGs and 3-D MRIs," *Brain Topography*, vol. 3, no. 1, pp. 53–64, 1990.

[46] R. Srinivasan, P. L. Nunez, D. M. Tucker, R. B. Silberstein, and P. J. Cadusch, "Spatial sampling and filtering of EEG with spline laplacians to estimate cortical potentials," *Brain Topography*, vol. 8, no. 4, pp. 355–366, 1996.

[47] F. Babiloni, C. Babiloni, F. Carducci, et al., "High resolution EEG: a new model-dependent spatial deblurring method using a realistically-shaped MR-constructed subject's head model," *Electroencephalography and Clinical Neurophysiology*, vol. 102, no. 2, pp. 69–80, 1997.

[48] O. R. M. Ryynanen, J. A. K. Hyttinen, and J. Malmivuo, "Effect of measurement noise and electrode density on the spatial resolution of cortical potential distribution with different resistivity values for the skull," *IEEE Transactions on Biomedical Engineering*, vol. 53, no. 9, pp. 1851–1858, 2006.

[49] R. Srinivasan, D. M. Tucker, and M. Murias, "Estimating the spatial Nyquist of the human EEG," *Behavior Research Methods, Instruments, & Computers*, vol. 30, no. 1, pp. 8–19, 1998.

[50] Y. Wang and B. He, "A computer simulation study of cortical imaging from scalp potentials," *IEEE Transactions on Biomedical Engineering*, vol. 45, no. 6, pp. 724–735, 1998.

[51] A. Berman and R. Plemmons, *Nonnegative Matrices in the Mathematical Sciences*, SIAM, Philadelphia, Pa, USA, 1994.

[52] W. H. Press, S. A. Teukolsky, W. T. Vetterling, and B. P. Flannery, *Numerical Recipes in C*, Cambridge University Press, Cambridge, UK, 1995.

[53] J. W. Ruge and K. Stüben, "Algebraic multigrid (AMG)," in *Multigrid Methods*, S. F. McCormick, Ed., vol. 3 of *Frontiers in Applied Mathematics*, pp. 73–130, SIAM, Philadelphia, Pa, USA, 1987.

[54] W. L. Briggs, V. E. Henson, and S. F. McCormick, *A Multigrid Tutorial*, SIAM, Philadelphia, Pa, USA, 2000.

[55] A. C. L. Barnard, I. M. Duck, and M. S. Lynn, "The application of electromagnetic theory to electrocardiography—I: derivation of the integral equations," *Biophysics Journal*, vol. 7, pp. 443–462, 1967.

[56] Z. Akalin-Acar and N. G. Gencer, "An advanced boundary element method (BEM) implementation for the forward problem of electromagnetic source imaging," *Physics in Medicine and Biology*, vol. 49, no. 21, pp. 5011–5028, 2004.

[57] Y. Ataseven, Z. Akalin-Acar, C. E. Acar, and N. G. Gencer, "Parallel implementation of the accelerated BEM approach for EMSI of the human brain," *Medical and Biological Engineering and Computing*, vol. 46, no. 7, pp. 671–679, 2008.

[58] S. L. Gonzalez Andino, R. Grave de Peralta Menendez, R. Biscay, J. C. Jimenez, R. D. Pascual, and J. Lemagne, "Projective methods for the magnetic direct problem," in *Advances in Biomagnetism*, New York, NY, USA, 1989.

[59] B. N. Datta, *Numerical Linear Algebra and Applications*, Brooks/Cole, Pacific Grove, Calif, USA, 1995.

[60] W. L. Briggs, *A Multigrid Tutorial*, SIAM, Philadelphia, Pa, USA, 1987.

[61] R. Hoekema, K. Venner, J. J. Struijk, and J. Holsheimer, "Multigrid solution of the potential field in modeling electrical nerve stimulation," *Computers and Biomedical Research*, vol. 31, no. 5, pp. 348–362, 1998.

[62] P. Laarne, J. Hyttinen, S. Dodel, J. Malmivuo, and H. Eskola, "Accuracy of two dipolar inverse algorithms applying reciprocity for forward calculation," *Computers and Biomedical Research*, vol. 33, no. 3, pp. 172–185, 2000.

[63] Y. Saad, *Iterative Methods for Sparse Linear Systems*, SIAM, Philadelphia, Pa, USA, 2nd edition, 2003.

[64] L. A. Neilson, M. Kovalyov, and Z. J. Koles, "A computationally efficient method for accurately solving the EEG forward problem in a finely discretized head model," *Clinical Neurophysiology*, vol. 116, no. 10, pp. 2302–2314, 2005.

[65] J. F. Thompson, B. K. Soni, and N. P. Weatherrill, *Handbook of Grid Generation*, CRC Press, Boca Raton, Fla, USA, 1998.

[66] N. Ottosen and H. Peterson, *Introduction to the Finite Element Method*, Prentice-Hall, Englewood Cliffs, NJ, USA, 1992.

[67] H. I. Saleheen and T. Kwong, "New finite difference formulations for general inhomogeneous anisotropic bioelectric problems," *IEEE Transactions on Biomedical Engineering*, vol. 44, no. 9, pp. 800–809, 1997.

[68] R. Plonsey, "The nature of sources of bioelectric and biomagnetic fields," *Biophysical Journal*, vol. 39, no. 3, pp. 309–312, 1982.

[69] M. Hamalainen, R. J. Ilmoniemi, and J. Sarvas, "Interdependence of information conveyed by the magnetoencephalogram and the electroencephalogram," in *Theory and Applications of Inverse Problems*, H. Hario, Ed., John Wiley & Sons, New York, NY, USA, 1988.

[70] J. Malmivuo, V. Suihko, and H. Eskola, "Sensitivity distributions of EEG and MEG measurements," *IEEE Transactions on Biomedical Engineering*, vol. 44, no. 3, pp. 196–208, 1997.

[71] J. Malmivuo and V. E. Suihko, "Effect of skull resistivity on the spatial resolutions of EEG and MEG," *IEEE Transactions on Biomedical Engineering*, vol. 51, no. 7, pp. 1276–1280, 2004.

[72] A. K. Liu, A. M. Dale, and J. W. Belliveau, "Monte Carlo simulation studies of EEG and MEG localization accuracy," *Human Brain Mapping*, vol. 16, no. 1, pp. 47–62, 2002.

[73] S. Waldert, H. Preissl, E. Demandt, et al., "Hand movement direction decoded from MEG and EEG," *Journal of Neuroscience*, vol. 28, no. 4, pp. 1000–1008, 2008.

[74] M. Hamalainen, R. Hari, R. J. Ilmoniemi, J. Knuutila, and O. V. Lounasmaa, "Magnetoencephalography—theory, instrumentation, and applications to noninvasive studies of the working human brain," *Reviews of Modern Physics*, vol. 65, no. 2, pp. 413–497, 1993.

[75] R. Grave de Peralta Menendez and S. L. Gonzalez-Andino, "A critical analysis of linear inverse solutions to the neuroelectromagnetic inverse problem," *IEEE Transactions on Biomedical Engineering*, vol. 45, no. 4, pp. 440–448, 1998.

[76] S. Supek and C. J. Aine, "Simulation studies of multiple dipole neuromagnetic source localization: model order and limits of source resolution," *IEEE Transactions on Biomedical Engineering*, vol. 40, no. 6, pp. 529–540, 1993.

[77] S. Supek and C. J. Aine, "Spatio-temporal modeling of neuromagnetic data—I: multi-source location versus time-course estimation accuracy," *Human Brain Mapping*, vol. 5, no. 3, pp. 139–153, 1997.

[78] M. S. Hamalainen and R. J. Ilmoniemi, "Interpreting magnetic fields of the brain: minimum norm estimates," *Medical and Biological Engineering and Computing*, vol. 32, no. 1, pp. 35–42, 1994.

[79] O. Hauk, "Keep it simple: a case for using classical minimum norm estimation in the analysis of EEG and MEG data," *NeuroImage*, vol. 21, no. 4, pp. 1612–1621, 2004.

[80] M. Scherg and D. Von Cramon, "Evoked dipole source potentials of the human auditory cortex," *Electroencephalography and Clinical Neurophysiology*, vol. 65, no. 5, pp. 344–360, 1986.

[81] M. Scherg and T. W. Picton, "Separation and identification of event-related potential components by brain electric source analysis," *Electroencephalography and Clinical Neurophysiology. Supplement*, vol. 42, pp. 24–37, 1991.

[82] F. Babiloni, C. Babiloni, L. Locche, F. Cincotti, P. M. Rossini, and F. Carducci, "High-resolution electro-encephalogram: source estimates of Laplacian-transformed somatosensory-evoked potentials using a realistic subject head model constructed from magnetic resonance images," *Medical and Biological Engineering and Computing*, vol. 38, no. 5, pp. 512–519, 2000.

[83] J. Capon, "High resolution frequency-wavenumber," *Proceedings of the IEEE*, vol. 57, no. 8, pp. 1408–1418, 1969.

[84] G. E. Backus and J. F. Gilbert, "The resolving power of gross earth data," *Geophysical Journal of the Royal Astronomical Society*, vol. 16, pp. 169–205, 1968.

[85] K. Sekihara, S. S. Nagarajan, D. Poeppel, and A. Marantz, "Performance of an MEG adaptive-beamformer technique in the presence of correlated neural activities: effects on signal intensity and time-course estimates," *IEEE Transactions on Biomedical Engineering*, vol. 49, no. 12 I, pp. 1534–1546, 2002.

[86] B. Lutkenhoner and R. Grave de Peralta Menendez, "The resolution-field concept," *Electroencephalography and Clinical Neurophysiology*, vol. 102, no. 4, pp. 326–334, 1997.

[87] R. Grave de Peralta Menendez, M. M. Murray, C. M. Michel, R. Martuzzi, and S. L. Gonzalez Andino, "Electrical neuroimaging based on biophysical constraints," *NeuroImage*, vol. 21, no. 2, pp. 527–539, 2004.

[88] N. K. Logothetis and B. A. Wandell, "Interpreting the BOLD signal," *Annual Review of Physiology*, vol. 66, pp. 735–769, 2004.

[89] S. L. Gonzalez Andino, R. Grave de Peralta Menendez, A. Khateb, A. J. Pegna, G. Thut, and T. Landis, "A glimpse into your vision," *Human Brain Mapping*, vol. 28, no. 7, pp. 614–624, 2007.

[90] S. L. Gonzalez Andino, C. M. Michel, G. Thut, T. Landis, and R. Grave de Peralta Menendez, "Prediction of response speed by anticipatory high-frequency (gamma band) oscillations in the human brain," *Human Brain Mapping*, vol. 24, no. 1, pp. 50–58, 2005.

Hindawi Publishing Corporation
Computational Intelligence and Neuroscience
Volume 2009, Article ID 813607, 10 pages
doi:10.1155/2009/813607

Review Article

Multimodal Imaging of Human Brain Activity: Rational, Biophysical Aspects and Modes of Integration

Katarzyna Blinowska,[1] Gernot Müller-Putz,[2] Vera Kaiser,[2] Laura Astolfi,[3,4] Katrien Vanderperren,[5] Sabine Van Huffel,[5] and Louis Lemieux[6]

[1] *Department of Biomedical Physics, Warsaw University, Hoza 69, 00-681 Warszawa, Poland*
[2] *Laboratory of Brain-Computer Interfaces, Institute for Knowledge Discovery, Graz University of Technology, 8010 Graz, Austria*
[3] *Department of Computer Science and Systems, University of Rome "Sapienza", Via Ariosto 25, 00185 Rome, Italy*
[4] *Fondazione S.Lucia,, Via Ardeatina 306, 00179 Rome, Italy*
[5] *Research Division SCD, Department of Electrical Engineering, Katholieke Universiteit Leuven, 3001 Leuven, Belgium*
[6] *Department of Clinical and Experimental Epilepsy, UCL Institute of Neurology, Queen Square, London WC1N 3BG, UK*

Correspondence should be addressed to Louis Lemieux, l.lemieux@ion.ucl.ac.uk

Received 3 April 2009; Accepted 5 April 2009

Recommended by Fabio Babiloni

Until relatively recently the vast majority of imaging and electrophysiological studies of human brain activity have relied on single-modality measurements usually correlated with readily observable or experimentally modified behavioural or brain state patterns. Multi-modal imaging is the concept of bringing together observations or measurements from different instruments. We discuss the aims of multi-modal imaging and the ways in which it can be accomplished using representative applications. Given the importance of haemodynamic and electrophysiological signals in current multi-modal imaging applications, we also review some of the basic physiology relevant to understanding their relationship.

1. Introduction

Since the mid 1990s there has been an increase in interest in synchronous multi-modal imaging, whereby two modalities or more are used simultaneously, which has arisen in large part from investigators interested in the study of spontaneous brain activity and in particular epilepsy. Although the electroencephalogram (EEG) was previously combined with PET, the advent of simultaneous EEG-fMRI (and optical imaging techniques, such as NIRS) with temporal resolutions of the order a second or less has lead to multiple applications in and outside the field of epilepsy.

The overarching motivation for integrating data from multiple modalities is to gain a more complete picture of the brain activity of interest. Implicit in the multi-modal integration or multi-modal imaging is the notion that all measurements relate to the same activity in space and time. Therefore at the most basic level, multi-modal integration can mean spatial coregistration of the observations. Coregistration in time can mean two things: either measurements are performed simultaneously (same time of day), simultaneous EEG-fMRI of randomly occurring epileptic discharges being an example; or monomodality measurements made at the same time relative to an event but not simultaneously, that is, serially. Examples include separate ERP and fMRI studies in relation to the same stimulus subsequently brought together through correlation of the responses (as a function of some externally controlled factor) or the spatial coregistration of independently derived source localisation estimates. Serial multi-modal integration implies a degree of predictability and more importantly reproducibility of the events: the retrospective integration of serially acquired datasets is actually restricted to the reproducible aspects of the activity of interest, such as effects averaged across repeated events.

The integration of electrophysiological and haemodynamic signals (BOLD, CBF, CBV) is particularly important in the context of this discussion for two reasons: their intrinsic

importance and complementarity, and data availability. Electrophysiological signals are particularly important given the direct link between EEG/MEG and neuronal synchrony. On the other hand localisation based on EEG/MEG is fundamentally limited. The more indirect link between haemodynamic signals and neuronal activity is partly compensated by our capacity to obtain 3D maps covering almost the entire brain and with good spatial resolution particularly for fMRI. While numerous observations have shown that BOLD changes can be related with various forms of brain activity, such as the haemodynamic response to external stimuli recently, which makes fMRI possible and useful, much remains to be learnt. Recently, experiments have focused more specifically on the relationship between neuronal activity measured at the microscopic level and the BOLD effect.

2. Basic Studies of the Relationship between the BOLD Signal and Brain Activity

2.1. The Neuronal Correlates of the BOLD Signal. The chain of events and factors that links neuronal activity to BOLD signal change is long (Figure 1), and the transitions between them are far from simple. Neural activity through neurovascular coupling influences the metabolic demand. Metabolic changes impact on haemodynamic response which is dependent on physiological factors such as local cerebral blood flow, deoxyhaemoglobin/oxyhaemoglobin ratio, blood volume, and vascular geometry. Therefore, inferences in fMRI concerning neural activity rely on the accuracy, validity, and efficiency of prespecified models and hypotheses.

A model elucidating the basis of BOLD signal was formulated by Friston et al. [1], furthering the Balloon model of Buxton et al. [2], which described how evoked changes in blood flow were transformed into fluctuations in blood oxygenation level. The Balloon model was embedded in a haemodynamic input-state-output model that included the dynamic of perfusion changes that are contingent on underlying synaptic activation. In the model of Friston et al. it was assumed that neural activity is linearly coupled to the metabolic demand, but the relationship between blood flows and BOLD is non-linear. The model provides a level of explanation for the biphasic shape of the haemodynamic response function, with a positive peak around 6 seconds following event or stimulus onset, followed by a negative undershoot at around 15 seconds (first to second peak amplitude ration ~6) and gradual recovery to baseline.

However, a general assumption is of a linear relationship between certain measures of neural activity and BOLD signal, which finds confirmation in some experimental studies for example: [3, 4]. Nevertheless it was demonstrated that nonlinear refractoriness of BOLD responses can occur at very short interstimulus intervals [5]. It was also reported in another study that BOLD signal increases linearly with positive stimulus amplitude, but for negative amplitude of stimulus highly nonlinear behaviour ensues and that the response to a second stimulus was compromised by first, evidencing a nonlinear refractoriness of the BOLD response, possibly of haemodynamic origin [6]. These studies point out that the results of the fMRI studies of evoked activity depend strongly on the choice of the interstimulus interval.

Several factors in the chain of events from neuronal activity to vascular changes are difficult to account for in models of the BOLD effect. For example, the details of the vascular architecture and the presence of large veins in the vicinity of the activated neurons. Microvascular density, which is lower than that of neurons and is affected by large vessel contribution, may influence the results and may be a limiting factor of spatial resolution of BOLD signal [7]. Which aspect, or expression, of neuronal activity is best reflected in the BOLD signal namely potential firing versus synaptic activity remains unclear. This problem was reviewed in [8, 9], where the contradictory opinions were discussed. Namely the empirical evidence was quoted suggesting that the spikes generated by cortical cells contribute little to the metabolic demand of brain, accounting for only 3% of the resting cortical energy consumption; also experiments performed on rates show that up to 95% of regional cerebral blood flow increases might be dependent on postsynaptic activity. However another contribution reported a correlation between spiking activity and BOLD signal [10]. In fact, spiking activity and synaptic potentials are related to each other. Nevertheless the comparative studies indicated that the BOLD signal matched (Local Field Potentials) LFPs better than multiunit spiking activity [4].The findings of the same study suggest that the BOLD contrast mechanism reflects the input and intracortical processing of a given area rather than its spiking output.

BOLD decreases (sustained decreases, in contrast to the transient negative undershoot of "positive" haemodynamic response function) have been reported in relation to some stimuli and events, such as epileptic spikes. Simultaneous fMRI measurements and electrophysiological recordings revealed a negative BOLD response beyond the stimulated regions of visual cortex, associated with local decreases in neural activity as expressed in terms of LFP power below the level of spontaneous (background) activity [11].

The relationship between neuronal inhibition and BOLD is currently under debate. Since the inhibitory activity similarly to excitatory processes requires energy, inhibition can be associated with increased metabolic demand which may be reflected as BOLD increase. On the other hand most connections in the brain are excitatory and decrease of excitatory activity caused by inhibition may lead to a decrease of blood flow. Experimental results point out that both arguments may be valid. Mathiesen et al. [12] found comparable cerebral blood flow increases during stimulation of excitatory and inhibitory pathways in cerebellum. However, studies using agonists of inhibitory transmitters have generally shown decreases in measured energy metabolism for example: [13, 14]. Modelling studies [15] have demonstrated that there are several factors that may play the role in the impact of inhibition on imaging results: local connectivity, type of inhibitory connection, and the kind of task. Depending on these factors neuronal inhibition may result in BOLD increases if the region is not driven by excitation or there is low local excitatory recurrence. Alternatively for active

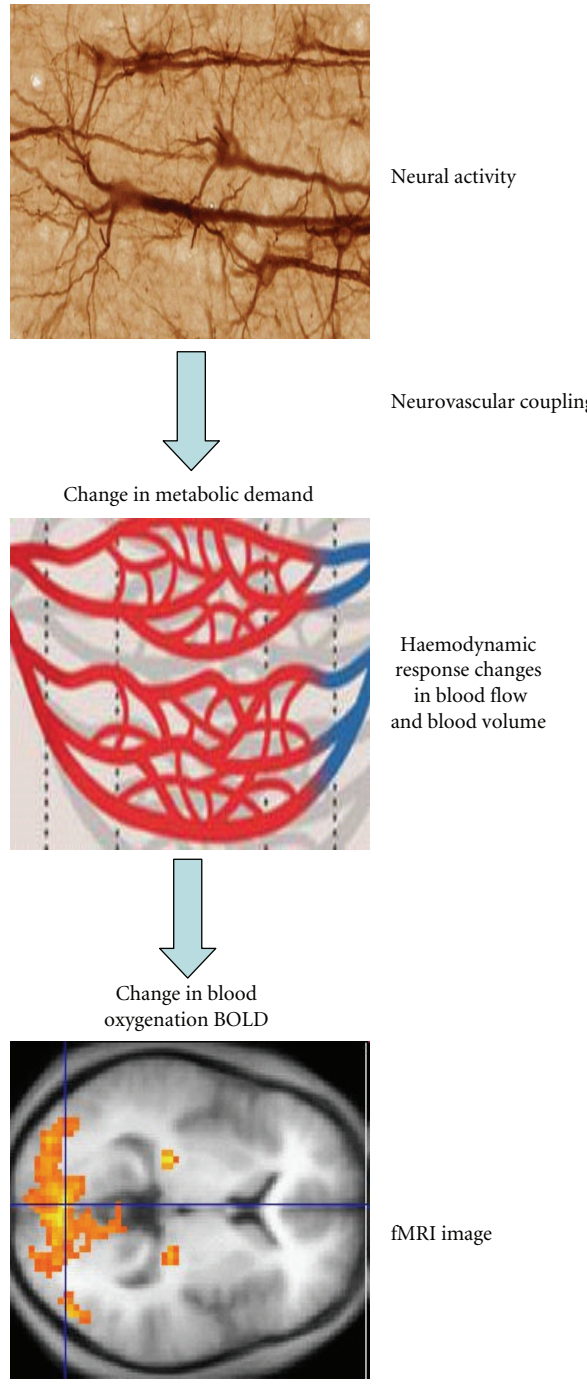

Figure 1: From neural activity to fMRI image.

excitation or high recurrence, inhibition may lead to BOLD decreases.

Another interesting and still unresolved problem is whether fMRI can differentiate between small activity changes in large cellular populations, and large changes in small populations. The resolution in typical fMRI scanner is ~8–50 mm^3, which corresponds to at least 10^6 neurons. The highest resolution corresponds to one cortical column which contains 10^5 neurons. Therefore in the case of an apparatus of typical resolution several neural populations of different activity patterns may be scanned.

2.2. BOLD versus Brain Oscillations. At the macroscopic level, while BOLD reflects the number of active neurons, EEG/MEG amplitude depends primarily on the number of neurons acting synchronously. As was pointed out by Nunez [16] the activity of synchronously acting neurons

is proportional to their number and for asynchronously acting neurons it is proportional to the square root of their number. There are about 10^8 neurons located within range of a standard EEG electrode; supposedly all of them are continuously active, but only 1% of them acting synchronously. The latter's contribution to the scalp signal will be 10^6/sqrt (10^8–10^6), that is, 100 times greater than the 99% nonsynchronised neurons. Therefore asynchronous neural activity will be hardly reflected in EEG, in contrast to fMRI.

The synchronous action of neural populations gives rise to the characteristic EEG rhythms, which have specific roles in the information processing by brain. Specific tasks such as movements or perceptions are connected with the synchronization and desynchronization of EEG in specific frequency bands. It is therefore of importance to establish the relations between the electroencephalographic rhythmical activity and fMRI results. A heuristic model relating haemodynamic changes to the spectral profile of ongoing EEG activity was elaborated by Kilner et al. [17]. The assumptions of the model were that the BOLD signal is proportional to the rate of energy dissipation, where dissipation was expressed as a product of trans-membrane potential and current. The authors found that the metabolic response is proportional to the "effective connectivity" and temporal covariance of the trans-membrane potentials. "Effective connectivity" in the sense of synaptic efficacies was expressed as a Jacobian J, with diagonal elements reflecting effective membrane conductance. The measure of change of effective connectivity is expressed by parameter α, defined by,

$$J(\alpha) = J(0) + \frac{\alpha \partial J}{\partial \alpha}, \tag{1}$$

where $J(\alpha) = J(0)$ corresponds to the resting state. This model of activation postulates that an increase of α caused an acceleration of dynamics of the neural system and consequent increase of the system's energy dissipation. Next the authors connected the acceleration with the spectral properties of the system. Namely they have shown that the activation modulates the EEG spectral density $g(\omega)$ according to

$$\tilde{g}(\omega) = \frac{g((1+\alpha)\omega)}{1+\alpha}, \tag{2}$$

where ω is the circular frequency and $\tilde{g}$ is the modulated spectral density.

From (1) and (2) it follows that activation causes a shift of EEG spectral profile towards higher frequencies with amplitude decrease. This means that as neuronal activation increases there is a concomitant increase in BOLD signal and shift in the spectral power towards higher frequencies.

Indeed, the relative decrease of BOLD signal for low frequency EEG rhythms and an increase in high frequencies found experimental confirmation. The simultaneous EEG/fMRI studies have shown that alpha rhythm is negatively correlated with BOLD signal, for example: [18, 19], also in the experiment involving low-frequency entrainment the reduction of BOLD was reported [20]. In the same publication predominantly positive correlations between EEG and fMRI were found in the higher frequency bands: 17–23 Hz and 24–30 Hz.

These findings support the model; however it does not account for some low frequency phenomena in brain, as the authors of [17] admit themselves. Namely it has been reported that very slow EEG activity fluctuations in the monkey visual cortex were reflected in the BOLD signal [21]. It seems that the further studies concerning simultaneous EEG-fMRI studies as well as improvement of models are needed to unravel the mechanisms underlying manifestation of rhythmic brain activity in the imaging studies.

Finally, the relationship between electrophysiological signals and BOLD will be greatly affected by the fluctuations of the background activity which may influence the evaluation of evoked activity hampering the estimation of stimulus-related responses. On the other hand the fMRI investigation of spontaneous activity offers the new possibilities in the investigations of brain rhythms, sleep patterns, and epilepsy [8].

3. Modes of Multimodal Fusion at the Macroscopic Level

3.1. EEG versus FMRI: Illustration in Motor Imagery. The purpose of even more advanced fusion of multi-modal data in relation to a specific type of brain activity is to overcome some of the limitations of individual measurements. In this section we will consider examples of single-modality studies of a specific cognitive, namely, motor imagery. More specifically, we will review and contrast investigations of motor execution, passive movements, and movement imagination in spinal cord injured (SCI) using EEG and fMRI separately.

In an EEG study by Müller-Putz et al. [22] event-related desynchronization/synchronization (ERD/ERS) patterns in paraplegic patients (suffering from a complete spinal cord injury) are compared with able-bodied controls during attempted (active) and passive foot movements. The aim was to address the question, whether patients do have the same focal beta ERD/ERS pattern during attempted foot movement as normal subjects. For this purpose EEG was recorded from sixteen sintered standard scalp electrodes. The results showed a mid-central focus of beta ERD/ERS patterns during passive, active, and imagined foot movements in normal subjects. This is in contrast to a diffuse and broad ERD/ERS pattern during attempted foot movements in patients. Only one patient showed an ERD/ERS pattern similar to able-bodied subjects. Furthermore, no significant ERD/ERS patterns during passive foot movement in the group of the paraplegics were found. In a further EEG study [23] a 3-class Brain-Computer Interface motor imagery screening (left hand, right hand, feet) was performed in a group of able-bodied and spinal cord injured participants. EEG was recorded from 15 scalp electrodes. Comparing Brain-Computer Interface classification accuracy we found a significantly lower classification rate in the patients compared to the healthy subjects. In conformity with the results

discussed above, ERD/ERS patterns are diffuse and scattered in the patients group.

Using fMRI Alkadhi et al. [24] measured imagination of foot movements in able-bodied and SCI participants (lesion height from Th3 to L1, range of age was 22–43 years). They found that the degree of BOLD activation (contra-lateral M1 and S1 foot representation; bilaterally SMA, pre-SMA, CMA, and further) was significantly higher in the SCI patients as compared to the able-bodied participants. It is of interest to note that the SCI patients showed a strong correlation with their vividness scores for motor imagery. One explanation for the enhanced activation in SCI patients could be that they were engaged in the task and displayed a higher mental effort as compared to the able-bodied subjects. In a further fMRI study Enzinger et al. [25] compared BOLD patterns of motor imagery patterns in a remarkable SCI patient, who was well trained in motor imagery (extensive training for a period of several years), to a group of able-bodied controls. In the patient significant activation of sensorimotor networks (sensorimotor cortex contralateral to side of movement imagination, SMA, pre-SMA, and further) occurred during imagery of repetitive hand and foot movements (versus rest); whereas in able-bodied subjects significant activation only occurred in relation to hand motor imagery and only in premotor areas (pre-SMA). No significant activation could be demonstrated within the sensorimotor cortex in the control group. The pattern of activation found in the patient during motor imagery corresponded to the pattern of activation found in controls during motor execution.

The possible explanations for the contrasting results of the EEG and fMRI studies include: experimental factors (such as intersubject variability and differences in experimental conditions) or biological factors. Using simultaneous EEG and fMRI acquisitions would eliminate intersession (and therefore intermodality) experimental confounds opening the way for greater biological insights. For example, one could assess whether the results reflect a mismatch between the BOLD effect, and whichever aspect of the EEG was used. Such studies have already been performed for ERD. For example Formaggio et al. [26] used combined EEG-fMRI over motor areas during finger movements and found a negative correlation between EEG power changes and BOLD activity contra-lateral to the movement. Significant ERD in alpha and beta frequency bands were associated with activation of the anterior and posterior central sulcus in both sensorimotor areas.

3.2. FMRI-Informed EEG: Haemodynamic Priors for Cortical Activity and Conectivity Estimation . In this section, we will review some examples of how information obtained from fMRI recordings can be used to improve the accuracy of the estimation of the cortical activity and connectivity from EEG recordings. There is experimental evidence suggesting that the estimation of the cortical activity performed with the use of neuroelectromagnetic recordings improves with the use of the haemodynamic information recording during the same task [27–30]. This was also demonstrated during simulation studies [27, 29, 31].

In [32] the impact of the use of a priori information from fMRI recordings in the EEG-based estimation of the cortical activity and connectivity was reported. The data used were related to high resolution EEG and fMRI signals collected during visually triggered finger tapping movements in four healthy subjects. The methods include the use of subjects' multicompartment head models (scalp, skull, dura mater, cortex) constructed from MRI, multidipole source model, and regularized linear inverse source estimates of cortical current density [33, 34]. The priors in the resolution of the linear inverse problem were derived from the haemodynamic responses of the cortical areas as revealed by block-designed (strength of activated voxels) and event-related (coupling of activated voxels) fMRI. The multimodal integration of EEG and fMRI data was performed using a metric which takes into account the haemodynamic information offered by the recorded fMRI data as a norm in the source space. As described in [31] the contribution of the fMRI priors in the estimation of the cortical current density is given by the statistically significant percentage increase of the fMRI signal during the task, compared to the rest state. The statistical significance of the cortical activity obtained was assessed by computing the z-score with respect to the rest period. Cortical activity was significantly increased in the left ROIs representing parietal (BA 5), premotor (BA 6A), sensorimotor (BA 3, 2, 1, BA 4), and prefrontal (BA 8 and BA 9) cortical areas, and similarly for the ROIs located in the right hemisphere in premotor (BA 6A) and prefrontal (BA 8) cortical areas.

Connectivity estimations on the cortical waveforms obtained by the multimodal integration of EEG and fMRI recordings were performed. The connectivity was estimated by means of the Directed Transfer Function [35], a method to determine the directed influences between any given pair of signals in a multivariate data set. The approach is based on the concept of Granger causality and uses a multivariate autoregressive model (MVAR) simultaneously modelling the entire set of signals [36]. The application of DTF to linear inverse estimate of the cortical activity was described in [37–39].

The main results obtained with the multimodal integration of ERP and fMRI data were related to the activity of a network involving the right frontoparietal cortical structures. The flow of the connections moved from the parietal and premotor areas towards the right and left prefrontal ones. The ROIs located at the parietal (B.A.5) and premotor areas (B.As 6) revealed as the source of an activity that spreads and reaches virtually all the other ROIs considered, from the occipital (B.A. 19) to the prefrontal (B.A. 9, 46) areas of both hemispheres.

These results were compared to those obtained on the same data set in [38] with the use of the EEG data without fMRI priors. A substantial agreement between the two sets of connectivity patterns (with and without fMRI priors) can be appreciated, although differences are present in some cortical areas, in the intensity of the cortical connections. While the parietal and frontal connections are revealed in both the estimations, a shift of the intensity is observed in the connectivity patterns computed by using EEG and fMRI

information when compared to those obtained using only the EEG data.

Similar results were obtained by estimating the cortical connectivity patterns in the beta band from the high resolution EEG recordings obtained during the execution of the Stroop task, with and without fMRI priors [40, 41]. In this case it can be noted that a substantial agreement exists for the connectivity patterns obtained, that show an involvement of the parietal and the frontal areas. This finding is similar to that already observed in the finger tapping experiment, as in this case the intensity of the DTF estimated by the cortical waveforms obtained with the multimodal integration was significantly higher than that obtained by using only the EEG information. Slight differences in the cortical pattern in different cortical areas were noted.

We conclude that the inclusion of fMRI priors in the estimation of cortical activity and connectivity from high resolution EEG can add information to the estimation and help to define the role of some specific cortical areas in the flow of information necessary to the execution of a specific task.

3.3. Simultaneous EEG-FMRI of Spontaneous Brain Activity: Epilepsy. Simultaneous multi-modal acquisitions make it possible to acquire signals in identical experimental conditions. Assuming that data quality is preserved continuous acquisition synchrony means that the same events are captured and can be studied across modalities. Therefore synchronous multi-modal acquisitions make it possible to study signals related to events over which one has no experimental control, that is, spontaneous brain activity in the resting state. An important example of this is epileptic activity which can be captured on EEG, an important investigative and clinical tool in the field of epilepsy (And visually of course, in the case of seizures; there have been a number of (single-modality) fMRI studies of seizures, for example, [42–44].).

Due to its potential clinical impact in cases with drug-resistant epilepsy considered for surgical resection, localisation of the generators of epileptic activity is a central issue in the field of epilepsy imaging. Although EEG provides important clinical information its ability to localise generators is fundamentally limited by the nonunicity of the inverse electromagnetic problem [45]. However, tomographic modalities such as fMRI do not suffer from this limitation. Therefore, as early as 1993, only a few years following the demonstration of BOLD fMRI, investigators in Boston started working on combined EEG and fMRI acquisitions [46–48]. The key driver for this methodological development is the lack of overt manifestation during or following an interictal spike (in contrast to seizures, which are rarer and generally more difficult to study using fMRI due to motion and safety considerations). In the context of fMRI this means that the only way of tagging scans according to brain state (e.g., IED versus. background) necessary for modelling the BOLD changes is to record the EEG simultaneously.

Studies using EEG-fMRI applied to epilepsy generally follow the asymmetric, EEG -> fMRI, mode of integration: the EEG's sole purpose is as a basis for fMRI modelling, that is, to answer the question, what are the BOLD correlates of the EEG events? For example, early applications used a spike-triggered acquisition mode whereby each fMRI scan (or burst of scans) was acquired following the visualisation of a spike, and a corresponding number of scans acquired following periods of background activity [49–54]. It is important to remark that this (nonperiodic) interleaved acquisition scheme was also motivated by one of the key issues in synchronous multi-modal data acquisition: data quality degradation due to interaction between each modality's hardware. In the case of EEG recording inside MR scanners, the problem of pulse-related and image acquisition artefacts arises. By implementing a pulse-artefact reduction scheme, the authors were able to increase the reliability of spike detection; by limiting scanning to short bursts following events of interest, they limited the impact of the image acquisition artefact [50, 51]. Subsequently, the development of software techniques to allow recording of good quality EEG during continuous scanning gave rise to the more flexible technique of continuous and simultaneous EEG-fMRI [55].

In the spike-triggered approach spike-related activation was determined by applying voxel-wise t-tests across the two scan sets. For datasets acquired using the analytical framework of event-related designs is employed, whereby EEG events of interest are identified, marked, and represented mathematically to form the basis of a general linear model of the entire BOLD time course and conforms to the EEG -> fMRI, mode of integration [55, 56]. In an extension of the straightforward EEG -> fMRI mode of integration Liston et al. tested the significance and localisation of BOLD changes linked to EEG epochs below the threshold of visual spike detection, but marked as possible spikes by an automated algorithm, and were able to demonstrate the epochs' probable epileptiform nature [57]. In the not so distant future, we envisage that the availability of biophysical models linking neuronal activity to EEG and BOLD signals that can be inverted should result in more symmetrical improved estimation of neuronal generators.

3.4. Simultaneous ERP-FMRI: Single Trials. Event-related potentials (ERPs) are EEG responses to specific sensory, cognitive and motor events [58]. Despite the rich temporal information provided by ERPs, they suffer from the same spatial resolution limitations as other scalp EEG patterns. The integration of ERP and fMRI may provide a more complete spatiotemporal characterisation of evoked responses through the study of individual trials.

To this end a major breakthrough was achieved when simultaneous EEG and fMRI recordings became feasible [59], safe [60], and of sufficient quality [61–63]. As mentioned above, synchronous acquisitions remove intermodality bias relative to experimental conditions [64]; for example, Novitski et al. [65] showed, that the loud noise of the scanner can influence how the brain reacts to certain stimuli.

In addition, simultaneous recordings allow the investigation of relationships between event-related potentials and BOLD responses across individual events.

In the following, we illustrate four approaches to the analysis of simultaneously acquired ERP-fMRI, namely, ERP-informed fMRI analysis, the use of constrained source localisation, parallel independent component analysis (ICA), and joint ICA.

The general idea behind *ERP-informed fMRI* analysis is to identify brain regions with fMRI responses that reflect paradigm-related amplitude modulations in individual ERPs. In [66], for instance, EEG data were acquired during an auditory target detection (oddball) paradigm and both ICA and wavelets were applied to denoise the data. Subsequently single-trial N1, P2 and P3 amplitudes [67] were extracted from the data. The resulting vectors were convolved with the haemodynamic response function (HRF) and used as regressors in a general linear model (GLM) for the BOLD time course. The findings confirmed that the combination of ERP and fMRI enables identification of regional responses in the fMRI, reflecting a specific aspect of varying potentials. Similarly, Debener et al. [68, 69] applied ICA to isolate task-related activity from a typical EEG mixture of overlapping brain and nonbrain sources. These single-trial amplitudes from selected independent components preserve event-related trial-by-trial fluctuations within each condition and can thus be correlated with the BOLD response. This research showed that ICA is a practical solution to minimise artefacts and identify functionally meaningful EEG activity on a trial-by-trial basis. Another example of this approach can be found in [63] where subjects performed an auditory oddball task during simultaneous EEG-fMRI measurements. They showed significant BOLD effects related to ERP latency and amplitude.

In a further refinement, regions of interest (ROIs) were extracted from the fMRI maps [70] and used as *constraints* in *source localisation* analysis. The cortical generators thus found, corresponded highly to findings by means of intracranial measurements and the different timing of activations associated with the task paradigm could also be appreciated. As such, this method improved the solution of the inverse EEG problem and enabled the study of the dynamic behaviour of ROIs.

The abovementioned methods rely on the assumption that scalp EEG data from both a selected channel and latency can predict BOLD changes in single voxels [71]. However, this is not physiologically plausible, because event-related processes might be spatially and temporally mixed across the brain. Therefore, Eichele et al. [71] propose "*parallel ICA*" to unmix EEG and fMRI separately and to match temporal sources from the EEG with spatial sources from the fMRI.

The above approaches are asymmetric in the use of data, namely, EEG for analysis of fMRI data or vice versa. Moosmann et al. [72] propose a symmetric approach by not only combining EEG and fMRI in one common data space but also by applying a *joint ICA* model to these data. Therefore features of neural sources whose trial-to-trial dynamics are jointly reflected in both modalities can now be studied.

ERP-informed fMRI is so far the most widely validated method; it has already been studied in numerous applications. Since it allows tracking and correlating the trial-to-trial variability of both EEG and fMRI, it provides detailed information about regional fMRI responses with the temporal accuracy typical of EEG. Furthermore, the second proposed method, constrained source localisation, is based on the same principles but additionally uses the ERP-informed fMRI regions as constraints for further source localisation. Unfortunately, both these methods suffer from several important drawbacks. First of all they leave room for improvement concerning the proportion of EEG data used for integration [72]. The reason for this is that all these studies take into account only certain features of the data and therefore possibly disregard important temporal or spatial information. In addition, the observed data from both modalities often represent a mixture of signals coming from multiple neural sources. A voxel-by-voxel prediction of the fMRI signals based on the ERP data (even after application of ICA on these ERPs) may therefore become unreliable when multiple sources contribute to either the predictor or the response variables. The parallel ICA approach tries to address both these issues, but still shares a disadvantage with the above methods, namely, the asymmetry of the procedure. In the joint ICA approach both modalities are therefore assembled and decomposed in one common data space. As such an asymmetric information flow is no longer present. A limitation of joint ICA is however that it cannot reflect the time domain of event related oscillations that are not time locked within one component [72].

ICA is clearly emerging as an important analytical tool, reflecting the exploratory nature of work on EEG and fMRI data fusion at the level of single events. However, the relevance of the assumptions on which ICA is based with regard to the separation of the source activity into electrical and haemodynamic components requires further testing. Furthermore, not enough validation has yet been performed to conclude whether one of the above methods performs much better than the others. So far the performance of the methods seems highly dependent on the application of interest.

4. Conclusion

The relationship between the BOLD signal and neural activity is complex, and depending on the experimental paradigm it can be linear or nonlinear. The relative contributions of slow wave activity versus spiking activity and the dependence of BOLD on spectral properties of neural activity also remain to be fully characterised but increasing evidence indicates that Local Field Potentials and the higher frequency components of brain rhythms are good correlates of the metabolic response. Experimentally, various modes of multimodal image integration are available to the investigator. The inclusion of fMRI priors in the linear inverse estimation of the cortical activity can be used to increase the spatial resolution of the EEG and improved estimation of cortical connectivity, which is one of the most challenging and

important objectives of neuroimaging. Synchronous acquisitions represent the most flexible solution in terms of analysis, allowing full exploitation of the data at the available temporal and spatial resolution, down to individual events and free of intersession bias. In the field of motor imagery, this approach has demonstrated a negative correlation between event-related desynchronization and the BOLD signal. In the field of epilepsy, simultaneous EEG-fMRI is necessary for the study of the haemodynamic correlates of interictal pathological discharges due to their subclinical nature. Such studies have demonstrated BOLD increases and decreases in relation to sharp waves and sharp- and slow-wave complexes. In the field of evoked response studies we envisage the extension of the connectivity estimators in the time-frequency domain, which would return more detailed information about the functional links established between different cortical sites during the evolution of the task. The proposed fusion procedures for single trial ERPs and fMRI enable us to study the temporal dynamics the spatial behaviour of information processing and cognitive functioning in greater detail. Future developments in biophysical modelling will permit more precise and complete estimations of neuronal activity using noninvasive means. This may lead to more symmetric data analysis approaches better capable of identifying salient spatiotemporal patterns and assist in the design of efficient experimental strategies.

Acknowledgments

K. J. Blinowska acknowledges a support from Polish Ministry of Science and Higher Education (Decision no. 119/N-COST/2008/0), awarded in connection with NEUROMATH action. L. Astolfi acknowledges the funding support of the Minister for Foreign Affairs, Division for Scientific and Technological Development, in the framework of a bilateral project between Italy and China, and the European COST Action NEUROMATH BM0601 is gratefully acknowledged. K. Vanderperren and S. Van Huffel are supported by GOA-AMBioRICS, IDO 05/010 EEG-fMRI, IWT PhD grant, IUAP P6/04 and, Neuromath (COST-BM0601). G. Müller-Putz and V. Kaiser acknowledge support from the "Allgemeine Unfallversicherung AUVA," Lorenz Böhler Gesellschaft and EU COST Neuromath (BM0601). L. Lemieux acknowledges funding received from the Medical Research Council (UK), Action Medical Research and the support of UCLH/UCL who received a proportion of funding from the UK Department of Health's NIHR Biomedical Research Centres funding scheme.

References

[1] K. J. Friston, A. Mechelli, R. Turner, and C. J. Price, "Nonlinear responses in fMRI: the balloon model, Volterra kernels, and other hemodynamics," *NeuroImage*, vol. 12, no. 4, pp. 466–477, 2000.

[2] R. B. Buxton and L. R. Frank, "A model for the coupling between cerebral blood flow and oxygen metabolism during neural stimulation," *Journal of Cerebral Blood Flow and Metabolism*, vol. 17, no. 1, pp. 64–72, 1997.

[3] O. J. Arthurs, E. J. Williams, T. A. Carpenter, J. D. Pickard, and S. J. Boniface, "Linear coupling between functional magnetic resonance imaging and evoked potential amplitude in human somatosensory cortex," *Neuroscience*, vol. 101, no. 4, pp. 803–806, 2000.

[4] N. K. Logothetis, J. Pauls, M. Augath, T. Trinath, and A. Oeltermann, "Neurophysiological investigation of the basis of the fMRI signal," *Nature*, vol. 412, no. 6843, pp. 150–157, 2001.

[5] K. J. Friston, O. Josephs, G. Rees, and R. Turner, "Nonlinear event-related responses in fMRI," *Magnetic Resonance in Medicine*, vol. 39, no. 1, pp. 41–52, 1998.

[6] A. Mechelli, C. J. Price, and K. J. Friston, "Nonlinear coupling between evoked rCBF and BOLD signals: a simulation study of hemodynamic responses," *NeuroImage*, vol. 14, no. 4, pp. 862–872, 2001.

[7] R. Turner, "How much codex can a vein drain? Downstream dilution of activation-related cerebral blood oxygenation changes," *NeuroImage*, vol. 16, no. 4, pp. 1062–1067, 2002.

[8] N. K. Logothetis, "What we can do and what we cannot do with fMRI," *Nature*, vol. 453, no. 7197, pp. 869–878, 2008.

[9] O. J. Arthurs and S. Boniface, "How well do we understand the neural origins of the fMRI BOLD signal?" *Trends in Neurosciences*, vol. 25, no. 1, pp. 27–31, 2002.

[10] G. Rees, K. Friston, and C. Koch, "A direct quantitative relationship between the functional properties of human and macaque V5," *Nature Neuroscience*, vol. 3, no. 7, pp. 716–723, 2000.

[11] A. Shmuel, M. Augath, A. Oeltermann, and N. K. Logothetis, "Negative functional MRI response correlates with decreases in neuronal activity in monkey visual area V1," *Nature Neuroscience*, vol. 9, no. 4, pp. 569–577, 2006.

[12] C. Mathiesen, K. Caesar, N. Akgören, and M. Lauritzen, "Modification of activity-dependent increases of cerebral blood flow by excitatory synaptic activity and spikes in rat cerebellar cortex," *The Journal of Physiology*, vol. 512, no. 2, pp. 555–566, 1998.

[13] J. M. Palacios, M. J. Kuhar, S. I. Rapoport, and E. D. London, "Effects of γ-aminobutyric acid agonist and antagonist drugs on local cerebral glucose utilization," *Journal of Neuroscience*, vol. 2, no. 7, pp. 853–860, 1982.

[14] P. A. T. Kelly, I. Ford, and J. McCulloch, "The effect of diazepam upon local cerebral glucose use in the conscious rat," *Neuroscience*, vol. 19, no. 1, pp. 257–265, 1986.

[15] M.-A. Tagamets and B. Horwitz, "Interpreting PET and fMRI measures of functional neural activity: the effects of synaptic inhibition on cortical activation in human imaging studies," *Brain Research Bulletin*, vol. 54, no. 3, pp. 267–273, 2001.

[16] P. Nunez, *Electric Fields of Brain*, Oxford University Press, New York, NY, USA, 1981.

[17] J. M. Kilner, J. Mattout, R. Henson, and K. J. Friston, "Hemodynamic correlates of EEG: a heuristic," *NeuroImage*, vol. 28, no. 1, pp. 280–286, 2005.

[18] R. I. Goldman, J. M. Stern, J. Engel Jr., and M. S. Cohen, "Simultaneous EEG and fMRI of the alpha rhythm," *NeuroReport*, vol. 13, no. 18, pp. 2487–2492, 2002.

[19] E. Martínez-Montes, P. A. Valdés-Sosa, F. Miwakeichi, R. I. Goldman, and M. S. Cohen, "Concurrent EEG/fMRI analysis by multiway partial least squares," *NeuroImage*, vol. 22, no. 3, pp. 1023–1034, 2004.

[20] H. Laufs, A. Kleinschmidt, A. Beyerle, et al., "EEG-correlated fMRI of human alpha activity," *NeuroImage*, vol. 19, no. 4, pp. 1463–1476, 2003.

[21] D. A. Leopold, Y. Murayama, and N. K. Logothetis, "Very slow activity fluctuations in monkey visual cortex: implications for functional brain imaging," *Cerebral Cortex*, vol. 13, no. 4, pp. 422–433, 2003.

[22] G. R. Müller-Putz, D. Zimmermann, B. Graimann, K. Nestinger, G. Korisek, and G. Pfurtscheller, "Event-related beta EEG-changes during passive and attempted foot movements in paraplegic patients," *Brain Research*, vol. 1137, no. 1, pp. 84–91, 2007.

[23] G. R. Müller-Putz, P. Linortner, R. Winkler, G. Korisek, and G. Pfurtscheller, "BCI accuracy in healthy persons and SCI patients," in *Proceedings of the Neuromath Workshop*, Jena, Germany, April 2008, COST BM0601.

[24] H. Alkadhi, P. Brugger, S. H. Boendermaker, et al., "What disconnection tells about motor imagery: evidence from paraplegic patients," *Cerebral Cortex*, vol. 15, no. 2, pp. 131–140, 2005.

[25] C. Enzinger, S. Ropele, F. Fazekas, et al., "Brain motor system function in a patient with complete spinal cord injury following extensive brain-computer interface training," *Experimental Brain Research*, vol. 190, no. 2, pp. 215–223, 2008.

[26] E. Formaggio, S. F. Storti, M. Avesani, et al., "EEG and fMRI coregistration to investigate the cortical oscillatory activities during finger movement," *Brain Topography*, vol. 21, no. 2, pp. 100–111, 2008.

[27] A. M. Dale, A. K. Liu, B. R. Fischl, et al., "Dynamic statistical parametric mapping: combining fMRI and MEG for high-resolution imaging of cortical activity," *Neuron*, vol. 26, no. 1, pp. 55–67, 2000.

[28] B. He, J. Hori, and F. Babiloni, "EEG inverse problems," in *Wiley Encyclopedia in Biomedical Engineering*, M. Akay, Ed., vol. 2, pp. 1355–1363, John Wiley & Sons, New York, NY, USA, 2006.

[29] C.-H. Im, Z. Liu, N. Zhang, W. Chen, and B. He, "Functional cortical source imaging from simultaneously recorded ERP and fMRI," *Journal of Neuroscience Methods*, vol. 157, no. 1, pp. 118–123, 2006.

[30] Z. Liu and B. He, "fMRI-EEG integrated cortical source imaging by use of time-variant spatial constraints," *NeuroImage*, vol. 39, no. 3, pp. 1198–1214, 2008.

[31] F. Babiloni, C. Babiloni, F. Carducci, et al., "Multimodal integration of high-resolution EEG and functional magnetic resonance imaging data: a simulation study," *NeuroImage*, vol. 19, no. 1, pp. 1–15, 2003.

[32] F. Babiloni, F. Cincotti, C. Babiloni, et al., "Estimation of the cortical functional connectivity with the multimodal integration of high-resolution EEG and fMRI data by directed transfer function," *NeuroImage*, vol. 24, no. 1, pp. 118–131, 2005.

[33] A. Urbano, C. Babiloni, P. Onorati, et al., "Responses of human primary sensorimotor and supplementary motor areas to internally triggered unilateral and simultaneous bilateral one-digit movements. A high-resolution EEG study," *European Journal of Neuroscience*, vol. 10, no. 2, pp. 765–770, 1998.

[34] F. Babiloni, C. Babiloni, L. Locche, F. Cincotti, P. M. Rossini, and F. Carducci, "High-resolution electro-encephalogram: source estimates of Laplacian-transformed somatosensory-evoked potentials using a realistic subject head model constructed from magnetic resonance images," *Medical & Biological Engineering & Computing*, vol. 38, no. 5, pp. 512–519, 2000.

[35] M. J. Kaminski and K. J. Blinowska, "A new method of the description of the information flow in the brain structures," *Biological Cybernetics*, vol. 65, no. 3, pp. 203–210, 1991.

[36] C. W. J. Granger, "Investigating causal relations by econometric models and cross-spectral methods," *Econometrica*, vol. 37, no. 3, pp. 424–438, 1969.

[37] L. Astolfi, F. Cincotti, D. Mattia, et al., "Estimation of the effective and functional human cortical connectivity with structural equation modeling and directed transfer function applied to high-resolution EEG," *Magnetic Resonance Imaging*, vol. 22, no. 10, pp. 1457–1470, 2004.

[38] L. Astolfi, F. Cincotti, D. Mattia, et al., "Assessing cortical functional connectivity by linear inverse estimation and directed transfer function: simulations and application to real data," *Clinical Neurophysiology*, vol. 116, no. 4, pp. 920–932, 2005.

[39] L. Astolfi, F. Cincotti, D. Mattia, et al., "Comparison of different cortical connectivity estimators for high-resolution EEG recordings," *Human Brain Mapping*, vol. 28, no. 2, pp. 143–157, 2007.

[40] L. Astolfi, F. De Vico Fallani, F. Cincotti, et al., "Imaging functional brain connectivity patterns from high-resolution EEG and fMRI via graph theory," *Psychophysiology*, vol. 44, no. 6, pp. 880–893, 2007.

[41] L. Astolfi, F. De Vico Fallani, F. Cincotti, et al., "Estimation of effective and functional cortical connectivity from neuroelectric and hemodynamic recordings," *IEEE Transactions in Neural Systems and Rehabilitation Engineering*. In press.

[42] A. Salek-Haddadi, M. Merschhemke, L. Lemieux, and D. R. Fish, "Simultaneous EEG-correlated ictal fMRI," *NeuroImage*, vol. 16, no. 1, pp. 32–40, 2002.

[43] A. Salek-Haddadi, L. Lemieux, M. Merschhemke, K. J. Friston, J. S. Duncan, and D. R. Fish, "Functional magnetic resonance imaging of human absence seizures," *Annals of Neurology*, vol. 53, no. 5, pp. 663–667, 2003.

[44] E. Kobayashi, C. S. Hawco, C. Grova, F. Dubeau, and J. Gotman, "Widespread and intense BOLD changes during brief focal electrographic seizures," *Neurology*, vol. 66, no. 7, pp. 1049–1055, 2006.

[45] D. B. Geselowitz, "Introduction to "some laws concerning the distribution of electric currents in volume conductors with applications to experiments on animal electricity"," *Proceedings of the IEEE*, vol. 92, no. 5, pp. 864–867, 2004.

[46] J. R. Ives, S. Warach, F. Schmitt, R. R. Edelman, and D. L. Schomer, "Monitoring the patient's EEG during echo planar MRI," *Electroencephalography and Clinical Neurophysiology*, vol. 87, no. 6, pp. 417–420, 1993.

[47] F. R. Huang-Hellinger, H. C. Breiter, G. McCormack, et al., "Simultaneous functional magnetic resonance imaging and electrophysiological recording," *Human Brain Mapping*, vol. 3, no. 1, pp. 13–23, 1995.

[48] S. Warach, J. R. Ives, G. Schlaug, et al., "EEG-triggered echo-planar functional MRI in epilepsy," *Neurology*, vol. 47, no. 1, pp. 89–93, 1996.

[49] M. Seeck, F. Lazeyras, C. M. Michel, et al., "Non-invasive epileptic focus localization using EEG-triggered functional MRI and electromagnetic tomography," *Electroencephalography and Clinical Neurophysiology*, vol. 106, no. 6, pp. 508–512, 1998.

[50] M. R. Symms, P. J. Allen, F. G. Woermann, et al., "Reproducible localization of interictal epileptiform discharges using eeg-triggered fMRI," *Physics in Medicine and Biology*, vol. 44, no. 7, pp. N161–N168, 1999.

[51] K. Krakow, F. G. Woermann, M. R. Symms, et al., "EEG-triggered functional MRI of interictal epileptiform activity in patients with partial seizures," *Brain*, vol. 122, no. 9, pp. 1679–1688, 1999.

[52] K. Krakow, L. Lemieux, D. Messina, et al., "Spatio-temporal imaging of focal interictal epileptiform activity using EEG-triggered functional MRI," *Epileptic Disorders*, vol. 3, no. 2, pp. 67–74, 2001.

[53] F. Lazeyras, O. Blanke, S. Perrig, et al., "EEG-triggered functional MRI in patients with pharmacoresistant epilepsy," *Journal of Magnetic Resonance Imaging*, vol. 12, no. 1, pp. 177–185, 2000.

[54] J. S. Archer, R. S. Briellman, D. F. Abbott, A. Syngeniotis, R. M. Wellard, and G. D. Jackson, "Benign epilepsy with centro-temporal spikes: spike triggered fMRI shows somato-sensory cortex activity," *Epilepsia*, vol. 44, no. 2, pp. 200–204, 2003.

[55] L. Lemieux, A. Salek-Haddadi, O. Josephs, et al., "Event-related fMRI with simultaneous and continuous EEG: description of the method and initial case report," *NeuroImage*, vol. 14, no. 3, pp. 780–787, 2001.

[56] A. Salek-Haddadi, B. Diehl, K. Hamandi, et al., "Hemodynamic correlates of epileptiform discharges: an EEG-fMRI study of 63 patients with focal epilepsy," *Brain Research*, vol. 1088, no. 1, pp. 148–166, 2006.

[57] A. D. Liston, J. C. De Munck, K. Hamandi, et al., "Analysis of EEG-fMRI data in focal epilepsy based on automated spike classification and Signal Space Projection," *NeuroImage*, vol. 31, no. 3, pp. 1015–1024, 2006.

[58] S. J. Luck, *An Introduction to the Event-Related Potential Technique*, MIT Press, Cambridge, Mass, USA, 2005.

[59] J. R. Ives, S. Warach, F. Schmitt, R. R. Edelman, and D. L. Schomer, "Monitoring the patient's EEG during echo planar MRI," *Electroencephalography and Clinical Neurophysiology*, vol. 87, no. 6, pp. 417–420, 1993.

[60] L. Lemieux, P. J. Allen, F. Franconi, M. R. Symms, and D. R. Fish, "Recording of EEG during fMRI experiments: patient safety," *Magnetic Resonance in Medicine*, vol. 38, no. 6, pp. 943–952, 1997.

[61] G. Bonmassar, K. Anami, J. Ives, and J. W. Belliveau, "Visual evoked potential (VEP) measured by simultaneous 64-channel EEG and 3T fMRI," *NeuroReport*, vol. 10, no. 9, pp. 1893–1897, 1999.

[62] K. Mullinger, S. Debener, R. Coxon, and R. Bowtell, "Effects of simultaneous EEG recording on MRI data quality at 1.5, 3 and 7 tesla," *International Journal of Psychophysiology*, vol. 67, no. 3, pp. 178–188, 2008.

[63] C.-G. Bénar, D. Schön, S. Grimault, et al., "Single-trial analysis of oddball event-related potentials in simultaneous EEG-fMRI," *Human Brain Mapping*, vol. 28, no. 7, pp. 602–613, 2007.

[64] N. J. Wesensten, P. Badia, and J. Harsh, "Time of day, repeated testing, and interblock interval effects on P300 amplitude," *Physiology and Behavior*, vol. 47, no. 4, pp. 653–658, 1990.

[65] N. Novitski, I. Anourova, S. Martinkauppi, H. J. Aronen, R. Näätänen, and S. Carlson, "Effects of noise from functional magnetic resonance imaging on auditory event-related potentials in working memory task," *NeuroImage*, vol. 20, no. 2, pp. 1320–1328, 2003.

[66] T. Eichele, K. Specht, M. Moosmann, et al., "Assessing the spatiotemporal evolution of neuronal activation with single-trial event-related potentials and functional MRI," *Proceedings of the National Academy of Sciences of the United States of America*, vol. 102, no. 49, pp. 17798–17803, 2005.

[67] R. Näätänen, *Attention and Brain Function*, Erlbaum, Hillsdale, NJ, USA, 1992.

[68] S. Debener, M. Ullsperger, M. Siegel, K. Fiehler, D. Y. von Cramon, and A. K. Engel, "Trial-by-trial coupling of concurrent electroencephalogram and functional magnetic resonance imaging identifies the dynamics of performance monitoring," *Journal of Neuroscience*, vol. 25, no. 50, pp. 11730–11737, 2005.

[69] S. Debener, M. Ullsperger, M. Siegel, and A. K. Engel, "Single-trial EEG-fMRI reveals the dynamics of cognitive function," *Trends in Cognitive Sciences*, vol. 10, no. 12, pp. 558–563, 2006.

[70] L. Marzetti, D. Mantini, S. Cugini, G. L. Romani, and C. Del Gratta, "High-resolution spatio-temporal neuronal activation in the visual oddball task: a simultaneous EEG/fMRI study," in *Proceedings of the Joint Meeting of the 6th International Symposium on Noninvasive Functional Source Imaging of the Brain and Heart and the International Conference on Functional Biomedical Imaging (NFSI-ICFBI '07)*, pp. 59–62, Hangzhou, China, October 2007.

[71] T. Eichele, V. D. Calhoun, M. Moosmann, et al., "Unmixing concurrent EEG-fMRI with parallel independent component analysis," *International Journal of Psychophysiology*, vol. 67, no. 3, pp. 222–234, 2008.

[72] M. Moosmann, T. Eichele, H. Nordby, K. Hugdahl, and V. D. Calhoun, "Joint independent component analysis for simultaneous EEG-fMRI: principle and simulation," *International Journal of Psychophysiology*, vol. 67, no. 3, pp. 212–221, 2008.

Hindawi Publishing Corporation
Computational Intelligence and Neuroscience
Volume 2009, Article ID 659247, 11 pages
doi:10.1155/2009/659247

Research Article

The Neuroelectromagnetic Inverse Problem and the Zero Dipole Localization Error

Rolando Grave de Peralta,[1,2] Olaf Hauk,[3] and Sara L. Gonzalez[1]

[1] *Electrical Neuroimaging Group, Neurology Department, Geneva University Hospital, 24 Rue Micheli du Crest, 1211 Geneva 14, Switzerland*
[2] *Neurodynamics Laboratory, Department of Psychiatry and Clinical Psychobiology, University of Barcelona, 08035 Barcelona, Catalonia, Spain*
[3] *Cognition and Brain Sciences Unit, Medical Research Council, 15 Chaucer Road, Cambridge, CB2 7EF, UK*

Correspondence should be addressed to Rolando Grave de Peralta, rolando.grave@hcuge.ch

Received 3 October 2008; Revised 29 January 2009; Accepted 24 March 2009

Recommended by Fabio Babiloni

A tomography of neural sources could be constructed from EEG/MEG recordings once the neuroelectromagnetic inverse problem (NIP) is solved. Unfortunately the NIP lacks a unique solution and therefore additional constraints are needed to achieve uniqueness. Researchers are then confronted with the dilemma of choosing one solution on the basis of the advantages publicized by their authors. This study aims to help researchers to better guide their choices by clarifying what is hidden behind inverse solutions oversold by their apparently optimal properties to localize single sources. Here, we introduce an inverse solution (ANA) attaining perfect localization of single sources to illustrate how spurious sources emerge and destroy the reconstruction of simultaneously active sources. Although ANA is probably the simplest and robust alternative for data generated by a single dominant source plus noise, the main contribution of this manuscript is to show that zero localization error of single sources is a trivial and largely uninformative property unable to predict the performance of an inverse solution in presence of simultaneously active sources. We recommend as the most logical strategy for solving the NIP the incorporation of sound additional a priori information about neural generators that supplements the information contained in the data.

1. Introduction

Determining the neural origin and strength of sources producing scalp maps of electric or magnetic fields requires the solution of an inverse problem. This so-called neuroelectromagnetic inverse problem (NIP) lacks a unique solution. In spite of this serious difficulty, there is an active past and ongoing research on this field (see [1] for a recent review) because of the extreme clinical and research importance of the problem. A reliable optimal solution to the NIP is thus far the only possible alternative to study a direct reflection of neuronal activity in normal human subjects with the high temporal resolution required to trace the highly dynamic behavior of the human brain.

Several linear and nonlinear solutions based on a diversity of approaches have been proposed. However, independently of the approach used, we need to evaluate the reliability of the estimates provided by the inverse procedure selected. While there is interesting ongoing research on this topic [2–5], no definitive or general answer to this problem hitherto *exists*. One alternative to evaluate the localization features of linear inverse solutions is the so-called model resolution matrix (MRM) [6, 7], although the way to use it in the evaluations remains as a highly controversial point because of the following reasons.

Some authors center their attention on the columns of the MRM, also called point spread functions (PSFs), that allow inferring how the solutions behave for single punctual sources. These authors consider the PSF as an adequate measure of the "goodness" of a linear inverse [8, 9]. An aspect to consider here is the existence in literature of two parallel

definitions of the single (punctual) source localization error [10].

(1) The bias in Dipole localization (BDL) defined in terms of the accuracy in estimating the location of each Cartesian component of the dipole. As such, it is a linear measure fully compliant with the linearity involved in the definition of the Model Resolution Matrix and can be directly estimated from the PSF.

(2) The Dipole Localization Error (DLE) defined as the error attained in localizing the modulus of the current density vector. This definition conceptually disagrees with the use of MRM and PSF since the modulus is a nonlinear transformation of the individual dipole components not directly reflected by the PSF. Besides, linking the dipole localization error with the superposition principle is a blatant error since the basis of superposition is linearity. Although it certainly holds that the PSF of two simultaneously active dipoles is the sum of their individual PSFs, this is not the case for the DLEs. The widespread use of the dipole localization error concept obeys to historical and practical reasons since the modulus is the magnitude currently displayed in brain imaging.

All along this paper we will use the term single source to denote each of the three orthonormal (i.e., orthogonal with unitary norm) dipoles associated with a solution point. This is in agreement with the structure of the model resolution matrix where each solution point is represented by three columns. Consequently, each column corresponds to one and only one of three Cartesian components of a dipole. As typically used in this field, the term perfect localization will be used whenever the DLE or the BDL of a single source is zero independently of the off-diagonal elements of that column.

Two linear inverse solutions have been reported in the NIP literature to explicitly optimize the localization of single sources. The EPIFOCUS solution [11] aims to minimize DLE and BDL for both noisy and noiseless data for all sources in the solution space. In contrast, the sLORETA inverse solution [9] minimizes DLE and BDL only for noiseless data.

Authors advocating the use of PSF employ the appealing argument of the superposition principle [12] as the basis to infer the capabilities of the solution for multiple source localization from results obtained on single source localization. They consequently concentrate their efforts in optimizing the columns of the MRM and will likely consider the zero dipole localization error as the ultimate goal to reach in the construction of inverse estimators. Another group of authors diverge from this point of view and insist that the performance of a linear inverse solution in the presence of multiple sources can only be inferred from the resolution kernels (the rows of the MRM). They consider the analysis of the PSF only valid for single source localization but not sufficient to describe the performance of distributed source models satisfactorily [3, 13]. They will therefore consider essential the incorporation of as much a priori information as possible into the solution to deal with the nonuniqueness, that is, they will aim to characterize the space where actual sources are contained [14, 15].

In this paper we introduce a "trivial" and easy-to-compute linear inverse solution coined Adjoint Normalized Approximation (ANA) that transforms the original inverse problem into a space in which the model resolution matrix shows optimal properties for single source localization. We demonstrate that in the transformed space, ANA inverse solution is able to correctly localize single sources in full extent, that is, with zero dipole localization bias and perfectly accurate strength. These properties are shown to be satisfied for arbitrary lead field models independently of the amount of scalp sensors. ANA solution is used to build a simple didactical example illustrating that perfect localization of single sources in position and strength *has* no implications for simultaneous source localization. The presented example serves to understand the emergence of spurious sources and how they totally distort the reconstruction when multiple sources are active. We further demonstrate that ANA can be applied to retrieve sources in the space of the original current density vector. Even if in this space the bias in dipole localization error is not zero everywhere, ANA solution is highly robust to noise outperforming the best methods presented so far for single source localization. Its robustness to noise and computational simplicity make of ANA a reasonable alternative for data generated by a single dominant source plus noise as can be the case in epilepsy. Still, ANA is more likely to contribute to further developments in this field, by providing the simplest possible evidence that optimizing single source localization is both trivial and useless. Therefore the only reasonable way to deal with the nonuniqueness of NIP is to add plausible physical and physiological constraints into the source space.

2. Methods

2.1. The Theoretical Basis of the Problem. The neuroelectromagnetic inverse problem (NIP), that is, the reconstruction of the current density vector inside the brain responsible for the electric and magnetic fields measured near/over the scalp, can be represented by a (first kind) Fredholm linear integral equation, denoting the relationship between the data measured at the external point, $d(s)$, and the superposition of the contribution of the unknown current source density distribution at locations r inside the brain [16]:

$$d(s) = \int_{\text{Brain}} L(s,r) * j(r)dr. \tag{1}$$

The (vector) lead field function $L(s,r)$ contains all the information about the boundary conditions as well as the media conductivities or permittivities for the electric and magnetic cases, respectively. The 3D vector $j(r)$ denotes the unknown current density vector, and r is the 3D position variable running over the volume of the brain.

Under experimental conditions, neither the measurements nor the lead field function is known for arbitrary surface/brain locations. However, assuming that the integral equation can be approximated by a discrete sum, (1) can

be represented by an underdetermined system of linear equations:

$$\mathbf{d} = \mathbf{L}\mathbf{j}. \tag{2}$$

Vectors $\mathbf{d}$ and $\mathbf{j}$ and matrix $\mathbf{L}$ represent the discretization of the continuous functions, that is, $\mathbf{d}_k = d(s_k)$, $\mathbf{j}_m = j(r_m)$, and $\mathbf{L}_{\mathrm{km}} = w_{\mathrm{km}} L(s_k, r_m)$, and w_{km} are the quadrature weights.

All linear solutions of (2) can be obtained solving a variational problem [7]. This yields the inverse matrix $\mathbf{G}$ that, when applied to the measured data, produces the estimated current density vector, that is,

$$\hat{\mathbf{j}} = \mathbf{G}\mathbf{d}. \tag{3}$$

Substitution of the measured data, as described in (2), into (3) yields the following fundamental equation for underdetermined linear systems:

$$\hat{\mathbf{j}} = \mathbf{G}\mathbf{d} = \mathbf{G}\mathbf{L}\mathbf{j} = \mathbf{R}\mathbf{j}. \tag{4}$$

Here, $\mathbf{R} = \mathbf{GL}$ denotes the model resolution matrix (MRM) describing the relationship between the estimate and the original magnitudes of the current density. In simpler terms, (4) tells us that our estimates separate from the original values by the transformation $\mathbf{R}$. The nearer this matrix is to the identity matrix, the better the estimated solution resembles the original sources.

For the noisy case where $\mathbf{d} = \mathbf{Lj} + \mathbf{Noise}$, we can always rewrite it as $\mathbf{d} = \mathbf{Lj} + \mathbf{Lj}_n$ where $\mathbf{j}_n$ is the minimum norm solution of the equation $\mathbf{Noise} = \mathbf{Lj}_n$, and thus

$$\hat{\mathbf{j}} = \mathbf{G}\mathbf{d} = \mathbf{G}\mathbf{L}(\mathbf{j} + \mathbf{j}_n) = \mathbf{R}(\mathbf{j} + \mathbf{j}_n). \tag{5}$$

For the particular example discussed here, the unknown current density vector contains the three Cartesian components at each solution point. Correspondingly, each solution point will be represented by 3 columns and 3 rows of the MRM. The rows of $\mathbf{R}$ are known as the resolution kernels [17]. Each resolution kernel provides information on how simultaneously active sources affect the estimates of $\mathbf{j}$ at the component associated to the row. The columns of $\mathbf{R}$ are the point spread functions (PSFs) and reflect the quality of single source reconstruction. That is, each column corresponds to the current source density estimated by the inverse solution when the associated unitary single source is active alone. Based on the linearity of matrix products, to compute the current source estimated for simultaneously active sources it is enough to add the associated columns. For further details about how to compute the bias in dipole localization and the dipole localization errors from the PSF, see [7, 10].

2.2. The Adjoint Normalized Approximation (ANA) of the Inverse. It is evident that for every invertible matrix $\mathbf{W}$, the following change of variable can be applied to (2):

$$\mathbf{d} = \mathbf{L}\mathbf{W}^{-1}\mathbf{W}\mathbf{j} = \mathcal{L}\mathbf{Z}, \tag{6}$$

where $\mathcal{L} = \mathbf{L}\mathbf{W}^{-1}$ and $\mathbf{Z} = \mathbf{W}\mathbf{j}$. Let us define $\mathbf{W}$ as the diagonal matrix containing the norm of each column of $\mathbf{L}$. It follows from the definition of $\mathbf{W}$ that it is a diagonal square matrix and thus invertible. Therefore (6) is identical to the original problem formulation in (2); what has been done is a simple change of variable where the model matrix is the column normalized lead field, and the unknown is the variable $\mathbf{Z}$.

To obtain a unique solution to (6) in the space of the transformed variable $\mathbf{Z}$, we need to invert the model matrix $\mathcal{L}$. Since we are dealing with an underdetermined inverse problem, matrix $\mathcal{L}$ is noninvertible. A typical choice for inverse problems is to use the Moore-Penrose pseudoinverse. We rather propose to use a particularly simple approximation of the inverse of a matrix, the adjoint or transpose (not to be confused with the adjugate matrix composed by the cofactors). This simple choice satisfies the third and fourth Moore-Penrose conditions, while violating the first two [18], that is, if $\mathbf{A}$ is a matrix (or vector) and $\mathbf{G}$ is its generalized inverse, then it must hold that (1) $\mathbf{AGA} = \mathbf{A}$. (2) $\mathbf{GAG} = \mathbf{G}$. (3) $(\mathbf{AG})^t = \mathbf{AG}$, and (4) $(\mathbf{GA})^t = \mathbf{GA}$. It also follows that the pseudoinverse of $\mathbf{G}$ is $\mathbf{A}$. Therefore the proposed Adjoint Normalized Approximation (ANA) inverse is given by

$$\mathbf{G} = \mathcal{L}^t = (\mathbf{L}\mathbf{W}^{-1})^t = \mathbf{W}^{-1}\mathbf{L}^t. \tag{7}$$

There is a close relationship between ANA and EPIFOCUS. While EPIFOCUS computes the pseudoinverse of three lead field columns (i.e., three single sources) associated with one solution point, ANA corresponds to the computation of the pseudoinverse of each column (i.e., single source) separately. This is straightforward since the Moore-Penrose inverse of a normalized (unitary norm) vector is the transposed vector which fulfills all the four conditions of the pseudoinverse mentioned before. We would also note that the adjoint corresponds to the simpler initial approximation of the inverse for iterative processes. The normalized adjoint is a step forward fulfilling one property of the inverse, that is, the product with the original matrix yields one at the diagonal. As it was the case for EPIFOCUS [11], the simulations of the next section confirm that ANA properties are not a consequence of the weighting or the transposition alone but a combined effect.

3. Results

3.1. Theoretical Properties of ANA's Resolution Matrix. According to (4), the resolution matrix associated with the transformed variable $\mathbf{z}$ is given by

$$\mathbf{R} = \mathcal{L}^t\mathcal{L} = \mathbf{W}^{-1}\mathbf{L}^t\mathbf{L}\mathbf{W}^{-1}. \tag{8}$$

From this, it follows that the resolution matrix of ANA inverse solution is the product of the transposed normalized lead field times the normalized lead field. Therefore the resolution matrix is symmetric.

Further properties of the resolution matrix $\mathbf{R}$ (8) can be derived by noting that the elements of the ith column of $\mathbf{R}$ are given by the scalar product of the potential map produced by the ith source with the potential map of all other sources.

This derives from the fact that each column of **L** represents the electric potential or magnetic field pattern measured at/near the head surface when only the ith dipolar source is active with unitary strength ("forward solutions"). Since each dipole produces a different activation map, it is then clear that each pair of columns of **L** is noncollinear. The resolution matrix of ANA in the transformed space $\mathcal{L}$ necessarily inherits the property of noncollinearity from **L** since the only change is a normalization factor. Consequently, the ith column of **R** contains the correlation coefficients between the ith potential pattern and the potential patterns of all other sources. Since the correlation coefficient between a given potential map with itself is necessarily one, then the elements at the main diagonal of **R** (the map autocorrelations) are inevitably equal to one. The nondiagonal elements, representing the correlations between one given map and all other maps, are necessarily lower than one since different unitary dipoles are unable to produce identical scalp maps. Since these properties hold for all sources, that is, all columns of **R**, then, the maximum of each column, defining the bias in dipole localization, is reached at the main diagonal and is exactly one. Thus, the following properties hold for the resolution matrix of this inverse independently of the lead field model considered.

(1) The point-spread functions (columns of **R**) reach their maxima at the diagonal elements trivially leading to perfect reconstruction of the positions of all single sources (all Cartesian components of the dipole at each solution point).

(2) Because the diagonal of the resolution matrix is one (due to normalization), the intensity of the estimated source is exactly the intensity activity of the original source.

(3) Since **R** is symmetric, then the resolution kernels shapes are close to the ideals attaining the maximum value at the correct places.

3.2. Does Perfect Localization of Single Sources Imply Correct Localization of Multiple Active Sources? The ideal properties of ANA's resolution matrix described in the previous section are independent from the lead field model. This implies that they will hold even for arbitrarily small sensor configurations and very large solution spaces provided that there are no collinear columns in the lead field. We have exploited this fact to construct a simple numerical example that might help to shed light on several aspects influencing the behavior of linear inverse solutions in the presence of multiple active sources. The computational simplicity of ANA will facilitate the task to readers interested in further simulating its behavior with simultaneous sources.

The example given here considers the case of two EEG sensors and four solution points as depicted in Figure 1. The four solution points lie in a coronal plane below the arc at which the two sensors are placed. Sensors are placed at the approximate positions of electrodes C3 and C4 of the international 10/20 placement system. The lead field was computed using a semirealistic head model derived from the Montreal Neurological Institute (MNI) average brain using the SYSMAC procedure described in [19]. It is noteworthy that the selection of the lead field matrix parameters (conductivities, electrode positions, and solution points) will have little effect on the main results described below. This argument justifies our selection of a very small problem to allow portraying the full model resolution matrix and its subsequent understanding.

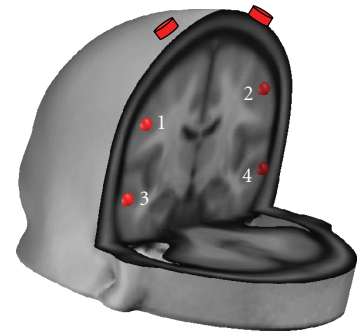

Figure 1: *Electrodes and solution points used for the analysis of ANA resolution matrix.* The two electrodes are located at the approximated positions of C3 and C4.

In the case of this simple example, the current density vector is a 12 component vector of the form

$$\mathbf{j} = \left[\begin{array}{cccccccccccc} \mathbf{j}_{\mathbf{x}}^{1} & \mathbf{j}_{\mathbf{y}}^{1} & \mathbf{j}_{\mathbf{z}}^{1} & \mathbf{j}_{\mathbf{x}}^{2} & \mathbf{j}_{\mathbf{y}}^{2} & \mathbf{j}_{\mathbf{z}}^{2} & \mathbf{j}_{\mathbf{x}}^{3} & \mathbf{j}_{\mathbf{y}}^{3} & \mathbf{j}_{\mathbf{z}}^{3} & \mathbf{j}_{\mathbf{x}}^{4} & \mathbf{j}_{\mathbf{y}}^{4} & \mathbf{j}_{\mathbf{z}}^{4} \end{array} \right]. \quad (9)$$

This vector is formed by the three Cartesian components of the dipoles (subscripts **x**, **y**, **z**) linked to each solution point (superscripts 1, 2, 3, 4). The spatial distribution of the modulus of the current density vector can be computed using

$$\mathbf{j}^{\mathbf{i}} = \sqrt{\left(\mathbf{j}_{\mathbf{x}}^{\mathbf{i}}\right)^2 + \left(\mathbf{j}_{\mathbf{y}}^{\mathbf{i}}\right)^2 + \left(\mathbf{j}_{\mathbf{z}}^{\mathbf{i}}\right)^2} \quad \text{for } \mathbf{i} = 1, 2, 3, 4, \quad (10)$$

resulting in the vector of the modulus given by

$$\mathbf{j}_{\mathbf{m}} = \left[\mathbf{j}^{1} \;\; \mathbf{j}^{2} \;\; \mathbf{j}^{3} \;\; \mathbf{j}^{4} \right]. \quad (11)$$

Table 1 shows the model resolution matrix **R** associated with ANA inverse solution for this problem. This is a 12 × 12 matrix where each group of three rows (or columns) represents the resolution kernels (or impulse responses) linked to the three Cartesian components of a dipole at the corresponding solution point.

The theoretical properties derived in the previous section obviously hold for the problem presented. The main diagonal is filled by ones that are the dominant elements within their respective rows (and columns since the matrix is symmetric). A first aspect to note is that while the recovery of each Cartesian component of the dipole (if alone) is perfect, the recovery of the modulus is not. Perfect recovery of the modulus can be obtained with ANA inverse by stating the original problem for the modulus rather than for the individual dipolar components. This can be done by determining a priori the orientation as in SAM beamformer [20] or by reformulating the problem as proposed in [21].

Table 1: *The resolution matrix for ANA and the configuration presented in Figure 1.* The 12-by 12-model resolution matrix for the configuration of Figure 1 is composed by two electrodes and 4 solutions points. The 12-dimensional unknown current density vector (9) is composed by the 3 Cartesian components of the dipolar moment for each solution point.

1	0.48	0.94	0.48	−0.84	−0.75	−0.67	−0.86	−0.93	−0.10	−0.93	0.16
0.48	1	0.74	0.99	−0.87	−0.94	−0.97	−0.85	−0.13	0.81	−0.14	0.94
0.94	0.74	1	0.75	−0.97	−0.92	−0.88	−0.98	−0.75	0.23	−0.76	0.48
0.48	0.99	0.75	1	−0.87	−0.94	−0.97	−0.85	−0.14	0.81	−0.15	0.94
−0.84	−0.87	−0.97	−0.87	1	0.98	0.96	0.99	0.60	−0.43	0.61	−0.66
−0.75	−0.94	−0.92	−0.94	0.98	1	0.99	0.98	0.46	−0.57	0.47	−0.77
−0.67	−0.97	−0.88	−0.97	0.96	0.99	1	0.95	0.36	−0.66	0.37	−0.83
−0.86	−0.85	−0.98	−0.85	0.99	0.98	0.95	1	0.62	−0.40	0.63	−0.63
−0.93	−0.13	−0.75	−0.14	0.60	0.46	0.36	0.62	1	0.45	0.99	0.20
−0.10	0.81	0.23	0.81	−0.43	−0.57	−0.66	−0.40	0.45	1	0.44	0.96
−0.93	−0.14	−0.76	−0.15	0.61	0.47	0.37	0.63	0.99	0.44	1	0.19
0.16	0.94	0.48	0.94	−0.66	−0.77	−0.83	−0.63	0.20	0.96	0.19	1

Here we stick, for the sake of simplicity and compliance with the MRM linearity, to the case of the component-by-component estimation.

The following two simple examples illustrate how the model resolution matrix is used to derive the inverse solution estimates for a single active source and for two simultaneously active sources.

According to (4), if the "true" current density vector has the form (9), then the ANA inverse solution estimate is given by the product of the MRM and the "true" vector. Let us imagine that the true source distribution is formed by a single active source, which is the z-component of the first solution point with strength k. In this case, the true vector is according to (9) given by $[0, 0, \mathbf{k}, 0, 0, 0, 0, 0, 0, 0, 0, 0]$. The current density vector estimated by ANA is the product of $\mathbf{R}$ by this column vector that yields precisely the third column of $\mathbf{R}$ multiplied by $\mathbf{k}$. Therefore, ANA solution leads to a maximum at the third component of the first point (third element of the third column), and the estimated strength is exactly $\mathbf{k}$. Note that all the other elements in the reconstruction, although smaller than the third one, are different from zero. All the nonzero elements are spurious sources.

In the same way, the reconstruction of each single active source of unitary strength is given by the PSF (column of MRM) linked to this source component. While the maximum always occurs at the right position and the source strength is correctly estimated, the reconstruction is rather noisy and contains spurious activity (ghost sources). This spurious activity appears at sites where the true source strength is zero and is a consequence of nonzero off-diagonal elements of the resolution matrix. To better understand the origin of nonzero off-diagonal elements in the MRM, we should remember that its ith column contains the correlation coefficients between the ith potential pattern and the potential patterns of all other sources. Nonzero off-diagonal elements of the resolution matrix appear therefore at the position of sources leading to correlated scalp patterns. For the particular case of ANA inverse solution, the value at the off-diagonal elements will be identical to the correlation coefficient between the respective potential patterns. Different sources might produce highly similar scalp potential patterns (highly correlated patterns) inducing large off-diagonal elements and therefore spurious sources.

Not only will off-diagonal elements lead to noisy single source reconstruction but also, even worse, they will totally mislead multiple source reconstruction. To see how, let us return to our example of Table 1 and assume that sources 1 and 12 are active (both with unitary strength). In practical terms, this means that the x-component of a dipole is active at the first solution point and the z-component of a dipole is active at the fourth solution point. The reconstruction provided in this case will be equal to the sum of columns 1 and 12 of the resolution matrix, and its numerical values are given in Table 2.

The largest positive value of the reconstruction appears at source component number four and therefore at the second solution point. The largest absolute value appears at the source component number six which also belongs to the second solution point. The modulus of the vector, given in Table 3, shows similar results. This means that neither the component-by-component reconstruction nor the modulus shows maxima at the actual source locations at solution points one and four. In fact the fourth solution point has the smallest modulus, and its active component the third smallest estimated strength. The failure of the solution to retrieve the two simultaneously active sources is once again due to the existence of large off-diagonal elements in the MRM. Hopefully, this numerical example helps to understand that the naïve intuitive application of the superposition principle to this problem is erroneous since exclusively based on the diagonal elements of the MRM.

As for a comparison, we depict on Table 4 the resolution matrix for the Minimum Norm (i.e., Moore Penrose pseudo inverse) solution. Note that while it is symmetric, the maxima for each row (or column) are not necessarily at the main diagonal. Note also that several elements are zero for the numerical precision (3 decimal digits) used.

Table 2: *The reconstruction provided by ANA when multiple sources are active is erroneous despite the perfect reconstruction of both sources alone*. Current density vector reconstruction for EEG data generated when the first and the last single sources are simultaneously active with unitary amplitude.

1.16	1.42	1.42	1.43	−1.50	−1.52	−1.51	−1.50	−0.72	0.86	−0.74	1.16

Table 3: *Modulus of the current density vector of Table 2*. Each value corresponds to the strength of the source at each solution point as computed using (10).

2.32	2.57	2.25	1.62

3.3. Single Source Localization with ANA in the Original Source Space of **j** *and Synthetic Noisy Data.* We have shown so far that ANA solution is capable to provide perfect localization of single sources within the space of the transformed variable **Z**. However, it is clear that on the original source space the symmetry of the resolution matrix will not hold and that we cannot insure that MRM elements are bounded. However, based on the rationale behind ANA and EPIFOCUS, there is no reason to believe that this will prevent ANA to correctly localize single sources in the original source space. To shed some light on this issue, we can resort to simulations with single sources. This issue is of concern because the problem of single dipole localization under the assumption of a dominant generator remains of interest in several practical neurophysiological applications such as epilepsy [22–25]. Linear inverse solutions constitute an appealing alternative to nonlinear dipole localizations because of their higher computational simplicity and their possibilities to be applied to irregular solution spaces required for modeling patient's brains [11]. We might therefore wonder if the good features of ANA for single source localization hold within the original source space **j**. For practical applications in clinical and research routine, we expect a solution which guarantees accurate localization but which is also robust, that is, capable to deal with experimental noise and modeling errors (sensor location, approximate head conductivities, etc.) and particularly with changes in the pattern/map of the dominant source induced by other weaker sources that are simultaneously active.

In this section we present some simulation results to study how much the theoretical performance degrades with noise in the original source space **j**. We compare the localization results for four linear solutions including three that are highly efficient for single source localization: (1) ANA, (2) EPIFOCUS [11, 26], and (3) sLORETA [9]. The fourth solution, that is, (4) the Moore-Penrose inverse of the normalized lead field was also included to confirm that the results of ANA are not simply due to the weighting strategy introduced in its design.

For reproducibility and compatibility with previous publications, we use in this section a lead field model corresponding to the sensor configuration and solution space described in ISBET NEWSLETTER number 6, December 1995, Grave and Gonzalez, 2000, Grave et al. 2001. Namely, a unit radius 3-shell spherical head model (Ary et al., 1981), with solution points confined to a maximum radius of 0.8. The sensor configuration comprises 148 electrodes. The solution space consists of 817 points on a regular grid with an intergrid distance of 0.133 cm, corresponding to 2451 focal sources. To simulate noisy data, we added to each electrode uncorrelated random noise in the range ±15% of the amplitude of the noiseless data. DLE and BDL are divided by the size of the grid unit (0.133) and are evaluated for x values in the set $[0, 0.5, 1, 1.5, 2, 2.5, 3, 3.5, 4, 4.5, 5, 5.5, 6, 6.5, 7]$. For each value x_i, we compute

(1) the empirical Probability Distribution Function, defined as follows: Probability(x_i) = {Number of sources with errors $\leqq x_i$}/2451;

(2) the empirical density function defined for $x_i < 7$ as follows: Density(x_i) = {Number of sources with errors in $[x_i, x_{i+1}]$}/2451.

Note that while the empirical density function describes the performance for each eccentricity range, the probability function provides a global assessment about how fast the maximum asymptotic value is attained.

Figure 2 presents the dipole localization error for ANA, EPIFOCUS, sLORETA, and MPNL inverse in the localization of the 2451 single sources when the data is contaminated with 15% of noise. While the results for sLORETA and MPNL are equally erratic for noisy data (Figure 2), they clearly differ for noiseless data (not shown here) where sLORETA attains zero DLE whereas MPNL remains unreliable. In contrast ANA and EPIFOCUS have very similar behavior for noiseless (not shown) and noisy data (Figure 2). All regularization parameters tested for sLORETA (namely, $\lambda = 0$, 1e-6, 0.1, 1, 10) yield similar erratic results for noisy data. Figure 2 depicts the results for sLORETA for just one of the values tested ($\lambda = 0$).

Figure 3 presents the bias in dipole localization for ANA, EPIFOCUS, sLORETA, and MPNL inverse in the localization of the 2451 single sources when the data is contaminated with 15% of noise. For the noiseless (not shown) data sLORETA and ANA attain zero BDL for all the sources, while for the noisy data (Figure 3) only ANA remains at zero BDL followed by EPIFOCUS. MPNL and sLORETA produce errors as large as 6.5 grid units. All regularization parameters tested for sLORETA (namely, $\lambda = 0$, 1e-6, 0.1, 1, 10) yield similar erratic results. The results shown in Figure 3 for sLORETA correspond to a regularization parameter of $\lambda = 1$.

4. Discussion

The ANA inverse solution described in this paper is, to the best of our knowledge, the first linear solution to the NIP simultaneously fulfilling (in the transformed space) the three following properties: (1) symmetric resolution matrix; (2) perfect single source localization, and (3) perfect

Table 4: *Resolution matrix for the minimum norm solution and the configuration presented in Figure 1.* Even though it is symmetric, the maxima are not always located at the main diagonal.

0.00	−0.02	−0.02	0.00	0.00	−0.01	0.00	0.00	0.00	0.00	0.00	0.00
−0.02	0.5	0.45	0.00	0.15	0.02	0.00	0.09	0.01	0.00	0.09	0.11
−0.02	0.45	0.45	−0.01	−0.01	0.16	0.00	0.06	0.05	0.00	0.06	0.11
0.00	0.00	−0.01	0.00	0.02	−0.02	0.00	0.00	−0.01	0.00	0.00	0.00
0.00	0.15	−0.01	0.02	0.5	−0.44	0.00	0.08	−0.13	0.00	0.08	−0.01
−0.01	0.02	0.16	−0.02	−0.44	0.45	0.00	−0.05	0.13	0.00	−0.06	0.04
0.00	0.00	0.00	0.00	0.00	0.00	0.00	0.00	0.00	0.00	0.00	0.00
0.00	0.09	0.06	0	0.08	−0.05	0.00	0.02	−0.02	0.00	0.02	0.01
0.00	0.01	0.05	−0.01	−0.13	0.13	0.00	−0.02	0.04	0.00	−0.02	0.01
0.00	0.00	0.00	0.00	0.00	0.00	0.00	0.00	0.00	0.00	0.00	0.00
0.00	0.09	0.06	0.00	0.08	−0.06	0.00	0.02	−0.02	0.00	0.02	0.01
0.00	0.11	0.11	0.00	−0.01	0.04	0.00	0.01	0.01	0.00	0.01	0.03

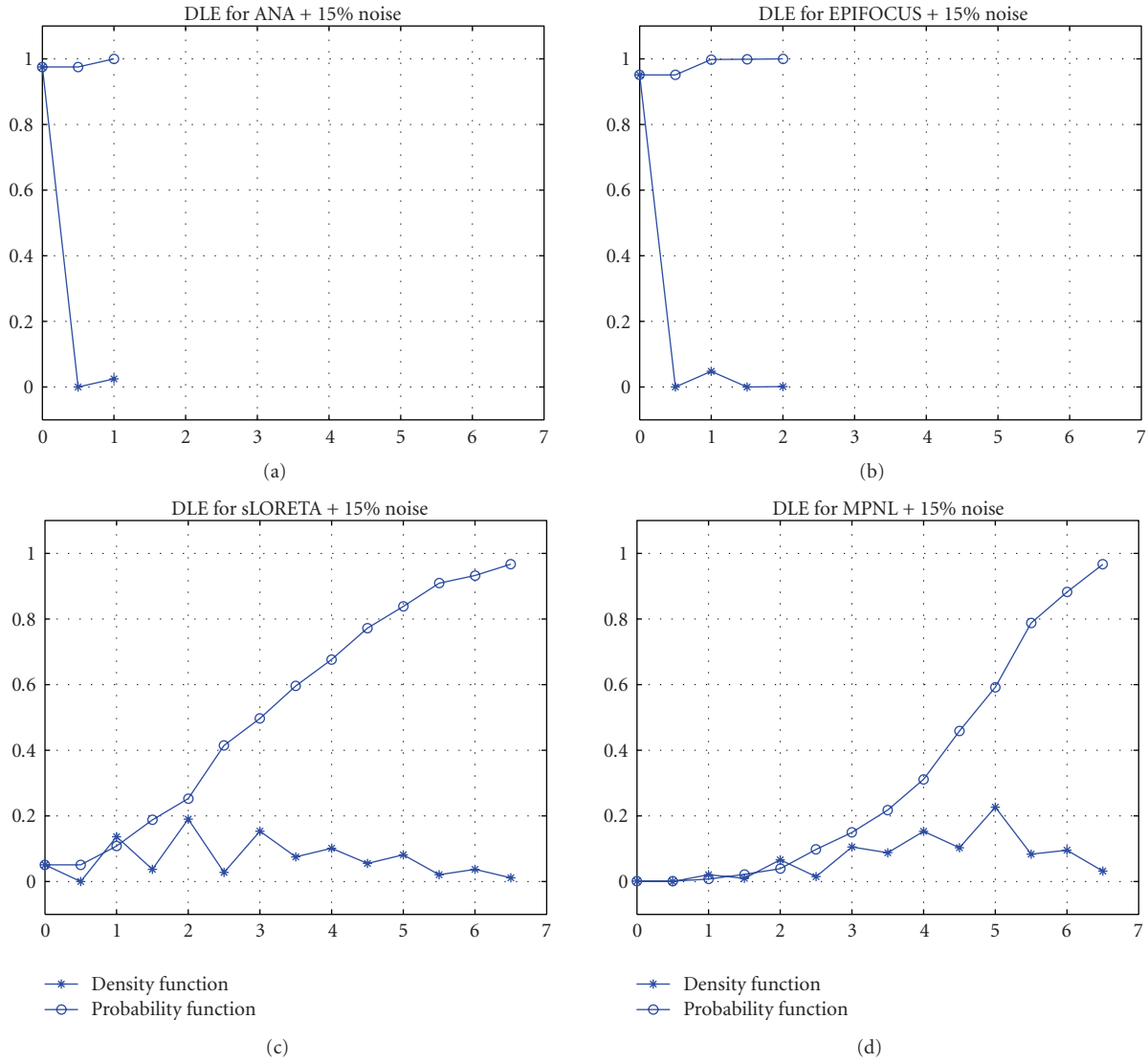

Figure 2: *Dipole Localization Error (DLE) results with synthetic data with 15% noise.* The model is composed of 148 electrodes and 2451 single dipoles at 817 solution points. Probability and Density functions (vertical axis) are plotted versus error sizes (horizontal axis) measured in grid units. Despite the noise in the data, DLE for EPIFOCUS and ANA are never bigger than two grid units while sLORETA and MPNL errors can be higher than 6 grid units.

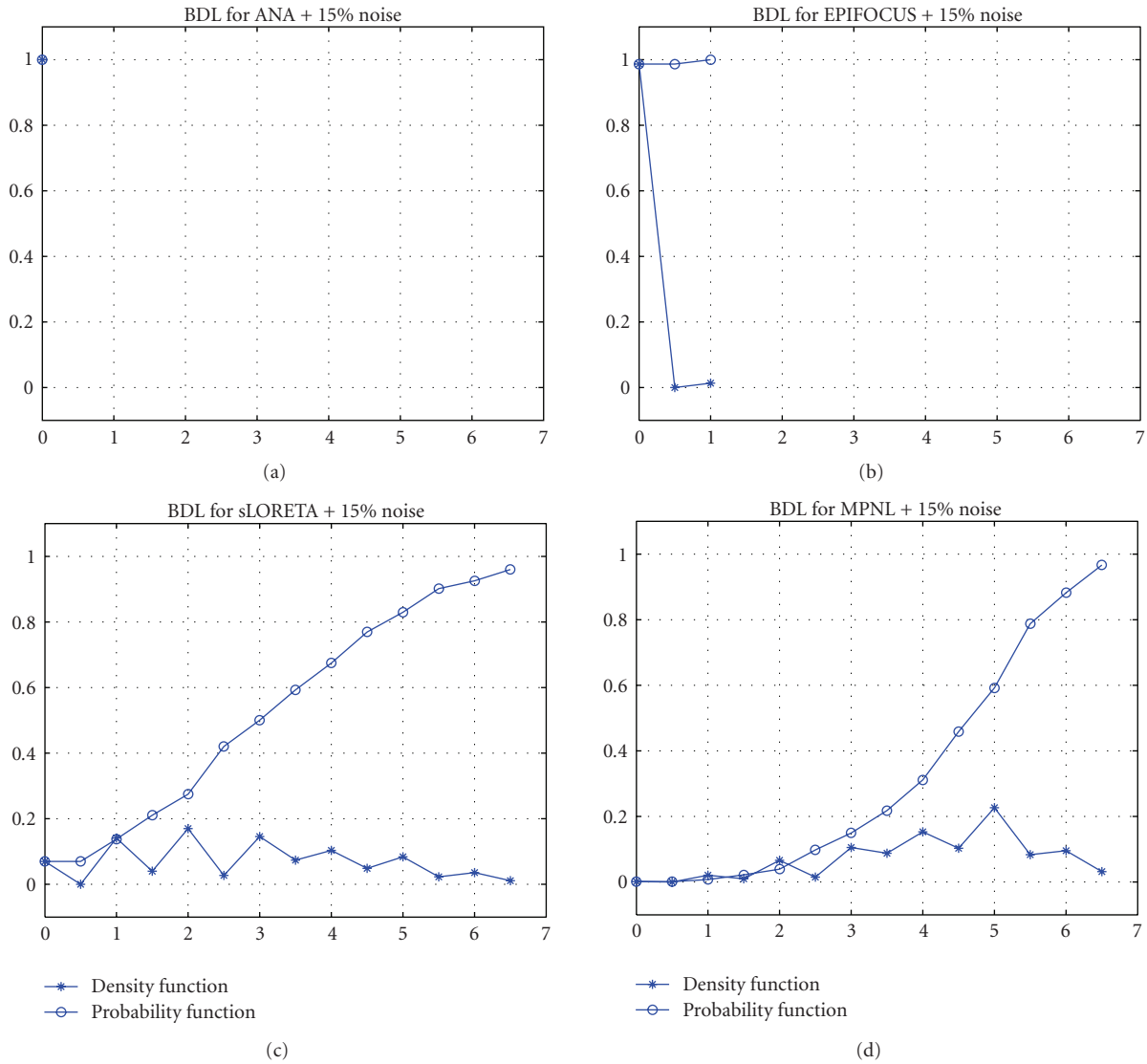

Figure 3: *Bias in dipole localization results for noisy data with 15% noise.* Model includes 148 electrodes and 2451 single dipoles placed at 817 solution points. Probability and Density functions (vertical axis) are plotted versus error sizes (horizontal axis). Despite the noise in the data, BDL for EPIFOCUS and ANA are never bigger than two grid units while sLORETA and MPNL errors can be higher than 6 grid units.

estimation of single source strength. Probably this is also the simplest (in the sense of numerical complexity) solution with these properties. Importantly, such properties stem from the theoretical resolution matrix and therefore hold for arbitrary (with noncollinear columns) lead field models.

In case we accept that perfect single source localization, that is, correct estimation of the location and the source strength as in ANA or correct estimation of the location as in sLORETA, suffices to insure perfect multiple source reconstruction, we must conclude that ANA or sLORETA is the solution to the NIP. This statement is in flagrant contradiction to any rationale. The mistake resides in the assumption that perfect single source localization, defined as zero DLE or zero BDL, implies accurate multiple source localization. This implication is true only for the ideal resolution matrix with zero off-diagonal elements, which is impossible for an underdetermined problem. As demonstrated here, ANA solution is theoretically perfect for single source reconstruction but failed in the simplest case of two simultaneously active sources. As shown in the example, the reason for such failure is the existence of nonzero off-diagonal elements within the model resolution matrix that are ignored by the DLE or BDL. As we saw, nonzero off-diagonal elements appear as a consequence of the correlation between scalp potential (magnetic fields) patterns associated with different punctual sources. Such off-diagonal elements are inherent to the problem statement (the lead field model) and will appear for all linear inverse solutions (e.g., sLORETA, MPNL, EPIFOCUS, etc.), although to different extent. Note that while noiseless data imply the selection of a single MRM column, noisy data can be interpreted as an additional source (generating the noise) implying that

multiple columns of the MRM should be added to get the final current density estimator. As shown before, off-diagonal elements might dominate such reconstruction even in the noiseless case. However, as long as the components of the additional source are lower than the correlation between patterns of neighboring dipoles, ANA (and the closely related EPIFOCUS) should yield low BDLs. Simulations suggest that this is not the case for sLORETA or MPNL with errors up to 6.5 grid units.

Importantly, it is widely accepted that localization accuracy will indefinitely improve by increasing the number of scalp recording sensors. While increasing the number of sensors augments the amount of information about the underlying sources, it does also enhance the correlation (redundancy) between the rows of the lead field matrix, that is, the way that one sensor sees all the sources. The increase in correlation between rows results in unstable (sensitive to noise) problems that need special regularization strategies to avoid noise amplification. This trade-off between the independent information conveyed by the new measurements and their redundancy will define a practical superior bound to the amount of electrodes to be used for source localization purposes.

We have seen that neither the perfect single source localization nor the unlimited increase in the amount of recording sensors will definitively solve the NIP. Obviously, the only remaining choice is to incorporate as much a priori information as possible about the generators into the problem. Such information should be independent of the information already contained in the measurements. A priori information can be incorporated within the discrete formalism by a right-side transformation of the lead field matrix, which in turn can be interpreted as a change of variable. Only this procedure, illustrated here for ANA solution (see (6)), will allow to effectively modify the shapes of resolution kernels. Nevertheless the question remains open which of these right-side modifications of the lead field will result in correctly centered resolution kernels. Examples of right-side transformations of the lead field already employed in the NIP literature are the irrotational source model of ELECTRA [15, 27] or the transformed lead field based on predefined directions of the sources used in SAM [8, 20].

The value of ANA solution is not only didactical. As shown by our simulation results, ANA can be applied to retrieve sources in the space of the original variable $\mathbf{j}$. Although in this space the dipole localization error is not zero everywhere, the bias in dipole localization remains zero and the results are very robust to noise. In this sense ANA solution compares to the more robust methods presented so far. Its computational simplicity, easiness of application to irregularly distributed solution spaces, and localization capabilities make of ANA a reasonable alternative for the analysis of data generated by a single dominant source plus noise. Such assumptions are not rare in one of the most important clinical applications of source localization, namely, the determination of the site of onset of epileptic activity [22, 25].

It is worth mentioning that the limitations described here are not specific to linear inverse solutions, and they will certainly appear under a different mask for nonlinear inverse procedures. While these difficulties are easily analyzed within the linear framework because of the possibilities offered by the model resolution matrix formalism, they actually reflect the ill-posed nature of the original inverse problem. Therefore, unless useful a priori information is found that cannot be incorporated within linear inverses, we see no good reasons to replace the comfortable linear framework with its inherent computational and interpretational simplicity.

The evaluation and design of linear inverse solutions over last decade have been misguided by the idea that only solutions able to accurately localize a large proportion of single sources will succeed in the quest for constructing a tomography of neural generators [9, 12]. Hopefully, the examples and arguments in this paper will help to reorient research within this field to the characterization of properties of neural generators as the sole way to overcome the nonuniqueness of the NIP inverse problem. Research in this direction is not doomed to failure, and existing inverse solutions can lead to relevant and novel findings within neuroscience when correctly exploited and interpreted. While often overlooked, some of the limitations of linear inverse solutions to the NIP are shared by the fMRI. For instance, the absolute size of the fMRI contrast signal cannot be relied upon to measure the amplitude of the neural responses at two different cortical locations [28]. In a similar manner we should be cautious comparing current source density estimates at two different solution points since amplitude estimates vary as a function of the actual current distribution as well as the diagonal and off-diagonal elements of the MRM. However, we can rely either on experimental contrasts as done with fMRI or on measures invariant to scale transformations such as spectral measures derived from temporal information of the estimated sources [29–31] to improve the reliability of the information retrieved from the inverses.

5. Conclusions

Here we introduced a linear inverse solution coined ANA which fulfills several optimal properties for the localization of single sources. We demonstrated by means of the model resolution matrix formalism that ANA localizes correctly the location and the amplitudes of all single sources. These properties hold for arbitrary lead fields and for arbitrarily small sensor configurations. This fact was exploited to introduce simple examples that clarify how spurious sources are formed and their large relevance for simultaneous source reconstruction. We further showed that ANA solution is highly robust to noise, outperforming established methods for single source localization (sLORETA and EPIFOCUS). Its robustness to noise and computational simplicity make ANA a reasonable alternative for data generated by a single dominant source plus noise, as can be the case in epilepsy.

The most important contribution of this manuscript is to provide definitive evidence that the apparently reasonable (although naïve) idea of inferring the behavior of linear solutions from their single source localization properties proves false. It is thus concluded that zero localization error alone is a trivial and useless property unable to predict the performance of an inverse solution in presence of simultaneously active sources. We expect that these results will help researchers to guide their choices of inverse methods, in methods development as well as for clinical and neuroscientific applications. We also hope that it will stimulate further interest in finding neurophysiologically plausible constraints that can be used as a priori information in the NIP, which should be the ultimate goal in this endeavour.

Acknowledgments

The authors thank two anonymous reviewers for their constructive comments. This work was supported by the European Project FP6-IST-027140 (BACS) and the COST Action BM0601 "NeuroMath." This paper only reflects the authors' views, and funding agencies are not liable for any use that may be made of the information contained herein. The COST Office is not responsible for the external websites referred to in this publication. We would like to acknowledge the financial support of the UK Medical Research Council for one of the authors (OH, U.1055.04.003.00001.01).

References

[1] C. M. Michel, M. M. Murray, G. Lantz, S. L. Gonzalez, L. Spinelli, and R. Grave de Peralta Menendez, "EEG source imaging," *Clinical Neurophysiology*, vol. 115, no. 10, pp. 2195–2222, 2004.

[2] J. Gross, L. Timmermann, J. Kujala, R. Salmelin, and A. Schnitzler, "Properties of MEG tomographic maps obtained with spatial filtering," *NeuroImage*, vol. 19, no. 4, pp. 1329–1336, 2003.

[3] A. K. Liu, A. M. Dale, and J. W. Belliveau, "Monte Carlo simulation studies of EEG and MEG localization accuracy," *Human Brain Mapping*, vol. 16, no. 1, pp. 47–62, 2002.

[4] O. David, D. Cosmelli, D. Hasboun, and L. Garnero, "A multitrial analysis for revealing significant corticocortical networks in magnetoencephalography and electroencephalography," *NeuroImage*, vol. 20, no. 1, pp. 186–201, 2003.

[5] L. J. Waldorp, H. M. Huizenga, R. P. P. P. Grasman, K. B. E. Böcker, and P. C. M. Molenaar, "Hypothesis testing in distributed source models for EEG and MEG data," *Human Brain Mapping*, vol. 27, no. 2, pp. 114–128, 2006.

[6] G. Backus and F. Gilbert, "The resolving power of gross earth data," *Geophysical Journal of the Royal Astronomical Society*, vol. 16, no. 2, pp. 169–205, 1968.

[7] R. Grave de Peralta Menendez and S. L. Gonzalez Andino, "A critical analysis of linear inverse solutions to the neuroelectromagnetic inverse problem," *IEEE Transactions on Biomedical Engineering*, vol. 45, no. 4, pp. 440–448, 1998.

[8] K. Sekihara, M. Sahani, and S. S. Nagarajan, "Localization bias and spatial resolution of adaptive and non-adaptive spatial filters for MEG source reconstruction," *NeuroImage*, vol. 25, no. 4, pp. 1056–1067, 2005.

[9] R. D. Pascual-Marqui, "Standardized low-resolution brain electromagnetic tomography (sLORETA): technical details," *Methods and Findings in Experimental and Clinical Pharmacology*, vol. 24, supplement D, pp. 5–12, 2002.

[10] R. Grave de Peralta Menendez, S. L. Gonzalez Andino, and B. Lütkenhöner, "Figures of merit to compare distributed linear inverse solutions," *Brain Topography*, vol. 9, no. 2, pp. 117–124, 1996.

[11] R. Grave de Peralta Menendez, S. L. Gonzalez Andino, G. Lantz, C. M. Michel, and T. Landis, "Noninvasive localization of electromagnetic epileptic activity. I. Method descriptions and simulations," *Brain Topography*, vol. 14, no. 2, pp. 131–137, 2001.

[12] R. D. Pascual-Marqui and C. M. Michel, "LORETA: new authentic 3D functional images of the brain," *ISBET Newsletter*, no. 5, pp. 4–8, November 1994, Edited by W. Skrandies.

[13] R. Grave de Peralta Menendez and S. L. Gonzalez Andino, "Discussing the capabilities of Laplacian minimization," *Brain Topography*, vol. 13, no. 2, pp. 97–104, 2000.

[14] C. Phillips, M. D. Rugg, and K. J. Friston, "Systematic regularization of linear inverse solutions of the EEG source localization problem," *NeuroImage*, vol. 17, no. 1, pp. 287–301, 2002.

[15] R. Grave de Peralta Menendez, S. L. Gonzalez Andino, S. Morand, C. M. Michel, and T. Landis, "Imaging the electrical activity of the brain: ELECTRA," *Human Brain Mapping*, vol. 9, no. 1, pp. 1–12, 2000.

[16] M. Hämäläinen, R. Hari, R. J. Ilmoniemi, J. Knuutila, and O. V. Lounasmaa, "Magnetoencephalography theory, instrumentation, and applications to noninvasive studies of the working human brain," *Reviews of Modern Physics*, vol. 65, no. 2, pp. 413–497, 1993.

[17] W. Menke, *Geophysical Data Analysis: Discrete Inverse Theory*, Academic Press, San Diego, Calif, USA, 1989.

[18] J. G. Berryman, "Analysis of approximate inverses in tomography. I. Resolution analysis of common inverses," *Optimization and Engineering*, vol. 1, no. 1, pp. 87–115, 2000.

[19] R. Grave de Peralta Menendez, P. Morier, F. Picard, T. Landis, and S. L. Gonzalez Andino, "Simple techniques for EEG source imaging," *International Journal of Bioelectromagnetism*, vol. 8, no. 1, pp. V/1–V/8, 2006.

[20] S. E. Robinson, "Localization of event-related activity by SAM(erf)," *Neurology & Clinical Neurophysiology*, vol. 2004, p. 109, 2004.

[21] S. L. Gonzalez Andino, O. Blanke, G. Lantz, G. Thut, and R. Grave de Peralta Menendez, "The use of functional constraints for the neuroelectromagnetic inverse problems: alternatives and caveats," *International Journal of Bioelectromagnetism*, vol. 3, no. 1, pp. 55–66, 2001.

[22] J. S. Ebersole, "Non-invasive localization of the epileptogenic focus by EEG dipole modeling," *Acta Neurologica Scandinavica*, vol. 89, supplement 152, pp. 20–28, 1994.

[23] T. Bast, O. Oezkan, S. Rona, et al., "EEG and MEG source analysis of single and averaged interictal spikes reveals intrinsic epileptogenicity in focal cortical dysplasia," *Epilepsia*, vol. 45, no. 6, pp. 621–631, 2004.

[24] M. Scherg, T. Bast, and P. Berg, "Multiple source analysis of interictal spikes: goals, requirements, and clinical value," *Journal of Clinical Neurophysiology*, vol. 16, no. 3, pp. 214–224, 1999.

[25] C. M. Michel, G. Lantz, L. Spinelli, R. Grave de Peralta Menendez, T. Landis, and M. Seeck, "128-channel EEG source imaging in epilepsy: clinical yield and localization precision,"

Journal of Clinical Neurophysiology, vol. 21, no. 2, pp. 71–83, 2004.

[26] G. Lantz, R. Grave de Peralta Menendez, S. L. Gonzalez Andino, and C. M. Michel, "Noninvasive localization of electromagnetic epileptic activity. II. Demonstration of sublobar accuracy in patients with simultaneous surface and depth recordings," *Brain Topography*, vol. 14, no. 2, pp. 139–147, 2001.

[27] R. Grave de Peralta Menendez, M. M. Murray, C. M. Michel, R. Martuzzi, and S. L. Gonzalez Andino, "Electrical neuroimaging based on biophysical constraints," *NeuroImage*, vol. 21, no. 2, pp. 527–539, 2004.

[28] N. K. Logothetis and B. A. Wandell, "Interpreting the BOLD signal," *Annual Review of Physiology*, vol. 66, pp. 735–769, 2004.

[29] S. L. Gonzalez Andino, C. M. Michel, G. Thut, T. Landis, and R. Grave de Peralta Menendez, "Prediction of response speed by anticipatory high-frequency (gamma band) oscillations in the human brain," *Human Brain Mapping*, vol. 24, no. 1, pp. 50–58, 2005.

[30] S. L. Gonzalez Andino, R. Grave de Peralta Menendez, A. Khateb, A. J. Pegna, G. Thut, and T. Landis, "A glimpse into your vision," *Human Brain Mapping*, vol. 28, no. 7, pp. 614–624, 2007.

[31] S. L. Gonzalez Andino, R. Grave de Peralta Menendez, A. Khateb, T. Landis, and A. J. Pegna, "Electrophysiological correlates of affective blindsight," *NeuroImage*, vol. 44, no. 2, pp. 581–589, 2009.

Hindawi Publishing Corporation
Computational Intelligence and Neuroscience
Volume 2009, Article ID 104180, 6 pages
doi:10.1155/2009/104180

Research Article

Discrimination of Motor Imagery-Induced EEG Patterns in Patients with Complete Spinal Cord Injury

G. Pfurtscheller,[1] P. Linortner,[1] R. Winkler,[2] G. Korisek,[2] and G. Müller-Putz[1]

[1] *Laboratory of Brain-Computer Interfaces, Institute for Knowledge Discovery, Graz University of Technology, Krenngasse 37, 8010 Graz, Austria*
[2] *Rehabilitation Clinic Tobelbad, Krenngasse 37, Dr.-Georg-Neubauer-Straße 6, 144 Tobelbad, Austria*

Correspondence should be addressed to G. Pfurtscheller, pfurtscheller@tugraz.at

Received 30 October 2008; Accepted 11 February 2009

Recommended by Fabio Babiloni

EEG-based discrimination between different motor imagery states has been subject of a number of studies in healthy subjects. We investigated the EEG of 15 patients with complete spinal cord injury during imagined right hand, left hand, and feet movements. In detail we studied pair-wise discrimination functions between the 3 types of motor imagery. The following classification accuracies (mean ± SD) were obtained: left versus right hand 65.03% ± 8.52, left hand versus feet 68.19% ± 11.08, and right hand versus feet 65.05% ± 9.25. In 5 out of 8 paralegic patients, the discrimination accuracy was greater than 70% but in only 1 out of 7 tetraplagic patients. The present findings provide evidence that in the majority of paraplegic patients an EEG-based BCI could achieve satisfied results. In tetraplegic patients, however, it is expected that extensive training-sessions are necessary to achieve a good BCI performance at least in some subjects.

1. Introduction

Functional magnetic resonance imaging (fMRI) and EEG studies have shown that executed and imagined movement activates overlapping and/or similar neural networks in primary motor and related areas [1–3]. This equivalence of motor execution and motor imagery in relation to cortical activation is one prerequisite for the restoration of motor functions in para- and/or tetraplegic patients using a brain-computer interface (BCI; [4, 5]). Whether patients with complete spinal cord injury (SCI) are able to control their brain oscillations reliable and safe through imagined limb movements and operate herewith a BCI is however still an open question.

Sensorimotor rhythms such as mu and central beta oscillations can be modified by executed and imagined movement [6–10]. By using multichannel EEG recordings and applying pair-wise discrimination functions to the EEG signals it is possible to discriminate between 3 different types of motor imagery (right or left hand or foot) [11, 12]. In this study we addressed the following questions: (i) is it possible to discriminate pair-wise between 3 motor imagery-related EEG patterns (right hand, left hand, and feet) in patients with complete spinal cord injury and (ii) is this discrimination different for paraplegic and tetraplegic patients. When a reliable detection of imagery-related brain states in ongoing EEG is possible the BCI output signal can be used to control, for example, a neuroprosthesis [5].

2. Methods

2.1. Subjects and Experimental Task. The patient group consisted of 15 patients (four females and eleven males) aged from 16 to 64 years (M = 41 years, SD = 14.50). All patients suffered from a complete sensor and motor paralysis at ASIA level C5 to T12 after a traumatic SCI between 1.6 months and 32.9 years prior to the measurements. Seven patients were tetraplegic, and eight patients were paraplegic. Information on the patients is summarized in Table 1.

Measurements were carried out at the Rehabilitation Clinic Tobelbad (Austria). The experiment was divided into 6–8 runs (depending on the physical condition of the patient), each consisting of 30 trials of three different motor imagery tasks (10 trials each). Between those runs participants could

Table 1: Patients characteristics.

Patient	Date of birth (year)	Date injury (year)	Duration (months)	ASIA level	Number of trials (artifact-free/total)
P01	1987	2007	3.9	C5 (Tetra)	207/240
P02	1981	2007	5.3	C6 (Tetra)	220/240
P03	1957	1991	192	Th12 (Para)	222/240
P04	1972	1989	226.5	C6 (Tetra)	163/240
P05	1956	2007	2.5	C5 (Tetra)	186/210
P06	1960	1982	38.9	Th5 (Para)	223/240
P07	1949	2007	4.2	C6 (Tetra)	155/180
P08	1959	1979	341.7	Th11 (Para)	199/240
P09	1943	2007	11.9	Th6 (Para)	149/210
P010	1949	1975	394.6	Th8 (Para)	113/210
P011	1966	2007	5.5	Th4 (Para)	161/180
P012	1992	2008	1.6	Th12 (Para)	165/210
P013	1963	2005	33.2	C7 (Tetra)	157/210
P014	1965	2007	6.8	C6 (Tetra)	159/240
P015	1984	2006	22.1	L1 (Para)	190/210
Mean	1965.53	1998.93	86.05		
Median	1963	2007	11.9		
SD	14.83	12.08	134.42		

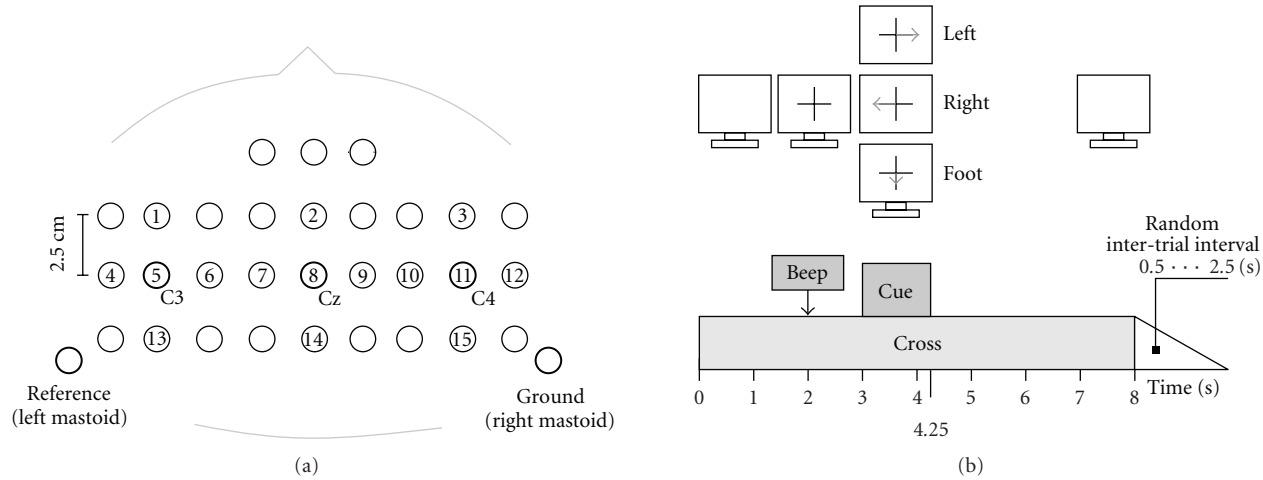

Figure 1: (a) Electrode positions. (b) Timing and experimental paradigm.

(and were encouraged to) take short breaks for recovery and in order to avoid fatigue.

Each trial began with the presentation of a fixation cross at the centre of the monitor, followed by a short warning tone at second 2. At second 3, an arrow pointing randomly left, right, or down, representing one of three different motor imagery tasks (left hand (L), right hand (R) and both feet (F), resp.), appeared on the screen for 1.25 seconds, additionally to the fixation cross. The fixation cross remained displayed on the screen until the end of the trial at second 8, indicating that the imagination still had to be performed. This implies a motor imagery lasting for 5 seconds was required. After that, a blank screen was presented until the beginning of the next trial. This intertrial period varied randomly between 0.5 and 2.5 seconds.

Timing and experimental paradigm are displayed in Figure 1(b).

2.2. EEG Recording. Continuous EEG signals were recorded from a grid of fifteen sintered Ag/AgCl ring electrodes (Easycap, Germany) that were mounted orthogonally in both, horizontal and vertical directions, over the electrode positions C3, Cz, and C4 (according to the international 10–20 electrode system, cf. Figure 1(a)). The closely spaced interelectrode distance was 2.5 cm. All electrodes were referenced to the left mastoid. The ground electrode was mounted

Table 2: Classification accuracy (%) of the maximal peak and its latency (delay) after cue onset for all 15 patients and all combinations. Accuracies in bold differ significantly from chance level according to the number of trials (cf. [13]).

Patient	Left versus right hand		Left hand versus feet		Right hand versus feet	
	Accuracy (%)	Delay (s)	Accuracy (%)	Delay (s)	Accuracy (%)	Delay (s)
P01	56.2	3.5	54.8	4.5	56.9	1.0
P02	**78.1**	2.0	**86.8**	2.0	**83.1**	3.0
P03	**63.5**	1.0	**62**	1.5	**63.3**	1.5
P04	**63.5**	1.5	**62.3**	2.0	**67.7**	1.5
P05	58.7	2.5	56.2	1.5	51.4	4.5
P06	57.9	1.5	**65.0**	2.5	58.5	2.5
P07	57.2	2.0	**64.3**	1.5	55.9	2.0
P08	**60.4**	1.5	**63.6**	2.0	**62.0**	1.5
P09	**83**	1.5	**86.3**	1.5	**71.1**	2.5
P010	**68.1**	2.0	**85.7**	2.0	**78.8**	2.0
P011	**76**	1.5	**77.7**	1.5	**75.2**	1.5
P012	59.8	2.0	**70.6**	1.5	**63.1**	0.5
P013	57.1	2.5	54.4	4.0	56.8	0.5
P014	**64**	0.0	**65.2**	3.0	60.1	3.5
P015	**71.8**	2.0	**67.9**	2.5	**71.8**	2.5
Mean	65.02	1.8	68.19	2.23	65.05	2.03
Median	63.5	2	65	2	63.1	2
SD	8.52	0.77	11.08	0.94	9.24	1.09

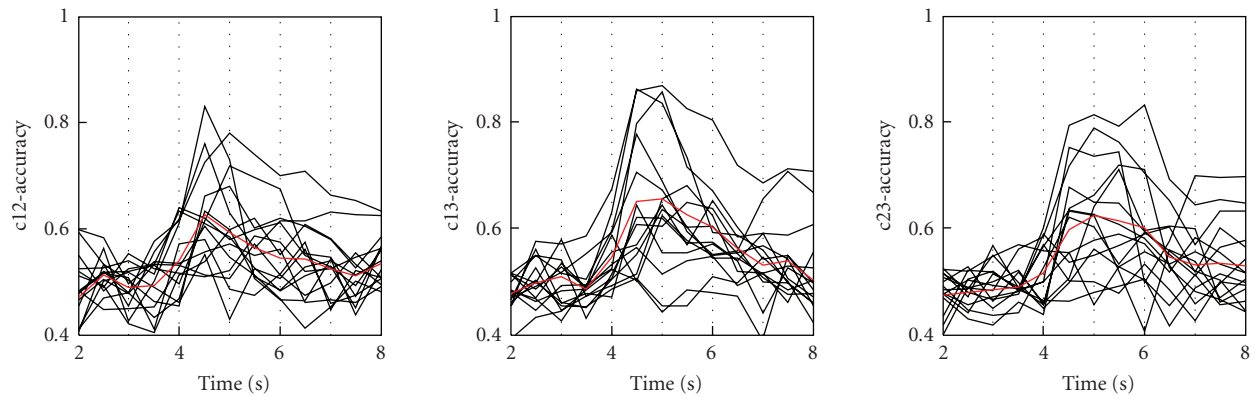

Figure 2: Discrimination time courses for a length of 5 s after cue onset. The onset of cue presentation is at second 3. Data from all 15 patients and all 3 brain states are displayed: right versus left hand MI (left panel), left hand versus feet MI (middle panel), and right hand versus feet MI (right panel).

at the right mastoid. Impedances were kept below 5 kOhm. For monopolar EEG derivation a portable amplifier (g.tec, Graz, Austria) was used. Signals were digitized at 256 Hz and bandpass filtered between 0.5 and 100 Hz. Sensitivity was set to 100 μV and a notch filter at 50 Hz was used.

2.3. Data Analysis. The method of Common Spatial Patterns (CSP) and Fischer's linear discriminant analysis (LDA) classifier were used to discriminate between any 2 classes. The CSP-method projects multichannel EEG data into a low-dimensional spatial subspace in such a way that the variances of the filtered time series are optimal for discrimination. The projection matrix, consisting of the weights of the EEG channels, is sorted in descending order of the eigenvalues. Before applying CSP and LDA, a fully automated method for reducing EOG artifacts was applied on the data. Then, the EEG recordings were visually inspected for remaining EOG and EMG artifacts and filtered between 8–30 Hz. To get a good generalization of the classifier a 10×10 cross-validation procedure was adopted. The EEG data from each trial was divided into time segments of 1 s overlapping by half of their length. For further details see [11, 14].

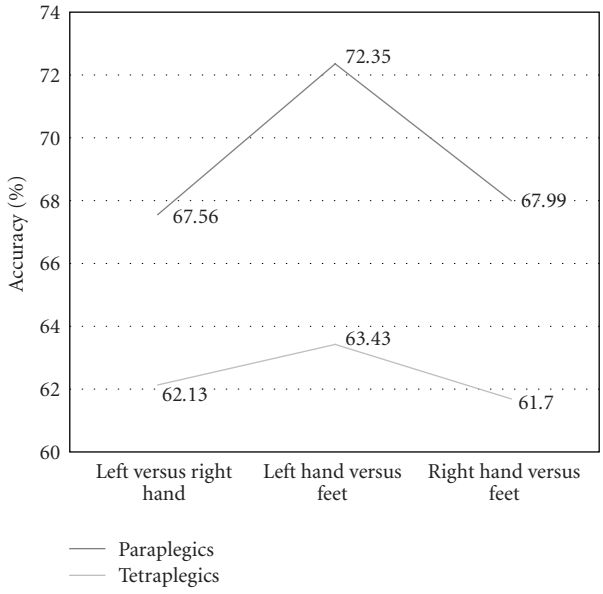

Figure 3: Two-class classification accuracy for paraplegic and tetraplegic patients.

2.4. Calculation of Time-Frequency Maps. To enhance local oscillations, orthogonal source derivations (Laplacian) were calculated [15]. After triggering the data, trials of 10 s duration were obtained including 3 seconds before the cue. The quantification of ERD/ERS was carried out in four steps: band pass filtering of each trial, squaring of samples (with smoothing) and subsequent averaging over trials and over sample points. The ERD/ERS is defined as the percentage power decrease (ERD) or power increase (ERS) in relation to a one-second reference interval (0.5–1.5 seconds) before the warning tone [3]. ERD/ERS values corresponding to 2-Hz frequency bands ranging from 6–18 Hz (with an overlap of 1 Hz) and 4-Hz frequency bands ranging from 18–38 Hz (with an overlap of 2 Hz) were calculated. All values for one EEG channel were subsequently used to construct time-frequency maps (ERD/ERS maps). The statistical significance of the ERD/ERS values was verified by applying a t-percentile bootstrap statistic to calculate confidence intervals with $\alpha = 0.05$.

2.5. Statistical Analysis. An ANOVA was computed in order to examine whether paraplegic versus tetraplegic patients differ regarding reached classification accuracy. This ANOVA consisted of the between-subject variable SCI (2 levels: paraplegics and tetraplegics) and the within-subject variable ACCURACY (3 levels: left hand versus right hand, left hand versus feet and right hand versus feet).

3. Results

The power of discrimination between two different brain states is indicated by the classification accuracy of single EEG trials analysed within 1-second time windows. The discrimination time courses for epochs of 6 seconds (with 1 second prior to cue-onset) for all task combinations (right versus left hand, left hand versus feet, and right hand versus feet) are shown in Figure 2. The maximal classification accuracies of the first peak together with the corresponding latencies, measured from cue onset are summarized in Table 2. The mean accuracy of all subjects (±SD) was 65.03% ± 8.51 (left versus right hand MI), 68.18% ± 11.08 (left hand versus feet MI) , and 65.05% ± 9.25 (right hand versus feet MI), respectively. (See Table 3 for the mean accuracy of paraplegic versus tetraplegic patients.)

Table 3: Mean classification accuracy for tetraplegic and paraplegic patients.

Motor imagery	Spinal cord injury			
	Paraplegic		Tetraplegic	
	Mean	SD	Mean	SD
L versus R (%)	67.56	8.86	62.13	7.7
L versus F (%)	72.35	9.72	63.43	11.25
R versus F (%)	67.99	7.23	61.70	10.67

In the tetraplegic patient group only one out of seven tetraplegics had an accuracy >70% while from the paraplegics five out of 8 reached a classification accuracy >70%. An accuracy of 70% is the border, where control can be possible [16]. In the majority of participants, feet motor imagery was involved in the best discrimination between two brain states (see Figure 2 and Table 2).

The results of the ANOVA show that the main effect ACCURACY is insignificant. Paraplegic patients (M = 69.3%) do not differ from tetraplegic patients (M = 62.41%), $F(1,13) = 530.292$, $p = .151$. Furthermore, no significant effect emerges for the three classification accuracies, left (L) hand versus right (R) hand (M = 64.85%), left (L) hand versus feet (F) (M = 67.89%), and right (R) hand versus feet (F) (M = 64.84%), but a tendency can be seen, $F(2,26) = 2.877$, $p = .074$ (cf. Figure 3).

Although the discriminations of any two different brain states were based on the analysis of 15 EEG channels recorded over premotor, motor, and parietal areas, different patterns were found in spatially filtered (Laplacian) recordings over the primary motor areas (electrode positions C3, Cz, and C4). For illustration, time-frequency maps (ERD-maps) of two representative subjects are displayed in Figure 4. In subject P02 (Figure 4(a)) clearly visible is the beta increase (ERS) at Cz during hand MI and the beta decrease (ERD) at Cz during feet MI. No clear EEG reactivity patterns can be recognized in subject P01 (Figure 4(b)). In P02 a high classification accuracy was obtained while in P01 no discrimination between the motor imagery states was possible.

4. Discussion

In our study, we applied a classification procedure to multichannel, single-trial EEG data recorded during classical brain-computer interface training sessions with 3-motor imagery tasks: right-hand, left-hand, and feet movement [17,

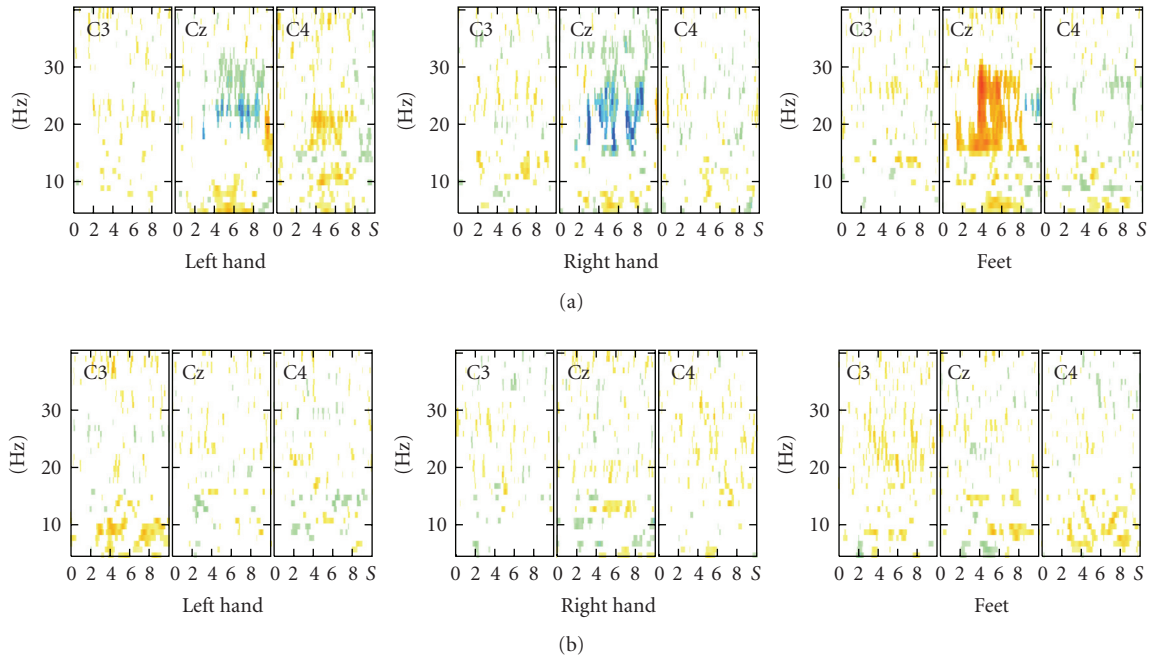

Figure 4: Time-frequency-maps for the three types of motor imagery (left hand, right hand, and feet) computed at electrode positions C3, C_Z, C4 (Laplacian) exemplarily for (a) a patient with good performance (p02) and (b) a patient with bad performance (p01).

18]. One method suitable for studying temporal aspects of brain activation using multichannel EEG recordings consists in computing common spatial patterns (CSPs) [14]. This CSP-method leads to spatial filters that are optimal in the sense that they extract signals which maximally discriminate between any 2 conditions. A subsequent linear classification of these extracted signals results in a good recognition rate. With the CSP-method it is possible to study the separability of EEG patterns associated with 2-motor imagery states with a high time resolution.

The discrimination time courses in the patients with complete spinal cord injury studied were highly variable in its shape and magnitude and started in generally with an initial peak about 1.5 seconds after cue-onset, with a fast increase before and a slow decline thereafter (Figure 2). The great intersubject-variability may be explained by the used mental strategy (e.g., visual versus kinaesthetic motor imagery, [19]), the vividness of the imagery process, the mental effort and other psychological factors as, for example, motivation and attention. Even in one and the same subject the same mental motor imagery strategy can result in completely different EEG reactivity patterns dependent on the degree of imagined effort [20].

The main finding of the present study is that there are distinct EEG patterns in the majority of patients with complete spinal cord injury when they imagine different movements of hands and feet the first time. These patterns are however not very pronounced and the mean classification rate was relatively low around 67%. In contrast, motor imagery in healthy subjects results in clearly discriminable EEG patterns, when 2-motor imagery tasks are compared. Blankertz et al. [17] reported a mean classification accuracy of 88.4% in a so-called calibration session with 3 types of motor imagery (right hand, left hand, and right foot) in untrained healthy subjects. This data are based on 128 EEG channels and CSP analysis. Also with CSP analysis applied to 32 EEG channels mean classification accuracies between 80.0% and 83.3% are reported for left versus right hand MI and hand versus feet MI [12]. In both studies in the majority of subjects the best classification results were achieved when foot MI was involved. One major difference between healthy subjects and patients is very often that patients have very often cramps and/or spasms and therefore a number of muscle artefacts in the EEG (see e.g., Table 1 artefact-free versus total trials).

Of interest is a recently published fMRI study where control subjects and patients had to kinaesthetically imagine movements of their feet [21]. In the paraplegic patient group the primary motor cortex was consistently activated, even to the same degree as during movement execution in the healthy controls. In contrast to this one other study [22] reported inconsistent fMRI activation in the primary motor cortex during self-paced foot motor imagery in complete SCI patients. Of interest is that in the study of Alkadhi et al. [21], a strong positive correlation was found between the vividness scores of motor imagery in paraplegics and the activation (fMRI BOLD signal) in cortical areas including the primary motor cortex and the supplementary motor area (SMA). This can be interpreted that vividness of motor imagery and/or their mental effort plays an important role in cortical activation and is perhaps more intensive in SCI patients than in healthy controls.

One point needs discussion, namely, the slightly higher (but not significant) classification accuracy of hand versus

feet MI as compared to right versus left hand MI found in patients but also reported in healthy subjects. This can be interpreted to mean that the EEG patterns induced by feet or foot MI are better discriminable from the brain state associated with either left or right hand MI. One reason for this could be the antagonistic behaviour of the upper mu ERD and ERS during motor imagery known as "focal ERD/surround ERS" [3]. Feet MI results not only in a midcentrally focused mu and/or beta ERD but very often also in a bilateral mu ERS over the hand representation area [23]. These authors reported on a much larger difference in band power changes in the 10–12 Hz frequency band when different (hand versus foot MI) and not homologous limbs (right versus left hand MI) are compared.

In conclusion, we demonstrated that in the majority of paraplegic patients motor imagery induced EEG patterns can be discriminated. From this follows that with a small number of feedback training sessions the separability between motor imagery-related brain states can be reinforced and a good BCI performance can be expected. In tetraplegic patients the situation is less clear. Only in one patient motor imagery-related EEG patterns could be discriminated in the initial training session. Here extensive trainings sessions without and with feedback are necessary to achieve a satisfied BCI performance at least in some patients.

Acknowledgments

This work was supported by Wings for Life—Spinal Cord Research Foundation (002/06), EU Project Presenccia 27731, EU COST BM0601 Neuromath, "Allgemeine Unfallversicherung AUVA", and Lorenz Böhler Gesellschaft.

References

[1] E. Gerardin, A. Sirigu, S. Lehéricy, et al., "Partially overlapping neural networks for real and imagined hand movements," *Cerebral Cortex*, vol. 10, no. 11, pp. 1093–1104, 2000.

[2] H. H. Ehrsson, J. P. Kuhtz-Buschbeck, and H. Forssberg, "Brain regions controlling nonsynergistic versus synergistic movement of the digits: a functional magnetic resonance imaging study," *Journal of Neuroscience*, vol. 22, no. 12, pp. 5074–5080, 2002.

[3] G. Pfurtscheller and F. H. Lopes da Silva, "Event-related EEG/MEG synchronization and desynchronization: basic principles," *Clinical Neurophysiology*, vol. 110, no. 11, pp. 1842–1857, 1999.

[4] J. R. Wolpaw, N. Birbaumer, D. J. McFarland, G. Pfurtscheller, and T. M. Vaughan, "Brain-computer interfaces for communication and control," *Clinical Neurophysiology*, vol. 113, no. 6, pp. 767–791, 2002.

[5] G. Pfurtscheller, G. R. Müller-Putz, R. Scherer, and C. Neuper, "Rehabilitation with brain-computer interface systems," *Computer*, vol. 41, no. 10, pp. 58–65, 2008.

[6] R. Salmelin and R. Hari, "Spatiotemporal characteristics of sensorimotor neuromagnetic rhythms related to thumb movement," *Neuroscience*, vol. 60, no. 2, pp. 537–550, 1994.

[7] L. Leocani, C. Toro, P. Manganotti, P. Zhuang, and M. Hallett, "Event-related coherence and event-related desynchronization/synchronization in the 10 Hz and 20 Hz EEG during self-paced movements," *Electroencephalography and Clinical Neurophysiology/Evoked Potentials Section*, vol. 104, no. 3, pp. 199–206, 1997.

[8] P. Derambure, L. Defebvre, J. L. Bourriez, F. Cassim, and J. D. Guieu, "Event-related desynchronization and synchronization. Reactivity of cortical electroencephalographic rhythms related to planning and performance of voluntary movement," *Clinical Neurophysiology*, vol. 29, no. 1, pp. 53–70, 1999.

[9] G. Pfurtscheller and C. Neuper, "Motor imagery activates primary sensorimotor area in humans," *Neuroscience Letters*, vol. 239, no. 2-3, pp. 65–68, 1997.

[10] C. Neuper and G. Pfurtscheller, "Motor imagery and ERD," in *Event-Related Desynchronization*, G. Pfurtscheller and F. H. Lopes da Silva, Eds., vol. 6 of *Handbook of Electroencephalography & Clinical Neurophysiology*, pp. 303–325, Elsevier, Amsterdam, The Netherlands, 1999.

[11] H. Ramoser, J. Müller-Gerking, and G. Pfurtscheller, "Optimal spatial filtering of single trial EEG during imagined hand movement," *IEEE Transactions on Rehabilitation Engineering*, vol. 8, no. 4, pp. 441–446, 2000.

[12] G. Pfurtscheller, R. Scherer, G. R. Müller-Putz, and F. H. Lopes da Silva, "Short-lived brain state after cued motor imagery in naive subjects," *European Journal of Neuroscience*, vol. 28, no. 7, pp. 1419–1426, 2008.

[13] G. R. Müller-Putz, R. Scherer, C. Brunner, R. Leeb, and G. Pfurtscheller, "Better than random? A closer look on BCI results," *International Journal of Bioelectromagnetism*, vol. 10, no. 1, pp. 52–55, 2008.

[14] J. Müller-Gerking, G. Pfurtscheller, and H. Flyvbjerg, "Classification of movement-related EEG in a memorized delay task experiment," *Clinical Neurophysiology*, vol. 111, no. 8, pp. 1353–1365, 2000.

[15] B. Hjorth, "An on line transformation of EEG scalp potentials into orthogonal source derivations," *Electroencephalography and Clinical Neurophysiology*, vol. 39, no. 5, pp. 526–530, 1975.

[16] J. Perelmouter and N. Birbaumer, "A binary spelling interface with random errors," *IEEE Transactions on Rehabilitation Engineering*, vol. 8, no. 2, pp. 227–232, 2000.

[17] B. Blankertz, G. Dornhege, M. Krauledat, K.-R. Müller, and G. Curio, "The non-invasive Berlin Brain-Computer Interface: fast acquisition of effective performance in untrained subjects," *NeuroImage*, vol. 37, no. 2, pp. 539–550, 2007.

[18] G. Pfurtscheller, C. Neuper, and N. Birbaumer, "Human brain-computer interface," in *Motor Cortex in Voluntary Movements*, A. Riehle and E. Vaadia, Eds., pp. 367–401, CRC Press, Boca Raton, Fla, USA, 2005.

[19] C. Neuper, R. Scherer, M. Reiner, and G. Pfurtscheller, "Imagery of motor actions: differential effects of kinesthetic and visual-motor mode of imagery in single-trial EEG," *Cognitive Brain Research*, vol. 25, no. 3, pp. 668–677, 2005.

[20] G. Pfurtscheller, R. Leeb, C. Keinrath, et al., "Walking from thought," *Brain Research*, vol. 1071, no. 1, pp. 145–152, 2006.

[21] H. Alkadhi, P. Brugger, S. H. Boendermaker, et al., "What disconnection tells about motor imagery: evidence from paraplegic patients," *Cerebral Cortex*, vol. 15, no. 2, pp. 131–140, 2005.

[22] P. Sabbah, S. de Schonen, C. Leveque, et al., "Sensorimotor cortical activity in patients with complete spinal cord injury: a functional magnetic resonance imaging study," *Journal of Neurotrauma*, vol. 19, no. 1, pp. 53–60, 2002.

[23] G. Pfurtscheller, C. Brunner, A. Schlögl, and F. H. Lopes da Silva, "Mu rhythm (de)synchronization and EEG single-trial classification of different motor imagery tasks," *NeuroImage*, vol. 31, no. 1, pp. 153–159, 2006.

Hindawi Publishing Corporation
Computational Intelligence and Neuroscience
Volume 2009, Article ID 537504, 8 pages
doi:10.1155/2009/537504

Research Article

Dimensionality Reduction and Channel Selection of Motor Imagery Electroencephalographic Data

Muhammad Naeem, Clemens Brunner, and Gert Pfurtscheller

BCI Lab, Institute for Knowledge Discovery, Graz University of Technology, 8010 Graz, Austria

Correspondence should be addressed to Clemens Brunner, clemens.brunner@tugraz.at

Received 27 October 2008; Revised 19 January 2009; Accepted 24 March 2009

Recommended by Fabio Babiloni

The performance of spatial filters based on independent components analysis (ICA) was evaluated by employing principal component analysis (PCA) preprocessing for dimensional reduction. The PCA preprocessing was not found to be a suitable method that could retain motor imagery information in a smaller set of components. In contrast, 6 ICA components selected on the basis of visual inspection performed comparably (61.9%) to the full range of 22 components (63.9%). An automated selection of ICA components based on a variance criterion was also carried out. Only 8 components chosen this way performed better (63.1%) than visually selected components. A similar analysis on the reduced set of electrodes over mid-central and centro-parietal regions of the brain revealed that common spatial patterns (CSPs) and Infomax were able to detect motor imagery activity with a satisfactory accuracy.

1. Introduction

The aim of brain-computer interfaces (BCIs) [1–5] is to create control signals by utilizing brain patterns generated by thoughts without the aid of peripheral nerves and muscles. There is a variety of invasive and noninvasive methods available to record signals from the brain. Among the noninvasive methods, the electroencephalogram (EEG) [6] is probably the most practical method available for BCI systems due to its fine temporal resolution and inexpensive recording equipment. However, due to volume conduction through the scalp, skull, and other layers of the brain, the spatial resolution of EEG signals needs to be improved. Moreover, EEG signals are usually recorded in a high-dimensional space, and it is a well-known fact that classification rules are difficult to learn and time consuming in a high-dimensional space.

To address these issues, several techniques of spatial filtering are used such as Laplacian derivations, common spatial patterns (CSPs) [7, 8], and various independent component analysis (ICA) algorithms, for example Infomax, FastICA, and SOBI [9–11]. An important attribute of a spatial filtering method is to reduce the number of dimensions and at the same time to retain all the information necessary for classification. In this regard, CSP has an internal mechanism of reducing the dimensionality of the data and was successfully used for the classification of EEG-based motor imagery data. On the other hand, ICA has an inherent indeterminacy to order and scaling, which means that the importance of the components cannot be determined on this basis. However, spatial filtering algorithms based on ICA can reduce the dimensionality of the data by visual selection of the components [12] on the basis of time-frequency maps [13] and scalp maps [14] or by applying principal component analysis (PCA) [15] as a preprocessing step before ICA.

The response of a command-related activity, depending upon the neurophysiological signal used in a BCI application, can be mapped to distinct areas of the brain. For example, ERD/ERS (event-related desynchronization/event-related synchronization) is dominant over the motor cortex, and visually evoked potentials (VEPs) are dominant over the occipital lobe. Since the approximate location of the activity associated with the control attempt is known a priori, an optimization of recording sites can also be done in advance. A reduced number of channels results in a low-dimensional

feature vector which is advantageous in terms of better generalization and also reduces processing requirements. Clearly, channel selection is a dimensionality reduction technique motivated by physiological considerations and can be considered, like component selection methods, similar to feature selection. The advantage of utilizing these techniques lies in the fact that they propose to go a step further and also remove redundancy and noise in the reduced set of dimensions.

The goal of this study is to find the optimum number of dimensions of 22-channel EEG data which represents all the information without redundancy for the classification of four class motor imagery tasks. For this purpose, first, the dimensions were reduced by employing PCA preprocessing before ICA and then the classification accuracies were calculated. Similarly, classification accuracies were also calculated on 6 visually selected ICA components. Further, an automated selection of ICA components (Infomax) based on a variance criterion was also carried out. In addition, a subset of electrodes was manually selected, and the classification results were obtained by employing ICA as well as CSP and these results were compared with Laplacian derivations [16]. The data analysis was performed without removing any artifacts.

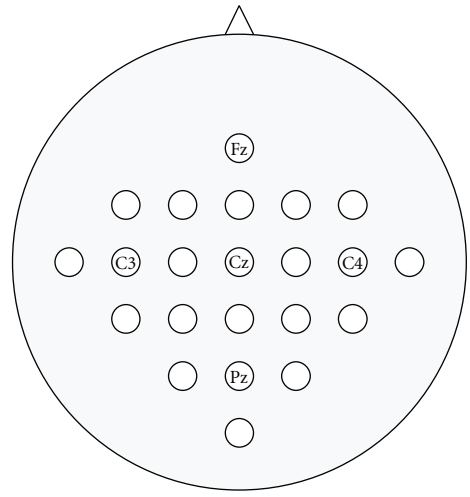

Figure 1: EEG electrode setup, some labels corresponding to positions in the international 10-20 system are marked. Electrodes are numbered from 1 to 22 in ascending order from top to bottom and left to right. The three subsets of electrodes used for channel selection are (1) 2–21, (2) 2–18, and (3) 2, 4, 6–14, 16, 18.

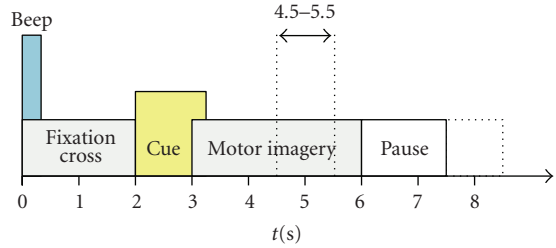

Figure 2: Timing of a trial of the training paradigm. The time slice between seconds 4.5 and 5.5 was used to train the classifiers. In the case of CSP the same time slice was also employed to calculate the spatial filters. However, for calculating ICA spatial filters the entire time period (0–7.5 seconds) was used.

2. Methods

2.1. Experimental Data. The EEG data of 4-class motor imagery was recorded with 22 electrodes placed according to the scheme in Figure 1. Monopolar derivations were used throughout all recordings (the left mastoid served as reference and the right mastoid as ground). The signals were sampled with 250 Hz and prefiltered in the range of 0.5 and 100 Hz. Furthermore, a 50 Hz notch filter was enabled to suppress line noise. The data sets were recorded from eight healthy subjects, all inexperienced in BCI training. They were sitting in a comfortable armchair in front of a computer monitor. Two sessions of each subject were recorded on different days. There were 288 trials (72 per motor imagery class) in each session distributed in a randomized order.

The experimental paradigm consisted of the imagination of left hand, right hand, foot, and tongue movement. A short beep (at $t = 0$ s) along with the display of a fixation cross in the middle of the screen indicated the beginning of the trial. A visual cue (at $t = 2$ s) in the form of an arrow pointing either left, right, up, or down appeared for 1.25 seconds on the screen. Each position of the arrow required the subject to perform the corresponding imaginary movement task. The disappearance of the fixation cross (at $t = 6$ s) indicated the subject to relax. Finally, 1.5–2.5 seconds of resting period with a blank screen followed before the next trial started. The experimental paradigm is illustrated in Figure 2.

2.2. Dimensionality Reduction and Channel Selection

2.2.1. PCA-Based ICA Components. PCA works on the premise of uncorrelatedness and sorts the components in decreasing order of variances. That is, it accumulates as much activity as possible in the first (and then in the second, third, etc.) component, constrained by the quite unreasonable assumption that the scalp maps are orthogonal. One can immediately see two consequences of this procedure: first, the constraint of orthogonality ensures the minimization of redundancy among the components. Second, a large variance is often translated as important in the field of signal processing. Therefore, the first few components are expected to contain most of the interesting dynamics, and removing the remaining components simply implies enhancing the signal-to-noise ratio. This is in contrast to ICA, which is blind to order and scaling and hence the importance of components cannot be determined automatically.

To overcome this shortcoming, PCA is often used as a preprocessing step before ICA decomposition [17, 18]. This procedure seeks to extract independent components (ICs) from the first few principal components (PCs), implicitly assuming that the relevant brain dynamics are contained in those few components. This assumption, however, has never been verified quantitatively, at least in the cases of

neuroimaging data sets. By discarding many small principal components, the risk of removing potentially interesting information cannot be neglected.

The low-variance components may not necessarily be unimportant ones, therefore choosing a certain number of PCA components for subsequent ICA decomposition is always an open question. To address this issue, the dimensions of the data sets were reduced in steps of one by applying PCA preprocessing. More specifically, each 22-channel EEG data set was first decomposed into 21, 20, ..., and 6 PCA components data sets (yielding 16 data sets), respectively, before ICA decomposition. The ICA algorithms chosen for this study were Infomax, FastICA, and SOBI [9–11]. Infomax seeks to find maximally independent components, whereas FastICA maximizes the nongaussianity between the output components. SOBI (second-order blind identification), on the other hand, achieves source resolution by a simultaneous diagonalization of covariance matrices. In the case of FastICA, a tangent hyperbolic was used instead of the default nonlinearity of a third-order polynomial. Moreover, the deflationary approach was employed instead of a symmetric decomposition. In contrast, all the default parameters were used in Infomax. Similarly, SOBI was implemented by utilizing a default value of 50 time delays [12].

2.2.2. Visual Selection of ICA Components. The discrimination between important (task-related) and unnecessary (noisy) components in this analysis was ascertained by inspecting time-frequency maps [13] and topographic maps [14] (see Figures 3 and 4). For example, important hand imagery components were the ones focused on contralateral regions over the motor cortex area containing mu or beta ERD. The ipsilateral components containing ERS activity were also important. In the case of foot or tongue imagery, midcentral or parietal components containing localized activity were considered. The components chosen to depict tongue imagery contained dominant ERS activity, whereas for foot imagery both ERD and ERS patterns were more significant [19]. In contrast, the components that showed scattered activity over the whole surface on a topographic map (which is merely a projection of the components $[\mathbf{w}_1, \ldots, \mathbf{w}_n]$ on a two-dimensional head surface) were not chosen [12].

Summarizing, a priori knowledge of the physiological processes underlying motor imagery helped in selecting the most important components. The idea was to choose a minimum number of components to depict the suitability of ICA itself for dimensional reduction. In the selection process, care was taken to include at least one component representing each task. However, in many subjects more than one significant component corresponding to a specific task were present. This was mostly true for contralateral components and rarely for central components. Therefore, two additional components were selected, somewhat heuristically but also based on analysis [13, 14]. It should be mentioned that this selection of six components may not be so adequate for all the subjects, as each can have an individual "best-number-of-components" that represent the sources of interest. However, a fixed number of components was needed to assess the relative performances of the three ICA algorithms. Finally, the preliminary results on the average (across the subjects) were comparable with those of the full range of 22 components.

2.2.3. An Automated Selection of ICA Components. As mentioned in the introduction ICA is ambiguous to scaling as well as order. Therefore, unlike PCA importance of components cannot be determined on the basis of variance of the components. However, a mechanism of pseudo-order is available in Infomax: the components are arranged according to their mean projected variance. This implies that the first component contributes most to the power of EEG signal, the second contributes the second most, and so forth. As a consequence of this order frontal and temporal components usually find their way in the top order. Additionally, nonspecific and nonlocalized components sometimes can also be found in the upper order. This makes automatic selection of motor imagination components difficult if not impossible.

A way to tackle this issue is to employ prior information in automatic selection of components. It is a well known fact that oscillatory patterns (ERD/ERS) are pronounced in 8–14 Hz (alpha rhythm) and 14–30 Hz (beta rhythm). Due to this reason, features of data sets belonging to motor imagination experiments are usually (as is the case in this paper) extracted in 8–30 Hz. Utilizing this prior information, components were first filtered in the range of 8–30 Hz and then their variances estimated. Sorting the components in the descending order would therefore depict the potential importance of the components. This way, first six, eight, and then ten components were selected. This analysis is performed only with Infomax.

2.2.4. Channel Selection. Similarly, prior information about task-related activity was used in the manual selection of a subset of the total number of 22 electrodes. For this analysis, 3 subsets of 22 electrodes were chosen (see Figure 1). The first subset consisted of electrode numbers 2 to 21, that is, the entire scalp except frontal and occipital regions. The second subset included electrode numbers 2 to 18, comprising midcentral and centro-parietal regions. Similarly, the third subset contained electrodes C3, C4, Cz, and electrodes surrounding them (in total 13 electrodes). With each of these three subsets of electrodes, spatial filters were calculated by employing three ICA methods as well as CSP.

2.3. Feature Extraction and Classification. The next paragraph describes the cross-validation, feature extraction, and classification procedures for the ICA components with or without dimensionality reduction and channel selection. In each instance of a reduced number of ICA components or a subset of channels selected, the number of band power features were also different. Other than that, identical procedures were employed for 6 visually selected ICA components, automatic selection of ICA components (6, 8, and 10) and also 6 Laplacian components. The same holds

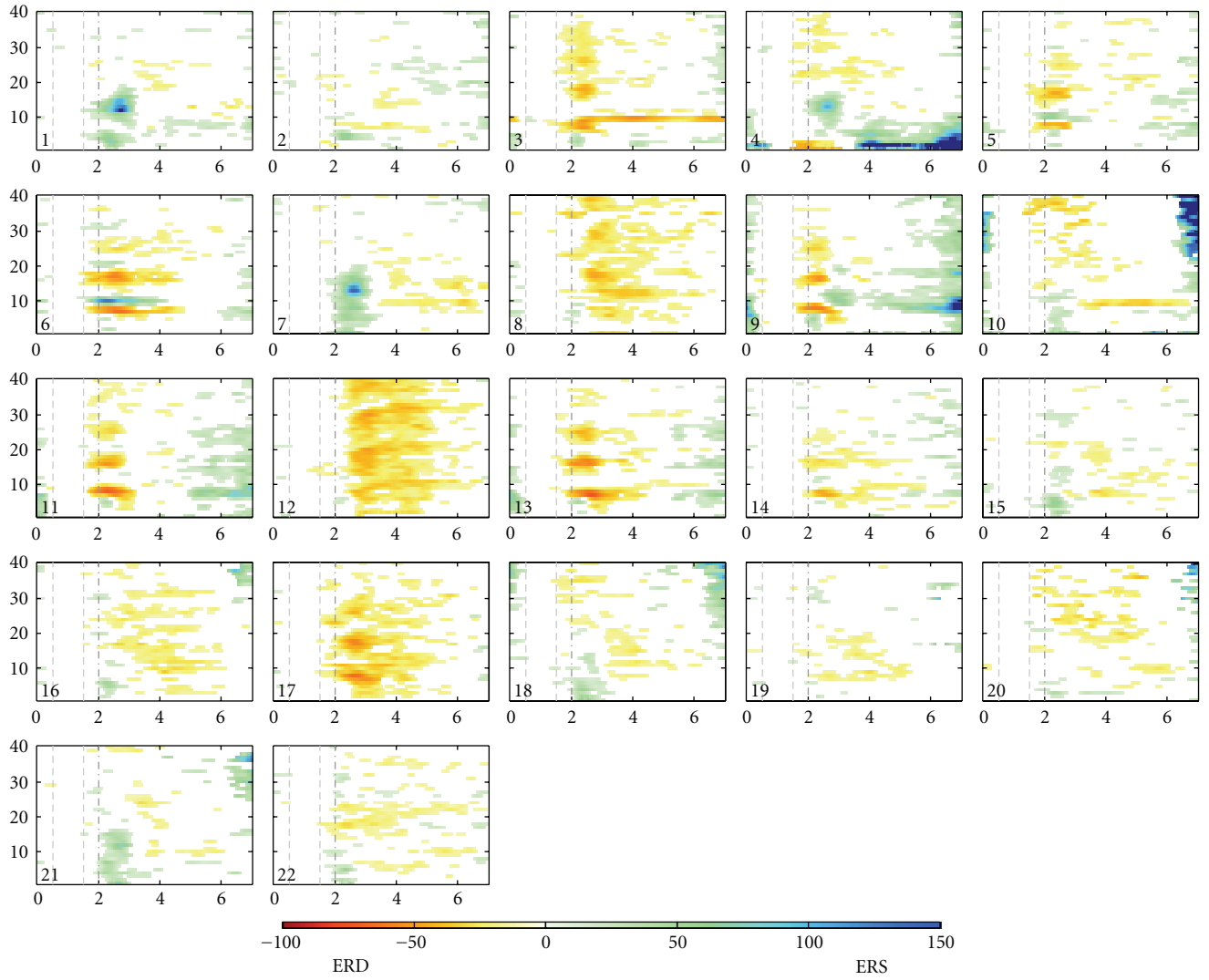

Figure 3: Time-frequency maps (Infomax-subject s5 session 1): components are numbered in order of mean projected variance. The six visually selected components are 5, 8, 12, 14, 16, and 18.

for the ICA components based on manual selection of the subset of electrodes and also for components extracted after dimensionality reduction with PCA.

First, the ICA unmixing matrix was multiplied to the raw signals to extract independent components. In the next step, logarithmic band power features in the range of 8–30 Hz were calculated. For example, 22 features were computed when utilizing all the 22 ICA components. Next, a 10×10-fold cross-validation procedure [20] was performed. In other words, 100 different combinations of trials were created. For each of this combination, 90% of the trials were used for training four linear statistical classifiers (Fisher's linear discriminant analysis, LDA) combined in a one-versus-the-rest classification scheme [20]. Within each trial, samples between seconds 4.5–5.5 were used to train the classifiers. These classifiers were then applied to the remaining 10% of the data, and the classification accuracy was calculated by choosing the class corresponding to the maximum value of the four LDAs. The whole process mentioned above was repeated for all the 100 combinations, and the classification accuracy was calculated. The overall performance of the system was evaluated by taking an average of the classification accuracy of each combination.

Similarly, classification results of the CSP-preprocessed data (manual selection of subsets of electrodes as well as the complete set) are also presented. First, signals were bandpass filtered in the range of 8–30 Hz and then a 10×10-fold cross-validation procedure [20] was performed by creating 100 different combinations of trials. Each of this combination was divided into 90% and 10% portions. The (four) spatial filters were calculated on the basis of the 90% portion and were then multiplied to this data. In the next step, 6 components (the first and last three) were chosen and log-transformed normalized variances were calculated for each

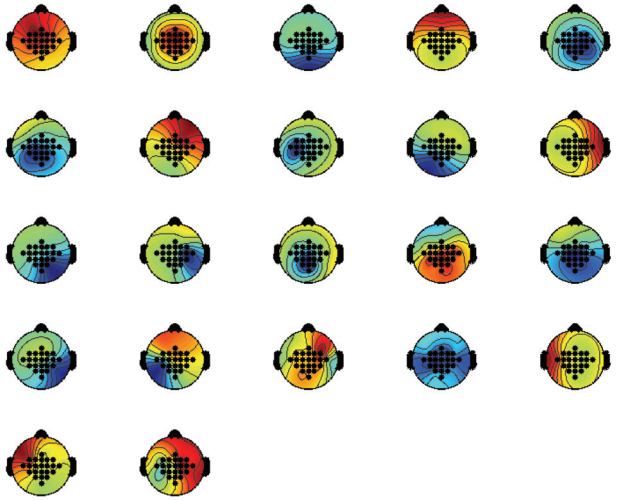

Figure 4: Topographic maps (Infomax-subject s5 session 1): components are numbered in order of mean projected variance. The six components (from left to right, top to bottom) selected are 5, 8, 12, 14, 16, and 18.

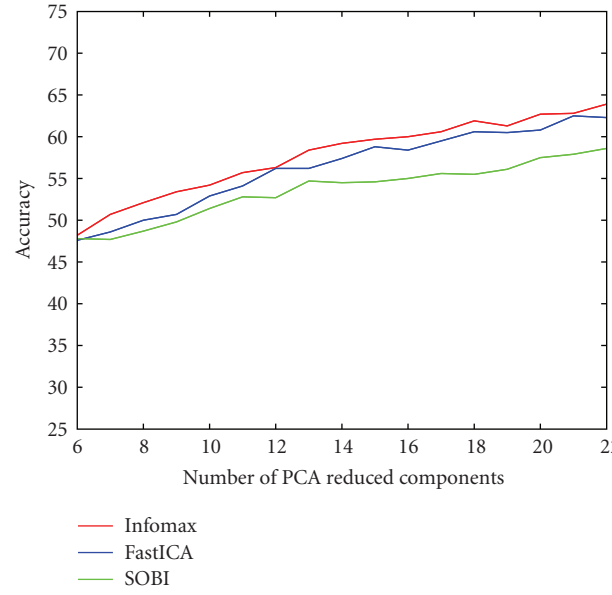

Figure 5: Comparison of three ICA algorithms with reduced dimensionality by PCA preprocessing in the step of one, that is, from a total of 22 components to 6 PCA reduced ICA components.

of the components. Next, these features were forwarded to four linear statistical classifiers (again using a one-versus-the-rest scheme). It should be noted that each classifier received the same 24 features. The classifier weights were calculated and these classifiers plus the four spatial filters were then applied to the remaining 10% of the data and the classification accuracy was calculated by choosing the class corresponding to the maximum value of the four LDAs. The whole process mentioned above was repeated for all the 100 combinations and the classification accuracy was calculated. Finally, the mean of these accuracy values was estimated. The same time slice (between seconds 4.5–5.5) was used to train the classifiers as in the case of ICA. In the case of CSP, this interval was also used to calculate the spatial filters.

3. Results

The mean accuracy values showed an almost linear increase with an increasing number of PCA-preprocessed components. This is true, in general, for all the ICA algorithms, as depicted in Figure 5. The maximum values obtained for Infomax and SOBI were 63.9% and 58.6%, respectively. In both cases, spatial filters were calculated without PCA decomposition. However, in the case of FastICA, the maximum value of 62.5% was achieved with 21 PCA-preprocessed components, which was only marginally better than the one obtained without PCA decomposition. Moreover, Infomax showed better results for each and every choice of PCA-preprocessed components in comparison to the corresponding choice with respect to FastICA and SOBI. The same is true for FastICA in comparison to SOBI. In fact, the performance of SOBI was generally poor and did not improve as markedly as Infomax and FastICA with an increasing number of PCA-preprocessed components (see Figure 5).

One immediate conclusion that can be drawn in the analysis with manual selection of electrodes is that the spatial

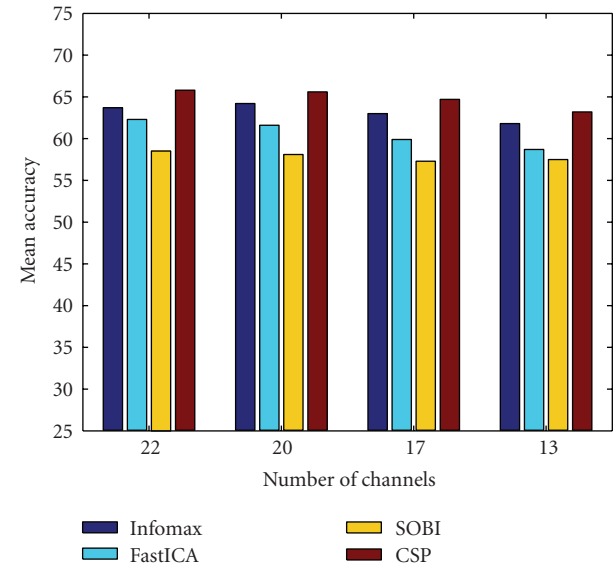

Figure 6: Comparison of three ICA algorithms (reduced number of electrodes) with CSP.

filters built from 20 channels (2–21) performed more or less similarly with the ones built from 22 channels (see Figure 6). More specifically, Infomax performed marginally better (64.2%) with 20 channels reduced data sets, whereas the other methods (FastICA, SOBI, and CSP) performed marginally worse with the same number of channels. Similarly, results with 17 channel data sets showed only a slight decrease in performance in comparison with either 22 channel or 20 channel data sets. In fact, the only exception

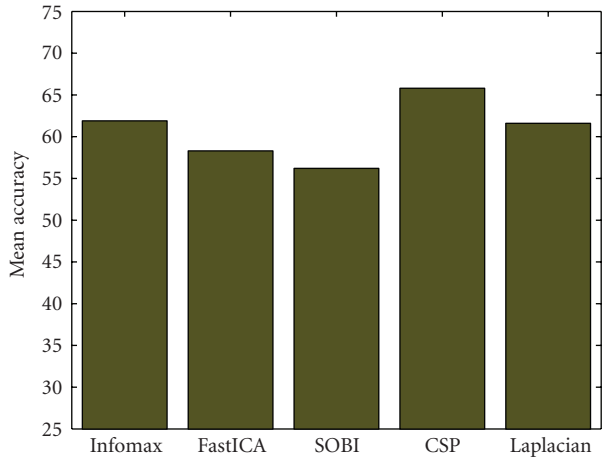

Figure 7: Comparison of three ICA algorithms (6 components selected by visual inspection) with Laplacian (6 components) and CSP.

Table 1: Infomax: mean accuracy values of automatically selected components, visually selected components, and the full range of components.

Components	6 (auto)	8 (auto)	10 (auto)	6 (visual)	22 (full)
Mean accuracy	61.4	63.1	63.8	61.9	63.9

was FastICA, where the performance was noticeably down by about (2.5%). However, in general, the 13 channel subset showed a pronounced deterioration for all the methods. For this analysis, CSP performed better than the rest but Infomax was only slightly worse, in comparison with CSP, for each subset of total number of electrodes considered.

For the visual selection of components with the ICA methods, Infomax (with 61.9%) performed much better than FastICA (58.3%) and SOBI (56.2%) (see Figure 7). However, CSP performed better than all methods and surprisingly, Laplacian derivations (with 6 components) performed almost as good as Infomax. In addition, the performance of Infomax with visual selection of components was better than the corresponding performance with 19 PCA-preprocessed components and only slightly worse than 21 components. Similarly, the performance of Infomax with the reduced set of 17 electrodes was only slightly better than the visually selected components by the same method. On the other hand, the result with visual selection of components of FastICA (58.3%) was comparable with 16 PCA-preprocessed components and also with the reduced set of 13 electrodes. In the case of SOBI, 19 PCA-preprocessed components performed comparably with 6 visually selected components by the same algorithm. However, the performance was comparatively lower than the reduced set of 13 electrodes.

The components in Figures 3 and 4 are arranged in the following order by the automatic selection procedure: 8, 12, 11, 17, 3, 13, 5, 10, 6, 16, 9, 22, 20, 18, 21, 1, 14, 7, 2, 19, 15, 4. That is, two contra-lateral components can be found among the first in this list. The frontal component (4) can be seen in the last position, whereas the temporal component (10) is at place 8. In fact, one of the temporal components was usually found to be present in the first 8 to 10 components. In few instances, components with scattered topography were also found among the first few. However, these components usually represented task-related activity. This is amply demonstrated in Table 1. The mean accuracy for 6 automatically selected components is comparable with the one for 6 visually selected components. The performance of 8 automatically selected components is even better and that of 10 components is almost equivalent to the full range of 22 components.

4. Conclusions

As the spatial filters built with ICA methods and CSP on the reduced set of 20 electrodes performed more or less comparably with the ones built with the total number of 22 electrodes, it can be concluded that frontal and occipital regions of the brain do not capture significant motor imagery patterns. Therefore, data recorded from these areas of the brain can safely be excluded before building spatial filters. Similarly, results with the reduced set of 17 electrodes showed that especially CSP and also Infomax were able to focus motor imagery activity in mid-central and centro-parietal regions. The exception of FastICA in this regard could be due to the algorithmic choice of the deflationary approach instead of a symmetric decomposition employed for source resolution.

The results presented for PCA-preprocessed ICA algorithms lead to the conclusion that at least 20 PCA components out of the 22 electrodes are necessary for preserving relevant information. For the 22 channels data sets considered in this analysis, PCA preprocessing was not found to be a suitable preprocessing method that could retain motor imagery information in a smaller set of components. It should also be mentioned that dimensional reduction even up to 6 PCA components still preserves about 98%–99% of the total variance in general. This fact simply implies that reducing the dimension by throwing away low-variance components more often than not results in a loss of important and relevant information.

The selection of ICA components on the basis of visual inspection of time-frequency maps and scalp maps has a subjective bias. Even this heuristic measure presented in this work outperforms the PCA-based method of dimensional reduction. Infomax in particular performed much better than the other ICA variants considered. The overall result of Infomax with 6 visually selected components was only 2.0% less than the corresponding result with all the components and about 14% higher than 6 PCA-preprocessed Infomax components. This implies that Infomax was able to incorporate most of the task-related activity in few components.

However, visual selection of components is a manual and subjective procedure. In order to automatically select

these few important components, a simple variance-based criterion was employed. This procedure proved to be a success as only 8 to 10 components were needed to capture relevant motor imagination activity. Based on the relative performances, especially with reference to the PCA-based method, this procedure can be recommended as a dimensional reduction technique for motor imagery data sets.

5. Discussion

The variance-based procedure is applicable to motor imagery data sets. Moreover, the number of required components can further be reduced if some of the unwanted components can be located a priori. Further, a very small set of correctly selected clean components has the potential of enhancing the performance of ICA algorithms. Therefore, an improved general purpose automated method needs to be developed for the determination of important components. This objective can be achieved for example by employing some of the new ideas such as constrained ICA. Various ways to incorporate prior information in ICA algorithms have already been suggested [21, 22]. For example, reference signals of different classes can be employed as constraints in ICA algorithms. Similarly, probability distribution functions of reference signals can be incorporated directly as models in ICA algorithms. Independent components can thus be extracted under the constraint of being similar to the reference signals or their probability distribution functions. Moreover, this method is oblivious to the square mixing assumption of standard ICA [21]. Therefore, in addition to enhancing the signal-to-noise ratio of neuroimaging data, constrained ICA can also deal effectively with the issue of dimensional reduction.

The standard PCA method cannot be recommended, at least for the data sets considered in this study. This leads to the interesting question whether there are other PCA-based strategies for the selection of the components to retain the most important information. A recent paper [18] proposed an alternative signal representation that is based on PCA for dimensionality reduction and ICA conducted across all subjects and conditions simultaneously. The results based on partial least squares (PLSs) analysis showed an enhancement of the task-related activity under compression. Another approach worth implementing is nonlinear PCA [23, 24]. Nonlinear PCA can be considered as a type of ICA under special conditions [23]. The nonlinearity is introduced in the objective function, but the output variables are still a linear combination of the input variables. It can therefore be seen as an ICA with an additional advantage of PCA.

A novel method in a very recent paper [25] utilized ICA for source localization. The method then found the optimal positions of two bipolar electrodes with the purpose of reducing the number of electrodes to four. The goal was to optimize the number of electrodes for practical BCI systems. The results showed promise for two-class motor imagery data. The extension to the four-class problem, such as the data analyzed in this paper, is also possible and could be carried out in future analyses.

Acknowledgments

This work was funded by the Higher Education Commission (HEC) Pakistan, the European projects Presenccia (IST-2006-27731) and Eye-To-IT (IST-2006-517590), and the Styrian government project GZ A3-16 B 74-05/1.

References

[1] M. A. L. Nicolelis, "Actions from thoughts," *Nature*, vol. 409, no. 6818, pp. 403–407, 2001.

[2] J. R. Wolpaw, N. Birbaumer, D. J. McFarland, G. Pfurtscheller, and T. M. Vaughan, "Brain-computer interfaces for communication and control," *Clinical Neurophysiology*, vol. 113, no. 6, pp. 767–791, 2002.

[3] N. Birbaumer, "Brain-computer-interface research: coming of age," *Clinical Neurophysiology*, vol. 117, no. 3, pp. 479–483, 2006.

[4] M. A. Lebedev and M. A. L. Nicolelis, "Brain-machine interfaces: past, present and future," *Trends in Neurosciences*, vol. 29, no. 9, pp. 536–546, 2006.

[5] G. Pfurtscheller, G. R. Müller-Putz, A. Schlögl, et al., "15 years of BCI research at Graz University of Technology: current projects," *IEEE Transactions on Neural Systems and Rehabilitation Engineering*, vol. 14, no. 2, pp. 205–210, 2006.

[6] H. Berger, "Über das Elektrenkephalogramm des Menschen," *Archiv für Psychiatrie und Nervenkrankheiten*, vol. 87, no. 1, pp. 527–570, 1929.

[7] H. Ramoser, J. Müller-Gerking, and G. Pfurtscheller, "Optimal spatial filtering of single trial EEG during imagined hand movement," *IEEE Transactions on Rehabilitation Engineering*, vol. 8, no. 4, pp. 441–446, 2000.

[8] S. Lemm, B. Blankertz, G. Curio, and K.-R. Müller, "Spatio-spectral filters for improving the classification of single trial EEG," *IEEE Transactions on Biomedical Engineering*, vol. 52, no. 9, pp. 1541–1548, 2005.

[9] A. J. Bell and T. J. Sejnowski, "An information-maximization approach to blind separation and blind deconvolution," *Neural Computation*, vol. 7, no. 6, pp. 1129–1159, 1995.

[10] A. Hyvärinen, "A family of fixed-point algorithms for independent component analysis," in *Proceedings of the IEEE International Conference on Acoustics, Speech, and Signal Processing (ICASSP '97)*, vol. 5, pp. 3917–3920, Munich, Germany, April 1997.

[11] A. Belouchrani, K. Abed-Meraim, J.-F. Cardoso, and E. Moulines, "A blind source separation technique using second-order statistics," *IEEE Transactions on Signal Processing*, vol. 45, no. 2, pp. 434–444, 1997.

[12] M. Naeem, C. Brunner, R. Leeb, B. Graimann, and G. Pfurtscheller, "Seperability of four-class motor imagery data using independent components analysis," *Journal of Neural Engineering*, vol. 3, no. 3, pp. 208–216, 2006.

[13] B. Graimann, J. E. Huggins, S. P. Levine, and G. Pfurtscheller, "Visualization of significant ERD/ERS patterns in multichannel EEG and ECoG data," *Clinical Neurophysiology*, vol. 113, no. 1, pp. 43–47, 2002.

[14] A. Delorme and S. Makeig, "EEGLAB: an open source toolbox for analysis of single-trial EEG dynamics including independent component analysis," *Journal of Neuroscience Methods*, vol. 134, no. 1, pp. 9–21, 2004.

[15] I. T. Jolliffe, *Principal Component Analysis*, Springer, New York, NY, USA, 1986.

[16] B. Hjorth, "An on line transformation of EEG scalp potentials into orthogonal source derivations," *Electroencephalography and Clinical Neurophysiology*, vol. 39, no. 5, pp. 526–530, 1975.

[17] S. Vaseghi and H. Jetelová, "Principal and independent component analysis in image processing," in *Proceedings of the 14th ACM International Conference on Mobile Computing and Networking (MOBICOM '06)*, pp. 1–5, San Francisco, Calif, USA, September 2006.

[18] N. Kovacevic and A. R. McIntosh, "Groupwise independent component decomposition of EEG data and partial least square analysis," *NeuroImage*, vol. 35, no. 3, pp. 1103–1112, 2007.

[19] G. Pfurtscheller, C. Brunner, A. Schlögl, and F. H. Lopes da Silva, "Mu rhythm (de)synchronization and EEG single-trial classification of different motor imagery tasks," *NeuroImage*, vol. 31, no. 1, pp. 153–159, 2006.

[20] R. O. Duda, P. E. Hart, and D. G. Stork, *Pattern Classification*, John Wiley & Sons, New York, NY, USA, 2001.

[21] C. J. James and O. J. Gibson, "Temporally constrained ICA: an application to artifact rejection in electromagnetic brain signal analysis," *IEEE Transactions on Biomedical Engineering*, vol. 50, no. 9, pp. 1108–1116, 2003.

[22] W. Lu and J. C. Rajapakse, "Approach and applications of constrained ICA," *IEEE Transactions on Neural Networks*, vol. 16, no. 1, pp. 203–212, 2005.

[23] A. Hyvärinen, J. Karhunen, and E. Oja, *Independent Component Analysis*, John Wiley & Sons, New York, NY, USA, 2001.

[24] J. Karhunen, P. Pajunen, and E. Oja, "The nonlinear PCA criterion in blind source separation: relations with other approaches," *Neurocomputing*, vol. 22, no. 1–3, pp. 5–20, 1998.

[25] B. Lou, B. Hong, X. Gao, and S. Gao, "Bipolar electrode selection for a motor imagery based brain-computer interface," *Journal of Neural Engineering*, vol. 5, no. 3, pp. 342–349, 2008.

Hindawi Publishing Corporation
Computational Intelligence and Neuroscience
Volume 2009, Article ID 369341, 9 pages
doi:10.1155/2009/369341

Research Article

A Theoretical Investigation of the Relationship between Structural Equation Modeling and Partial Correlation in Functional MRI Effective Connectivity

Guillaume Marrelec[1,2] and Habib Benali[1,2]

[1] *Inserm, U678, Laboratoire d'Imagerie Fonctionnelle, F-75013 Paris, France*
[2] *UPMC Univ Paris 06, UMR-S 678, Laboratoire d'Imagerie Fonctionnelle, F-75013 Paris, France*

Correspondence should be addressed to Guillaume Marrelec, marrelec@imed.jussieu.fr

Received 31 October 2008; Accepted 15 May 2009

Recommended by Fabio Babiloni

An important field of blood oxygen level dependent (BOLD) functional magnetic resonance imaging (fMRI) is the investigation of effective connectivity, that is, the actions that a given set of regions exert on one another. We recently proposed a data-driven method based on the partial correlation matrix that could provide some insight regarding the pattern of functional interaction between brain regions as represented by structural equation modeling (SEM). So far, the efficiency of this approach was mostly based on empirical evidence. In this paper, we provide theoretical fundaments explaining why and in what measure structural equation modeling and partial correlations are related. This gives better insight regarding what parts of SEM can be retrieved by partial correlation analysis and what remains inaccessible. We illustrate the different results with real data.

1. Introduction

Blood oxygen level dependent (BOLD) functional magnetic resonance imaging (fMRI) is an imaging technique that allows to dynamically and noninvasively follow metabolic and hemodynamic consequences of brain activity [1, 2]. Since Biswal et al. [3], an increasing number of studies have suggested that fMRI data could be used to explore how brain regions interact to perform functional tasks. A key concept in investigation of functional brain interactions is effective connectivity, which has been defined as the influence that regions exert on one another [4].

Path analysis, or structural equation modeling (SEM), has been the major way to examine effective connectivity in fMRI [5–7]. Starting from a set of D regions, a model is set a priori that expresses the time course $z_i(t)$ of each region as a linear function of the time course of other regions

$$z_i(t) = \sum_{j \neq i} \lambda_{ij} z_j(t) + e_i(t), \tag{1}$$

with some coefficients λ_{ij} being constrained to 0, the others are free to vary. λ_{ij} quantifies the strength that region j exerts on region i. Setting an SEM is equivalent to defining a directed graph, where each node stands for a region, a given arrow $j \rightarrow i$ is present if and only if the corresponding coefficient λ_{ij} is not constrained to zero, and, finally, λ_{ij} represents the intensity of arrow $j \rightarrow i$. Once the structural model is completely set, the unconstrained coefficients λ_{ij} are estimated. To this aim, the model covariance matrix $\mathbf{\Sigma}$, which is a function of the parameters, is compared to the sample covariance matrix $\mathbf{S}$ using a discrepancy function that is minimized [8, 9]. In fMRI data analysis, the following maximum likelihood function is often used [7]:

$$l(\mathbf{\Sigma}) = \operatorname{tr}\left(\mathbf{S}\mathbf{\Sigma}^{-1}\right) - \ln\left|\mathbf{\Sigma}^{-1}\mathbf{S}\right| - D, \tag{2}$$

where $\operatorname{tr}(\cdot)$ stands for the standard matrix trace function. The major flaw of this approach is that it requires the prior definition of a structural model, that is, of regions and arrows, each arrow requiring itself information regarding connection and direction. By contrast, information regarding the functional interactions present within the network of interest is likely to be scarce, since it is often the very reason why an fMRI study of effective connectivity is carried

out. This is all the more problematic that the approach does not really provide any clear way to challenge the model or to provide information relative to where or how the model under investigation could be improved.

We recently proposed a novel approach to gain insight on effective connectivity. We first showed that, unlike marginal (i.e., regular) correlation, conditional correlation could account for many patterns of interaction as modeled by SEM [10, 11]. We then proposed to focus on a specific set of conditional correlations, namely partial correlations [12]. Given a set of D regions, denoted by $\mathbb{R}$, and a variable y_i associated to each region i (of which $z_i(t)$ mentioned in (1) is a realization), the method estimates the partial correlation of any region pair (i, j) given the set of $D-2$ remaining regions,

$$\mathrm{Corr}\left[y_i, y_j \mid \mathbf{y}_{\mathbb{R}\setminus\{i,j\}}\right]. \tag{3}$$

On both real [13] and synthetic data [14], it was observed that a large partial correlation value between two regions was often associated with the presence of an effective connectivity between these regions. However, the reason for such a behavior remained unclear. In the present paper, we further delve into the relationship between SEM and partial correlation in order to better understand why and in what measure partial correlation can extract information that is relevant for effective connectivity analysis. To this aim, we provide a theoretical relationship between SEM and partial correlation through the computation of the inverse covariance matrix (also-called concentration or precision matrix). To illustrate the results so obtained, we use a dataset on which SEM analysis has already been performed and published [7].

2. From SEM to Partial Correlation

2.1. Bullmore et al. [7] SEM Study. We here quickly recall the essentials of a previous study on which our investigation of partial correlation relies. For more detail, we refer the reader to Bullmore et al. [7]. The study focused on $D = 5$ left hemispheric cortical regions of interest: the ventral extrastriate cortex (VEC), the prefrontal cortex (PFC), the supplementary motor area (SMA), the inferior frontal gyrus (IFG), and the inferior parietal lobule (IPL). Each region was associated to a time course for a total of five time courses of length $T = 96$ time samples. The sample marginal and partial correlation matrices corresponding to these time courses are reported in Table 1. The time courses were a group average over the subjects, and the correlation matrix corresponds to the correlations of the averaged time series.

A plausible structural model, henceforth referred to as the "theoretically preferred model" (or "TP"), was proposed and is represented in Figure 1(a). Using the correlation matrix of Table 1, a procedure implemented in the LISREL proprietary software package (http://www.ssicentral.com/lisrel/) computed a so-called "best fit" model from the data, henceforth referred to as such (or "BF") and represented in Figure 1(b). While similar in some ways, the two models had different features:

Table 1: Sample marginal correlation coefficients of the real data set examined in Bullmore et al. [7].

		(1) VEC	(2) PFC	(3) SMA	(4) IFG	(5) IPL
(1)	VEC	1				
(2)	PFC	0.661	1			
(3)	SMA	0.525	0.660	1		
(4)	IFG	0.486	0.507	0.437	1	
(5)	IPL	0.731	0.630	0.558	0.517	1

(i) VEC → IPL and SMA → IFG were present in the theoretically preferred model but were not selected in the best fit model;

(ii) PFC → IFG and SMA → IPL were absent in the theoretically preferred model but appeared in the best fit model.

We now go back to a different perspective. Indeed, the structure of any SEM entails specific constraints on the covariance matrix, as well as other matrices characteristic of the process, such as the concentration matrix and the marginal and partial correlation matrices.

2.2. SEM Modeling. Generally speaking, a structural model can be defined in matrix form as

$$\mathbf{y} = \mathbf{K}\mathbf{y} + \mathbf{e}, \tag{4}$$

where $\mathbf{y}$ is the D-dimensional variable characterizing the state of each region and $\mathbf{e}$ is a temporally independent and identically distributed (i.i.d.) Gaussian noise with diagonal covariance matrix. $\mathbf{K} = (K_{ij})_{i,j=1,\ldots,D}$ contains the path coefficients. The N time samples $(\mathbf{z}(t_n))_{n=1,\ldots,N}$, where $\mathbf{z}(t_n)$ is the signal measured in each of the D regions at time t_n, are supposed to be N i.i.d. realizations of $\mathbf{y}$. The matrices corresponding to the theoretically preferred and the best fit models are, respectively, given by (see also Figure 1)

$$\mathbf{K}_{\mathrm{TP}} = \begin{pmatrix} 0 & 0 & 0 & 0 & 0 & \lambda_{15} \\ \lambda_{21} & 0 & 0 & 0 & 0 & 0 \\ 0 & \lambda_{32} & 0 & 0 & 0 & 0 \\ 0 & 0 & \lambda_{43} & 0 & 0 & 0 \\ \lambda_{51} & 0 & 0 & \lambda_{54} & 0 & 0 \end{pmatrix},$$
$$\mathbf{K}_{\mathrm{BF}} = \begin{pmatrix} 0 & 0 & 0 & 0 & 0 & \mu_{15} \\ \mu_{21} & 0 & 0 & 0 & 0 & 0 \\ 0 & \mu_{32} & 0 & 0 & 0 & 0 \\ 0 & \mu_{42} & 0 & 0 & 0 & 0 \\ 0 & 0 & \mu_{53} & \mu_{54} & 0 & 0 \end{pmatrix}. \tag{5}$$

2.3. SEM and Covariance. Classically, we further assume that the noise $\mathbf{e}$ of (4) is composed of spatially and temporally

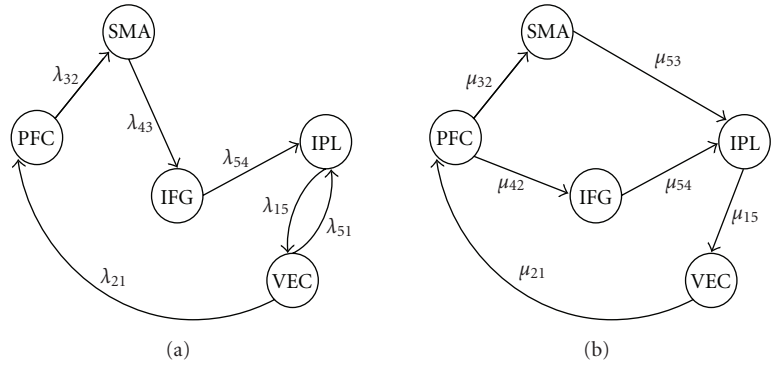

Figure 1: Structural models and path coefficients corresponding to the theoretically preferred (a) and best fit (b) models (from [7]).

independent Gaussian variables with diagonal covariance matrix:

$$\mathrm{Var}[\mathbf{e}] = \mathbf{V} = \begin{pmatrix} V_1 & & 0 \\ & \ddots & \\ 0 & & V_D \end{pmatrix}. \tag{6}$$

Since (4) rereads $\mathbf{y} = (\mathbf{I} - \mathbf{K})^{-1}\mathbf{e}$, where $\mathbf{I}$ stands for the D-dimensional unit matrix, it is straightforward to show that $\mathbf{y}$ is also Gaussian distributed with covariance matrix [15]

$$\mathbf{\Sigma} = (\mathbf{I} - \mathbf{K})^{-1}\mathbf{V}\left[(\mathbf{I} - \mathbf{K})^{-1}\right]^{\mathrm{t}}, \tag{7}$$

where "t" stands for matrix transposition. Since $\mathbf{K}$ is a function of the path coefficients, so is $\mathbf{\Sigma}$. This relationship is central to SEM analysis, for most methods rely on comparing the covariance matrix $\mathbf{\Sigma}$ implied by a structural model to the data sample covariance matrix using normal theory maximum likelihood—leading to the discrepancy function of (2)—, generalized least squares, or ordinary least squares [8, 9]. Note that, in (2), $\mathbf{\Sigma}$ only appears through its inverse $\mathbf{\Upsilon} = \mathbf{\Sigma}^{-1}$. $\mathbf{\Upsilon}$ is called the concentration, or precision, matrix and it is on this matrix that we will focus to get a better understanding of the data structure.

2.4. SEM and Concentration. Indeed, $\mathbf{\Upsilon}$ has intriguing structural properties when related to a structural model. Using (7), this matrix is given by

$$\mathbf{\Upsilon} = (\mathbf{I} - \mathbf{K})^{\mathrm{t}}\mathbf{V}^{-1}(\mathbf{I} - \mathbf{K}). \tag{8}$$

$\mathbf{V}$ being a diagonal matrix, the expression for each element Υ_{ij} of the concentration matrix can easily be expanded as

$$\Upsilon_{ij} = \sum_l \frac{(\delta_{li} - K_{li})\left(\delta_{lj} - K_{lj}\right)}{V_l}. \tag{9}$$

Given that $K_{ii} = 0$, the previous equation yields

$$\Upsilon_{ii} = \frac{1}{V_i} + \sum_{l \neq i} \frac{K_{li}^2}{V_l}, \tag{10}$$

and, for $i \neq j$,

$$\Upsilon_{ij} = -\frac{K_{ij}}{V_i} - \frac{K_{ji}}{V_j} + \sum_{l \notin \{i,j\}} \frac{K_{li}K_{lj}}{V_l}. \tag{11}$$

Equation (11) can be used to compute the concentration coefficients corresponding to the TP and BF structural models. For instance, we have for the TP model

$$\begin{aligned} \Upsilon_{12} &= -\frac{\lambda_{21}}{V_2}, \\ \Upsilon_{13} &= 0, \\ \Upsilon_{14} &= \frac{\lambda_{51}\lambda_{54}}{V_5}. \end{aligned} \tag{12}$$

From this example, we see that two cases can arise. In the first case (e.g., Υ_{13}), the value of the concentration coefficient is equal to zero, not because of the specific numerical values that have been assigned to the path coefficients, but because of the structure of the SEM itself. In the second case (e.g., Υ_{12} or Υ_{14}), the concentration coefficient is equal to zero only if the path coefficients are set to certain values (e.g, $\lambda_{21} = 0$ for Υ_{12}; $\lambda_{51} = 0$ or $\lambda_{54} = 0$ for Υ_{15}). For our purpose, the exact values taken by the nonzero Υ_{ij} are of minor importance; we rather focus on the elements that, such as Υ_{13}, are structurally equal to zero, that is, that are equal to zero independently of the values taken by the path coefficients. More generally, it can be shown using (11) that Υ_{ij} is identically equal to zero regardless of the numerical values of the path coefficients if and only if the three terms of the right-hand side of (11) are equal to zero, that is,

- (C_1) $K_{ij} = 0$ and $K_{ji} = 0$: neither region i nor region j has an effect on each other;
- (C_2) $K_{li}K_{lj} = 0$: regions i and j do not jointly influence region l, for all $l \neq i, j$.

In other words, $\Upsilon_{ij} = 0$ if and only if there are no such structures as $i \rightarrow j$, $i \leftarrow j$, or $i \rightarrow l \leftarrow j$ for any l in the structural graph: according to (C_1), there is no structural connection between i and j and, according to (C_2), regions i and j do not jointly influence a third region l. When a pair of

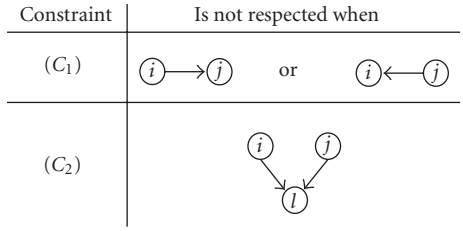

Figure 2: Structures that render either constraint (C_1) or (C_2) invalid for the pair i-j, thereby leading to $\Upsilon_{ij} \neq 0$ or, equivalently, $\Pi_{ij} \neq 0$.

regions is not directly connected in the structural model or both regions do not jointly point to any common region, the coefficient of partial correlation between these two regions is expected to be structurally equal to zero. On the other hand, if either condition is not satisfied, the corresponding coefficient of partial correlation is not structurally equal to zero (see Figure 2). Turning our attention back to the TP model, we see that, while regions VEC and SMA satisfy both (C_1) and (C_2) (implying $\Pi_{13} = 0$), regions VEC and PFC do not satisfy (C_1) (since we have VEC → PFC) and regions VEC and IFG do not satisfy (C_2) (since we have VEC → IPL←IFG). As a matter of fact, all cases can be found in both the TP and the BF models, as shown in Tables 2 and 3. Using the aforementioned rule, we are able to retrieve the following structural constraints for partial correlation:

(i) for the TP model: $\Upsilon_{13} = \Upsilon_{24} = \Upsilon_{25} = \Upsilon_{35} = 0$;

(ii) for the BF model: $\Upsilon_{13} = \Upsilon_{14} = \Upsilon_{25} = 0$.

2.5. SEM and Partial Correlation. As correlation matrices are often easier to interpret than covariance matrices, we can decide to examine partial correlation matrices rather than concentration matrices. The partial correlation coefficient between two regions i and j, denoted by Π_{ij}, is here defined as a particular conditional correlation coefficient; it is the correlation between these two regions conditioned on the set of remaining regions, that is,

$$\Pi_{ij} = \mathrm{Corr}\left[y_i, y_j \mid \mathbf{y}_{\mathbb{R}\setminus\{i,j\}} \right]. \tag{13}$$

There are hence $D(D-1)/2$ partial correlation coefficients (10 in our example) that form the D-by-D partial correlation matrix $\mathbf{\Pi} = (\Pi_{ij})$. $\mathbf{\Pi}$ can readily be calculated from $\mathbf{\Upsilon}$ through the following relationship [17]:

$$\Pi_{ij} = -\frac{\Upsilon_{ij}}{\sqrt{\Upsilon_{ii} \cdot \Upsilon_{jj}}} \tag{14}$$

for two distinct regions i and j, and $\Pi_{ii} = 1$. Consequently, we have

$$\Upsilon_{ij} = 0 \Longleftrightarrow \Pi_{ij} = 0, \tag{15}$$

and what has been said about the relationship between the structural model and the structural zeros of the concentration matrix, namely conditions (C_1) and (C_2), also holds for the partial correlation matrix. Furthermore, since the partial correlation coefficients are correlation coefficients, they are not influenced by any scale effect and remain between -1 and 1; for this reason, they are much easier to analyze and interpret than elements of the concentration matrix.

3. Validating Partial Correlation Structures

As we saw, a structural model has unique implications in terms of the structural pattern of partial correlation that can be expected from the data. Since the partial correlation matrix is a quantity that can be inferred from the data, we can use partial correlation analysis as a way to validate a structural model by comparing what is expected and what is observed.

3.1. Local Hypotheses. The approach consists of translating the structural hypotheses in terms of partial correlation. Indeed, according to Tables 2 and 3, the two structural models entail different hypotheses in term of partial correlation. For the theoretically preferred model, we have

$$\begin{aligned} \Pi_{13} &= 0 \quad (H_{\mathrm{TP1}}), \\ \Pi_{24} &= 0 \quad (H_{\mathrm{TP2}}), \\ \Pi_{25} &= 0 \quad (H_{\mathrm{TP3}}), \\ \Pi_{35} &= 0 \quad (H_{\mathrm{TP4}}), \end{aligned} \tag{16}$$

and, for the best fit model,

$$\begin{aligned} \Pi_{13} &= 0 \quad (H_{\mathrm{BF1}}), \\ \Pi_{14} &= 0 \quad (H_{\mathrm{BF2}}), \\ \Pi_{25} &= 0 \quad (H_{\mathrm{BF3}}). \end{aligned} \tag{17}$$

While some hypotheses are identical for both models, $(H_{\mathrm{TP1}}) = (H_{\mathrm{BF1}})$ and $(H_{\mathrm{TP3}}) = (H_{\mathrm{BF3}})$, others have no equivalent in the other model, such as (H_{TP1}), (H_{TP4}), and (H_{BF2}). The objective is then to infer the validity of these hypotheses with regard to the data.

3.2. Inference. Assessing the validity of the various hypotheses can be done by first estimating the partial correlation matrix. Inference of $\mathbf{\Pi}$ can be performed in a Bayesian framework using a numerical sampling scheme ([11, 13], see also the appendix). While direct computation of $\mathrm{p}(\mathbf{\Pi} \mid \mathbf{z})$ is rather complex, this technique provides a simple approximation by sampling L (e.g., $L = 5000$) matrices $(\mathbf{\Pi}^{[l]})_{l=1,..,L}$ from $\mathrm{p}(\mathbf{\Pi} \mid \mathbf{z})$. We then quantify the relevance of all hypotheses as follows. First, the probability of a coefficient Π_{ij} to be higher than 0 can be approximated by

$$p_{ij}^{+} = \Pr\left(\Pi_{ij} > 0\right) \approx \frac{1}{L} \#\left\{ l : \Pi_{ij}^{[l]} > 0 \right\}, \tag{18}$$

where "#" stands for the cardinal of a set (i.e., its size). The probability p_{ij}^{-} of a coefficient to be lower than 0 could be approximated in a similar way, but only one of these two

Table 2: Partial correlation constraints in the TP and BF models (1/2). For each link between regions and each model, examination of whether (C_1) and (C_2) are satisfied.

Link i-j	TP model			BF model		
	(C_1) satisfied	(C_2) satisfied	Υ_{ij}	(C_1) satisfied	(C_2) satisfied	Υ_{ij}
VEC-PFC	no: 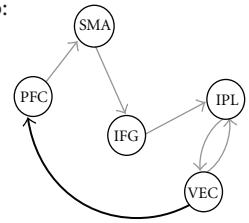	yes	$\neq 0$	no: 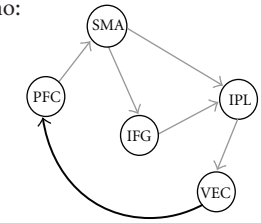	yes	$\neq 0$
VEC-SMA	yes	yes	$= \mathbf{0}$	yes	yes	$= \mathbf{0}$
VEC-IFG	yes	no: 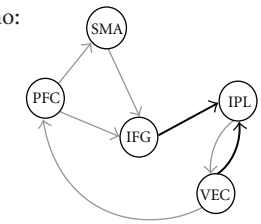	$\neq 0$	yes	yes	$= \mathbf{0}$
VEC-IPL	no: 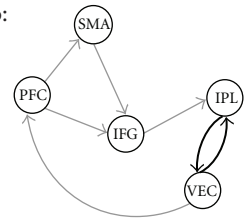	yes	$\neq 0$	no: 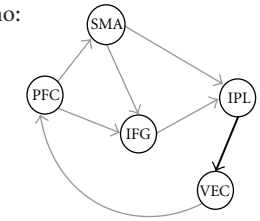	yes	$\neq 0$
PFC-SMA	no: 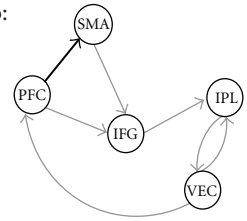	yes	$\neq 0$	no: 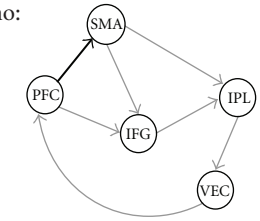	yes	$\neq 0$

quantities need to be computed, since we have $p_{ij}^{+} + p_{ij}^{-} = 1$. From there, the bearing of having $\Pi_{ij} > 0$ can be quantified by the log-odd ratio

$$e_{ij} = 10 \log_{10} \frac{p_{ij}^{+}}{p_{ij}^{-}} = 10 \log_{10} \frac{p_{ij}^{+}}{1 - p_{ij}^{+}}. \tag{19}$$

If e_{ij} is large and positive, we are more inclined to accept $\Pi_{ij} > 0$, while, if it is large and negative, we are more inclined to accept $\Pi_{ij} < 0$. Usually, a value of 10 dB can be considered as good evidence in favor of the hypothesis (see Table 4 for some relationships between p_{ij}^{+} and e_{ij}). We finally take $|e_{ij}|$ as a measure of how Π_{ij} differs from zero and, hence, as a way to quantify the deviation of the data from hypothesis $\Pi_{ij} = 0$: values close to zero indicate a coefficient close to zero, while large values suggest a large coefficient value.

Since we here focus on the partial correlation constraints entailed by the structural models, (16) and (17), we only need the corresponding log odd ratios, summarized in Table 5. If all these hypotheses were true, then we would expect the absolute values of all log odd ratios to be lower than 10 dB. While this is the case for the three hypotheses related to the BF model, it is not the case for two of the four hypotheses related to the TP model: according to these results, (H_{TP2}) and (H_{TP4}) are rather unlikely to be true.

4. Discussion and Perspectives

In this paper, we further examined how partial correlation could be used to investigate effective connectivity in fMRI. We introduced theoretical fundaments explaining why and in what measure the structure of the partial correlation matrix

Table 3: Partial correlation constraints in the TP and BF models (2/2). For each link between regions and each model, examination of whether (C_1) and (C_2) are satisfied.

Link i-j	TP model			BF model		
	(C_1) satisfied	(C_2) satisfied	Υ_{ij}	(C_1) satisfied	(C_2) satisfied	Υ_{ij}
PFC-IFG	yes	yes	$= \mathbf{0}$	no: 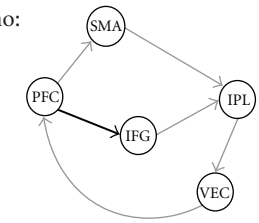	yes	$\neq 0$
PFC-IPL	yes	yes	$= \mathbf{0}$	yes	yes	$= \mathbf{0}$
SMA-IFG	no: 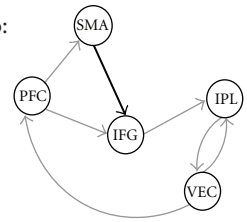	yes	$\neq 0$	yes	no: 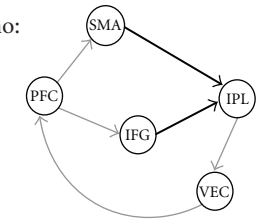	$\neq 0$
SMA-IPL	yes	yes	$= \mathbf{0}$	no: 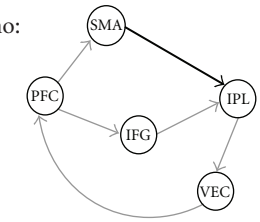	yes	$\neq 0$
IFG-IPL	no: 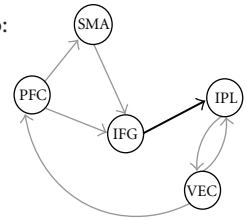	yes	$\neq 0$	no: 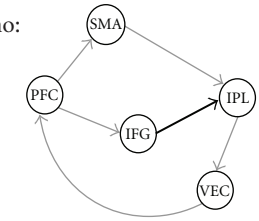	yes	$\neq 0$

Table 4: Evidence e_{ij} and probability p_{ij}^{+} (from [16]). For evidences of 3 and 6, p_{ij}^{+} is only approximately equal to the fraction.

e_{ij} (dB)	p_{ij}^{+}
0	$1/2 = 0.50$
3	$2/3 \approx 0.67$
6	$4/5 = 0.80$
10	$10/11 \approx 0.91$
20	$100/101 \approx 0.99$
30	$1000/1001 \approx 0.999$
40	$10000/10001 \approx 0.9999$

can be related to a structural model. More precisely, we showed that, given a structural model, the partial correlation Π_{ij} between i and j is structurally equal to zero if and only if (C_1) neither region i nor region j has an effect on each other, and (C_2) regions i and j do not jointly influence a third region l; in other words, if and only if none of the following patterns are observed: $i \leftarrow j$, $i \rightarrow j$, or $i \rightarrow l \leftarrow j$ for any l. From there, the definition of a structural model entails a unique set of constraints that can be tested from the data, supporting or invalidating the plausibility of the corresponding structural model.

When examining the global relevance of partial correlation analysis to the investigation of effective connectivity, we must jointly consider two complementary effects, namely, the theoretical relationship between structural models and partial correlation matrices on the one hand and, on the other hand, the quality of the inference process. From a purely theoretical standpoint, this result shows that partial correlation analysis comes up as a combination of two effects. First, constraints (C_1) and (C_2) imply that

$$\Pi_{ij} = 0 \Longrightarrow \neg(i \leftarrow j),\ \neg(i \rightarrow j), \tag{20}$$

Table 5: Real data. Relevance of hypotheses related to the TP and the BF models, respectively. Log odd ratios above a threshold of 10 dB are represented in bold.

Structural model	Constituting hypotheses	Structural constraints	$\lvert e_{ij} \rvert$
TP	(H_{TP1})	$\Pi_{13} = 0$	1.6 dB
	(H_{TP2})	$\Pi_{24} = 0$	**12.4 dB**
	(H_{TP3})	$\Pi_{25} = 0$	9.7 dB
	(H_{TP4})	$\Pi_{35} = 0$	**13.1 dB**
BF	(H_{BF1})	$\Pi_{13} = 0$	1.6 dB
	(H_{BF2})	$\Pi_{14} = 0$	6.4 dB
	(H_{BF3})	$\Pi_{25} = 0$	9.7 dB

where $\neg$ stands for the negation. In other words, a zero partial correlation between i and j implies the absence of a direct link between these two regions. Were there only (C_1), this implication would be an equivalence and having $\Pi_{ij} \neq 0$ would imply a direct link between i and j. However, this is not true in general and, more specifically, for any pair of regions for which constraint (C_2) is satisfied. Such pairs are not connected but still have a nonzero partial correlation coefficient. As a consequence, all that can be said is that the set of set of pairs of regions with a zero partial correlations is a subset of the sets of pairs not directly connected in the structural model or, equivalently, that the set of pairs of regions connected in the structural model is a subset of the set of pairs of regions with a nonzero partial correlations. These features can easily be related to basic graph theoretic concepts. Condition (C_1) states that regions i and j are not neighbors; condition (C_2) states that i and j satisfy the so-called Wermuth condition [17]. As a consequence, the partial correlation constraints imposed by a structural model can be read off the graph obtained by adding undirected edges to eliminate all Wermuth configurations (for condition (C_2)) and transforming all arrows into undirected edges (for condition (C_1)). Such a graph is called the moral graph associated with the structural model. Depending on how many variables share common parents, the moral graph can be more or less close to the structural graph. For instance, in each of the two models used in this paper, condition (C_2) was only met once. Whether this is a general feature of fMRI data or only a characteristic induced by the structure selected remains to be cleared.

Another theoretical issue that needs to be tackled is the fact that having a partial correlation that is not constrained to 0 (e.g., Π_{14} for the theoretically preferred model) does not preclude its value to be equal to zero, due to a numerical coincidence. Indeed, (11) shows that specific values of $\mathbf{K}$ and $\mathbf{V}$ could be selected to induce $\Upsilon_{ij} = 0$ and, consequently, also $\Pi_{ij} = 0$. Even though this event is possible, it should be considered as rather unlikely, unless there is an underlying constraint at stake that forces the coefficient values to respect a certain relationship.

Another, more important issue deals with inference and how confident we can be in the partial correlation estimates and, critically, in the tests that their values are different from zero. The major difference between partial correlation and marginal correlation is that the former is obtained by removing the effect of $D - 2$ regions as evidenced by (14). Importantly, the partialization process tends to decrease the value of correlation regardless of the exact relationship between the two variables and the conditioning set. Consequently, the values of partial correlation coefficients usually tend to be lower than their marginal counterparts; this is an observation that we have made consistently, and with only few exceptions. Also, as a rule of thumb, the posterior variance associated with a (marginal or partial) correlation coefficient (e.g., $\text{Var}[\Pi_{ij} \mid \mathbf{y}]$ for partial correlation) is roughly a decreasing function of the absolute value of its posterior mean (e.g., $\text{E}[\Pi_{ij} \mid \mathbf{y}]$ for partial correlation). For instance, it is asymptotically $(1 - \Pi_{ij}^2)^2/(N - 1)$ (which is indeed a decreasing function of Π_{ij}) for partial correlation and a similar result hold for marginal correlation [15]. A lower mean value therefore also implies a higher variance and, essentially, a bigger difficulty to discriminate a nonzero value from zero.

Altogether, these various factors, both theoretical and inferential, have different consequences on the relationship between the inferred pattern of partial correlation and the underlying structural model. Although we have observed a rather good agreement between expected and inferred patterns so far, in the lack of gold standard, these consequences must be further investigated.

Still, one of the main reasons why partial correlation analysis might become an important tool for the investigation of effective connectivity is that it is, to our knowledge, the only fully exploratory approach. Its key feature is its ability to retrieve local patterns of interaction. Indeed, while the method developed for the estimation of structural parameters, for example, (2), globally assesses the goodness of fit of the whole model and accordingly provides a general measure of it, partial correlation analysis provides a rather local assessment of effective connectivity, since the fact that two regions have a nonzero partial correlation depends on their connection with each other and of a potential connection with a common third region. For instance, in our example, while Bullmore et al. [7] concluded that the data did not contain enough evidence to prefer the BF model over the TP model (global statement), we showed that the TP model entails two partial correlation constraints ($\Pi_{24} = 0$ and $\Pi_{35} = 0$) that are rather unlikely to be true in the data (local statements). According to this result, we should discard the BF model or, at least, exert great caution

when using it. Furthermore, if one only had the theoretically preferred model and were testing it, the large log odd ratios corresponding to hypotheses $\Pi_{24} = 0$ and $\Pi_{35} = 0$ would hint that the corresponding constraints might not hold and that there might be a direct connection between regions PFC and IFG on the one hand and, on the other hand, between regions SMA and IPL.

In this paper, we determined whether certain coefficients could be considered as different from zero or not in a Bayesian framework. This led us to the use of the evidence e_{ij} of (19). While increasingly used, evidence admittedly remains rather uncommon in the brain imaging literature, where significance is often asserted with respect to a significance threshold, or P-value. It would therefore be tempting to propose a direct connection between P-values and evidence or, at least, interpret results of our Bayesian approach in terms of significance and P-value (see, e.g., [12]). Unfortunately, doing so is both inaccurate and misleading, because of the strong difference between Bayesian probability intervals and their frequentist counterparts, confidence intervals. Under the null hypothesis (H_0): $\Pi_{ij} = 0$, thresholding a statistic $\hat{\Pi}_{ij}$ at 10% in a frequentist framework (corresponding to a statistic of $P_{10\%}$) implies that, assuming that (H_0) is true, there is only 10% to obtain data with a statistic above the threshold, that is,

$$\mathrm{p}\left(\hat{\Pi}_{ij} > P_{10\%} \mid H_0\right) = 0.10. \tag{21}$$

In this case, there is no mention whatsoever of any alternative hypothesis: we only assess how typical the data under consideration are. By contrast, thresholding a Bayesian probability at 10% means that we only consider cases where the alternative hypothesis (H_1) of (H_0): $\Pi_{ij} \leq 0$ has a probability of more that 0.9, that is,

$$\mathrm{p}\left(H_1 \mid P_{ij}\right) > 0.90. \tag{22}$$

While a frequentist threshold of 10% might appear permissive, a Bayesian threshold of 10% is already conservative, since it implies that (H_1) is about 10 times more probable than (H_0). For more details on this topic, the reader can refer to Jaynes [18].

A last question is the possibility to apply partial correlation to other imaging modalities, such as electroencephalography (EEG) and magnetoencephalography (MEG). While the issue of removing the effect of other regions when considering the interactions between two regions remains relevant, whether partial correlation as defined here can provide a cogent solution remains to be investigated. One of the major properties of the fMRI signal is that, due to the convolution with the hemodynamic response, the temporal information that it conveys is usually considered as less relevant than in EEG or MEG. This is one of the major reasons why most EEG or MEG analyses are performed in the frequency domain. Of interest would therefore be to use partial correlation in this frequency domain. This analysis could be performed over time windows that are narrow enough to assume stationarity of the signal. How such an approach could be related to partial coherence [19, 20] remains to be clarified.

Appendix

Numerical Sampling Scheme

Using standard Bayesian theory, it can be shown that the covariance matrix $\boldsymbol{\Sigma}$ given the data z follows an inverse Wishart distribution with $T-1$ degrees of freedom and scale matrix $\mathbf{U} = \mathbf{S}^{-1}$, where

$$\mathbf{S} = \sum_{t=1}^{T} (z_t - \overline{z_t})(z_t - \overline{z_t})^{\mathrm{t}} \tag{A.1}$$

is proportional to the sample covariance matrix, and $\overline{z_t}$ is the temporal mean [21]. Calculation of the posterior probability density function (pdf) of the partial correlation matrix, $\mathrm{p}(\boldsymbol{\Pi} \mid \mathbf{z})$ cannot be performed in close form from this distribution. To approximate this distribution, we can nevertheless resort to the following sampling scheme [11, 13]. For sample l,

(1) sample $\boldsymbol{\Sigma}^{[l]}$ according to its inverse Wishart distribution ([21], Appendix A);

(2) calculate $\boldsymbol{\Upsilon}^{[l]} = \left(\boldsymbol{\Sigma}^{[l]}\right)^{-1}$, and $\boldsymbol{\Pi}^{[l]}$ from $\boldsymbol{\Upsilon}^{[l]}$ according to (14).

Once a large number L of samples have been drawn following this process, the marginal pdf of a given quantity can be approximated by the frequency histogram obtained from the sample. Likewise, all statistics and estimators can be approximated by their sample counterparts. For instance,

$$\begin{aligned} \mathrm{E}\left[\Pi_{ij} \mid \mathbf{z}\right] &\approx M_{ij} = \frac{1}{L}\sum_{l=1}^{L} \Pi_{ij}^{[l]}, \\ \mathrm{Var}\left[\Pi_{ij} \mid \mathbf{z}\right] &\approx X_{ij} = \frac{1}{L}\sum_{l=1}^{L} \left(\Pi_{ij}^{[l]} - M_{ij}\right)^2. \end{aligned} \tag{A.2}$$

One can also compute evidence as explained in the main text.

References

[1] W. Chen and S. Ogawa, "Principles of BOLD functional MRI," in *Functional MRI*, C. Moonen and P. Bandettini, Eds., pp. 103–113, Springer, Berlin, Germany, 1999.

[2] S. A. Huettel, A. W. Song, and G. McCarthy, *Functional Magnetic Resonance Imaging*, Sinauer, Sunderland, UK, 2004.

[3] B. Biswal, F. Z. Yetkin, V. M. Haughton, and J. S. Hyde, "Functional connectivity in the motor cortex of resting human brain using echo-planar MRI," *Magnetic Resonance in Medicine*, vol. 34, no. 4, pp. 537–541, 1995.

[4] K. J. Friston, "Functional and effective connectivity in neuroimaging: a synthesis," *Human Brain Mapping*, vol. 2, no. 1-2, pp. 56–78, 1994.

[5] A. R. McIntosh and F. Gonzalez-Lima, "Structural equation modeling and its application to network analysis in functional brain imaging," *Human Brain Mapping*, vol. 2, no. 1-2, pp. 2–22, 1994.

[6] F. Gonzalez-Lima and A. R. McIntosh, "Analysis of neural network interactions related to associative learning using structural equation modeling," *Mathematics and Computers in Simulation*, vol. 40, no. 1-2, pp. 115–140, 1995.

[7] E. Bullmore, B. Horwitz, G. Honey, M. Brammer, S. Williams, and T. Sharma, "How good is good enough in path analysis of fMRI data?" *NeuroImage*, vol. 11, no. 4, pp. 289–301, 2000.

[8] K. A. Bollen, *Structural Equation with Latent Variables*, Wiley-Interscience, New York, NY, USA, 1989.

[9] R. Cudeck, K. J. Klebe, and S. J. Henly, "A simple Gauss-Newton procedure for covariance structure analysis with high-level computer languages," *Psychometrika*, vol. 58, no. 2, pp. 211–232, 1993.

[10] G. Marrelec, J. Daunizeau, M. Pélégrini-Issac, J. Doyon, and H. Benali, "Conditional correlation as a measure of mediated interactivity in fMRI and MEG/EEG," *IEEE Transactions on Signal Processing*, vol. 53, no. 9, pp. 3503–3516, 2005.

[11] G. Marrelec, J. Doyon, M. Pélégrini-Issac, and H. Benali, "Heading for data-driven measures of effective connectivity in functional MRI," in *Proceedings of the International Joint Conference on Neural Networks*, pp. 1528–1533, 2005.

[12] G. Marrelec, A. Krainik, H. Duffau, et al., "Partial correlation for functional brain interactivity investigation in functional MRI.," *NeuroImage*, vol. 32, no. 1, pp. 228–237, 2006.

[13] G. Marrelec, B. Horwitz, J. Kim, M. Pélégrini-Issac, H. Benali, and J. Doyon, "Using partial correlation to enhance structural equation modeling of functional MRI data," *Magnetic Resonance Imaging*, vol. 25, no. 8, pp. 1181–1189, 2007.

[14] G. Marrelec, J. Kim, J. Doyon, and B. Horwitz, "Large-scale neural model validation of partial correlation analysis for effective connectivity investigation in functional MRI," *Human Brain Mapping*, vol. 30, no. 3, pp. 941–950, 2009.

[15] T. W. Anderson, *An Introduction to Multivariate Statistical Analysis*, Wiley Publications in Statistics, John Wiley & Sons, New York, NY, USA, 1958.

[16] E. T. Jaynes, *Probability Theory: The Logic of Science. Vol. I: Principles and Elementary Applications*, Cambridge University Press, Cambridge, UK, 2003.

[17] J. Whittaker, *Graphical Models in Applied Multivariate Statistics*, John Wiley & Sons, Chichester, UK, 1990.

[18] E. T. Jaynes, "Confidence intervals vs. Bayesian intervals," in *Foundations of Probability Theory, Statistical Inference, and Statistical Theories of Science*, W. L. Harper and C. A. Hooker, Eds., pp. 175–257, D. Reidel, Dordrecht, The Netherlands, 1976.

[19] F. H. Lopes da Silva, J. E. Vos, J. Mooibroek, and A. V. Rotterdam, "Relative contributions of intracortical and thalamo-cortical processes in the generation of alpha rhythms, revealed by partial coherence analysis," *Electroencephalography and Clinical Neurophysiology*, vol. 50, no. 5-6, pp. 449–456, 1980.

[20] J. R. Rosenberg, D. M. Halliday, P. Breeze, and B. A. Conway, "Identification of patterns of neuronal connectivity—partial spectra, partial coherence, and neuronal interactions," *Journal of Neuroscience Methods*, vol. 83, no. 1, pp. 57–72, 1998.

[21] A. Gelman, J. B. Carlin, H. S. Stern, and D. B. Rubin, *Bayesian Data Analysis. Texts in Statistical Science*, Chapman & Hall, London, UK, 1998.

Hindawi Publishing Corporation
Computational Intelligence and Neuroscience
Volume 2009, Article ID 164958, 12 pages
doi:10.1155/2009/164958

Research Article

Measurement of Brain Function of Car Driver Using Functional Near-Infrared Spectroscopy (fNIRS)

Hitoshi Tsunashima[1] and Kazuki Yanagisawa[2]

[1] *Department of Mechanical Engineering, College of Industrial Technology, Nihon University, 1-2-1 Izumi-cho, Narashino-shi, Chiba 275-8575, Japan*
[2] *Department of Mechanical Engineering, Graduate school of Nihon University, 1-2-1 Izumi-cho, Narashino-shi, Chiba 275-8575, Japan*

Correspondence should be addressed to Hitoshi Tsunashima, tsuna@cit.nihon-u.ac.jp

Received 3 November 2008; Revised 5 March 2009; Accepted 2 April 2009

Recommended by Laura Astolfi

The aim of this study is to propose a method for analyzing measured signal obtained from functional Near-Infrared Spectroscopy (fNIRS), which is applicable for neuroimaging studies for car drivers. We developed a signal processing method by multiresolution analysis (MRA) based on discrete wavelet transform. Statistical group analysis using Z-score is conducted after the extraction of task-related signal using MRA. Brain activities of subjects with different level of mental calculation are measured by fNIRS and fMRI. Results of mental calculation with nine subjects by using fNIRS and fMRI showed that the proposed methods were effective for the evaluation of brain activities due to the task. Finally, the proposed method is applied for evaluating brain function of car driver with and without adaptive cruise control (ACC) system for demonstrating the effectiveness of the proposed method. The results showed that frontal lobe was less active when the subject drove with ACC.

1. Introduction

In recent years, various driving assistance systems have been developed to ensure safety by reducing driver workloads. Examples include the Adaptive Cruise Control (ACC) system, which maintains a safe distance between the driver's vehicle and the vehicle ahead of it and the lane-keeping assistance system, which keeps the car in a lane through steering support.

However, it is also possible that while driver workload is reduced, the driver's attention is also reduced, resulting in unexpected accidents. Therefore, it is necessary to examine driver workload from the viewpoints of cognitive engineering and human physiology. It is necessary to clarify the relationship between driver workload and brain activity, which includes recognition and judgment. It is then necessary to evaluate the driver's attention and to clarify the relationship between brain activity and driving performance.

A small number of neuroimaging studies using driving simulator examine brain activity in car driving. In these studies [1, 2], functional magnetic resonance imaging (fMRI) has been used. However, fMRI has many shortcomings in evaluating driving performance, because it requires the subject to lie in a narrow cylinder during evaluation and does not permit movement of the body, particularly the head. This situation makes the driving task unrealistic and unnatural.

Near-Infrared Spectroscopy (NIRS) has gained attention in recent years [3, 4]. This noninvasive technique uses near-infrared light to evaluate an increase or decrease in oxygenated hemoglobin or deoxygenated hemoglobin in the tissue from the body surface.

NIRS can detect the hemodynamic of the brain in real time while the subject is moving. Therefore, brain activity can be measured in various environments. Recent research has used functional Near-Infrared Spectroscopy (fNIRS) to measure brain activity of train driver [5, 6]. Shimizu et al. used fNIRS to evaluate the mental activity of car driver using a driving simulator [7].

Various arguments have focused on interpretation of signals obtained from fNIRS, and no uniform signal-processing method has yet been established. Averaging and base-line correction are conventional signal-processing methods used

for the fNIRS signal. These methods require block design, an experimental technique that involves repeating the same stimuli (tasks) and resting multiple times in order to detect brain activation during a task. However, it has been pointed out that brain activation gradually declines when one subject repeats the same task multiple times [8].

Fourier analysis, which is frequently used for signal analysis, transforms information in the time domain into the frequency domain through the Fourier transform. However, time information is lost in the course of transform. As the fNIRS signal has unsteady nature, time-frequency analysis is suitable for the fNIRS signal.

The wavelet transform is an efficient method of time-frequency analysis [9]. It adapts the window width in time and frequency so that the window width in frequency becomes smaller when the window width in time is large, or the window width in frequency becomes larger when the window width in time is small. Multiresolution analysis (MRA) [10] decomposes the signal into different scales of resolution. The MRA with orthonormal wavelet base facilitates complete decomposition and reconstruction of the signal effectively without losing original information of the signal.

In addition to this, oxygenated hemoglobin and deoxygenated hemoglobin measured in fNIRS are relative value from the beginning of measurement, which is changeable for subject and part of the brain. Thus, simple averaging of fNIRS signal should not be applied for statistical analysis. To solve this problem, we propose Z-scored fNIRS signal for statistical analysis.

The aim of the study is to propose the signal processing method suitable for fNIRS signal which is applicable for neuroimaging studies for car drivers using fNIRS. In this paper, we first describe the principle of measurement of brain activity with fNIRS. Then, we propose the discrete wavelet-based MRA to extract the task-related signal from the original fNIRS recordings. We conducted simultaneous measurement experiments with fNIRS and fMRI using mental calculation tasks to confirm the validity of the proposed method. The Z-scored fNIRS signal is proposed for statistical analysis. We show the possibility of the proposed method for evaluating driver's brain activity in realistic driving environment.

2. Principle of fNIRS

Using near-infrared rays, fNIRS noninvasively measures changes in cerebral blood flow. Its principle of measurement, which was developed by Jöbsis [11], is based on measurement of oxygenation of hemoglobin in the cerebral blood flow.

In uniformly distributed tissue, incident light is attenuated by absorption and scattering. Therefore, the following expression, a modified Lambert-Beer law, was used:

$$\mathrm{Abs} = -\log\left(\frac{I_{\mathrm{out}}}{I_{\mathrm{in}}}\right) = \varepsilon d C + S. \tag{1}$$

Here, I_{in} is the irradiated quantity of light; I_{out} is the detected quantity of light; ε is the absorption coefficient; C is the concentration; d is the averaged path length; S is the scattering term.

If it is assumed that no scattering changes in brain tissue occur during activation of the brain, the change in absorption across the activation can be expressed by the following expression:

$$\Delta\mathrm{Abs} = -\log\left(\frac{\Delta I_{\mathrm{out}}}{\Delta I_{\mathrm{in}}}\right) = \varepsilon d \Delta C(\Delta\mathrm{oxyHb}, \Delta\mathrm{deoxyHb}). \tag{2}$$

Furthermore, if it is assumed that the change in concentration (ΔC) is proportional to the changes in oxygenated hemoglobin (ΔoxyHb) and deoxygenated hemoglobin (ΔdeoxyHb), the following relational expression can be obtained:

$$\Delta\mathrm{Abs}(\lambda_i) = d\left[\varepsilon_{\mathrm{oxy}}(\lambda_i)\Delta\mathrm{oxyHb} + \varepsilon_{\mathrm{deoxy}}(\lambda_i)\Delta\mathrm{deoxyHb}\right]. \tag{3}$$

The absorption coefficients of oxygenated hemoglobin and deoxygenated hemoglobin at each wavelength, $\varepsilon_{\mathrm{oxy}}(\lambda_i)$ and $\varepsilon_{\mathrm{deoxy}}(\lambda_i)$, are known; therefore, $d\Delta$oxyHb and $d\Delta$deoxyHb can be obtained by performing measurements with near-infrared rays of two different wavelengths and solving simultaneous equations (3). However, the physical quantity obtained here is the product of the change in concentration and the averaged path length; so care should be taken.

In general, the averaged path length d varies largely from one individual to another and from one part to another. Therefore, caution must be exercised in evaluating the results.

3. Signal Processing Methods for fNIRS

3.1. Recording of fNIRS Signal. Mental calculation tasks, low-level task: simple one-digit addition (e.g., 3 + 5), high-level task: subtraction and division with decimal fraction (e.g., 234/(0.61 − 0.35)), were set to obtain fNIRS signal. The brain activity in the prefrontal lobe was measured using fNIRS. The measuring instrument was the multichannel fNIRS instrument, OMM-3000, Shimadzu Corporation, Japan [12].

Figure 1 illustrates the arrangement of optical-fiber units and the location of each channel (3×7 matrix, 32 channels). Figure 2 shows the recorded time history of oxygenated hemoglobin (red line, indicated as oxy-Hb) and deoxygenated hemoglobin (blue line, indicated as deoxy-Hb) of channel number 20.

3.2. Analysis of fNIRS Signals. In fNIRS analysis, it is necessary to separate noise that is related to a task from that which is not, since fNIRS measures not only the signals of brain activity during a task but also other signals, including measurement noise.

In general, changes in oxygenated hemoglobin and deoxygenated hemoglobin when the brain is activated and restored to the original state exhibit the trend illustrated in Figure 1 [13]. Therefore, if these signals can be extracted

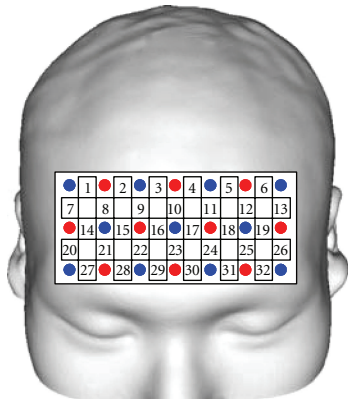

Illuminator
Detectot
Channel

(a)

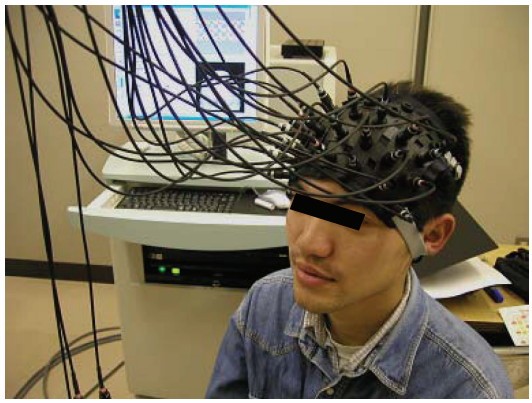

(b)

Figure 1: Position of optical fibers and channels in recoding fNIRS signal (Mental calculation task: 3×7 matrix, 32 channels).

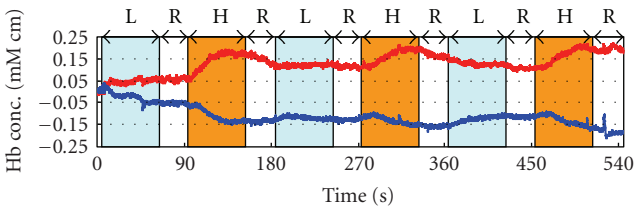

R: Rest
L: Low difficulty task
H: High difficulty task
OxyHb
DeoxyHb

Figure 2: Time history of fNIRS signal in mental calculation (channel number 20).

from the measured signals, it is obvious that the brain has been activated.

Averaging and base-line correction are conventional signal processing methods. These methods require block design, an experimental technique that involves repeating the same stimuli (tasks) and resting multiple times in order to detect brain activation during a task.

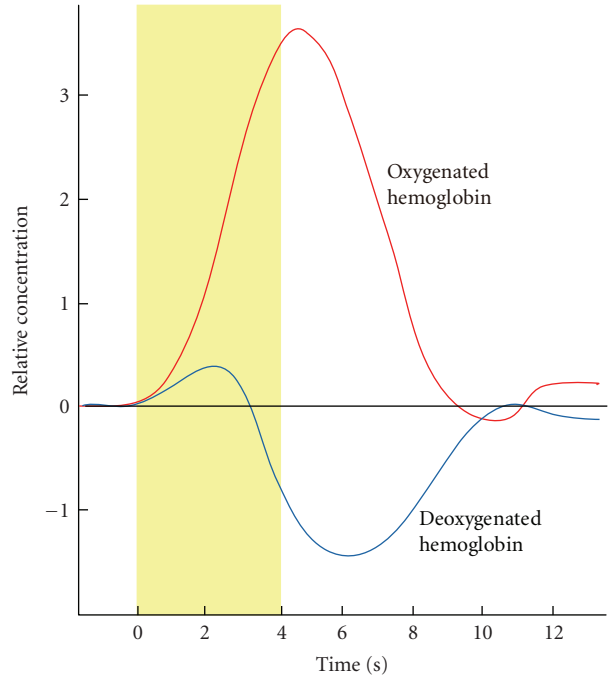

Figure 3: Schematic hemoglobin concentration change due to neural activity.

Averaging is the method by which data is averaged for each task. Randomly generated noises approach zero by averaging, and only periodical data is left. Averaging is effective when similar reactions are generated repeatedly. However, for cerebral blood flow that has large scattering of reactions to the same stimuli, the reliability of averaged signals is low, and false signals may be created. Furthermore, it is possible that even significant signals may become undetectable after averaging.

Base-line correction corrects the start point and end point of a block to zero to remove gentle trends, based on the assumption that blood flow is restored to its original state during a task block. However, because blood flow involves irregular fluctuations, the reference points are unstable. Therefore, if the whole block is corrected based on those two points alone, signals may be distorted.

Figure 4 shows the result of base-line correction applied for fNIRS signal (Figure 2) after removing high-frequency noise by moving average of 25 data. Figure 5 indicates the functional brain imaging of frontal. It should be noted that the brain activation gradually declines when one subject repeats the same task multiple times.

3.3. Decomposition and Reconstruction of fNIRS Signals Using Wavelet Transform

3.3.1. Wavelet Transform. Fourier analysis, which is frequently used for waveform analysis, transforms information in the time domain into information in the frequency domain through the Fourier transform. However, time information is lost in the course of transform.

Short-time Fourier transform, or windowed Fourier transform, can be used for time-frequency analysis of signals.

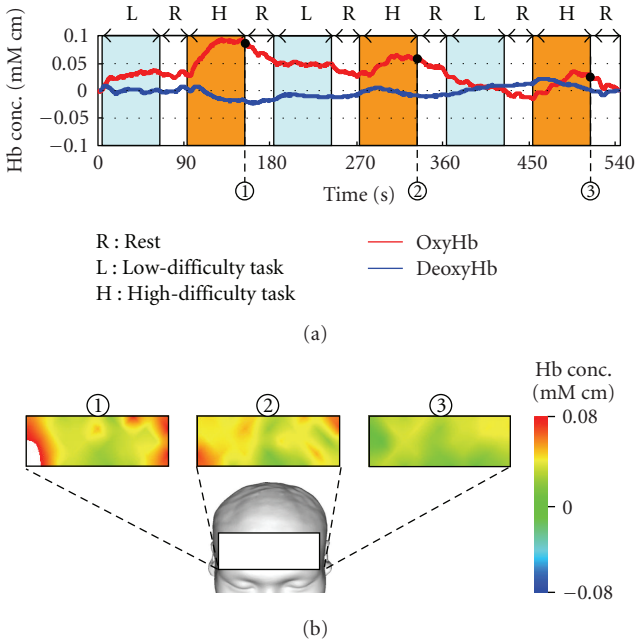

FIGURE 4: Results of signal processing with base-line correction and denoising.

However, the detecting capacity varies largely, depending on the setting of the window.

In contrast, wavelet transform is an efficient method of time-frequency analysis. It adapts the window width in time and frequency so that the window width in frequency becomes smaller when the window width in time is large, or the window width in frequency becomes larger when the window width in time is small.

Wavelet transform expresses the local shape of the waveform to be analyzed, $S(t)$, by shifting and dilating the waveform called the mother wavelet, $\psi(t)$, and then analyzes the waveform.

Continuous wavelet transform is given by

$$\left(W_\psi S\right)(a,b) = \int_{-\infty}^{\infty} \frac{1}{\sqrt{|a|}} \overline{\psi\left(\frac{t-b}{a}\right)} S(t)dt. \tag{4}$$

In the continuous wavelet transform, information is duplicated, requiring many calculations. Therefore, the method that is expressed by (5), where a and b are discretized, is called discrete wavelet transform:

$$D_m = \int_{-\infty}^{\infty} S(t)\psi_{m,n}(t)dt, \tag{5}$$

where

$$\psi_{m,n}(t) = 2^{-m/2}\psi(2^{-m}t - n). \tag{6}$$

Discrete wavelet transform handles a smaller volume of information than continuous wavelet transform does, but it is able to transform signals more efficiently. Furthermore, its use of an orthonormal base facilitates complete reconstruction of original signals without redundancy. The following section describes decomposition and reconstruction of signals using multiresolution analysis (MRA).

3.3.2. Multiresolution Analysis (MRA). MRA decomposes signals into a tree structure using the discrete wavelet transform. MRA decomposes the object time-series signals, $S(t)$, into an approximated component (low-frequency component) and multiple detailed components (high-frequency components).

Signal $S(t)$ can be expressed as follows by discrete wavelet transform using an orthonormal base:

$$S(t) = \sum_{n=-\infty}^{\infty} A_{m_0,n}\phi_{m_0,n}(t) + \sum_{m=-\infty}^{m_0}\sum_{n=-\infty}^{\infty} D_{m,n}\psi_{m,n}(t). \tag{7}$$

Here, $\phi_{m,n}(t)$ is the scaling function as defined by the following equation.

The coefficient of the approximated component is calculated by

$$A_{m,n} = \int_{-\infty}^{\infty} S(t)\phi_{m,n}(t). \tag{8}$$

The detailed components of the signals on level m can be expressed by

$$d_m = \sum_{n=-\infty}^{\infty} D_{m,n}\psi_{m,n}(t). \tag{9}$$

Thus, the original signal, $S(t)$, can be expressed as

$$S(t) = a_{m_0} + \sum_{m=-\infty}^{m_0} d_m. \tag{10}$$

Therefore, it is possible to reconstruct task-related components from multiple detailed components.

In the wavelet transform, the choice of a mother wavelet $\psi_{m,n}(t)$ is important. We employed *Daubechies* wavelet [14], which is orthonormal base and compactly supported wavelet. The vanishing moments of *Daubechies* wavelet can be changed by index N. We decided to use a relatively high-order generating index, $N = 7$.

Figure 5 presents the MRA results for oxygenated hemoglobin in channel number 20, where task-related changes were remarkable. Here the measured signal is decomposed into ten levels. The trend of the whole experiment was extracted on the approximated component (a_{10}), lowest-frequency range. Here, d_1 and d_2, highest-frequency range, had a relatively large amplitude. It is possible that these were measurement noises. Because the interval of repetition of tasks and rests was 64 seconds, the d_8 component was the central component of task-related changes. Therefore, signals were reconstructed by adding the d_7, d_8, and d_9 components.

Reconstructed signals are illustrated in Figure 6. It should be noted that the activation pattern of oxygenated hemoglobin and deoxygenated hemoglobin, shown in Figure 3, is observed very clearly. Comparison between Figure 4 (conventional method) and Figure 6 (proposed method) shows the better performanceof the proposed method. Results revealed that oxygenated hemoglobin increased, and the brain was activated during mental calculation tasks.

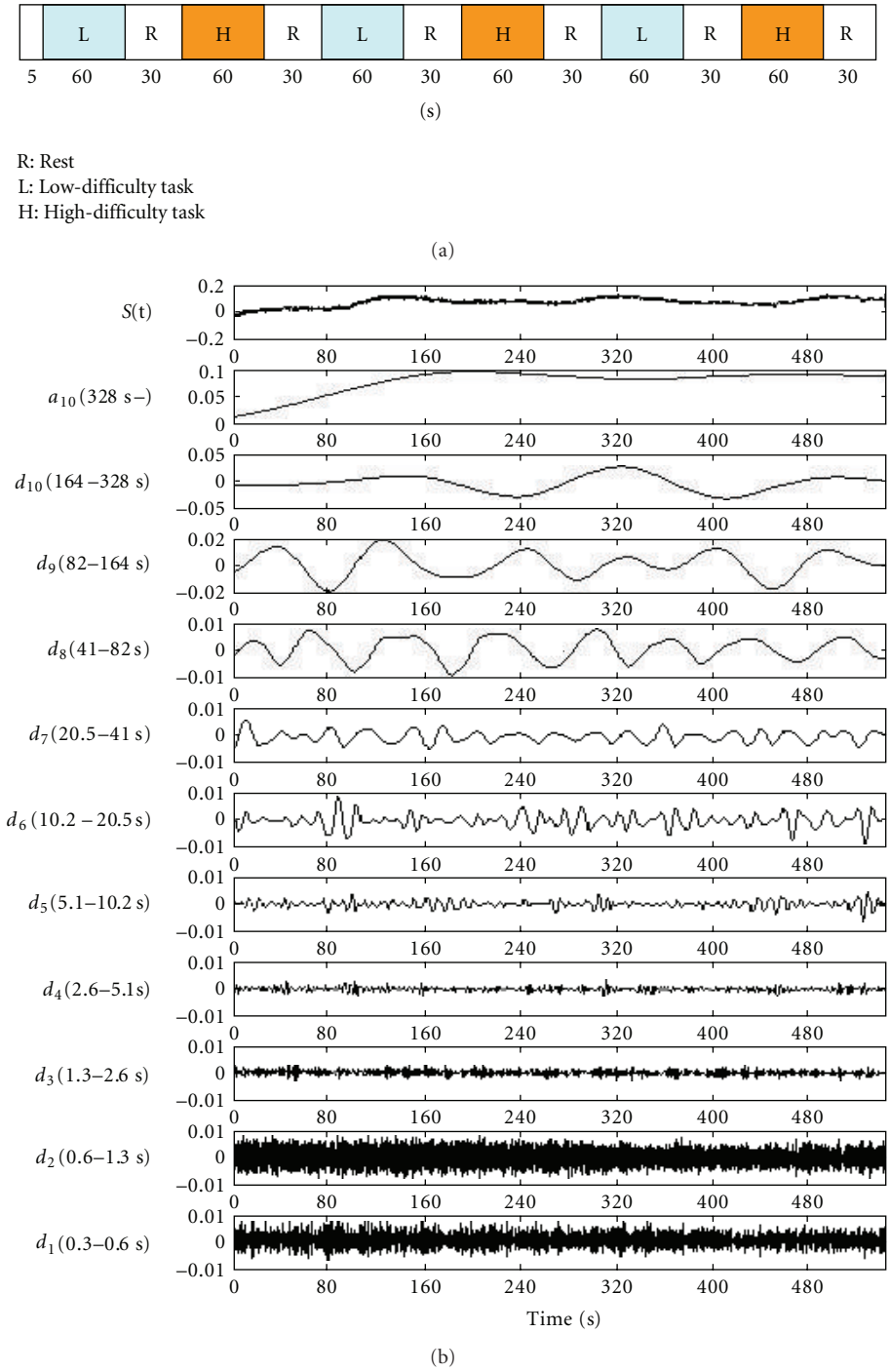

Figure 5: Decomposition of fNIRS signal using MRA.

4. Measurement of Brain Functions under Workload Using Mental Calculation Tasks

To confirm the validity of the signal processing method explained in the previous section, we measured brain functions through simultaneous use of fNIRS and fMRI.

4.1. Setting of Workload. To measure brain activity under workload, we used the workload of mental calculation. Mental calculation tasks were set to low, medium, and high levels as follows:

(i) Low-level task: simple one-digit addition (e.g., 3 + 5);

(ii) Medium-level task: one-digit addition of three numbers (e.g., 6 + 5 + 9);

(iii) High-level task: subtraction and division with decimal fraction (e.g., 234/(0.61 − 0.35)).

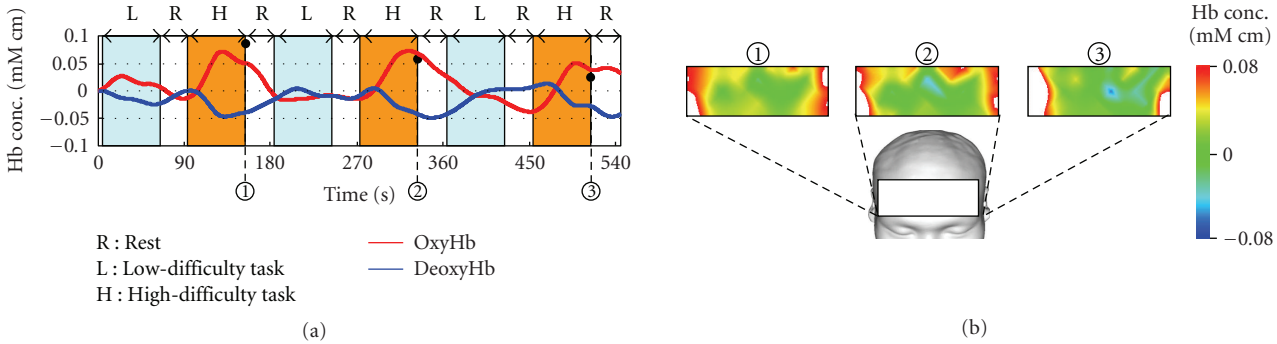

Figure 6: Results of signal processing using MRA.

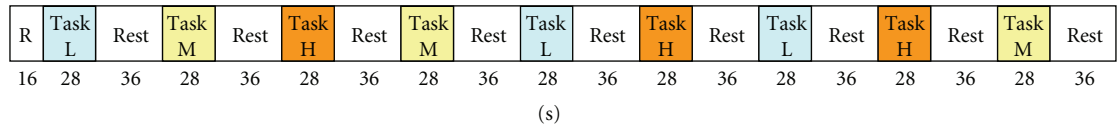

Figure 7: Design of experiment.

The design of the experiment is presented in Figure 7. Each set was composed of 28 seconds of task and 36 seconds of rest in that order. By arranging three sets for each level in random order, a total of nine sets of experiment were conducted over 592 seconds.

A 28 seconds-task consisted of 14 questions at 2 seconds-intervals for the low level, 10 questions at 2.8 seconds-intervals for the intermediate level, or two questions at 14 seconds-intervals for the high level. The subject answered the questions displayed on the PC screen without speaking. During the 36 seconds-rest time, the subject rested while steadily gazing at the cross mark displayed on the PC screen.

4.2. fNIRS and fMRI Recording. The brain activity in the prefrontal lobe was measured using fNIRS and fMRI simultaneously. fNIRS data were collected on OMM-3000, Shimadzu Corporation, Japan, in MRI scanner.

fMRI data (3 mm thickness, 40 slices) were collected on Siemens Symphony 1.5 T (T2*-weighted gradient-echo sequence, TR = 4000 milliseconds, TE = 50 milliseconds, FA = 90 deg, 64 × 64 pixel, FOV = 192 mm). Whole brain image is obtained as T1-weighted image (TR = 2200 milliseconds, TE = 3.93 milliseconds, FA = 15 deg, TI = 1100 milliseconds, 1 mm^3 voxel , FOV = 256 mm).

fMRI data were preprocessed using Statistical Parametric Mapping (SPM99, Welcome Department of Imaging Neuroscience, UK) Normalized contrast images were smoothed with an isotropic Gaussian kernel (FWHM = 12 mm). Regions of interests (ROIs) were defined as clusters of 10 or more voxels in which parameter estimate values differed significantly from zero ($P < .01$).

The subjects were nine healthy men and women. The arrangement of optical fiber units and measurement positions is shown in Figure 1.

4.3. Decomposition and Reconstruction of fNIRS Signals. Figure 8 presents the measurement results through all channels for Subject A during the first three tasks. During the mental calculation task at the high level (i.e., the third task), oxygenated hemoglobin increased deoxygenated hemoglobin decreased on both outer sides of the frontal lobe.

Figure 9 presents the MRA results for oxygenated hemoglobin in channel number 26, where task-related changes were remarkable. The trend of the whole experiment was extracted on the approximated component (a_{10}). Because the interval of repetition of tasks and rests was 64 seconds, the d_8 component was the central component of task-related changes. Therefore, signals were reconstructed by adding the d_7, d_8, and d_9 components

Reconstructed signals of channel number 26 are illustrated in Figure 10. Results revealed that oxygenated hemoglobin increased, and the brain was activated during mental calculation tasks. Furthermore, such changes became larger as the level of mental calculation task became higher.

Figure 11 shows the comparison of the functional brain imaging by fMRI and fNIRS with proposed method. The rectangular in fMRI image indicate the region of measurement with fNIRS. The fNIRS images agree to that of fMRI in different workload levels. This results support the effectiveness of MRA with discrete wavelet transform.

4.4. Statistical Analysis. The fNIRS signal expresses the quantity of relative changes using the start point as the reference;

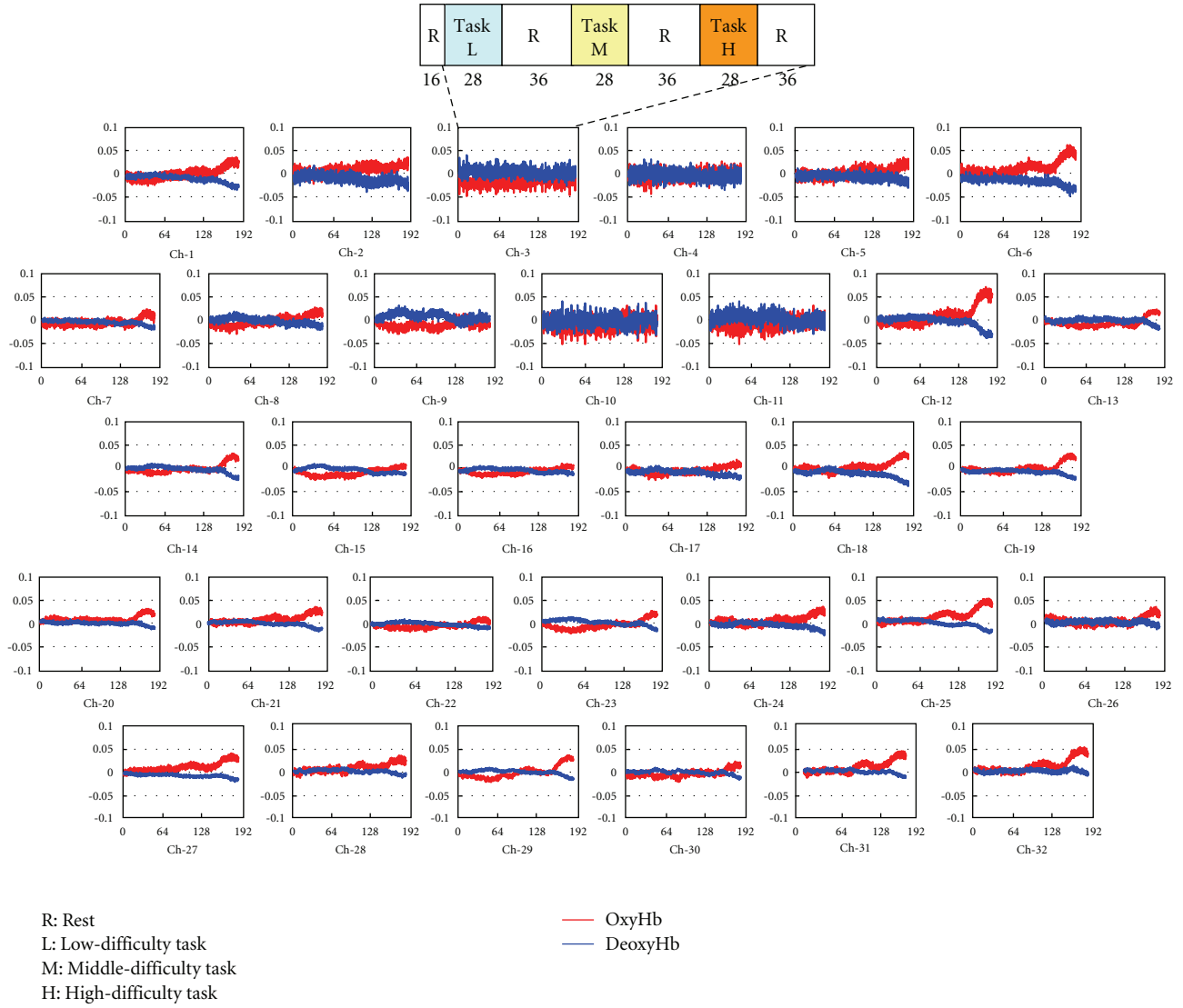

Figure 8: Hemoglobin concentration changes in frontal.

however, comparisons of measurements between subjects or statistical processing of measurements of all subjects cannot be implemented using this signal as it is. Therefore, we propose a method for converting data of oxygenated hemoglobin and deoxygenated hemoglobin reconstructed by MRA into Z-scores using the following expression, so that the mean value is 0 and standard deviation is 1:

$$Z = \frac{X - \mu}{\sigma}. \tag{11}$$

Here, X is the signal of oxygenated hemoglobin or deoxygenated hemoglobin reconstructed using MRA; μ is their mean value; σ is the standard deviation.

Figure 12 shows the averaged fNIRS signals using Z-score for nine subjects. It should be noted that the difference of the workload level is reflected on the gradient of oxygenated hemoglobin concentration. Figure 13 shows the results of group analysis for nine subjects. The rectangular in fMRI image indicates the region of measurement with fNIRS. The fNIRS images agree to that of fMRI in different workload levels. This results support the effectiveness of the proposed method.

4.5. Subjective and Objective Evaluation of Workload. In this experiment, the workload of each subject was measured using the Japanese version of NASA-TLX to evaluate the correlations between the workload of mental calculation tasks and the objective evaluation with fNIRS. NASA-TLX is composed of six measures: mental requirements, physical requirements, temporal demand, work performance, effort, and frustration. Before workload evaluation, the subject performed one-to-one comparisons of the importance of elements of the workload involved in task performance.

The weight of each measure was based on the number of times an element was selected as more important during

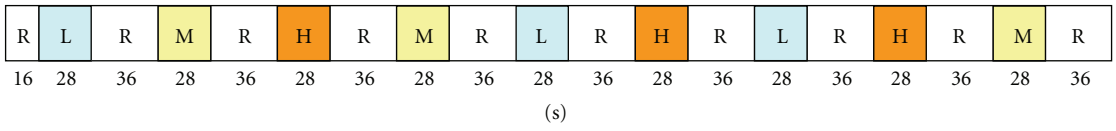

R : Rest
L: Low-difficulty task
M: Middle-difficulty task
H: High-difficulty task

(a)

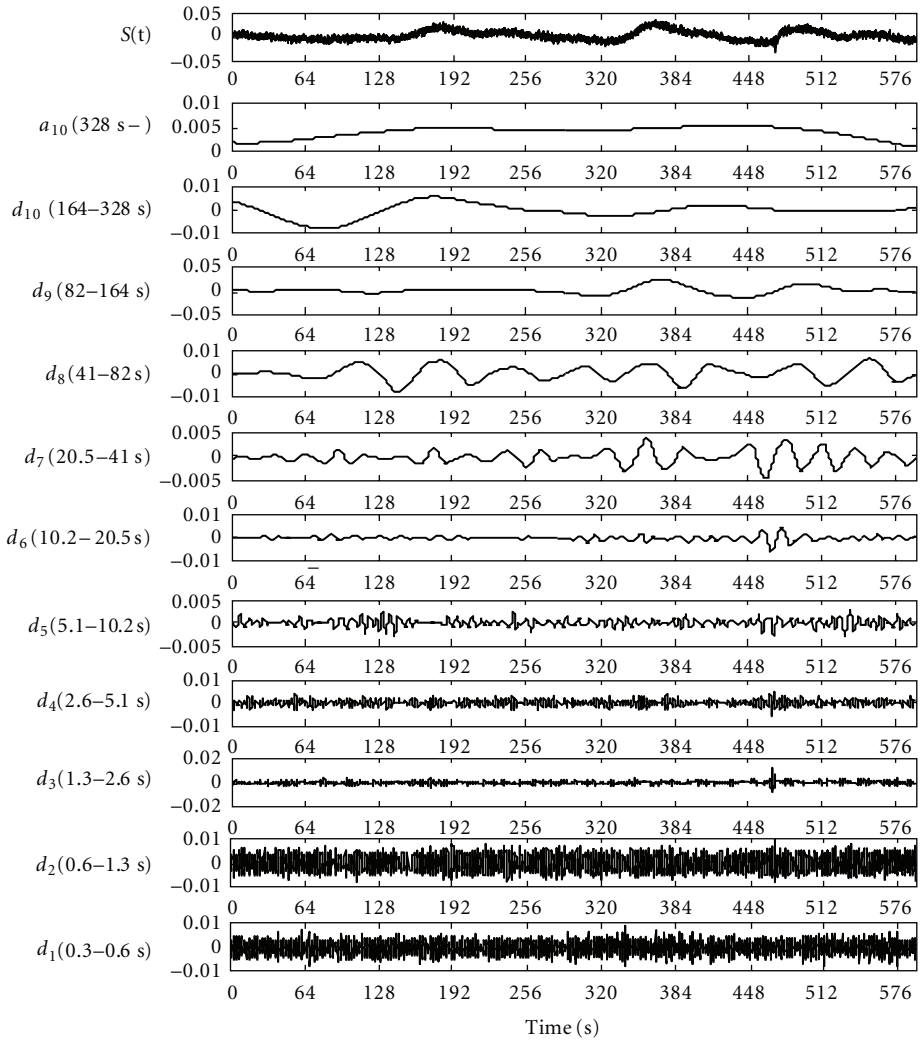

(b)

Figure 9: Decomposition of fNIRS signal using MRA (channel number 26).

15 one-to-one comparisons. When evaluating the workload of each task, the subject placed a mark at the appropriate position on the segment drawn between both extremes for each of the six measures.

A Weighted Workload (WWL) score was obtained by reading the position of each evaluation mark on a scale of 0 to 100 and multiplying it by the weight for each measure determined by one-to-one comparison, and then averaging all the products.

Figure 14 presents the WWL score of Subject A as determined by NASA-TLX. The workload became higher when the task level was higher.

Figure 15 shows the results of 9 subject evaluated using the maximum gradient of oxygenated hemoglobin in the task with different workload level. Multivariate test using Ryan method is used. Significant difference between high-level task and low-level task or between high-level task and medium-level task can be observed ($P < .05$). It exhibited

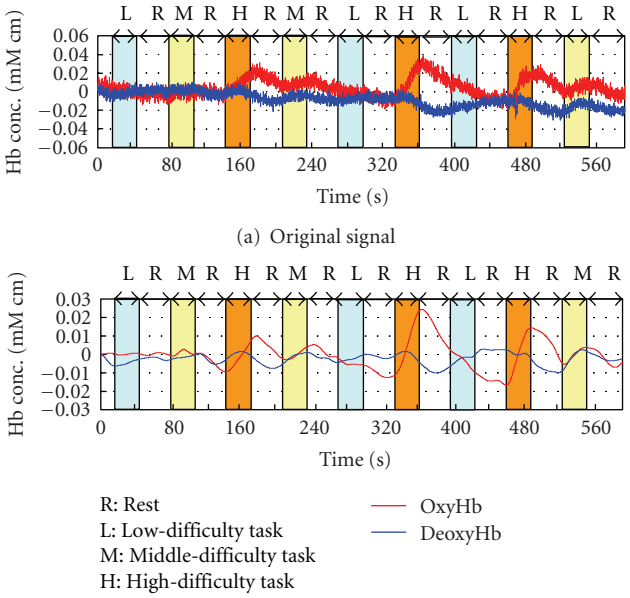

(a) Original signal

(b) Reconstructed fNIRS signal

Figure 10: Comparison of original signal and task-related signal (channel number 26).

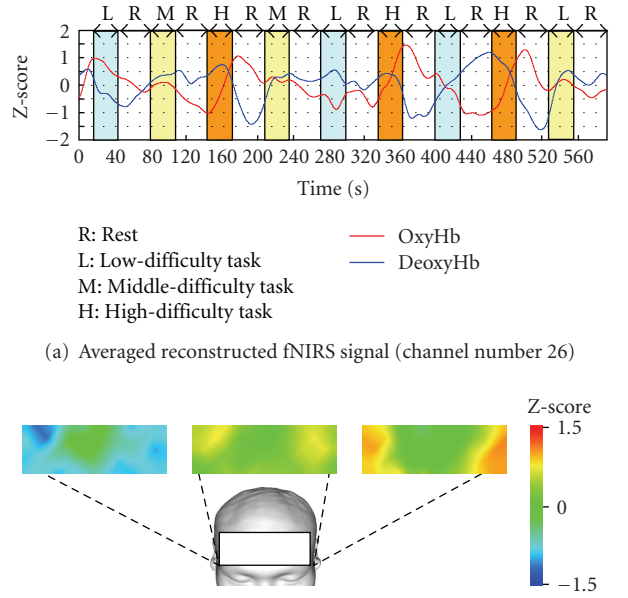

(a) Averaged reconstructed fNIRS signal (channel number 26)

(b) Brain activity imaged by averaged fNIRS signals

Figure 12: Results of group analysis of fNIRS signals for nine subjects.

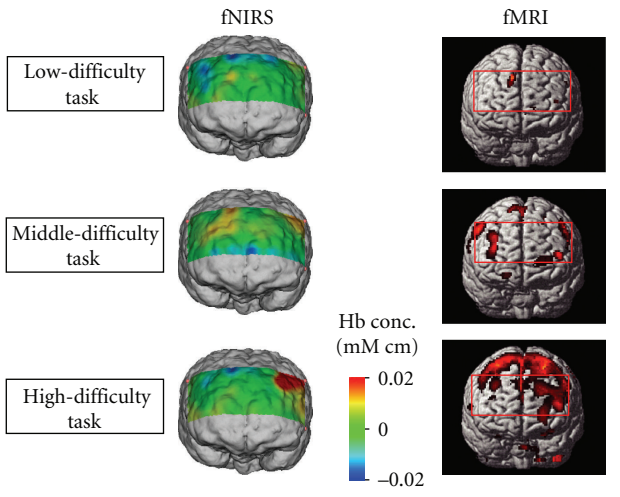

Figure 11: Functional brain imaging by fMRI and fNIRS.

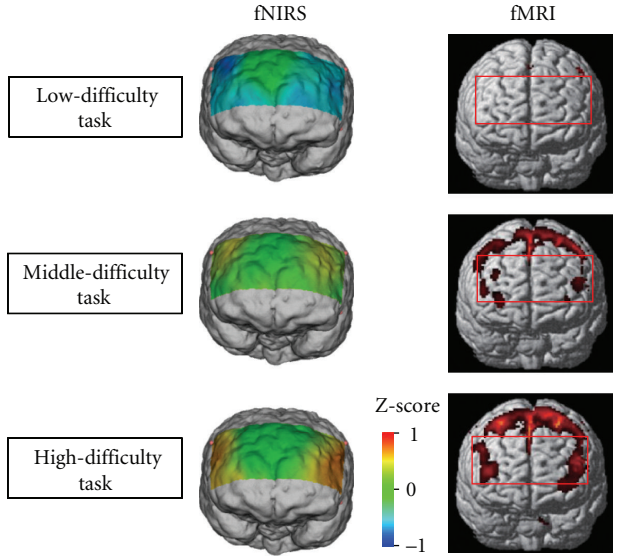

Figure 13: Functional brain imaging by fMRI and fNIRS (Group analysis for nine subjects).

good correlation with subjective evaluation with NASA-TLX. This result confirmed the feasibility of evaluating workload using the signal of cerebral blood flow obtained from fNIRS.

5. Measurement of Brain Functions of Car Driver

Drivers of motor vehicles obtain visual information on the surrounding environment, recognize and judge that information suitably, and then control their vehicle through steering wheel, accelerator, and brake pedal operations. Human brain activity functions to control all of these processes. In situations where it is necessary to predict unexpected danger, it is thought that a driver's brain activity strengthens the cognition function by spontaneously raising the level of attention. In the course of developing driver support systems, it is important to have a clear understanding of human brain activity in such driving situations.

5.1. Contents of the Task. To verify that the driving workload reduction of Adaptive Cruise Control (ACC) could be evaluated from brain activity, we conducted an experiment that involved the use of a driving simulator to follow a vehicle (Figure 16).

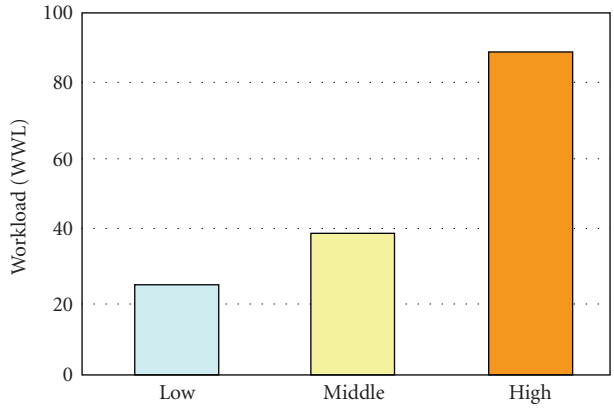

Figure 14: Workload evaluation by NASA-TLX.

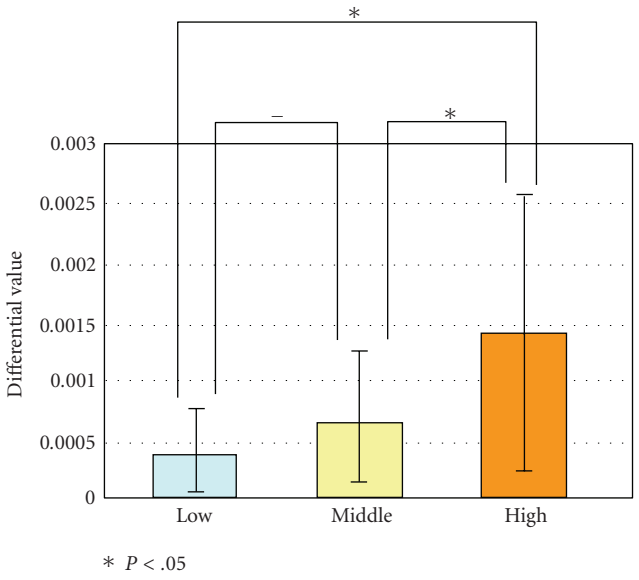

Figure 15: Maximum gradient of fNIRS signal during the task.

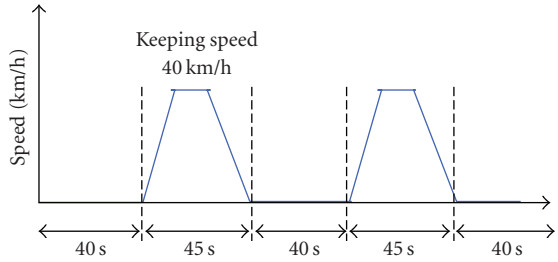

Figure 16: Speed pattern of leading car.

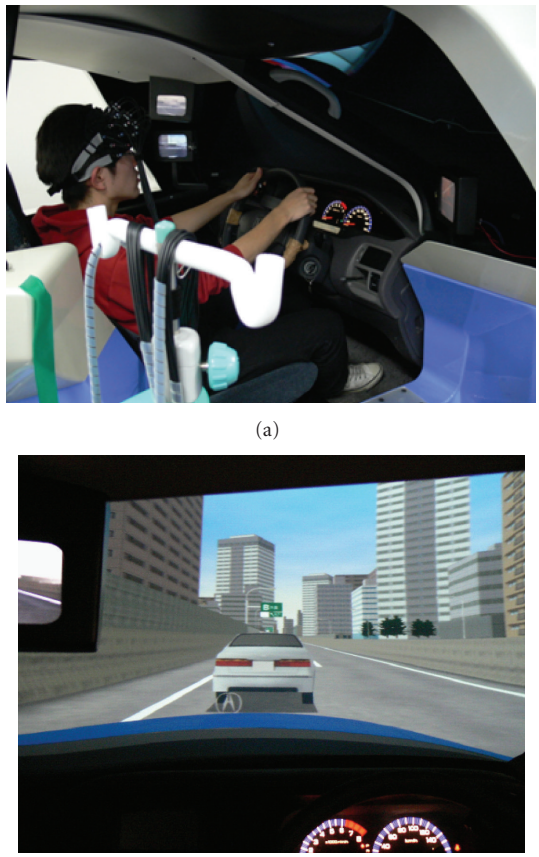

Figure 17: Experiment with driving simulator (driver follows the proceeding vehicle with and without ACC).

Main specification of the driving simulator is as follows: Dimension: 2440 mm (W)∗ 2280 mm (H)∗1850 mm (D), front view: wide filed (138 degrees) screen projection, DLP projector with total pixel count of 780000 (XGA), rear view: 3 mirror independent LCD display 640∗480 pixel (VGA), computer graphics: redraw speed: 30 to 60 flame/s, and simulation system: 6 axis motion base system using 6 electric screw cylinders.

Driving tests were conducted under two conditions: one involved following a vehicle by utilizing ACC, and the other involved following a vehicle while driving without ACC. The subject performed practice runs to become somewhat skillful in handling the driving simulator and then drove two times under each condition. Brain activity during one condition was compared with that during the other condition.

5.2. Measurement Method. Brain activity in the frontal lobe was measured using fNIRS. Figure 17 depicts a scene of the experiment. The measuring instrument was a near-infrared imaging device, OMM-300, Shimadzu Corporation, Japan. Figure 18 illustrates the arrangement of optical-fiber units (3 × 9 matrix, 42 channels). The numbers between the light-emitting fiber unit and the light-receiving fiber unit denote the measurement channels; measurements were performed through a total 42 channels. Furthermore, driving performance was also recorded on the driving simulator while measuring brain activity. The four male subjects, who were in their 20 s in healthy condition and who had ordinary driving licenses, participated.

5.3. Decomposition and Reconstruction of fNIRS Signals. The fNIRS signals include signals that are not related to

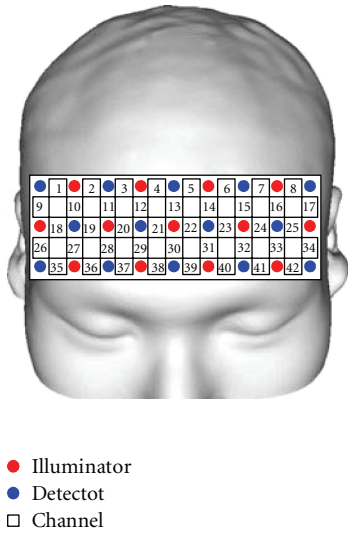

Figure 18: Position of optical fibers and channels (driving task: 3×9 matrix, 42 channels).

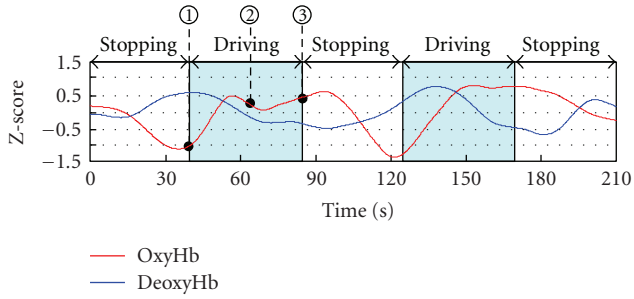

(a) Averaged reconstructed fNIRS signal (channel number 26)

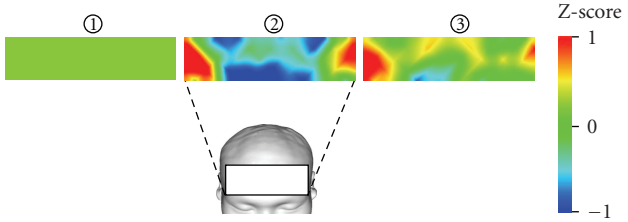

(b) Functional brain imaging

Figure 19: Result of group analysis for four drivers without ACC system.

brain activity (e.g., noise of the measurement instrument, influences of breathing, and changes in blood pressure). It was necessary to remove these unrelated signals to evaluate brain activity in detail. Therefore, the measured fNIRS signals were decomposed through MRA using discrete wavelet transform, and the components related to the driving task were reconstructed. Then, group analysis using Z-score was conducted for all subjects.

5.4. Results. Figures 19 and 20 depict the relationships between brain activity when the subject followed the forerunning vehicle manually without using ACC and that when

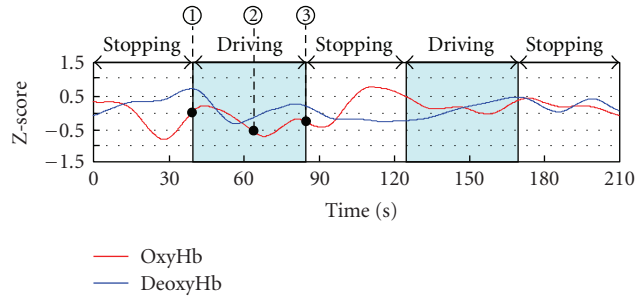

(a) Averaged reconstructed fNIRS signal (channel number 26)

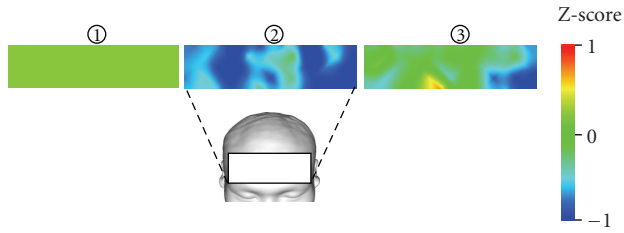

(b) Functional brain imaging

Figure 20: Result of group analysis for four drivers with ACC system.

the subject used ACC (26 channels at the outer right portion of the frontal lobe) and vehicle speed.

Figure 19 presents the result of group analysis for four drivers without ACC, and Figure 20 presents the result with ACC. Figure 19(a) confirms that oxygenated hemoglobin increased when the subject drove without ACC and exhibited a high value in the latter half of the task. The brain function imaged in Figure 19(b) confirms that, as common brain activity, both outer portions of the frontal lobe became active during the driving task.

Figure 20(a) indicates that oxygenated hemoglobin did not increase while driving with the use of ACC. Also, the brain function image in Figure 20(b) reveals that the frontal lobe was less active than when the subject drove without ACC. This result may reflect the reduction of driving workload by ACC.

6. Conclusions

Signal processing method to extract the task-related components with multiresolution analysis (MRA) based on discrete wavelet transform is proposed for fNIRS. Then the integration of data of multiple subjects using Z-scores is developed for statistical group analysis.

The brain activity of the subject who was given workload by different levels of mental calculation tasks was measured with fNIRS and fMRI. The fNIRS images constructed with the proposed method agree to fMRI images in different workload levels. Those results show that the proposed method is effective for evaluation brain activity measured by fNIRS.

The changes in brain activity in connection with workload were compared with the subjective evaluation of workload by NASA-TLX. Good correlation was observed between

the brain activity detected by fNIRS and the workload scores obtained from NASA-TLX. This result indicates that it is possible to evaluate workload from the cerebral blood flow signals obtained from fNIRS.

Whether the reduction of driving workload by ACC can be evaluated from brain activity was evaluated through experiments using a driving simulator. The results revealed that while the outer portions of the frontal lobe were active in connection with driving performance when the subject drove without ACC, it indicated no activity related to driving performance with the use of ACC. These results suggest the possibility of evaluating driving assistance systems through evaluation of the driving workload from measurement of brain activity using fNIRS.

Neuroimaging studies of car drivers using fNIRS should be conducted with increased number of subjects. We cannot conclude that lowering brain activity by reducing driving workload leads to safe driving; thus, in the future, we will design and evaluate driving assistance systems that require an appropriate level of brain activity.

Acknowledgment

This work was supported by the Nihon University Multidisciplinary Research Grant for 2006 and 2007.

References

[1] Y. Uchiyama, K. Ebe, A. Kozato, T. Okada, and N. Sadato, "The neural substrates of driving at a safe distance: a functional MRI study," *Neuroscience Letters*, vol. 352, no. 3, pp. 199–202, 2003.

[2] H. J. Spiers and E. A. Maguire, "Neural substrates of driving behaviour," *NeuroImage*, vol. 36, no. 1, pp. 245–255, 2007.

[3] Y. Hoshi, N. Kobayashi, and M. Tamura, "Interpretation of near-infrared spectroscopy signals: a study with a newly developed perfused rat brain model," *Journal of Applied Physiology*, vol. 90, no. 5, pp. 1657–1662, 2001.

[4] M. Tamura, "Functional near-infrared spectoroscopy," *Advances in Neurological Science; Series C*, vol. 47, no. 6, pp. 891–901, 2003.

[5] T. Kojima, H. Tsunashima, T. Shiozawa, H. Takada, and T. Sakai, "Measurement of train driver's brain activity by functional near-infrared spectroscopy (fNIRS)," *Optical and Quantum Electronics*, vol. 37, no. 13–15, pp. 1319–1338, 2005.

[6] T. Kojima, H. Tsunashima, and T. Y. Shiozawa, "Measurement of train driver's brain activity by functional near-infrared spectroscopy (fNIRS)," in *Computers in Railways X*, WIT Press, Southampton, UK, 2006.

[7] T. Shimizu, S. Hirose, H. Obara, et al., "Measurement of frontal cortex brain activity attributable to the driving workload and increased attention," SAE paper 2009-01-0545, SAE International, Warrendale, Pa, USA, April 2009.

[8] K. Takahashi, N. Kobayashi, N. Watanabe, and T. Harada, "Preliminary experiment of the evaluation of a VR based training system using brain activity," in *Proceedings of the 11th Annual Conference of Virtual Reality Society of Japan*, vol. 11, pp. 354–355, Sendai, Japan, September 2006.

[9] S. Mallat, *A Wavelet Tour of Signal Processing*, Academic Press, London, UK, 1998.

[10] S. G. Mallat, "A theory for multiresolution signal decomposition: the wavelet representation," *IEEE Transactions on Pattern Analysis and Machine Intelligence*, vol. 11, no. 7, pp. 674–693, 1989.

[11] F. F. Jöbsis, "Noninvasive, infrared monitoring of cerebral and myocardial oxygen sufficiency and circulatory parameters," *Science*, vol. 198, no. 4323, pp. 1264–1267, 1977.

[12] S. Kohno, A. Ishikawa, S. Tsuneishi, T. Amita, K. Shimizu, and Y. Mukuta, "Application development of functional near-infrared imaging system," *Shimadzu Review*, vol. 63, no. 3-4, pp. 195–200, 2006.

[13] S. A. Huettel, A. W. Song, and G. McCarthy, *Functional Magnetic Resonance Imaging*, Sinauer Associates, Sunderland, Mass, USA, 2004.

[14] I. Daubechies, *Ten Lectures on Wavelets*, CBMS-NSF Regional Conference Series in Applied Mathematics no. 61, SIAM, Philadelphia, Pa, USA, 1992.

Hindawi Publishing Corporation
Computational Intelligence and Neuroscience
Volume 2009, Article ID 652078, 7 pages
doi:10.1155/2009/652078

Research Article

The Track of Brain Activity during the Observation of TV Commercials with the High-Resolution EEG Technology

Laura Astolfi,[1,2] Giovanni Vecchiato,[3] Fabrizio De Vico Fallani,[1,3] Serenella Salinari,[2] Febo Cincotti,[1] Fabio Aloise,[1] Donatella Mattia,[1] Maria Grazia Marciani,[2] Luigi Bianchi,[4] Ramon Soranzo,[3] and Fabio Babiloni[1,3]

[1] *IRCCS, Fondazione Santa Lucia, 00179 Rome, Italy*
[2] *Dipartimento di Informatica e Sistemistica, Università di Roma "La Sapienza", 00185 Rome, Italy*
[3] *Department of Physiology and Pharmacology, University of Rome "La Sapienza", 00185 Rome, Italy*
[4] *Department of Neuroscience, University of Rome "Tor Vergata", 00100 Rome, Italy*

Correspondence should be addressed to Laura Astolfi, laura.astolfi@uniroma1.it

Received 15 December 2008; Accepted 8 April 2009

Recommended by Andrzej Cichocki

We estimate cortical activity in normal subjects during the observation of TV commercials inserted within a movie by using high-resolution EEG techniques. The brain activity was evaluated in both time and frequency domains by solving the associate inverse problem of EEG with the use of realistic head models. In particular, we recover statistically significant information about cortical areas engaged by particular scenes inserted within the TV commercial proposed with respect to the brain activity estimated while watching a documentary. Results obtained in the population investigated suggest that the statistically significant brain activity during the observation of the TV commercial was mainly concentrated in frontoparietal cortical areas, roughly coincident with the Brodmann areas 8, 9, and 7, in the analyzed population.

1. Introduction

In the recent years, researchers have begun to use neuroimaging tools to examine human behaviour in economic games and decision making between different commercial advertisements. This field is known as Neuromarketing. Principal issue of this branch is to understand mechanisms underlying customer's engagement with brand or company advertised [1–3]. In particular, the question is to explain how the exposure of a message, made up of images, text, and audio, is able to trigger in the consumer mind persisting stimuli leading to an interest, preference, purchase, and repurchase of a given product. In the same way they try to explain how video's emotional contents work after observing a humanitarian TV spot. Since marketers need to be reassured that a new advertising campaign will work before airing it, they trust an advertising test made on small groups of people which allows them to decide whether promoting the campaign or not. This test consists in an interview asking about the likeability, emotional involvement, persuasion, and intention to purchase.

In the last decades, several authors have investigated the capability of subjects to memorize and retrieve sensible "commercial" information observed during a TV spot [4–9]. The most used neuroimaging tool to track the brain response to the commercial advertisements is the functional Magnetic Resonance Imaging (fMRI) technique, able to return the profile of brain areas that elicited increased blood flow during the task when compared to a resting state. However, there are precise limitations in the actual state of the art of this technique. Essentially, the main limitation is linked to the insufficient temporal resolution of fMRI. In fact, temporal resolution of hundred of milliseconds or less is necessary to track the shifts of brain activity closely related to the processing of visual and acoustic stimuli provided by the fast moving of visual commercial spots.

For this reason other authors also adopt different tools such as magnetoencephalography (MEG). This technique is

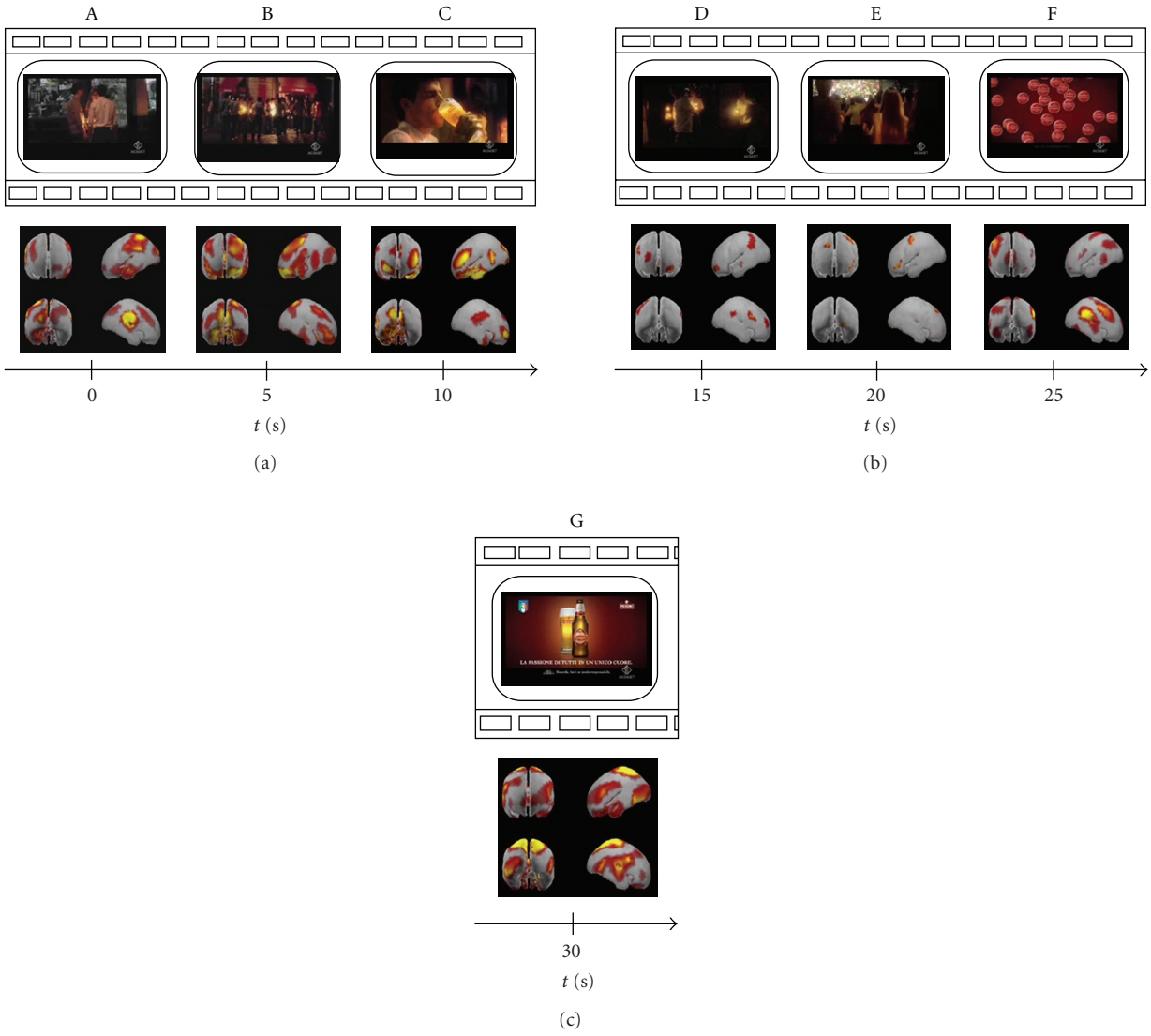

Figure 1: Tracking of the mean cortical activity of the group of "drinkers" in the theta frequency band spot. The statistical significant activity in this population is shown in seven panels (A–G), each representing subsequent film segments of a TV spot with corresponding brain activity. Temporal axes beat the spot time every 5 seconds: in this way panel A represents the first frame of the commercial while panel G shows the last one. This example illustrates how it is possible to track human cortical activity by means of the highresolution EEG technique.

sensitive to changes of magnetic fields that are induced by the electrical brain activity, and it is able to detect rapid changes of the neural activity on a temporal scale of milliseconds and on a spatial scale of centimetres.

It is worth noticing that the past several studies also used electroencephalography (EEG) as brain imaging tool for the analysis of brain activity during the observation of TV commercials. However, at that time, EEG limitations in spatial resolution due to an insufficient number of electrodes used as well as to the limited processing capabilities were responsible for a series of inconclusive and fragmented observations of these phenomena. Nowadays, high-resolution EEG technology has been developed to enhance the poor spatial information content of the EEG activity in order to detect the brain activity with a spatial resolution of a squared centimetre and the unsurpassed time resolution of milliseconds [10–14].

The purpose of this paper is to illustrate the potential of the high-resolution EEG techniques when applied to the analysis of brain activity related to the observation of TV commercials. In particular, we would like to describe how by using appropriate statistical analysis it could be possible to recover significant information about cortical areas engaged by particular scenes inserted within the TV commercial analyzed.

In order to do that, we recorded a series of normal subjects with high resolution EEG techniques during the observation of a documentary in which an interruption was generated. The subjects were not aware of the aim of the study. The brain activity was evaluated in both time and

frequency domains by solving the associate inverse problem of EEG with the use of realistic head models.

Cortical activity estimated during the observation of the TV commercial was then compared with the brain activity computed in the analyzed population during the observation of the documentary.

2. Materials and Methods

2.1. Experimental Design. The whole dataset is composed by EEG registrations of 13 healthy subjects (mean age 30 ± 4 years) watching a documentary of 30 minutes intermingled by a TV commercial (see [15]). Each subject is exposed to the observation of a same documentary. The subjects were not aware of the aim of the recording, and they only knew to pay attention to the material showed on the screen during the entire 30 minutes. The TV commercial, whose length was 30 seconds, was inserted at the middle of the documentary. Such commercial was realized for a popular brand of beer in Italy, that was on-air on the national TV channels on the days in which the experiment was realized. After the EEG registration each subject was recalled in laboratory, where an interview was performed. In such interview, the subjects were asked if they usually drink beer or light alcohol at least once per week. If yes, subjects were considered within the dataset of "drinkers" in opposition to the dataset of "no drinkers." In order to increase the sensitivity of the analysis performed, only the EEG spectral analysis for the "drinkers" was analyzed and presented here.

The hypothesis was that the TV commercial could be better followed by a class of subjects who usually drink beer instead that from other "nondrinkers" subjects.

2.2. High-Resolution EEG: Recordings and Processing Techniques. High-resolution EEG technologies have been developed to enhance the poor spatial information content of the EEG activity [10, 16, 17]. Basically, these techniques involve the use of a large number (64–256) of scalp electrodes. In addition, high-resolution EEG techniques rely on realistic MRI-constructed head models [18, 19] and spatial deconvolution estimations, which are usually computed by solving a linear-inverse problem based on Boundary-Element Mathematics [13, 20]. Subjects were comfortably seated on a reclining chair, in an electrically shielded, dimly lit room. A 64-channel EEG system (BrainAmp, Brainproducts GmbH, Germany) was used to record electrical potentials by means of an electrode cap, accordingly to an extension of the 10–20 international system. In the present paper, the cortical activity was estimated from scalp EEG recordings by using realistic head models whose cortical surface consisted of about 5000 triangles uniformly disposed. The current density estimation of each one of the triangle, which represents the electrical dipole of the underlying neuronal population, was computed by solving the linear-inverse problem according to the techniques described in the previous papers [14, 15, 21].

Thus, a time-varying waveform relative to the estimated current density activity at each single triangle of the modeled cortical surface was obtained. Such waveform was then subjected to the time-varying spectral analysis by computing the spectral power in the different frequency bands usually employed in EEG analysis, that is, theta (4–7 Hz), alpha (8–12 Hz), beta (13–24 Hz), and gamma (24–45 Hz).

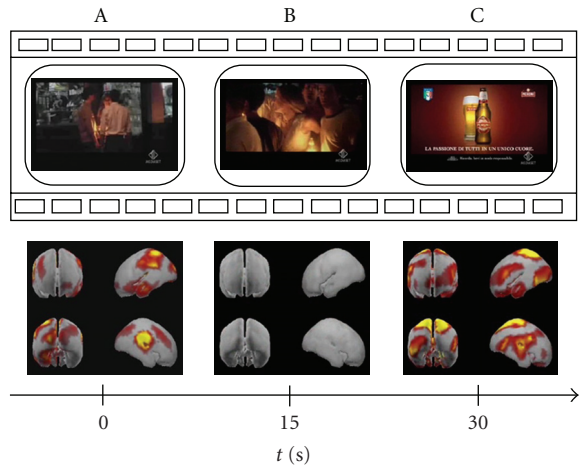

Figure 2: Tracking of the mean cortical activity of the group of "drinkers" in the theta frequency band spot. The statistical significant activity in this population is shown in 3 panels (A–C), each representing subsequent film segments of a TV spot with corresponding brain activity. Temporal axes beat the spot in correspondence of the beginning (A), the middle (B), and the end (C) of the entire film sequence.

Although we estimated brain activity in all the described frequency bands, in the following we presented those related to theta and alpha frequency bands. In fact, in the EEG literature, these frequency bands have been suggested to be maximally responsive during the observation and the memorization tasks when compared to the beta and gamma bands [22].

In each subject recorded, the statistical significance of the spectral values during the observation of the TV commercials was then measured against the activity evaluated during the observation of the documentary for the same subject. This was obtained by computing a time-varying z-score variable for each subject and for each dipole placed on the cortical mantle in the analyzed frequency band. The mean and the standard deviation for such z-score variable was estimated in the documentary period, while the time-varying values of the spectral power in the theta band during the observation of the TV commercial for each dipole were employed.

In order to present these results relative to the experimental conditions for the entire population, we needed a common cortical representation to map the different activated areas of each subject. For this purpose we used the average brain model available from the McGill University website. In this way we were able to display the cortical areas that are statistically significant activated during different experimental conditions in all subjects analyzed. In fact, we highlighted in yellow a voxel of the average brain model if it was a cortical site in which a statistical significant variation of the spectral power between the experimental conditions was found in all the subjects; if such brain voxel was statistically significant in all but one of the subjects analyzed, we depicted

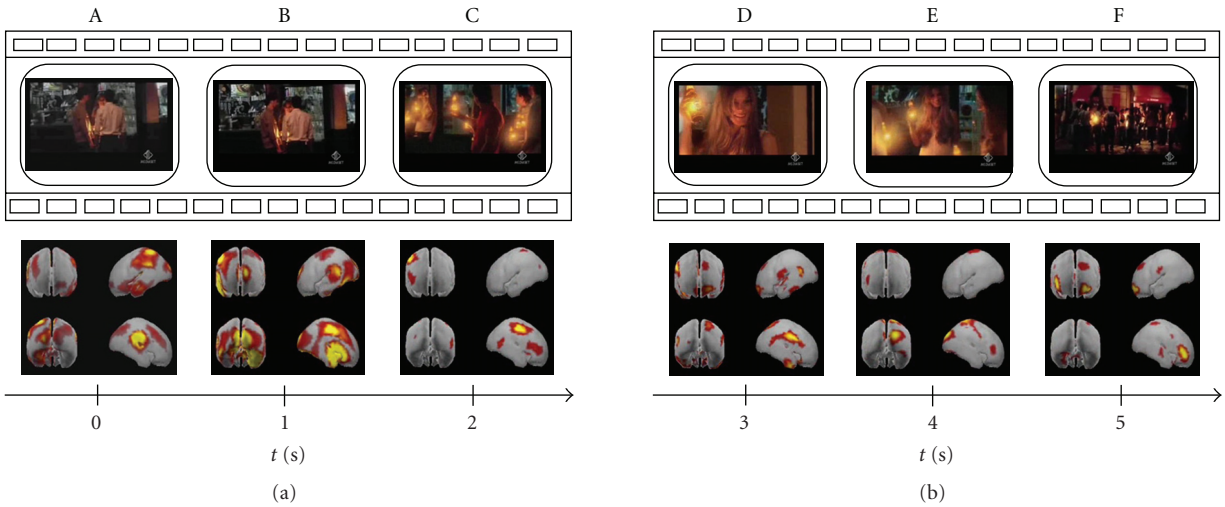

Figure 3: Tracking of the mean cortical activity in the theta frequency band of the first 5 seconds of the commercial spot. The statistical significant activity in this population is shown in six panels (A–F), each representing subsequent film segments of a TV spot with corresponding brain activity. Temporal axes beat the spot time every second: in this way panel A represents the first frame of the commercial while panel F shows the film segment shown after 5 seconds from the beginning.

it in red. In all the other cases the voxel was represented with a gray colour.

By construction, the analyzed maps are then relative to the evolution of the time-cortical activity of the spectral power in the theta band. However, only the statistical significant variation of such spectral power when compared to the documentary period was highlighted in colour. The use of z-score will allow us to have a variable that can be averaged and can be used to synthesize the results of the entire population investigated.

3. Results

Of the 13 subjects recorded, only seven are "drinkers." Hence, the successive analysis and results are presented for seven of such subjects.

We summarized all results for the "drinkers" group in a series of figures showing the statistically significant differences of cortical activation concerning this dataset in the theta frequency band (4–7 Hz). Data regarding the alpha frequency band (8–12 Hz) were equivalent to the theta band and for this reason not shown here. Our figures are formed by a series of subsequent panels each containing two images: the upper one represents a frame of the TV commercial while the lower one displays the corresponding mean brain activity. In particular, the image at the bottom of the panel shows four different views of the average brain model organized in two rows: the upper row comprises the front and left perspective while the lower one the rear and right brain perspective. The temporal axes beat the time of the commercial.

In Figure 1 we present a first series of 7 film segments spanning the whole length of a certain TV spot. Frames are taken each 5 seconds from the beginning of the clip. In such a way panel A represents the first frame of the commercial while panel G shows the last one. By examining this strip it results evident how the temporal evolution of the mean cortical activity changes according to the images viewed by the subjects. In particular, an enhancement of cerebral activity is suggested by the result of the application of the statistic tests at the beginning and at the end of the videoclip presented. In fact, from the lower row of the figures, it is possible to observe how in the middle film segments very restricted areas provide statistically significant differences when compared to the ones watched at the beginning and at the end of the commercial. This drastic change of activity is more evident in Figure 2. The present figure is composed by 3 panels representing the first (panel A), the middle (B), and the last (C) frame of the TV spot, respectively. The corresponding mean cortical activity completes each panel of the figure. By observing these three images it is clear how the middle part of the commercial is characterized by cerebral zones displaying no statistical differences across ROIs, while there are two peaks of activity at the beginning and at the end of the clip.

The analysis of the temporal evolution of the brain activity has been performed even on shorter intervals in order to track its variations in closer time instants. Subsequent Figures 3, 4, and 5 follow the cerebral activity with a higher temporal resolution. Time intervals spanned in the following figures correspond to the first 5 seconds (Figure 3), middle 5 seconds (Figure 4), and last 5 seconds of the commercial (Figure 5), respectively. These examples show how it is possible to catch statistically significant differences in the activation of cortical areas even reducing the time interval of interest.

4. Discussion

Thanks to the high resolution EEG techniques we tracked subjects' brain activity during visualization of the commercials: in such manner it is possible to obtain a global measure

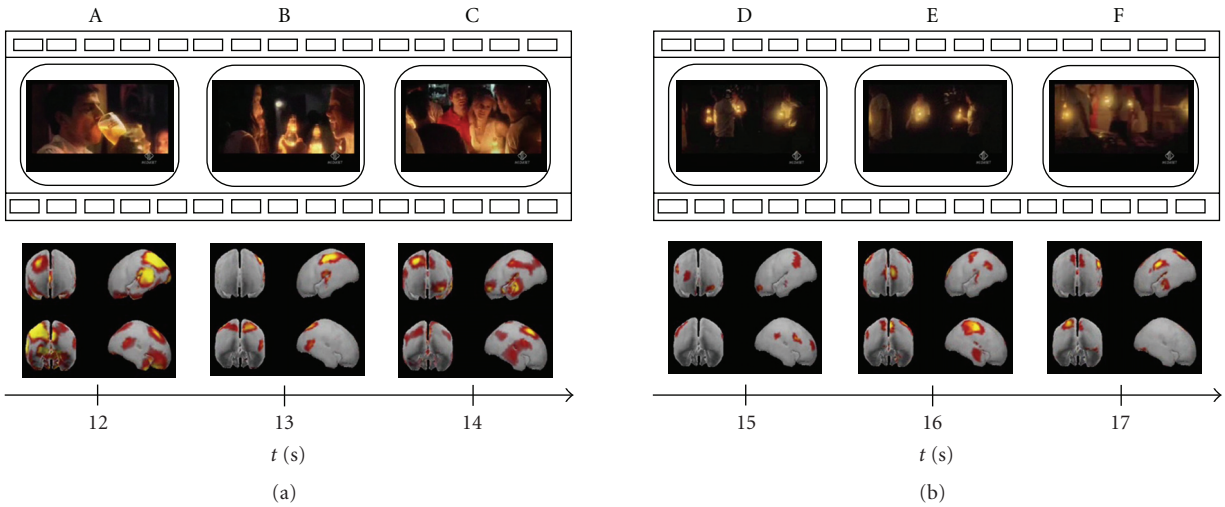

Figure 4: Tracking of the mean cortical activity of seven drinkers in the theta frequency band of the central 5 seconds of the commercial spot. The statistical significant activity in this population is shown in six panels (A–F), each representing subsequent film segments of a TV spot with corresponding brain activity. Temporal axes beat the spot time every second: in this way panel A represents the film segment after 12 seconds from the beginning of the commercial; panel F shows the film segment after 17 seconds.

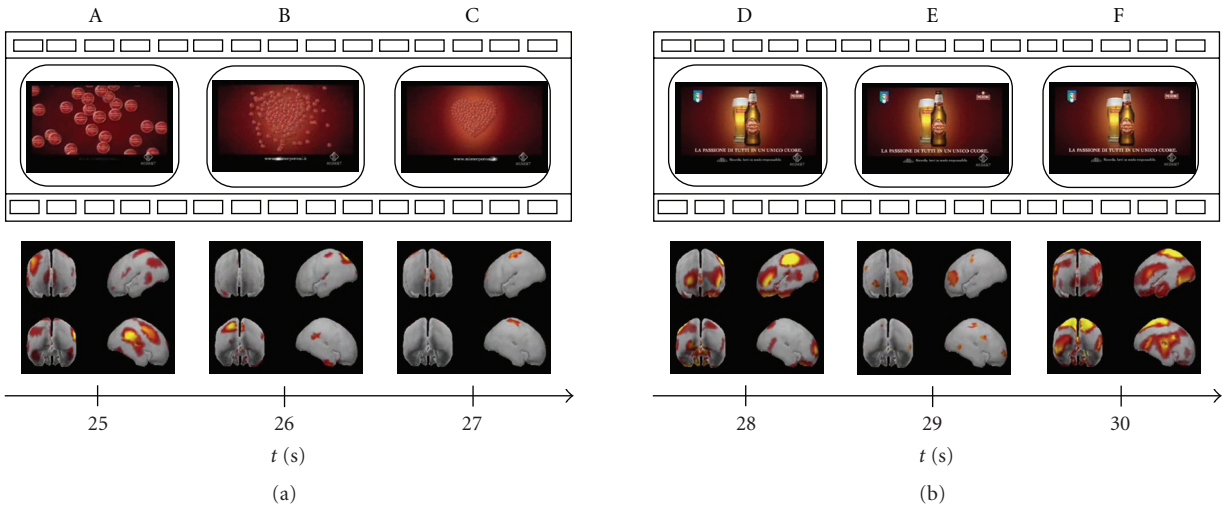

Figure 5: Tracking of the mean cortical activity of the last 5 seconds of the commercial spot. The statistical significant activity in this population is shown in six panels (A–F), each representing subsequent film segments of a TV spot with corresponding brain activity. Temporal axes beat the spot time every second: in this way panel F represents the last film segment of the commercial; panel A shows the film segment after 25 seconds from the beginning.

of the reconstructed cortical signals by means of a simple graphic tool which allows us to distinguish the activity of different cortical areas. The above-mentioned results allow us to comment temporal and spatial events observed.

In fact, the observed phenomena suggest an active role of the prefrontal and parietal areas in the coding of the information possibly retained by the users from the TV commercials. A statistical increase of EEG spectral power in the prefrontal (namely, BA 8, 9) and parietal areas is in agreement with the suggested role of these regions during the transfer of sensory percepts from short-term memory to long-term memory storage. The results suggest a strong prevalence of a 'common' prefrontal bilateral (involving BA 8 and 9) activity in all the subjects analyzed during the observation of the TV commercials. In addition a stronger engagement of the left frontal areas has been noted, in agreement with the HERA model [23] in which such hemisphere plays a decisive role during the encoding phase of information from the short-term memory to the long-term memory, whereas the right hemisphere plays a role in the retrieval of such information. It must be noted, however, that the role of the right cortices in storing images has been also recognized for many years in neuroscience [2, 24].

As presented in the previous works performed both with EEG analysis and MEG recordings [5, 15], the observed phenomena suggest an active role of the prefrontal and

parietal areas in coding of the information that will be retained by users from the TV commercials. In particular, activations of these cortical areas can be associated with attentional and memorization processes. As shown in the previous figures, peaks of activity emerge at the beginning and at the end of clip (Figures 1, 2). In these periods subjects' attention is more focused on what he/she sees, in particular when they watch scenes showing meeting moments (such as panels A, B in Figure 3) and the advertised product (panels D and F of Figure 5). Instead, in the middle of the TV clip, we observed a peak of activity only when subjects watch a person utilizing the advertised product (such as a beer in panel A of Figure 4). These processes could reflect memorization of significant frames' sequence which would help the subject to understand the whole video clip and messages provided. Climax of this elaboration will be achieved in the last film segments of the sequence when the meaning of the commercial will be completely understood (last panel of Figure 5).

The present paper intends to stress the useful properties of the high-resolution EEG technologies. In particular this tool is able to help us in observing and analysing the temporal trend of the cortical activities thanks to a high temporal and spatial resolution. These features allow us to distinguish a certain precision changes of activation of ROIs corresponding to different cortical areas, by means of a graphical representation on an average brain model. Our analysis focused the attention on tracking human brain activity with different time resolution, all offering the same spatial resolution able to discriminate activation's intensity of Brodmann areas.

The reconstruction of the cortical activity by means of the high resolution EEG technique [25–30] and by combining the above statistic treatment of our data allowed us to track subjects' brain activity during visualization of the commercials. In such a way for each film segment of a clip it was possible to distinguish cortical areas that were significantly activated when compared to the observation of the documentary. This could be useful in the evaluation of the cortical responses to particularly type of visual solicitations, performed by film or commercial clips, that at the moment is a largely unexplored field by neuroscience.

Acknowledgment

This work was supported by the COST Action BM0601 "NeuroMath." Neither the COST Office nor any person acting on its behalf is responsible for the use which might be made of the information contained in this publication. The COST Office is not responsible for the external websites referred to in this paper.

References

[1] T. Ambler, S. Braeutigam, J. Stins, S. P. R. Rose, and S. Swithenby, "Salience and choice: neural correlates of shopping decisions," *Psychology and Marking*, vol. 21, no. 4, pp. 247–261, 2004.

[2] S. Braeutigam, S. P. R. Rose, S. J. Swithenby, and T. Ambler, "The distributed neuronal systems supporting choice-making in real-life situations: differences between men and women when choosing groceries detected using magnetoencephalography," *European Journal of Neuroscience*, vol. 20, no. 1, pp. 293–302, 2004.

[3] J. Cappo, *The Future of Advertising: New Media, New Clients, New Consumers in the Post-Television Age*, McGraw-Hill, New York, NY, USA, 2005.

[4] H. E. Krugman, "Brain wave measures of media involvement," *Journal of Advertising Research*, vol. 11, no. 9, pp. 3–9, 1971.

[5] A. A. Ioannides, L. Liu, D. Theofilou, et al., "Real time processing of affective and cognitive stimuli in the human brain extracted from MEG signals," *Brain Topography*, vol. 13, no. 1, pp. 11–19, 2000.

[6] T. Ambler and T. Burne, "The impact of affect on memory of advertising," *Journal of Advertising Research*, vol. 39, no. 2, pp. 25–34, 1999.

[7] M. Rotschild and J. Hyun, "Predicting memory for components of TV commercials from EEC," *Journal of Consumer Research*, pp. 472–478, 1989.

[8] J. R. Rossiter and R. B. Silberstein, "Brain-imaging detection of visual scene encoding in long-term memory for TV commercials," *Journal of Advertising Research*, vol. 41, no. 2, pp. 13–21, 2001.

[9] C. Young, "Brain waves, picture sorts®, and branding moments," *Journal of Advertising Research*, vol. 42, no. 4, pp. 42–53, 2002.

[10] P. L. Nunez, *Neocortical Dynamics and Human EEG Rhythms*, Oxford University Press, New York, NY, USA, 1995.

[11] X. Bai, V. L. Towle, E. J. He, and B. He, "Evaluation of cortical current density imaging methods using intracranial electrocorticograms and functional MRI," *NeuroImage*, vol. 35, no. 2, pp. 598–608, 2007.

[12] B. He, Y. Wang, and D. Wu, "Estimating cortical potentials from scalp EEG's in a realistically shaped inhomogeneous head model by means of the boundary element method," *IEEE Transactions on Biomedical Engineering*, vol. 46, no. 10, pp. 1264–1268, 1999.

[13] A. M. Dale, A. K. Liu, B. R. Fischl, et al., "Dynamic statistical parametric mapping: combining fMRI and MEG for high-resolution imaging of cortical activity," *Neuron*, vol. 26, no. 1, pp. 55–67, 2000.

[14] F. Babiloni, F. Cincotti, C. Babiloni, et al., "Estimation of the cortical functional connectivity with the multimodal integration of high-resolution EEG and fMRI data by directed transfer function," *NeuroImage*, vol. 24, no. 1, pp. 118–131, 2005.

[15] L. Astolfi, F. De Vico Fallani, S. Salinari, et al., "Brain activity related to the memorization of TV commercials," *International Journal of Bioelectromegnetism*, vol. 10, no. 3, pp. 1–10, 2008.

[16] J. Le and A. Gevins, "Method to reduce blur distortion from EEG's using a realistic head model," *IEEE Transactions on Biomedical Engineering*, vol. 40, no. 6, pp. 517–528, 1993.

[17] A. Gevins, J. Le, N. K. Martin, P. Brickett, J. Desmond, and B. Reutter, "High resolution EEG: 124-channel recording, spatial deblurring and MRI integration methods," *Electroencephalography and Clinical Neurophysiology*, vol. 90, no. 5, pp. 337–358, 1994.

[18] F. Babiloni, C. Babiloni, L. Locche, F. Cincotti, P. M. Rossini, and F. Carducci, "High-resolution electro-encephalogram: source estimates of Laplacian-transformed somatosensory-evoked potentials using a realistic subject head model constructed from magnetic resonance images," *Medical and Biological Engineering and Computing*, vol. 38, no. 5, pp. 512–519, 2000.

[19] F. Babiloni, C. Babiloni, F. Carducci, et al., "High resolution EEG: a new model-dependent spatial deblurring method using a realistically-shaped MR-constructed subject's head model," *Electroencephalography and Clinical Neurophysiology*, vol. 102, no. 2, pp. 69–80, 1997.

[20] R. Grave de Peralta Menendez and S. L. Gonzalez Andino, "Distributed source models: standard solutions and new developments," in *Analysis of Neurophysiological Brain Functioning*, C. Uhl, Ed., pp. 176–201, Springer, New York, NY, USA, 1999.

[21] L. Astolfi, F. Cincotti, D. Mattia, et al., "Comparison of different cortical connectivity estimators for high-resolution EEG recordings," *Human Brain Mapping*, vol. 28, no. 2, pp. 143–157, 2007.

[22] W. Klimesch, M. Doppelmayr, and S. Hanslmayr, "Upper alpha ERD and absolute power: their meaning for memory performance," *Progress in Brain Research*, vol. 159, pp. 151–165, 2006.

[23] E. Tulving, S. Kapur, F. I. Craik, M. Moscovitch, and S. Houle, "Hemispheric encoding/retrieval asymmetry in episodic memory: positron emission tomography findings," *Proceedings of the National Academy of Sciences of the United States of America*, vol. 91, no. 6, pp. 2016–2020, 1994.

[24] S. Braeutigam, "Neuroeconomics—from neural systems to economic behaviour," *Brain Research Bulletin*, vol. 67, no. 5, pp. 355–360, 2005.

[25] C. Babiloni, F. Babiloni, F. Carducci, et al., "Mapping of early and late human somatosensory evoked brain potentials to phasic galvanic painful stimulation," *Human Brain Mapping*, vol. 12, no. 3, pp. 168–179, 2001.

[26] L. Astolfi, F. Cincotti, C. Babiloni, et al., "Assessing cortical functional connectivity by linear inverse estimation and directed transfer function: simulations and application to real data," *Clin Neurophysiol*, vol. 116, no. 4, pp. 32–920, 2005.

[27] A. Urbano, F. Babiloni, C. Babiloni, A. Ambrosini, P. Onorati, and P. M. Rossini, "Human short-latency cortical responses to somatosensory stimulation," *A High Resolution Study, NeuroReport*, vol. 8, no. 15, pp. 3239–3243, 1997.

[28] A. Urbano, C. Babiloni, F. Carducci, L. Fattorini, P. Onorati, and F. Babiloni, "Dynamic functional coupling of high resolution EEG potentials related to unilateral internally triggered one-digit movements," *Electroencephalography and Clinical Neurophysiol*, vol. 106, no. 6, pp. 477–487, 1998.

[29] L. Astolfi, F. De Vico Fallani, F. Cincotti, et al., "Imaging functional brain connectivity patterns from high-resolution EEG and FMRI via graph theory," *Psychophysology*, vol. 44, no. 6, pp. 880–93, 2007.

[30] F. De Vico Fallani, L. Astolfi, F. Cincotti, et al., "Extracting information from cortical connectivity patterns estimated from high resolution EEG recordings: A theoretical graph approach," *Brain Topography*, vol. 19, no. 3, pp. 36–125, 2007.

Hindawi Publishing Corporation
Computational Intelligence and Neuroscience
Volume 2009, Article ID 279515, 12 pages
doi:10.1155/2009/279515

Research Article

Changes in EEG Power Spectral Density and Cortical Connectivity in Healthy and Tetraplegic Patients during a Motor Imagery Task

Filippo Cona,[1] Melissa Zavaglia,[1] Laura Astolfi,[2,3] Fabio Babiloni,[2,3] and Mauro Ursino[1]

[1] *Department of Electronics, Computer Science and Systems, University of Bologna, Via Venezia 52, 47023 Cesena, Italy*
[2] *Department of Human Physiology and Pharmacology, Sapienza University of Rome, 00185 Rome, Italy*
[3] *Istituti di ricovero e cura a carattere scientifico (IRCCS) Fondazione Santa Lucia, 00179 Rome, Italy*

Correspondence should be addressed to Mauro Ursino, mauro.ursino@unibo.it

Received 12 December 2008; Accepted 8 April 2009

Recommended by Andrzej Cichocki

Knowledge of brain connectivity is an important aspect of modern neuroscience, to understand how the brain realizes its functions. In this work, neural mass models including four groups of excitatory and inhibitory neurons are used to estimate the connectivity among three cortical regions of interests (ROIs) during a foot-movement task. Real data were obtained via high-resolution scalp EEGs on two populations: healthy volunteers and tetraplegic patients. A 3-shell Boundary Element Model of the head was used to estimate the cortical current density and to derive cortical EEGs in the three ROIs. The model assumes that each ROI can generate an intrinsic rhythm in the beta range, and receives rhythms in the alpha and gamma ranges from other two regions. Connectivity strengths among the ROIs were estimated by means of an original genetic algorithm that tries to minimize several cost functions of the difference between real and model power spectral densities. Results show that the stronger connections are those from the cingulate cortex to the primary and supplementary motor areas, thus emphasizing the pivotal role played by the CMA_L during the task. Tetraplegic patients exhibit higher connectivity strength on average, with significant statistical differences in some connections. The results are commented and virtues and limitations of the proposed method discussed.

1. Introduction

It is well known that the execution of even simple motor and/or cognitive tasks by the brain requires the participation of multiple cortical regions, which are mutually interconnected and exchange their information via plastic long-range synapses. Consequently, knowledge of brain connectivity is becoming an essential aspect of modern neuroscience, especially useful to understand how the brain realizes its basic functions and what the role of the different regions is. Connectivity, however, is an elusive concept, which can have different definitions depending on the emphasis of the investigators [1]. In particular, the definition of connectivity is strictly related to the mathematical method used to extract connectivity parameters from data, that is, it is "model dependent" and should always be used together with the particular method adopted. For instance, most methods presently used to derive connectivity graphs (such as the Direct Transfer Function or the Partial Directed Coherence [2–8]) are based on the assumption of linearity, whereas neurons are intrinsically nonlinear. Moreover, these methods use empirical equations (i.e., they are based on black box models), which do not provide a description of the underpinning physiological mechanisms (e.g., they do not explicitly consider the time constant and strength of synapses, the role of inhibitory interneurons, etc.). On the other hand, the main advantage of these methods is that they provide analytical solutions to the problem, which are not "modeler driven."

As an alternative method to study effective connectivity, a few authors in recent years have employed the so-called "neural mass models." These models were originally proposed in the mid seventies [9, 10] and subsequently improved in the late nineties [11, 12]. They mimic the activity of entire neural populations via the feedback arrangement of excitatory and inhibitory groups, which are assumed to share a similar membrane potential and work in synchronism. The interaction between excitatory and inhibitory groups can produce oscillatory rhythms, either via an intrinsic instability of the model (like a limit

cycle) or by a resonance amplification of an external noise. In particular, similar models have been used to simulate alpha rhythms [11], dynamics in the olphactory cortex [13], or paradoxical epileptic discharges [12, 14]. A few recent studies used these models to study effective connectivity among different regions of interest (ROIs), to analyze the dependence of cortical EEG on connectivity patterns [15, 16] and to evaluate the EEG power spectral density [17]. Recently, we also used neural mass models, including fast inhibitory dynamics, to simulate the power spectral density of cortical EEG [18–20] during simple motor tasks. The main indication of these studies is that neural populations with different dynamics (e.g., different time constants of excitatory and inhibitory synapses) suitably interconnected, can produce EEG rhythms similar to those measured in human subjects via high-resolution EEG methods.

Application of neural mass models to estimate effective connectivity is, however, a very hard task, due to the elevated number of parameters involved and the presence of nonlinear terms, which preclude the use of analytical solutions. For instance, in a recent paper [21] we derived some connectivity patterns between three cortical regions (the cyngulate and the primary and supplementary motor cortices) during a simple foot-movement task, by minimizing a least-square criterion function of the difference between model and data spectral densities. However, just a few exemplary cases could be analyzed, since the minimization algorithm often converges to a suboptimal solution (i.e., a local minimum) which may exhibit just a poor fitting and, moreover, may be characterized by unphysiological parameter values. Furthermore, also the metrics used to compare model and patient spectral densities may be questionable and affect the final minimisation results.

For this reason, in the present paper we designed a new method, based on a genetic algorithm, to provide an automatic fitting between model and real data. The method tries to find absolute minima of alternative cost functions within the same procedure. Genetic algorithms have already been used to estimate the parameters of a neural mass model in order to fit real data (see, e.g., [22]). The algorithm has been applied to high-resolution scalp EEG data measured during a simple foot-movement task; scalp EEG was preliminarily propagated to the cortex via a propagation model, to infer cortical electrical activity in three Regions of Interest (ROIs). The model [20] assumes that each ROI is characterized by an intrinsic rhythm (established by the time constants of synapses) and can receive additional rhythms from other connected ROIs. Results have been applied to a group of normal subjects and a group of tetraplegic patients to establish simple patterns of connectivity between the cyngulate, motor, and premotor cortices, and to look for possible differences in the two populations.

2. Method

2.1. Model of a Single Population. The model of a single population was obtained by modifying equations proposed by Wendling et al. [12]. It consists of four neural groups which communicate via excitatory and inhibitory synapses: pyramidal cells, excitatory interneurons, inhibitory interneurons with slow synaptic kinetics, and inhibitory interneurons with faster synaptic kinetics. Each neural group simulates a pool of neurons which are lumped together and which are assumed to receive similar input and to behave in a similar manner. One lumped circuit communicates with another through the average firing rate corresponding to what that given population of cells is firing on average.

Each neural group receives an average postsynaptic membrane potential from the other groups, and converts the average membrane potential into an average density of spikes fired by the neurons. This conversion is simulated via a static sigmoidal relationship. The effect of the synapses is described via second-order linear transfer functions, which convert the presynaptic spike density into the postsynaptic membrane potential. Three different kinds of synapses, with impulse response h_e, h_i, and h_g, are used to describe the synaptic effect of excitatory neurons (both pyramidal cells and excitatory interneurons), of slow inhibitory interneurons and of fast inhibitory interneurons, respectively. Model equations can be written as follows.

Pyramidal Neurons:

$$\frac{dy_0(t)}{dt} = y_5(t), \tag{1}$$

$$\frac{dy_5(t)}{dt} = A \cdot a_1 \cdot z_0(t) - 2 \cdot a_1 \cdot y_5(t) - a_1^2 \cdot y_0(t), \tag{2}$$

$$z_0(t) = \frac{(2 \cdot e_0)}{1 + e^{r \cdot (s_0 - v_0)}}, \tag{3}$$

$$v_0(t) = C_2 \cdot y_1(t) - C_4 \cdot y_2(t) - C_7 \cdot y_3(t). \tag{4}$$

Excitatory Interneurons:

$$\frac{dy_1(t)}{dt} = y_6(t), \tag{5}$$

$$\frac{dy_6(t)}{dt} = A \cdot a_1 \cdot \left(z_1(t) + \frac{p(t)}{C_2} \right) - 2 \cdot a_1 \cdot y_6(t) - a_1^2 \cdot y_1(t), \tag{6}$$

$$z_1(t) = \frac{(2 \cdot e_0)}{1 + e^{r \cdot (s_0 - v_1)}}, \tag{7}$$

$$v_1(t) = C_1 \cdot y_0(t). \tag{8}$$

Slow Inhibitory Interneurons:

$$\frac{dy_2(t)}{dt} = y_7(t), \tag{9}$$

$$\frac{dy_7(t)}{dt} = B \cdot b_1 \cdot z_2(t) - 2 \cdot b_1 \cdot y_7(t) - b_1^2 \cdot y_2(t), \tag{10}$$

$$z_2(t) = \frac{(2 \cdot e_0)}{1 + e^{r \cdot (s_0 - v_2)}}, \tag{11}$$

$$v_2(t) = C_3 \cdot y_0(t). \tag{12}$$

Fast Inhibitory Interneurons:

$$\frac{dy_3(t)}{dt} = y_8(t), \tag{13}$$

$$\frac{dy_8(t)}{dt} = G \cdot g_1 \cdot z_3(t) - 2 \cdot g_1 \cdot y_8(t) - g_1^2 \cdot y_3(t), \tag{14}$$

$$z_3(t) = \frac{(2 \cdot e_0)}{1 + e^{r \cdot (s_0 - v_3)}}, \tag{15}$$

$$v_3(t) = C_5 \cdot y_0(t) - C_6 \cdot y_2(t). \tag{16}$$

In these equations, the symbols v_i represent the average membrane potentials ($i = 0, 1, 2, 3$ for the four groups). These are the input for the sigmoid function which converts them into the average density of spikes (z_i, $i = 0, 1, 2, 3$) fired by the neurons. Then, these outputs enter into the synapses (excitatory, slow inhibitory, or fast inhibitory), represented via the second-order linear functions. Each synapse is described by an average gain (A, B, G for the excitatory, slow inhibitory, and fast inhibitory synapses, resp.) and a time constant (the reciprocal of a_1, b_1, and g_1, resp.). The outputs of these equations, which can be excitatory, slow inhibitory, or fast inhibitory, represent the postsynaptic membrane potentials (y_i, $i = 0, 1, 2, 3$). Interactions among neurons are represented via seven connectivity constants (C_i). Finally, $p(t)$ represents all exogenous contributions, both excitation coming from external sources and the density of action potentials coming from other connected regions.

2.2. Model of Connectivity Among ROIs. The previous model was used to simulate a single ROI, the dynamic of which ensues from the interactions among the four neural subgroups. In order to study how the ROIs interact, we consider N ROIs which are interconnected through long-range excitatory connections. To simulate this connectivity we assumed that the average spike density of pyramidal neurons (z_0) affects the input $p(t)$ in (6) via a weight factor, W, and a time delay, T. Hence, the input $p_i(t)$ in the ith ROI can be computed as follows:

$$p_i(t) = n_i(t) + \sum_j W_{ij} z_{0,j}(t - T), \tag{17}$$

where W_{ij} is the weight of the synaptic link from the jth (presynaptic) ROI to ith (postsynaptic) ROI, T is the time delay (assumed equal for all synapses), $n_i(t)$ represents a gaussian white noise with mean value m_i and standard deviation σ_i, and the sum in the right hand member of (17) is extended to all ROIs, j, which target into the ROI i.

2.3. Acquisition and Processing of EEG Data. The experiment took place in the laboratories of the Santa Lucia Foundation, Rome, after the informed consent was obtained. The subject was comfortably seated in an armchair with both arms relaxed, in an electrically shielded, dimly lit room. He was asked to perform a brisk protrusion of the lips (lip pursing) while he was performing a right foot movement. A 58-channel EEG system (BrainAmp, Brainproducts GmbH, Germany) was used to record electrical potentials by means of an electrode cap, accordingly to an extension of the 10–20 international system. A/D sampling rate was 200 Hz. During motor task, subject was instructed to avoid eye blinks, swallowing, or any movement other than the required foot movements. Bipolar EMG was recorded from control and spinal cord injury (SCI) subjects, with surface electrodes from the right tibialis anterior muscle and orbicularis oris muscle to detect the onset of foot and lip movements, respectively. The electro-oculograms (EOGs) were recorded to avoid trials with artifacts due to eye-blink movements. The EMG was monitored throughout recordings from electrodes placed as described above to avoid poor quality of the recordings due to muscular artifacts. Artifact rejection was performed on a wide segmentation of the trials (from −4.0 s to +4.0 s) while a narrow segmentation (from −2.5 s to +0.5 s) was used as analysis period.

A 3-shell Boundary Element Model (BEM) of the head was used to estimate the cortical current density (CCD) distribution in some regions of interest (ROI) of the cortex (the cingulate cortex (CMA_L), the primary motor area (M1F_L), and the supplementary motor area (SMAp_L)) starting from activity measured on the scalp. The procedure used is described in previous works [18, 19, 23]. From the CCD, the average estimated cortical activity in the region has then been evaluated. The latter has been successively subjected to spectral analysis in order to produce the spectra used for the estimation of the model parameters.

Power spectra have been computed by using the Welch's average modified periodogram method [24]. In particular, the model Power Spectral Density (PSD) was computed using simulated signal with duration 100 seconds, and averaging 50% overlapping sections each with duration 1 second. The use of a 100 seconds simulated signal is justified by the necessity to reduce the variance of the estimated spectrum to an acceptable level. We verified, using a random repetition of the same simulation by changing the input noise, that these spectra are only scarcely affected by the single noise realization. All power spectra have been preliminary normalized to have unitary area in the same frequency range (6–50 Hz). Since the signal beyond 40 Hz may be corrupted, the limit of our investigated gamma range was 30–40 Hz. In particular, we did not investigate the so-called high-gamma range (above 50 Hz).

We examined 5 subjects with spinal cord injury (SCI; 4 males, 1 female, mean age 26.4 ± 2.8 years) and 5 healthy subjects (4 males, 1 female, mean age 25.1 ± 1.5 years). Informed consent was obtained from all the subjects. The study was approved by the local ethics committee. The SCIs were all of traumatic aetiology and were located at the cervical level (C6 in 3 SCI subjects; C5 and C7 in the remaining 2 subjects); at the time of the study, all the patients had a stabilized lesion (mean time since trauma 19.4 ± 7.2 months). Neurological status was assessed according to the American Spinal Injury Association (ASIA) standards on the basis of the patients' motor and sensory scores, neurological level, and neurological impairment. The completeness of the lesion was defined according to the concept of sacral sparing: sensory preservation of the peri-anal zone and/or motor function of the external anal sphincter (preservation

of the lower sacral segments). The lesion was complete in all 5 patients (ASIA-A: complete motor and sensory loss below the lesion level). None of the SCI patients had suffered a head or brain lesion in concomitance with the spinal injury. Neither uncontrollable spasticity-induced body movements nor dysaesthetic pain syndrome were reported by any of the patients. All subjects were right-handed as assessed by the Edinburgh inventory [25].

In order to perform a subsequent fitting, we chose only those EEG tracings for which alpha and gamma rhythms were located at approximately the same frequencies in the three ROIs. This corresponds to model hypothesis (see in what follows) that each of these rhythms is generated by a single external source (limitations of this choice will be discussed at the end). 102 tracings satisfied this criterion. The algorithm was able to fit 59 of these trials: 36 trials on healthy subjects and 23 trials on tetraplegic ones.

2.4. The Model of the Motor Task. Analysis of real EEGs (see also [20, 21]) demonstrates that power spectral density during the task may exhibit three simultaneous rhythms, in the alpha, beta, and gamma ranges, respectively. In order to simulate this behavior, we assumed that the cortical ROIs involved in the movement (i.e., the M1F_L, the CMA_L, and the SMAp_L), when activated, oscillate with an intrinsic rhythm in the beta range. This hypothesis reflects the frequent idea that, during behavioral activation, beta rhythms are generated locally, perhaps by a recurrent feedback loop involving pyramidal cells and inhibitory interneurons [26]. These waves represent excitement of the cortex to a higher state of alertness or tension. Moreover, we assumed that the alpha rhythm is sent to the cortex by an external area (probably located in the thalamus and reticular nucleus). This hypothesis corresponds to the idea [32, page 201] that alpha rhythms arise from the endogenous rhythmicity of thalamic populations, which are then transmitted to other thalamocortical populations even in the absence of an external stimulus. Finally, an important problem is how to produce gamma rhythms in the model. A first possibility is that all ROIs can generate not only their intrinsic beta rhythm, but also a gamma oscillation, via a second group of populations with faster kinetics, and that these gamma rhythms are then synchronized via long-range synapses. The idea of multiple rhythms in the same ROI was proposed by David and Friston [15], and was used by us in a previous model for connectivity estimation [17]. A second possibility, which allows PSD to be mimicked with a smaller number of parameters, is that gamma oscillation is generated by a single far region of the cortex, and then transmitted to the other ROIs via long-range synapses.

In the present study we adopted the second hypothesis. First, we assumed that the thalamus receives an external input (simulated as a significant white noise term) and drives the other populations but does not receive any connectivity from them (i.e., any possible feedback from the cortex to the thalamus is neglected). Hence, the motor command originates from the low-frequency region (LF), and spreads toward the cortex. Moreover, the three ROIs in the cortex (CMA_L, M1F_L, and SMAp_L) can recruit a gamma or high-frequency rhythm from another region (named HF), which may be located in the prefrontal cortex. This rhythm should reflect the cognitive or conscious aspects of the task. Finally, the cingulate cortex can also modulate the HF region and drives the other two ROIs (i.e., the primary and supplementary motor areas). The latter are linked via a feedback loop. A sketch of the overall model is illustrated in Figure 1.

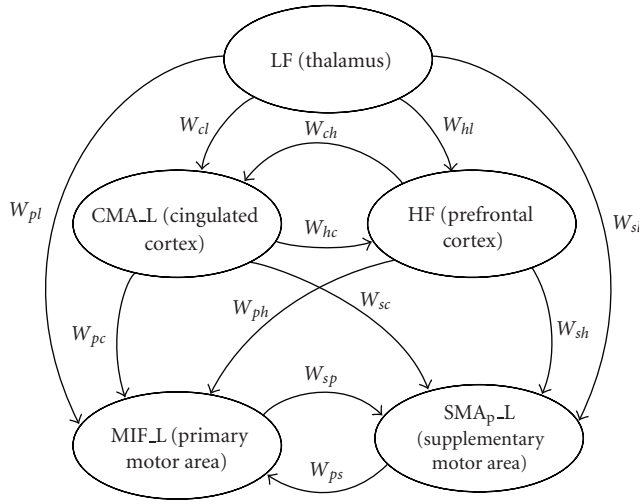

Figure 1: Model of interconnected ROIs used in the present work to simulate power spectral densities in prefrontal regions during a foot-movement task. W_{ij} are connectivity weights, estimated from real data using the genetic algorithm described in the text. The regions CMA_L, M1F_L and SMA_p_L oscillate in the beta range when stimulated with white noise. The LF region oscillates in the alpha range, whereas the HF region generates a rhythm in the gamma band (see Table 1 for parameter numerical values within the regions).

2.5. The Model Parameters. The model has a relatively large number of parameters, but only a few of them were used as variables for the fitting procedure. It appears that letting the fitting algorithm modulate all of the model parameters leads to incoherent solutions: the same simulated power spectra can be obtained with different sets of parameters. So the parameters estimated by the fitting algorithm were only the reciprocal of time constants of excitatory synapses (to tune power peaks frequencies) and connectivity strengths (to adjust power peaks relative amplitudes). The other parameters have constant values, given in Table 1. Most of these values are biologically plausible [11] and let the model oscillate in the alpha (8–12 Hz), beta (12–30 Hz), and gamma band (>30 Hz) [18, 19]. Still the input mean m and variance σ^2 have been estimated via the fitting procedure, since no plausible values for these parameters have been found yet. In fact, as usual in neural mass models [12, 15, 20], this noise simulates all random contributions coming from external sources not included in the model and also accounts for internal neural variability. To do this we run a preliminary set of fittings in which m and σ^2 were used as fitting variables in order to find their optimum values for each trial. The values

Table 1: Model parameters.

Parameters	LF	CMA_L, M1F_L, SMAp_L	HF
$A(mV)$	2.67	5.17	5.55
$B(mV)$	3.15	4.45	3.8
$G(mV)$	22.3	57.1	173
$b_1(s^{-1})$	20	30	40
$g_1(s^{-1})$	300	350	790
$m(mV)$	−103.3011	−130.4829	−16.1439
$\sigma^2(mV^2)$	27807	10028	23642
		All Regions	
C		135	
C_1		C	
C_2		0.8 C	
C_3		0.25 C	
C_4		0.25 C	
C_5		0.3 C	
C_6		0.1 C	
C_7		0.8 C	
$r(mV^{-1})$		0.56	
$s_0(mV)$		6	
$e_0(s^{-1})$		2.5	

found were averaged and used as constants (Table 1) in the following fitting procedures.

2.6. Genetic Algorithm and Fitting Procedure. A Genetic Algorithm (GA) is a search technique that solves optimization problems by simulating the Darwinian natural selection [27]. We used the GA to find the set of model parameters for which the model output fits a given real EEG signal. Parameters used for the fitting procedures are the reciprocal of time constants of excitatory synapses (a_1), and connectivity strengths.

The GA is divided into generations. Each generation consists of a lot of individuals that are candidate solutions (sets of model parameters) for the fitting. The first generation is typically random. Parameters are represented as bit arrays (chromosomes). Each individual is ranked with a fitting coefficient (FC) in the range $[0, 1]$ by calculating the model output and comparing it to the real EEG signal: the better the fitting between the simulated signal and the real one, the higher the FC of the individual. Best-ranked individuals (higher FC) have higher probability to reproduce. During reproduction couples of parents are randomly selected according to their FCs. Each couple generates two new individuals whose chromosomes are obtained from applying genetic operators to the parents' ones. Typical genetic operators are crossover and mutation (Figure 2). Crossover is the exchange of genetic material between parents to generate the sons' chromosomes. Mutation simply switches the values of a low percentage of bits (mutation rate). The worst individuals of the previous generation are replaced with the best newborn individuals. In this way, each generation tends to preserve the best genetic material. The algorithm converges to a population composed of sets of parameters that fit the real EEG signal well.

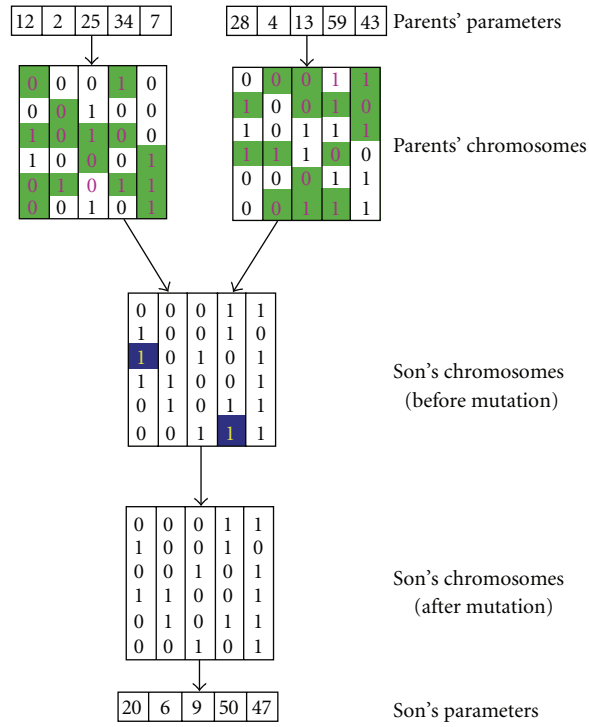

Figure 2: An exemplum of the mechanism for son generation implemented in the genetic algorithm.

The major challenge in implementing a GA is to find an efficient fitting function for determining the FCs and rank the individuals, so that the algorithm is able to converge in reasonable time. To compare the simulated signal to the real one, we used their PSD. Actually, analysis of the peak frequencies and amplitudes in the PSD allows evaluations of the rhythms characterizing the signal, their frequencies, and the relative power associated to each frequency band.

We introduced some changes to the original GA to improve its speed of convergence.

(i) The global population was divided in 4 tribes. Each tribe has its own fitting function. The algorithm allows migration between tribes, so that each individual may choose the tribe that consent its offspring to converge to the solution in the fastest way. In order to compute the FCs of each tribe, we first calculated three alternative cost functions. The first is the classic mean square error. The second aims at quantifying the similarity in the ratios between the local maxima and the local minima (i.e., it gives more emphasis to the maxima and minima of the PSD than to other values of the PSD). The third focuses the attention especially to the position of the peaks (i.e., the frequencies of the three rhythms). These three functions were then combined with different weights, in order to obtain four alternative FCs to be used in the four tribes. The fourth tribe (also named *melting pot*) is the one characterized by the strictest requirements.

(ii) The algorithm uses a dynamic mutation rate. The probability of a bit to switch is related to the similarity between the parents' chromosomes: the more similar the chromosomes, the higher the mutation rate. A high similarity between parents means that the population converged to a local maximum; in this condition, an increase in the mutation rate would favour the escape from the maximum attraction field.

(iii) An aging factor was introduced. This means that members of the previous generation can still generate sons and daughters, but starting with a decreased FC. Otherwise, the creation of new populations would erase all good old individuals, and if they had poor sons and daughters their legacy would be lost. On the other hand, if old individuals are not weakened, evolution may be too slow.

(iv) The order of bits inside chromosomes can be shuffled. Commonly each parameter is encoded in a single chromosome, but such a coding system is inefficient when combined with the dynamic mutation rate described above. When one of the parameters approaches its best value, it tends to be inherited by all the members of the population. This means that all the individuals have an almost identical chromosome, thus the mutation rate for the bits encoding this parameter grows rapidly and the partial information reached may be wasted in the successive generation. This problem can be avoided by spreading the information of each parameter among all the chromosomes. Figure 2 illustrates a more standard coding system.

The algorithm stops either when individuals finish improving their FCs, or after 400 generations. At the end of the simulation the best individual belonging to the melting pot is taken as the best solution.

We noticed that the most beneficial changes are those which best resemble the natural selection.

3. Results

Exempla of model fitting in four exemplary cases are shown in Figure 3. The left panels refer to two healthy subjects, while the right panels refer to two tetraplegic patients. It is worth noting that the model is able to simulate the position and the relative amplitude of the three peaks in all three ROIs quite well. The other fitted PSDs are similar to those presented here, both for what concerns the shape and the quality of fitting.

The average values of estimated synaptic weights in the healthy population and in the tetraplegic patients are shown in the histogram of Figure 4. Two main aspects of this figure deserve attention.

First, by considering the overall fitting parameters, without distinguishing between healthy and tetraplegic subjects, one can observe that some weights are predominant compared with others. In particular, the stronger connections are those from the cyngulate cortex to the primary motor cortex, and from the cyngulate cortex to the supplementary motor cortex. A visual summary of the synaptic strengths, computed by using the average parameters in both populations, is shown in the bottom panel of Figure 4.

Second, from a separate parameter estimates, one can detect statistically significant differences in the synaptic strength between healthy and tetraplegic subjects. In particular, connectivity in tetraplegic patients is about 12% higher (on average) compared with that of healthy volunteers. Differences in connection weights between the two classes are very significant ($p < .01$ evaluated with an untailed t-test) from the thalamus to the primary motor cortex and from the thalamus to the supplementary motor cortex. The differences in the connection weights are also significant ($p < .05$) from the high frequency region to some cortical ROIs.

Finally, we used the average values of the synaptic strengths in the two populations to compute paradigmatic PSDs (one for a typical healthy subject using the average parameters of that class and the other for a typical tetraplegic subject). The results are illustrated in Figure 5. As it is evident from this figure, the paradigmatic tetraplegic subject exhibits a stronger peak in the gamma band compared with that evident in the paradigmatic healthy volunteer and a smaller peak in the beta range. This difference is a consequence of the higher connectivity weights from the HF region and from the LF region.

4. Discussion

The aim of this work was to derive patterns of connectivity among the main regions of interest (the cingulate cortex and the primary and supplementary motor areas) involved in simple motor tasks. To this end, we used neural mass models and electrophysiological data obtained with scalp EEG, propagated to the cortex. Moreover, we analyzed differences between normal and tetraplegic subjects. Although various attempts to derive connectivity from EEG, and to characterize EEG in pathological conditions are present in the literature, most works make use of empirical model (e.g., based on coherence and correlation among time series). Just a few attempts to elucidate existing data via interpretative models can be found in the literature [15–17].

In an interpretative model, parameters have a clear biophysical significance, and the model allows the formulation of hypotheses on the physiological mechanisms, the neural architecture, and the parameter changes responsible for data generation. Promising models assume the presence of interacting neural masses, which are reciprocally connected and generate the neural signals responsible for the measured electrical activity. Similar models integrated with Bayesian inference (a framework named "Dynamic causal models" by the authors) were used by Friston and coauthors to estimate effective connectivity from neuroimaging data [15, 28], to analyze event-related potentials [29] or to predict the spectral profile of local field potentials in the rat [17]. Neural mass models were used to study the transition to seizures and to model epileptic activity [12, 30], to analyze the effect of drugs on EEG spectra [31], or to simulate the effect of the overall brain connectivity on individual EEG rhythms measured on the scalp [16].

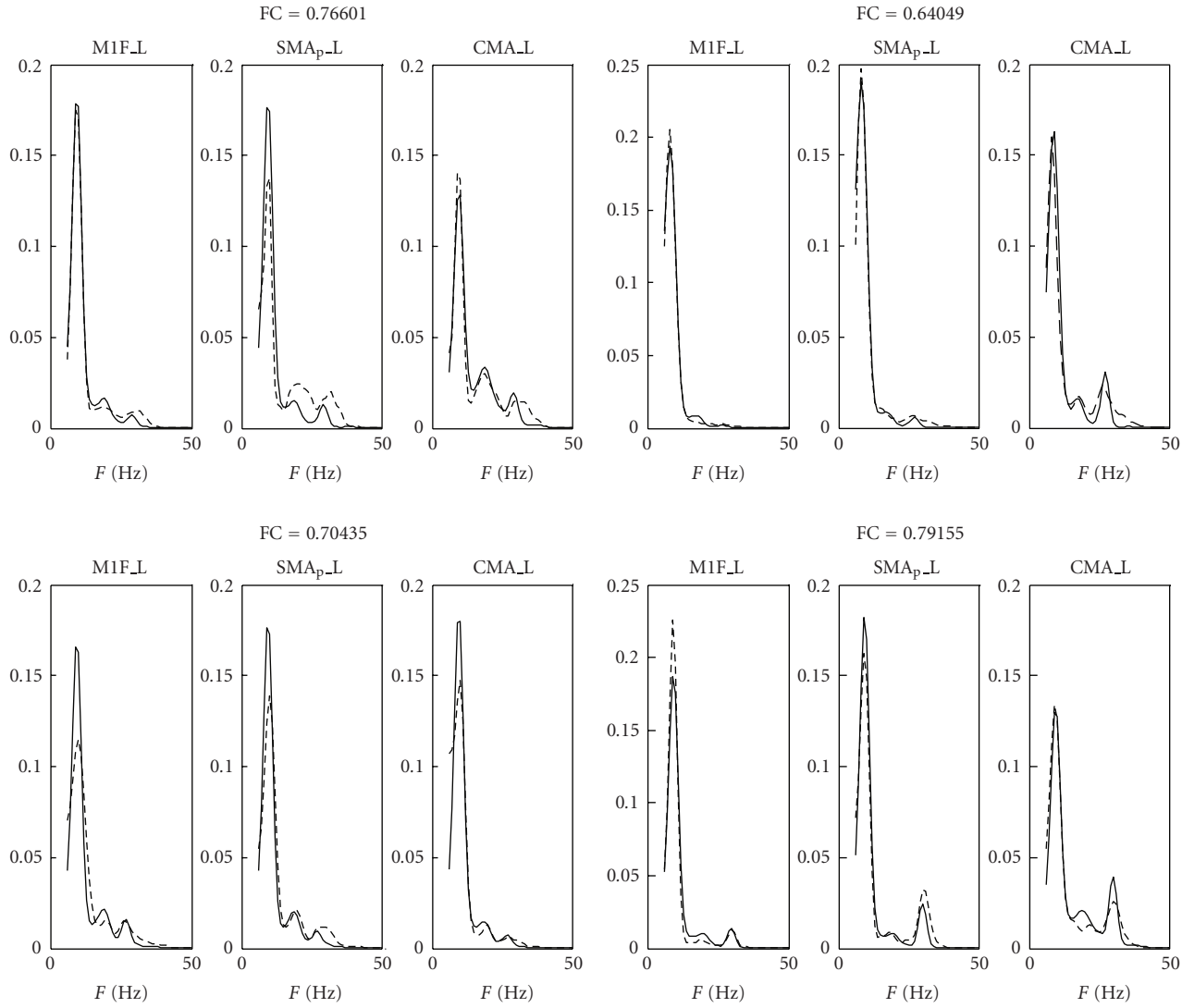

Figure 3: Comparison between real (dashed line) and simulated (continuous line) power spectral densities in the three regions M1F_L (primary motor cortex), SMA$_p$_L (supplementary motor cortex), and CMA_L (cingulate cortex) of the left hemisphere during execution of the foot imagery motor task. The left panels refer to two healthy subjects, while the right panels refer to two tetraplegic patients. All spectra are normalized to have unitary area in the range 6–50 Hz. The value of the fitting coefficient (ranging between 0 and 1) is shown above each panel.

Our work goes in the same direction as previous papers. However, three main innovative methodological aspects deserve a critical discussion: the kind of information used to validate the model, the structure adopted for the model, and the fitting procedure for parameter estimation.

The first important issue concerns what kind of data the model is intended to reproduce, and so, which measurement is compared to model output. This is a crucial point, since the type and structure of a model are strictly dependent on the problem under study. In this work, as in previous ones [18–21], we focused attention on the frequency content of cortical EEG, in particular on the peaks of power spectral density. Indeed, spectral measures are commonly used to summarize cortical dynamics and to assess changes in cortical activity during cognitive and/or motor tasks. It is generally believed that the alpha rhythm originates from the thalamus and is distinctive of a relaxed state. The beta rhythm is associated with normal waking activity, as it occurs during natural human motor behavior or after proprioceptive stimulation. A shift from alpha to beta rhythms is considered a marker of alerting. Gamma rhythms appear to be involved in higher mental activity, including perception and consciousness. Although these rhythms are currently described and analyzed in the neurophysiological literature [32, 33], the problem of how to link their changes to the underlying neural processes, the neural architecture and connectivity strength is still largely unsolved.

An important aspect is that we focused attention just on three ROIs, and we never tried a fitting to other ones. The ROIs were selected according to widely accepted considerations on their involvement in the preparation and execution of simple self-generated movements. In fact, there is a general

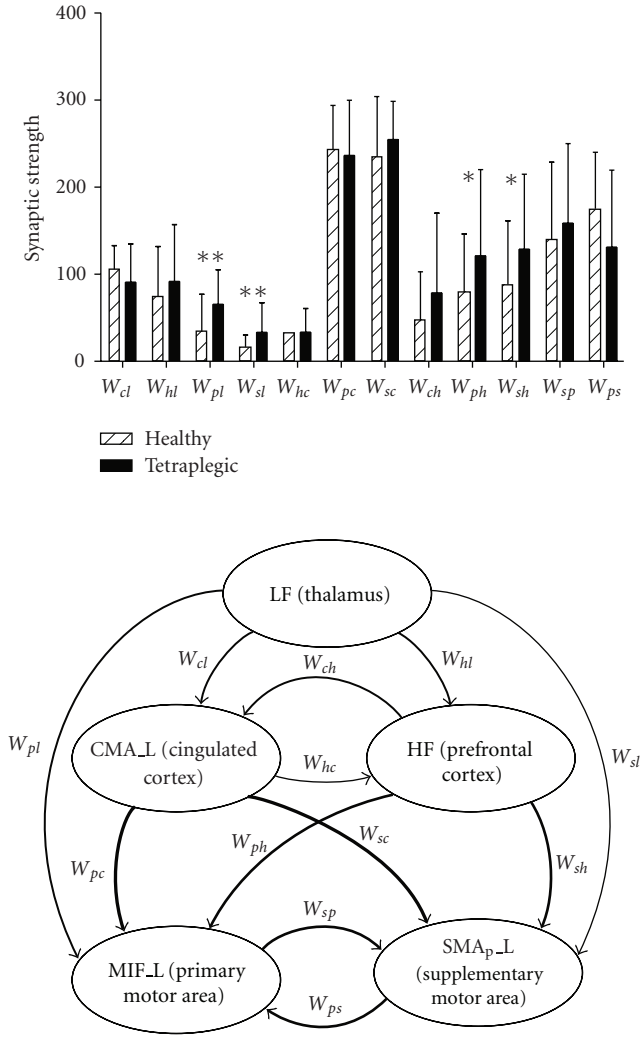

Figure 4: Connectivity weights (mean value + SD) estimated on 5 healthy subjects and on 5 tetraplegic patients with the genetic algorithm described in the text. A qualitative exemplum of the resulting connectivity, based on the average values on the entire population, is depicted in the bottom panel, where line thickness is proportional to the connectivity weight. It is worth noting in the upper panel the presence of very significant statistical differences ($p < .01$, columns with $**$) between healthy subjects and tetraplegic patients for what concerns the connections from the LF region to the primary motor and supplementary motor areas. Significant statistical differences ($p < .05$, columns with $*$) are also evident in the connections which link the HF region to the primary motor and supplementary motor areas.

consensus that the M1F and the medial aspect of the SMA_p are amongst the main generator sources of the early and late components of the motor-related cortical potentials (reviewed by [34]) which, in turn, reflect the physiological excitation of the cortical areas involved in preparing and producing movements. Anatomical and physiological studies on nonhuman primates have demonstrated that among the distinct cingulate motor areas buried in the cingulate sulcus, those roughly located at the same rostrocaudal level as the SMA_p proper (caudal CMA, dorsal, and ventral parts) are primarily implicated in movement execution itself rather than in higher cognitive control of voluntary movements (for review see [35, 36]).

In order to simulate EEG spectral patterns in these areas, including both alpha and beta as well as gamma rhythms, we adopted a simple model structure based on a few a priori assumptions. First we assumed that the cingulate cortex drives the primary motor area and the supplementary motor area during execution of the task, but it receives only negligible feedback from them. This assumption seemed justified by the attention that the cingulate cortex has received in the neuroscientific literature recently [37]. In these contributions the cingulate cortex is seen as a part of the cortex, that is, mainly involved in the promotion of action and movements of decisions. By contrast, the two motor areas may be connected by a reciprocal feedback. These areas are important in our model since the primary motor area is responsible for the execution of all voluntary movements, while the supplementary motor area implements internally generated or well-learned actions, that is, actions which do not require monitoring the external environment.

A further assumption is that the three ROIs under analysis, if stimulated, can oscillate with an intrinsic beta rhythm. This assumption agrees with present knowledge. Indeed, as traditionally described in the literature, a motor related activity in the beta range is frequently located close to the sensory motor area following finger movements [38] and is reflected to the premotor area [39]. As suggested by [40] beta oscillations may be "indicative of a resonant behavior of the connected networks in the sensorimotor areas." This reflects our basic model assumption.

Beyond this fundamental aspect, the model incorporates two other important assumptions, which are used to generate alpha and gamma rhythms, but have a less evident physiological and neural counterpart.

First, model assumes that a low frequency alpha rhythm originates from an external area (that we named "thalamic area") and then propagates to the other regions of interest. Indeed, a classic idea on the genesis of alpha rhythms [32, page 201] is that this rhythm arises from the endogenous activity of thalamic neurons, or from thalamocortical connections, especially involving the occipital region. Recent works on the cat, support the critical role of the thalamus for the generation of occipital oscillations [41]. A recent study on the location of EEG rhythms in humans confirms that alpha rhythms are especially evident in the occipital or occipitotemporal regions, that is, they mainly arise from posterior neural sources [39]. Hence, although we cannot exclude that a source of alpha rhythms may also be present in the examined frontoparietal regions, the most likely hypothesis is that this rhythm originates in thalamic and/or occipital regions, and is then transmitted toward the other regions of interest.

An important simplification, which deserves a brief comment, is that we neglected any feedback synapse from cortical regions to the "thalamic area." Of course, corticothalamic feedbacks exist in the brain and may have a role in the modulation of the alpha spectral content. Our choice has been adopted just to reduce the number of parameters

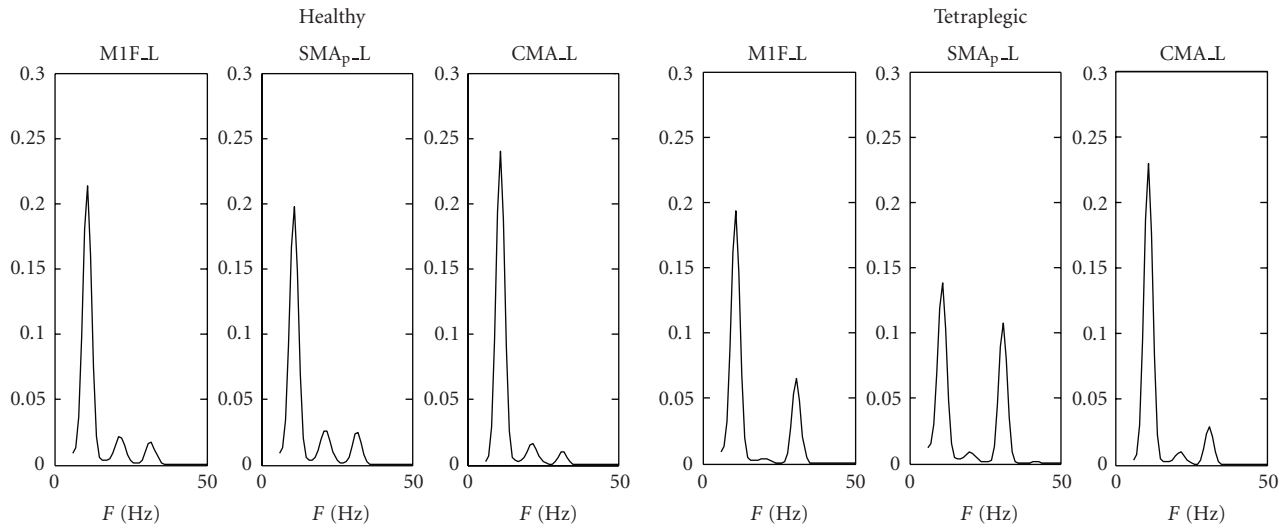

Figure 5: Example of paradigmatic power spectral densities simulated with the model using the average connection weights estimated on healthy volunteers (left panel) and on tetraplegic patients (right panel). All spectra are normalized to have unitary area in the range 6–50 Hz. It is worth noting the higher peak in the gamma range, and the lower peak in the beta range in tetraplegic patients compared with the healthy subjects.

in the fitting procedure, in order to avoid the problem of "overfitting." In fact, increasing the number of unknown parameters improves the quality of fitting, but worsens the reliability of parameter estimates.

A further important assumption is that also the gamma rhythm originates from an external area, that we supposed to be located in the frontal cortex. This hypothesis is corroborated by the observation that neurons in the frontal cortex shows the intrinsic capacity to oscillate at 40 Hz [42, 43]. However, alternative hypotheses on the origin of gamma rhythms can be found in the literature (see [44] for an excellent review) and we cannot exclude that this rhythm originates internally in the considered ROIs due to recurrent excitation and inhibition mechanisms (especially involving fast inhibitory interneurons). Hence, the gamma region in the model should be considered as a "latent source," that has not necessarily a physiological counterpart. This problem requires further theoretical and experimental work.

Once this model structure has been designed, a fundamental point concerns what aspects of the spectra should be used to perform a best fitting between model predictions and real data. In previous works we used a least-square criterion function of the difference between model and measured spectra [18–21]. Assuming a Gaussian distribution of the measurement error, a least square criterion corresponds to a maximal likelihood estimation, that is, maximization of the a priori conditioned probability. A more complex Bayesian procedure has been adopted by Moran et al., recently [17] under the framework of dynamic causal models [28, 45]. A Bayesian procedure involves also the inclusion of some a priori knowledge on the probability distribution of the estimated parameters.

In the present work we tried an innovative strategy, based on the idea that not all aspects of the PSD are of equal interest. In particular, we focused attention especially on the position and relative amplitude of the main peaks in the power spectra, thinking that these summarize the underlying mechanisms generating EEG rhythms. Moreover we tried different complementary "cost functions" in the implementation of the genetic algorithm (GA). Although GA are time consuming compared with other minimization techniques, they offer the possibility to try different alternative solutions for the problem (implementing different tribes) and to overcome the problem of local minima (which often makes the result of fitting procedures untenable) by generating different sons through mutations in the parameter space.

Two main objectives have been pursued with this technique: to discover possible simple circuits, connecting the three aforementioned ROIs, able to explain the observed PSDs, and to detect possible differences in connectivity circuits between healthy subjects and tetraplegic patients. Results point out the existence of significant differences between the two classes, especially for what concerns the weights which link the LF (thalamic) and HF regions to the primary and the supplementary motor cortices. In particular, these weights are stronger in tetraplegic patients compared with healthy individuals and these differences are statistically significant. Differences in connectivity weights might reflect a higher awareness (related with the gamma component) and a greater attention (related with thalamic inputs) in the tetraplegic patient than in the normal individuals, that is, greater concentration toward the task. The existence of larger and stronger connectivity weights in the cortical connectivity networks estimated in tetraplegic patients compared with those estimated in healthy volunteers has been previously observed by several authors [46, 47].

A further interesting result of our work is that the greatest weights in the neural circuit are those which link the

cingulate cortex to motor areas. This result underlines the importance of a feedforward signals from the frontal cortex in the initiation and planning of the voluntary movement.

In the present work we performed 12 statistical tests, hence a possible objection is that the significance level should be corrected to account for multiple hypotheses. The problem of whether correction is appropriate or not is quite complex and depends on the objective of the work. As clearly stated in recent publications [48] if the main goal is generation hypothesis or initial screening for potential solutions, it may be appropriate to use the standard significance level without corrections to avoid Type II errors (not detecting real differences or trends). Conversely, if the main goal is rigorous testing of a hypothesis, then an adjustment for multiple tests (like Bonferroni or Holm's methods) is needed. The objective of the present work is certainly "hypothesis generation," hence we preferred to use classical t test to avoid type II error. Of course, in order to "test the hypotheses" generated with our procedure, one needs to repeat the experiment with new "fresh" data, considering only the individual hypotheses to be verified, and using a correction. This may be the subject of future works.

Finally, it is important to discuss the main limitations of the present preliminary work, and possible lines for future changes.

A first aspect concerns the variability of parameter estimates within the same subject. Although this variability is less accentuate compared with that between the two classes, and between different subjects in the same class, it is still quite elevated. Analysis of how the connectivity pattern may vary in the same subject from one trial to the next still requires a deeper future analysis.

In the present model we assumed that connectivity originates from pyramidal neurons, and reaches the input of excitatory interneurons, that is, we did not consider possible lateral connections from pyramidal neurons to inhibitory interneurons. Inhibitory interarea connections, however, may be important to reduce neural activity, to avoid instability, and to improve synchronization among rhythms. Lateral inhibitory synapses were considered by David et al. [29], and Stephan et al. [28], in their DCM schema of neural populations for the analysis of event related responses. In particular, these authors assumed that lateral connections originating from pyramidal neurons target to all other populations (both excitatory and inhibitory) in the lateral ROIs, although they did not consider the presence of inhibitory interneurons with fast kinetics. Inclusion of lateral connections toward inhibitory interneurons may be of value in future works, to improve two aspects of results. First, it may help to maintain the activity of the motor and premotor ROIs far from saturation. Indeed, with the present values of parameters, these two populations are strongly activated and often work close to the upper saturation region of their sigmoid. Second, activation of fast inhibitory interneurons might help to explain the presence of gamma rhythms, even without introducing an ad hoc rhythm from an external population. The idea that gamma rhythms may originate from stimulation of fast inhibitory interneurons (or alternatively from gap junctions) has been proposed by various authors recently [32, 49]. Of course, a flaw of introducing lateral synapses to inhibitory interneurons is the increase in the number of free parameters, which may further complicate the convergence of the fitting procedure and the interpretation of results.

Another important limitation of the present work is that the model is able to simulate PSD spectra only if the rhythms in the three ROIs (in the alpha and gamma bands) have almost the same frequency. In view of that, we excluded all trials which present different frequencies in the spectra from the best fitting procedure. The reason for this limitation is that the three ROIs receive the alpha and gamma oscillations from the same external ROIs (i.e., the alpha rhythm from the LF region or thalamus; the gamma rhythms from the HF ROI, prefrontal, see Figure 1). In order to generate rhythms with different frequencies in the alpha and gamma bands, one should hypothesize the presence of more LF and HF regions. However, this aspect would further complicate parameter estimation and would make the model less parsimonious. It is possible that introduction of lateral interregion synapses directed to inhibitory interneurons may allow a more flexible positioning of rhythms in individual ROIs.

Finally, we are aware that use of the genetic algorithm, although very flexible in finding a good solution avoiding local minima, is time consuming. Alternative more efficient fitting methods (maybe introducing some prior probability for the estimate, according to a Bayesian approach [50]) may be attempted in future studies.

In conclusion, the present work represents a first attempt to explain the presence of multiple rhythms in three ROIs involved in motor tasks, and their variability, using a simple model of interconnected populations. Encouraging results concern the capacity to obtain reliable PSD spectra, by acting on a few parameters representing the connection weights, and to detect significant differences between the two classes. However, important limitations are still evident: they are especially concerned with a lack of inhibitory interactions among ROIs, with the dispersion of individual parameter estimates, and with the difficulty to generate more flexible peaks in the spectra. Overcoming these limitations deserve much future work.

Nevertheless, despite their present limitations, we claim models of interacting neural mass may be of great value to gain a deeper insight into the mechanisms of rhythms generation in EEG, and to start the formulation of more quantitative hypotheses on the neural architecture and connectivity changes underlying motor/cognitive tasks.

Acknowledgments

This work was supported by the COST Action BM0601 "NeuroMath." Neither the COST Office nor any person acting on its behalf is responsible for the use which might be made of the information contained in this publication. The COST Office is not responsible for the external websites referred to in this publication.

References

[1] B. Horwitz, "The elusive concept of brain connectivity," *NeuroImage*, vol. 19, no. 2, pp. 466–470, 2003.

[2] L. Astolfi, F. Cincotti, D. Mattia, et al., "Estimation of the effective and functional human cortical connectivity with structural equation modeling and directed transfer function applied to high-resolution EEG," *Magnetic Resonance Imaging*, vol. 22, no. 10, pp. 1457–1470, 2004.

[3] L. A. Baccalá and K. Sameshima, "Partial directed coherence: a new concept in neural structure determination," *Biological Cybernetics*, vol. 84, no. 6, pp. 463–474, 2001.

[4] M. Kamiński, K. Blinowska, and W. Szelenberger, "Investigation of coherence structure and EEG activity propagation during sleep," *Acta Neurobiologiae Experimentalis*, vol. 55, no. 3, pp. 213–219, 1995.

[5] M. Kamiński, K. Blinowska, and W. Szelenberger, "Topographic analysis of coherence and propagation of EEG activity during sleep and wakefulness," *Electroencephalography and Clinical Neurophysiology*, vol. 102, no. 3, pp. 216–227, 1997.

[6] M. Kamiński, M. Ding, W. A. Truccolo, and S. L. Bressler, "Evaluating causal relations in neural systems: granger causality, directed transfer function and statistical assessment of significance," *Biological Cybernetics*, vol. 85, no. 2, pp. 145–157, 2001.

[7] M. Kamiński and K. J. Blinowska, "A new method of the description of the information flow in the brain structures," *Biological Cybernetics*, vol. 65, no. 3, pp. 203–210, 1991.

[8] A. Korzeniewska, M. G. Mańczak, M. Kamiński, K. J. Blinowska, and S. Kasicki, "Determination of information flow direction among brain structures by a modified directed transfer function (dDTF) method," *Journal of Neuroscience Methods*, vol. 125, no. 1-2, pp. 195–207, 2003.

[9] W. J. Freeman, "Models of the dynamics of neural populations," *Electroencephalography and Clinical Neurophysiology*, vol. 34, pp. 9–18, 1978.

[10] F. H. Lopes da Silva, A. van Rotterdam, P. Barts, E. van Heusden, and W. Burr, "Models of neuronal populations: the basic mechanisms of rhythmicity," *Progress in Brain Research*, vol. 45, pp. 281–308, 1976.

[11] B. H. Jansen and V. G. Rit, "Electroencephalogram and visual evoked potential generation in a mathematical model of coupled cortical columns," *Biological Cybernetics*, vol. 73, no. 4, pp. 357–366, 1995.

[12] F. Wendling, F. Bartolomei, J. J. Bellanger, and P. Chauvel, "Epileptic fast activity can be explained by a model of impaired GABAergic dendritic inhibition," *European Journal of Neuroscience*, vol. 15, no. 9, pp. 1499–1508, 2002.

[13] W. J. Freeman, "Simulation of chaotic EEG patterns with a dynamic model of the olfactory system," *Biological Cybernetics*, vol. 56, no. 2-3, pp. 139–150, 1987.

[14] F. Wendling, J. J. Bellanger, F. Bartolomei, and P. Chauvel, "Relevance of nonlinear lumped-parameter models in the analysis of depth-EEG epileptic signals," *Biological Cybernetics*, vol. 83, no. 4, pp. 367–378, 2000.

[15] O. David and K. J. Friston, "A neural mass model for MEG/EEG: coupling and neuronal dynamics," *NeuroImage*, vol. 20, no. 3, pp. 1743–1755, 2003.

[16] R. C. Sotero, N. J. Trujillo-Barreto, Y. Iturria-Medina, F. Carbonell, and J. C. Jimenez, "Realistically coupled neural mass models can generate EEG rhythms," *Neural Computation*, vol. 19, no. 2, pp. 478–512, 2007.

[17] R. J. Moran, K. E. Stephan, S. J. Kiebel, et al., "Bayesian estimation of synaptic physiology from the spectral responses of neural masses," *NeuroImage*, vol. 42, no. 1, pp. 272–284, 2008.

[18] M. Ursino, M. Zavaglia, L. Astolfi, and F. Babiloni, "Use of a neural mass model for the analysis of effective connectivity among cortical regions based on high resolution EEG recordings," *Biological Cybernetics*, vol. 96, no. 3, pp. 351–365, 2007.

[19] M. Zavaglia, L. Astolfi, F. Babiloni, and M. Ursino, "A neural mass model for the simulation of cortical activity estimated from high resolution EEG during cognitive or motor tasks," *Journal of Neuroscience Methods*, vol. 157, no. 2, pp. 317–329, 2006.

[20] M. Zavaglia, L. Astolfi, F. Babiloni, and M. Ursino, "The effect of connectivity on EEG rhythms, power spectral density and coherence among coupled neural populations: analysis with a neural mass model," *IEEE Transactions on Biomedical Engineering*, vol. 55, no. 1, pp. 69–77, 2008.

[21] M. Zavaglia, L. Astolfi, F. Babiloni, and M. Ursino, "A model of rhythm generation and functional connectivity during a simple motor task: preliminary validation with real scalp EEG data," *International Journal of Bioelectromagnetism*, vol. 10, no. 1, pp. 68–75, 2008.

[22] F. Wendling, A. Hernandez, J.-J. Bellanger, P. Chauvel, and F. Bartolomei, "Interictal to ictal transition in human temporal lobe epilepsy: insights from a computational model of intracerebral EEG," *Journal of Clinical Neurophysiology*, vol. 22, no. 5, pp. 343–356, 2005.

[23] F. Babiloni, F. Cincotti, C. Babiloni, et al., "Estimation of the cortical functional connectivity with the multimodal integration of high-resolution EEG and fMRI data by directed transfer function," *NeuroImage*, vol. 24, no. 1, pp. 118–131, 2005.

[24] P. D. Welch, "The use of fast Fourier transform for the estimation of power spectra: a method based on time averaging over short, modified periodograms," *IEEE Transactions on Audio and Electroacoustics*, vol. 15, no. 2, pp. 70–73, 1967.

[25] R. C. Oldfield, "The assessment and analysis of handedness: the Edinburgh inventory," *Neuropsychologia*, vol. 9, no. 1, pp. 97–113, 1971.

[26] S. Salenius and R. Hari, "Synchronous cortical oscillatory activity during motor action," *Current Opinion in Neurobiology*, vol. 13, no. 6, pp. 678–684, 2003.

[27] J. Holland, *Adaptation in Natural and Articial Systems*, University of Michigan Press, Ann Arbor, Mich, USA, 1975.

[28] K. E. Stephan, L. M. Harrison, S. J. Kiebel, O. David, W. D. Penny, and K. J. Friston, "Dynamic causal models of neural system dynamics: current state and future extensions," *Journal of Biosciences*, vol. 32, no. 1, pp. 129–144, 2007.

[29] O. David, S. J. Kiebel, L. M. Harrison, J. Mattout, J. M. Kilner, and K. J. Friston, "Dynamic causal modeling of evoked responses in EEG and MEG," *NeuroImage*, vol. 30, no. 4, pp. 1255–1272, 2006.

[30] D. T. J. Liley and I. Bojak, "Understanding the transition to seizure by modeling the epileptiform activity of general anesthetic agents," *Journal of Clinical Neurophysiology*, vol. 22, no. 5, pp. 300–313, 2005.

[31] J. B. Rowe, K. E. Stephan, K. Friston, R. S. J. Frackowiak, and R. E. Passingham, "The prefrontal cortex shows context-specific changes in effective connectivity to motor or visual cortex during the selection of action or colour," *Cerebral Cortex*, vol. 15, no. 1, pp. 85–95, 2005.

[32] G. Buzsàki, *Rhythms of the Brain*, Oxford University Press, New York, NY, USA, 2006.

[33] L. M. Ward, "Synchronous neural oscillations and cognitive processes," *Trends in Cognitive Sciences*, vol. 7, no. 12, pp. 553–559, 2003.

[34] H. Shibasaki and M. Hallett, "What is the Bereitschaftspotential?" *Clinical Neurophysiology*, vol. 117, no. 11, pp. 2341–2356, 2006.

[35] T. Paus, "Primate anterior cingulate cortex: where motor control, drive and cognition interface," *Nature Reviews Neuroscience*, vol. 2, no. 6, pp. 417–424, 2001.

[36] N. Picard and P. L. Strick, "Motor areas of the medial wall: a review of their location and functional activation," *Cerebral Cortex*, vol. 6, no. 3, pp. 342–353, 1996.

[37] M. I. Posner, M. K. Rothbart, B. E. Sheese, and Y. Tang, "The anterior cingulate gyrus and the mechanism of self-regulation," *Cognitive, Affective & Behavioral Neuroscience*, vol. 7, no. 4, pp. 391–395, 2007.

[38] A. Stancák Jr. and G. Pfurtscheller, "Event-related desynchronisation of central beta-rhythms during brisk and slow self-paced finger movements of dominant and nondominant hand," *Cognitive Brain Research*, vol. 4, no. 3, pp. 171–183, 1996.

[39] C. M. Gómez, J. Marco-Pallarés, and C. Grau, "Location of brain rhythms and their modulation by preparatory attention estimated by current density," *Brain Research*, vol. 1107, no. 1, pp. 151–160, 2006.

[40] C. Neuper and G. Pfurtscheller, "Evidence for distinct beta resonance frequencies in human EEG related to specific sensorimotor cortical areas," *Clinical Neurophysiology*, vol. 112, no. 11, pp. 2084–2097, 2001.

[41] F. H. Lopes da Silva, J. E. Vos, J. Mooibroek, and A. van Rotterdam, "Relative contributions of intracortical and thalamo-cortical processes in the generation of alpha rhythms, revealed by partial coherence analysis," *Electroencephalography and Clinical Neurophysiology*, vol. 50, no. 5-6, pp. 449–456, 1980.

[42] Y. Gutfreund, Y. Yarom, and I. Segev, "Subthreshold oscillations and resonant frequency in guinea-pig cortical neurons: physiology and modelling," *The Journal of Physiology*, vol. 483, part 3, pp. 621–640, 1995.

[43] R. R. Llinás, A. A. Grace, and Y. Yarom, "In vitro neurons in mammalian cortical layer 4 exhibit intrinsic oscillatory activity in the 10- to 50-Hz frequency range," *Proceedings of the National Academy of Sciences of the United States of America*, vol. 88, no. 3, pp. 897–901, 1991.

[44] J. G. R. Jefferys, R. D. Traub, and M. A. Whittington, "Neuronal networks for induced '40 Hz' rhythms," *Trends in Neurosciences*, vol. 19, no. 5, pp. 202–208, 1996.

[45] K. J. Friston, L. Harrison, and W. Penny, "Dynamic causal modelling," *NeuroImage*, vol. 19, no. 4, pp. 1273–1302, 2003.

[46] F. de Vico Fallani, L. Astolfi, F. Cincotti, et al., "Brain network analysis from high-resolution EEG recordings by the application of theoretical graph indexes," *IEEE Transactions on Neural Systems and Rehabilitation Engineering*, vol. 16, no. 5, pp. 442–452, 2008.

[47] D. Mattia, F. Cincotti, L. Astolfi, et al., "Motor cortical responsiveness to attempted movements in tetraplegia: evidence from neuroelectrical imaging," *Clinical Neurophysiology*, vol. 120, no. 1, pp. 181–189, 2009.

[48] P. J. Roback and R. A. Askins, "Judicious use of multiple hypothesis tests," *Conservation Biology*, vol. 19, no. 1, pp. 261–267, 2005.

[49] R. D. Traub, A. Bibbig, A. Fisahn, F. E. N. Lebeau, M. A. Whittington, and E. H. Buhl, "A model of gamma-frequency network oscillations induced in the rat CA3 region by carbachol in vitro," *European Journal of Neuroscience*, vol. 12, no. 11, pp. 4093–4106, 2000.

[50] K. J. Friston, W. Penny, C. Phillips, S. Kiebel, G. Hinton, and J. Ashburner, "Classical and Bayesian inference in neuroimaging: theory," *NeuroImage*, vol. 16, no. 2, pp. 465–483, 2002.

Hindawi Publishing Corporation
Computational Intelligence and Neuroscience
Volume 2009, Article ID 950403, 9 pages
doi:10.1155/2009/950403

Research Article

Some Computational Aspects of the Brain Computer Interfaces Based on Inner Music

Wlodzimierz Klonowski,[1] Wlodzisław Duch,[2] Aleksandar Perovic,[3] and Aleksandar Jovanovic[3]

[1] *Laboratory of Biosignal Analysis Fundamentals, Institute of Biocybernetics & Biomedical Engineering, Polish Academy of Sciences, 02109 Warsaw, Poland*
[2] *Department of Informatics, Nicolaus Copernicus University, 87-100 Torun, Poland*
[3] *Group for Intelligent Systems, School of Mathematics, University of Belgrade, 11000 Belgrade, Serbia*

Correspondence should be addressed to Aleksandar Jovanovic, aljosha.jovanovich@gmail.com

Received 21 September 2008; Revised 11 January 2009; Accepted 11 March 2009

Recommended by Fabio Babiloni

We discuss the BCI based on inner tones and inner music. We had some success in the detection of inner tones, the imagined tones which are not sung aloud. Rather easily imagined and controlled, they offer a set of states usable for BCI, with high information capacity and high transfer rates. Imagination of sounds or musical tunes could provide a multicommand language for BCI, as if using the natural language. Moreover, this approach could be used to test musical abilities. Such BCI interface could be superior when there is a need for a broader command language. Some computational estimates and unresolved difficulties are presented.

1. Introduction

The recent impressive developments of brain computer interfaces, BCI, after initial great success, especially, by the group of Babiloni [1–5], and earlier biofeedback achievements [6], open room for optimism in diverse directions. Work on BCI has been concentrated on motor imagery; here an alternative direction is proposed, musical imagery [7, 8].

Just like an imagination of hand or finger movement is related to changes in activity of the brain somehow resembling those connected with the real movement, so the process of mental hearing and comprehending music is related to changes in brain activity somehow resembling those occurring in the brain when listening to real physical sounds of music. Such a cognitive process of *auditory imagery*, of singing in the mind, is also called *audiation*; audiation of music is analogous to thinking in a language. We propose that it is possible to construct a BCI based on the Inner Tones and Inner Music, that is, the BCI in which discrimination of the imagined or inner tones is used as the basic brain signal for the formation of the BCI set of commands—musical language.

After partial success in the identification of inner tones, as reported in [7, 9–13], in spite of encountering serious difficulties, we propose that more attention should be given to the BCI based on the Inner Tones and Inner Music. We have developed systems for the real-time acquisition and analysis of unlimited number of EEG and other neural signals (in banks of up to 64), in the acoustic and higher ranges, that is, with diverse rates starting from 2 KHz, using mainly Innovative Integration (http://www.innovative-dsp.com) DSP-embedded systems (ADC64, M62/7, multiprocessor QUATRO, Chico). We experimented with recognition of inner tones and have hundreds of recordings with 8-channel EEG, with sampling rates 4–11 KHz. We concentrated mainly on simple experiments. A subject was listening to a calibration tone shortly, then started imagining the same tone, then we had EEG registration for short time, 5–10 seconds. We performed also experiments with simple melodies of external or imagined origin. Our basic tool is Fourier real-time analysis. Examples of the power spectra and spectrograms of EEG recordings of externally played tones, exhibiting the spectral lines corresponding to the played tones, are shown in Figures 1 and 2.

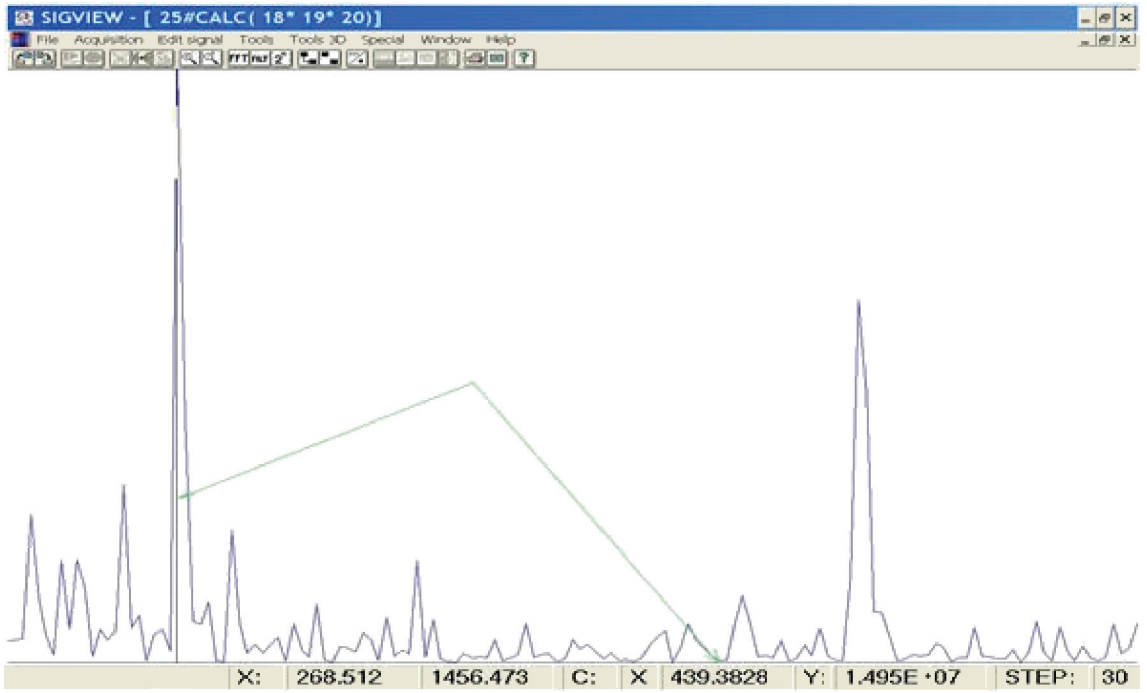

Figure 1: A part of a power spectrum of EEG recording of sequentially played tones d and a, marked the spectral line corresponding to the tone a.

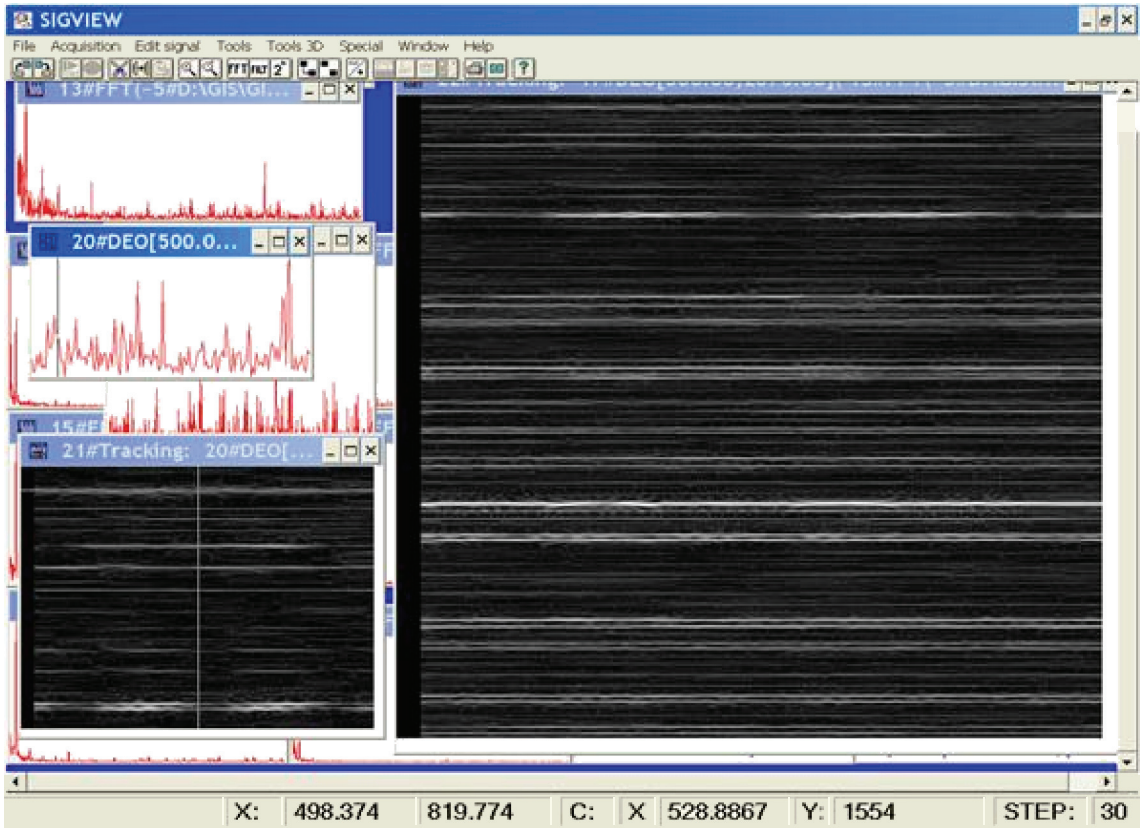

Figure 2: A power spectrum of EEG signal recording with simultaneously played tones c2 and g2, top left; its part containing c2 and g2 lines, left center; the spectrogram of the extracted portion of the spectrum, with prominent c2 and g2 lines, low left; the major part of the spectrogram exhibiting some artifacts and other high-frequency features, right side. Low frequency—bottom; intensity—brightness coded; time—recent at the right edge.

With the inner tones, power spectra and spectrograms are similar to the examples with external tones, but the spectral lines corresponding to the individual tones and their harmonics in the spectrograms are often less prominent or closer to the noise level, hence harder to detect. The complete spectra exhibit a number of features in the HF part of the spectra, not corresponding to the produced inner tones. However, we have positive evidence: in a significant number of experiments (123 out of 147), spectral lines corresponding to imagined inner tones were detected, while the lines corresponding to the tones which were not imagined were not detectable. The experiments with subjects lacking music ability were negative: the tones they imagined were not detectable as the presence of the spectral lines corresponding to the calibration frequencies. We will present some examples with successful extraction of inner tones; more details are available in the mentioned reports. Our signal library and software are available at http://www.matf.bg.ac.yu/~aljosha and http://www.gisss.matf.bg.ac.yu.

2. Method

The problem of detection of the inner tones can be seen from two sides. One is when we know which the generated inner tones are, whose traces we are detecting. More difficult is the inverse problem: in the given spectra determine the present inner tones. The complete solution of the former will facilitate solution of the other, which is of importance in the BCI as we propose it. More precisely, we will consider simple tones, that is, those with constant frequency and constant intensity, with a beginning and an end in time. At the beginning all tones could be of the same (similar) length. We call tonal sequence a sequence of simple tones. In this way we omit some of common melodious patterns. A spectrogram of a tonal sequence is a tonal spectrogram. Let us consider a correspondence:

$$f : Ts \longrightarrow S_\pi, \tag{1}$$

that is, f is a correspondence between the space of tonal sequences and the space of tonal spectrograms. For our needs, let S_π be the space of spectrograms of EEG recordings with tonal stimuli of external origin or imagined. We know that f cannot be a bijection (hence, the f^{-1} is not a function). However, if we make some restrictions/simplifications on T_s, that will have the same effect as introducing an equivalence relation in T_s, some sort of glue, identifying certain spectra, which are similar with respect to some properties. Instead of T_s, we will be dealing with its homomorphic image. Then, after a reduction of nontonal spectral lines in our EEG spectrograms, we might be able to determine the inverse.

Our initial space S_π consists of the spectrograms of EEG recordings of acoustic stimuli, the tonal sequences, and our basic task is to determine the original tonal sequences from the corresponding spectrograms of EEG recordings. Obviously, the recovery of a tonal sequence is reducible to the sequence of the identifications of individual tones, which simplifies the basic task. Precision constraints are well known in techniques for long time; in the low part, the tonal difference perception, that is, minimum the quarter semitone, determines minimal spectral resolution of 1/4 Hz, while the tonal coloring aliquots have to reach 16 to 20 KHz. Thus, in standard acoustics we need vectors in our simplified spectrograms of up to 80 K coordinates (e.g., the higher quality acoustic standard in broad use is 96 KHz/24bit), adding the number of recording inputs, which is here the number of EEG/MEG electrodes. Hence, we are working in the space whose dimension is beyond 80 000.

For the inner music-based BCI needs, when a subject generates an inner tone, it should be detected and recognized by the BCI. We will introduce simplifications which will reduce this dimension substantially, downscale problem complexity, and bring it closer to be feasible. The composition of all simplifications/restrictions on tonal sequences will define the target homomorphic image of the space T_s. But because the nature of music this dimension can hardly go under 4 K. Hopefully, we can neglect a large number of these coordinates at each moment, focusing our attention on the very short subsequences. These are harmonic sequences of individual tones, with <10 aliquots, which have the following form:

$$\langle \lambda_k k\nu \mid \lambda_k \varepsilon R, \quad k\varepsilon N \ \cap 10\rangle, \text{ for a basic frequency } \nu, \tag{2}$$

or with fuzzification:

$$\langle [\lambda_k k\nu - \delta, \ \lambda_k k\nu + \delta] \mid \lambda_k \varepsilon R, k\varepsilon N \cap 10, \delta\varepsilon R\rangle \tag{3}$$

and all have the same length in time. They would form very simple manifolds in those large dimension spaces. Our task is to detect and identify them. Recognition of individual tones of a tonal sequence in the (acoustic) registration of loud singing is simple. The similar task of recognition of an inner (simple) tonal sequence is not so simple and has not been achieved satisfactorily yet.

This approach has some attractive features and leads to some difficulties that may limit its applicability for some time. Generally, we can imagine whatever we can hear. Especially musical contents consisting of consecutive tone series and synchronous tones—intervals and accords. It is simpler to imagine tones to sing mute what can be sung aloud. Our initial restriction to (simple) tonal sequences will be extended by restricting the frequency range to that of a human voice. We have about two and half octaves available as easily controllable (mute) inner tones, that is, the set of about 24 to 32 states. Talented singers control up to 4 octaves, or 48 states, while imaginable tonal interval expands to nearly 100. This gives an opportunity for generation of imagined musical sequences—words, using alphabet of about 30 or more elements.

Tonal sequences can be produced with similar speed of spoken words. The constraints present in certain tonal sequences roughly correspond to the set of unused sequences in the spoken language. Roughly, with serial tones BCI we are in the range of the verbal communication transfer rates and information flow capacity. Using brain states corresponding to intervals and accords would expand this capacity largely. There are other living species communicating musically and

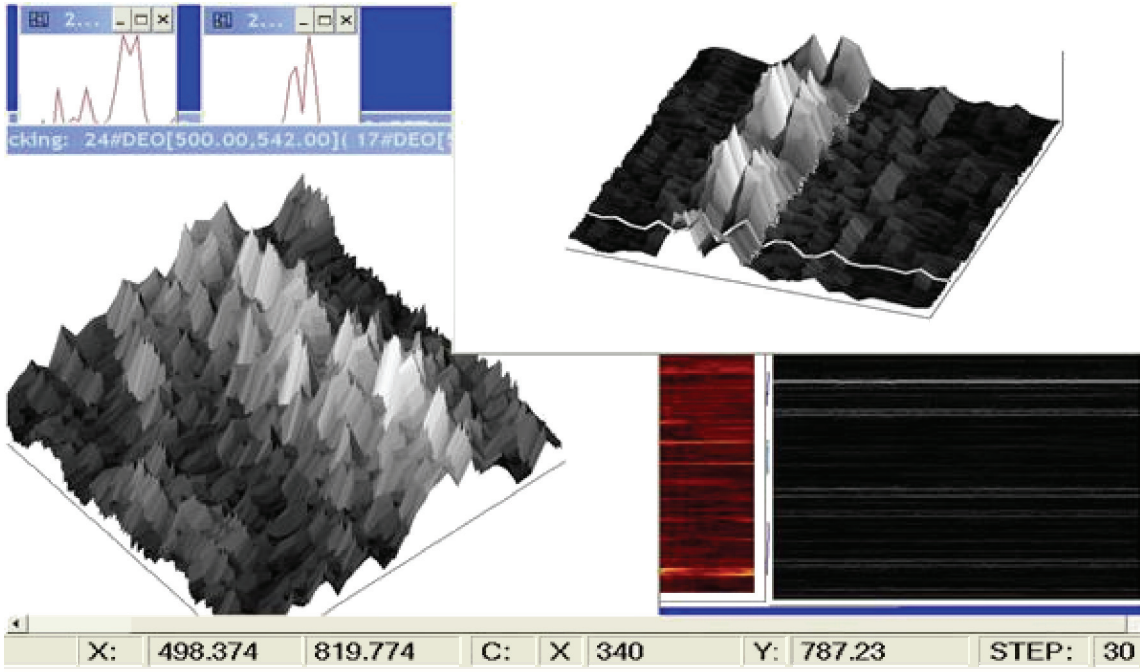

Figure 3: An example of spectrogram feature profiles, magnification of details in the Figure 2, the local neighborhood of c2 and g2 (shown up-787 Hz)—externally played on little organ; both tone profiles show the tonal time stability, but both have spectral width of 15 Hz, while the frequency structure top is stable and reasonably narrow.

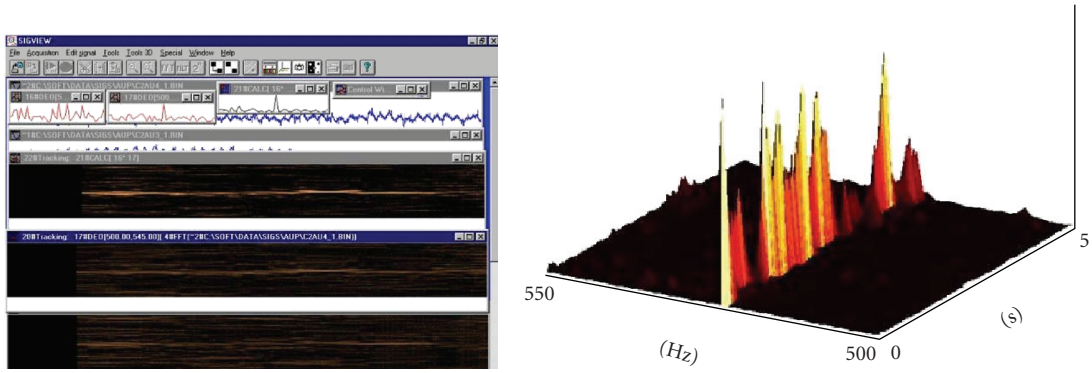

(a) (b)

Figure 4: Left side: spectrograms with 800 power spectra parts (frequency interval 500–550 Hz) of two EEG channels with the inner tone c2, lower and middle; their dot product-left top-top view and the side view on the right side-giving the enhanced c2 in the composite spectrogram, well discernible. Time duration 5 seconds.

there are natural languages with serious musical components. In either case the development of richer musical languages should follow and would be a nice challenge per se.

3. Computational Aspects

Computational aspects will be discussed further with a simple example. Suppose we have two individuals, one producing inner tones in the range c–c2, the other in the range c1–c3 interval. Thus, each is using two octaves. With the tuning fork **a** at 440 Hz, this gives frequency range 132–1056 Hz for both individuals. Suppose that the shortest event time duration corresponds to 1/16th in tempo moderato (ornaments are performed at double and triple speed), which is around 0.2 second.

The above values set the sampling rate at 2.2 K samples or higher, just to record the first harmonics of the involved tones. Actually the double rate would be necessary. A half quarter tone resolution is needed, which at the lower end of frequency interval gives required spectral resolution of about 2 Hz. The FFT on the input 2 K time series should then provide the desired spectral resolution. The 2 K input FFT covers the time interval of nearly 0.5 second, usually denoted as uncertainty time (because in that time interval the time order is not directly observable from the spectra, which is clear from basic calculations). That means that

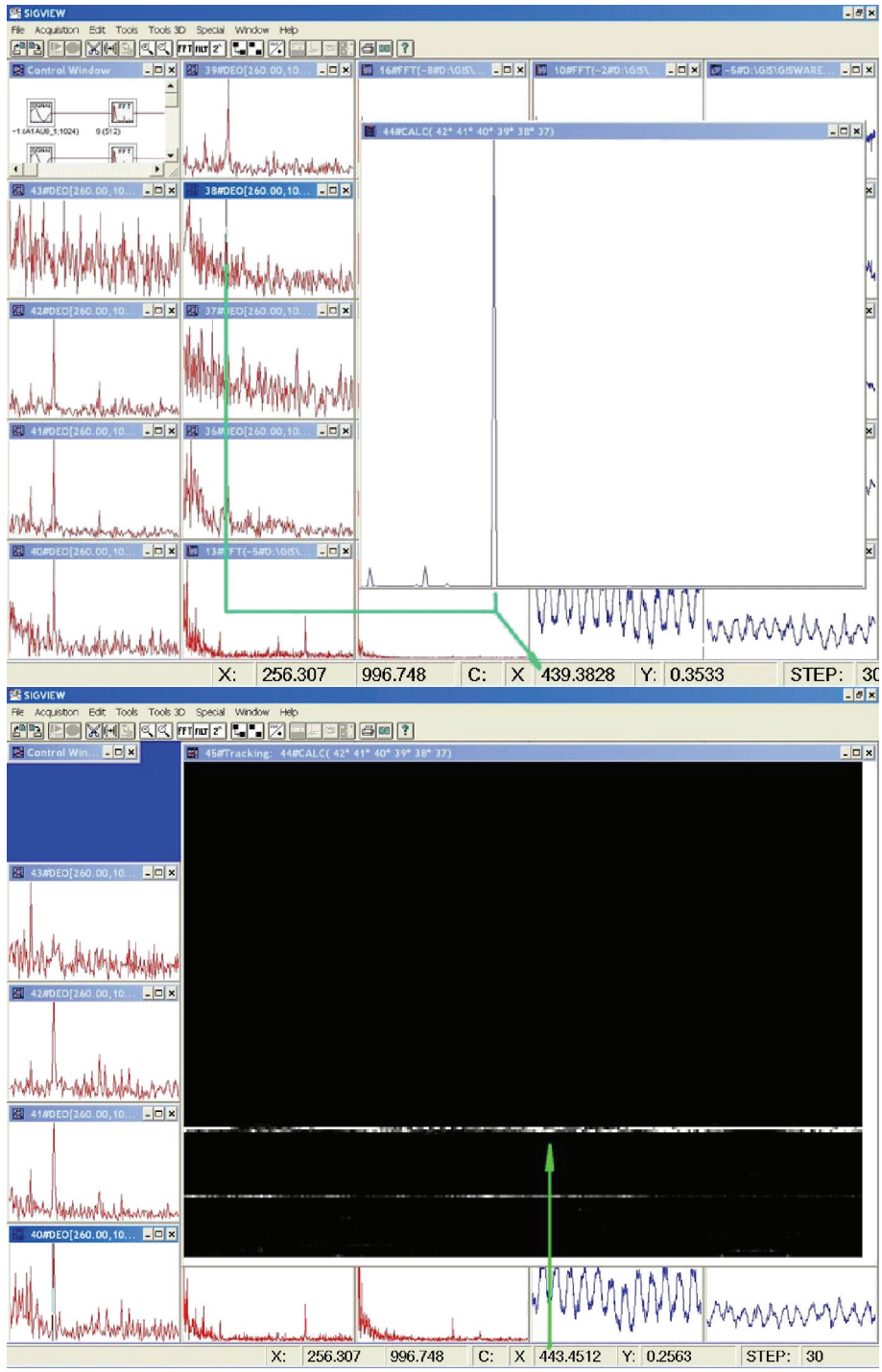

Figure 5: Top: Recording of Inner tone—a tuning fork **a** at 440 Hz, 8 EEG channels, spectral parts from 207 to 2078 Hz, marked 440–443 Hz feature in the dot product of best responding 6 channel spectra with overall well extracted 440–443 Hz line. Lower: (accumulated) time composite spectra—the dot product from the top part of the figure; time horizontal, frequency vertical, intensity coded by brightness.

approximately tone rhythmical values of 1/8th and longer can be located precisely in time. Their amplitudes will be presented correctly.

In order to resolve shorter rhythmic values and to determine their proper amplitudes, which are essential in the involved inner tones, we would need a recalculation of spectra toward the recalibrated spectra, which can be done easily for the restricted sorts of input tonal sequences, from the obtained spectrograms—time spectra. However, it involves time delay, which is hardly smaller than the time atom.

Suppose further that we have to deal only with the tonal values from semitonal tempered (classical tonal) system.

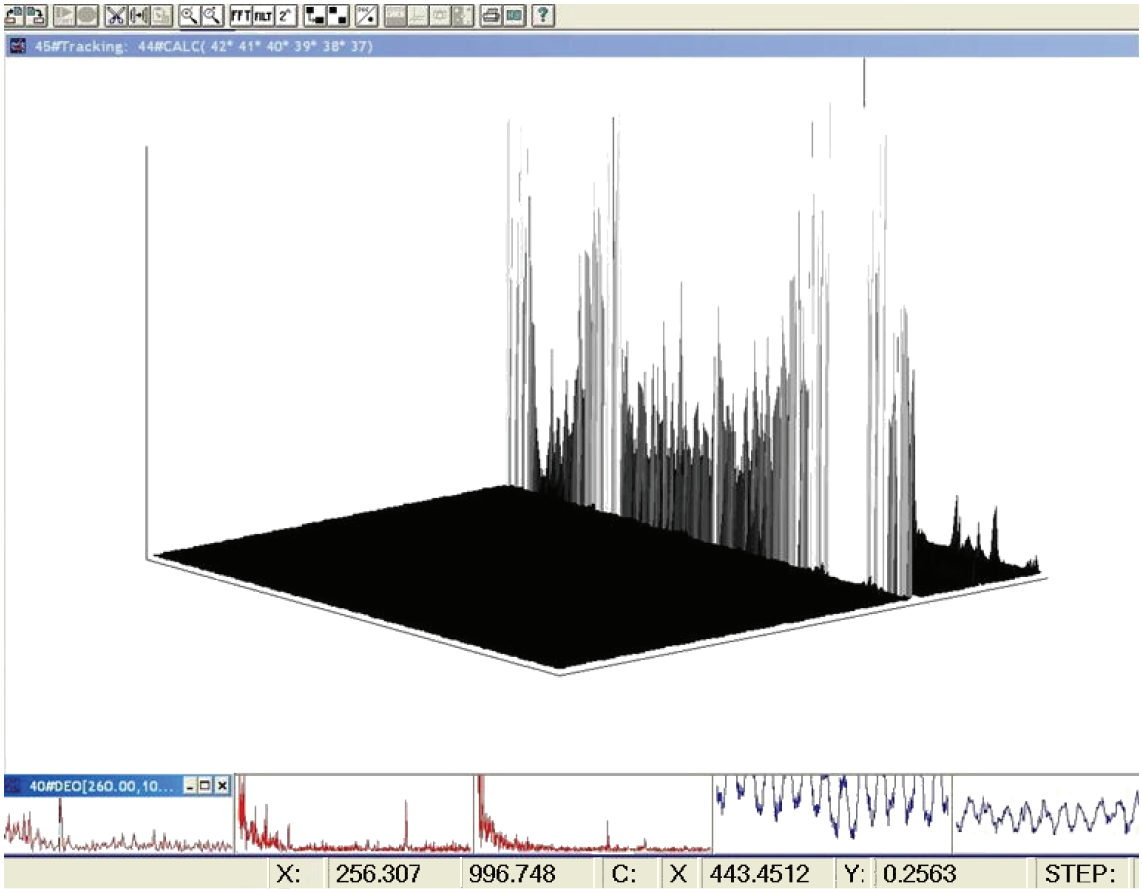

Figure 6: 1000 consecutive composite spectra—the dot products of the 6 best responding channels (as in the previous figure top view), the side view, prominent a 440–443 Hz feature-spectral profile, time duration 5 seconds.

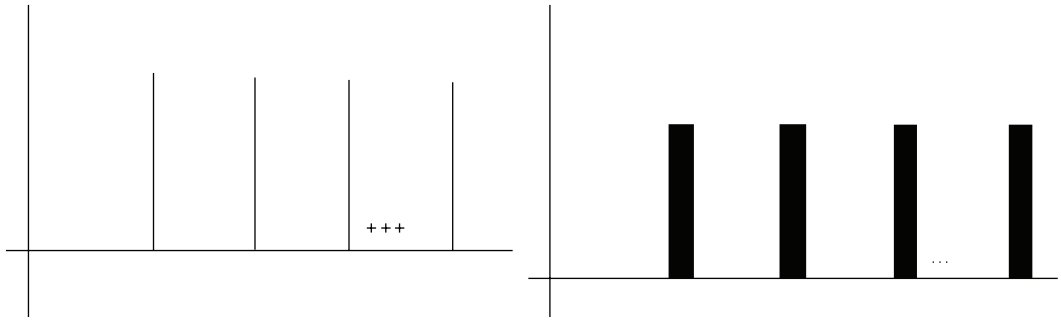

Figure 7: The comb-like tonal representation and its fuzzification are used for the design of the corresponding comb like filters, one for each tone, which support the automatic spectrogram and composite spectrogram analysis using combing operators and subsequent matching measurements within the strategy for the detection of inner tones.

At the beginning of BCI use, and at any moment after, a calibrating scale can be played. Figure 3 shows how wide in the spectrum could be the externally played tone in an EEG spectrogram. A lot of usual songs satisfy these constrains and simplify further our starting space of tonal sequences T_s for BCI needs.

Extraction of inner tones may be done in two ways. The first one is to train a neural network to recognize the fingerprints of the inner tones. It can hardly avoid (some sort of) spectrograms as initial objects. This approach is fruitful and can provide easier way to recognize the inner tones. We are experimenting with adaptations of neural networks for speech recognition, developed with the Institute for Applied Mathematics and Electronics (Yugoslav national army/Serbian armed forces), [14].

Independently, we have developed a system with components of the extractor that include open calculator, with a number of operations on signals and spectra. The inner

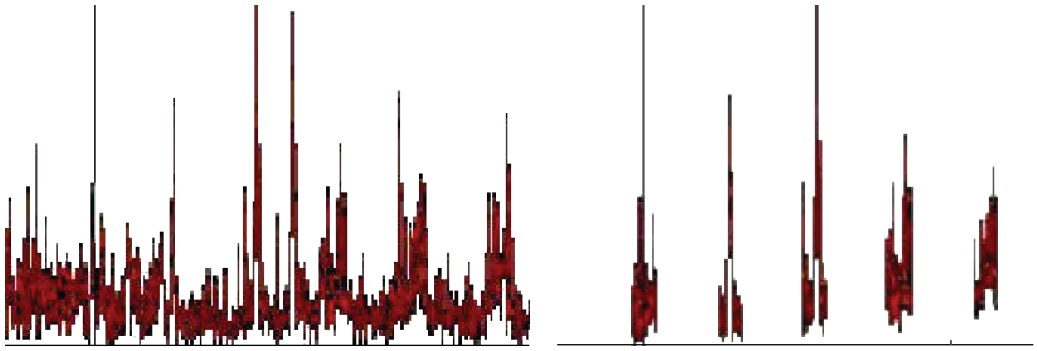

Figure 8: A power spectrum of the externally generated tone c1 on the left; right: the result of its combing with the c1 fuzzy-comb filter in the procedure of measurement of linear dependence between the spectrograms with tonal patterns and the tonal fuzzy comb like filters. The higher the linear dependence, the higher the volume, consequently, the better the matching of spectrogram with a tonal pattern.

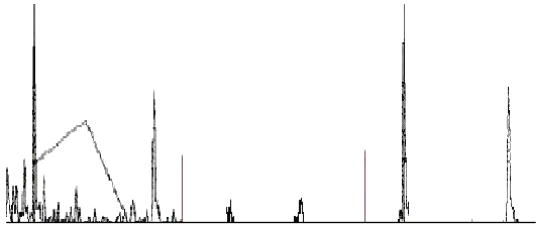

Figure 9: Left: A (part of a) power spectrum of externally sequentially played tones (d, a) (overlapped in the FFT epoch), prominent line corresponding to the tone a; in the middle: the same spectrum combed with the fuzzy comb for c1; right: the same spectrum combed with the fuzzy comb for minor a. This illustrates the response of combing with the wrong and proper matching comb-like filter.

tone harmonics are present in the signals from different electrodes. Activity recorded with an electrode is partly local. The inner tones harmonics are of smaller magnitude compared to the low frequency (LF) part of the EEG spectra activity, but they are in the HF area. Often, they are hardly discernible in their spectral neighborhood. The spectra are locally linearly dependent in the coordinates with harmonics of inner tones and locally linearly independent in the frequency intervals where the local activity prevails. This means that the composite spectrograms obtained with the dot products of combinations of spectra from different electrodes would enhance the everywhere present spectral lines, which includes the inner tone harmonics, while the spectral zones with prevailing local activity would be zeroed. Some examples with nice spectral localization of inner tones using these properties are presented in Figures 4, 5, and 6.

We have implemented comb-like filters and their fuzzifications, corresponding to the tonal structures in (3), at calibrating scale frequencies. These provide a way for an automatic analysis of spectra and composite spectra based on the combing operations and the afterward comparisons with the tonal system-calibrated values, with measurement of best matching, as illustrated with the examples in Figures 7, 8, and 9. This offers a simple strategy and algorithm for the identification of inner tones. The comb-like filters corresponding to the set of tones used for inner singing are coordinate vise multiplied with the spectrograms or composite spectrograms, ordering the outcomes by the maximal volume. We have developed algorithms for the automatic detection of spectrogram feature contours complementing the combing operations.

Next needs are the parallel multiple resolution FFT (which we have in fragments) for short event precise location in time and separation of adjacent tones, feature frequency instability compensation, and separation of tones and their aliquots.

The tuning system should include a scanning of all channels and a selection of those with better response, a reduction of other HF features not related to external and internal tones, based on the time length discrimination and separation from the calibrating scale tones.

This approach could lead to the intelligent extractor which would be aware of the detected inner tone. In order to improve performance, both approaches can be combined concurrently in parallel. For the further convergence, more experimentation with higher resolution EEG would be necessary. In this way, with proposed steps (some of which are realized), reaching a number of simplifications and partially answering the list of encountered problems, the BCI based on inner tones and inner music would be cured of some deficiencies and instability and will become closer to real applications.

4. Discussion

Current BCIs are based on a discrimination of a few commands only. The application of high-resolution EEG in research on inner tones should strongly support further developments of a multicommand system, at least for musically gifted people. It could provide a tool to study causes of musical perception deficiencies, determine and locate problems shared by a large population. It could provide better insight in the difference of musical processing by music professionals and nontrained people, which is highly interesting for cognitive and brain development studies. A number of researchers are successfully involved

in inner tones and music [8]. Especially interesting is the recent success of Mick Grierson of Goldsmiths, University of London, who demonstrated high-rate guessing of inner tones with his BCI (reports with real-time show, BBC June 2008, forthcoming [15]). Precise positioning of electrodes will reduce the current complexity of inner tone detection problems with simplified automatic extraction of inner tones and support evolution of the BCI based on inner music [16]. We plan to expand our open system soon with a spatiotemporal analysis and analysis of global trajectories in the transformed space [17]. Other researchers are developing the BCI based on HF EEG [18–20] and further proceeding from biofeedback and with motor imagery-based BCI [20–23].

The exciting MEG experiments with musical stimuli presented by Andreas Ioannidis in his lecture at the NEUROMATH'2007 workshop in Rome, December 2007, (system and methods presented in [24]), with one millisecond time resolution, demonstrated that a large number of very fast switching interconnected centers are engaged in music processing. This establishes serious hopes that inner music could be subjected to much more sophisticated and sensitive investigation. When we learn more details on mechanisms of this interconnectivity, revealing delays and modulations involved, we might get complementary powerful methods applicable for the study of inner tones, which would result in the improvement of certainty of inner tone detection and representation of details.

Acknowledgments

The authors are grateful to Katarina Tomašević from Musicology Institute, Serbian academy of sciences and arts, for her guidance and contribution in the inner music analysis and precision in generation of first detected inner tones in early 1994, which stimulated strongly their later work and supported their self confidence in final success. The authors are thankful to their graduate student Stevan Kordic for his contributions in the development and integration of early digital EEG using DSP systems, which were applied in the investigations of inner tones and inner music.

References

[1] F. Babiloni, F. Cincotti, M. Marciani, et al., "The estimation of cortical activity for brain-computer interface: applications in a domotic context," *Computational Intelligence and Neuroscience*, vol. 2007, Article ID 91651, 7 pages, 2007.

[2] F. Babiloni, A. Cichocki, and S. Gao, "Brain-computer interfaces: towards practical implementations and potential applications," *Computational Intelligence and Neuroscience*, vol. 2007, Article ID 62637, 2 pages, 2007.

[3] F. Cincotti, D. Mattia, C. Babiloni, et al., "Classification of EEG mental patterns by using two scalp electrodes and Mahalanobis distance-based classifiers," *Methods of Information in Medicine*, vol. 41, no. 4, pp. 337–341, 2002.

[4] F. Cincotti, D. Mattia, C. Babiloni, et al., "The use of EEG modifications due to motor imagery for brain-computer interfaces," *IEEE Transactions on Neural Systems and Rehabilitation Engineering*, vol. 11, no. 2, pp. 131–133, 2003.

[5] J. del R Millan, J. Mourino, M. Franze, et al., "A local neural classifier for the recognition of EEG patterns associated to mental tasks," *IEEE Transactions on Neural Networks*, vol. 13, no. 3, pp. 678–686, 2002.

[6] J. P. Rosenfeld, "An EEG biofeedback protocol for affective disorders," *Clinical EEG Electroencephalography*, vol. 31, no. 1, pp. 7–12, 2000.

[7] A. Jovanovic, "Brain signals in computer interface," *Intelektualnie Sistemi*, vol. 3, no. 1-2, pp. 109–117, 1998 (Russian).

[8] R. J. Zatorre and A. R. Halpern, "Mental concerts: musical imagery and auditory cortex," *Neuron*, vol. 47, no. 1, pp. 9–12, 2005.

[9] A. Jovanovic, "Inner music, report on the conference Mathematics and other sciences," Greek Math Soc. Crete, Greece, 1995.

[10] A. Jovanovic, "CD-ROM: CCD microscopy, image & signal processing," School of Mathematics, University of Belgrade, 1997.

[11] A. Jovanovic, "Research in the group for intelligent systems at Belgrade University, problems and results," *Intelektualnie Sistemi*, vol. 6, no. 1–4, pp. 163–182, 2001 (Russian).

[12] A. Jovanovic, M. Jovanovic, A. Perovic, and M. Maric, "A system for neural acoustics analysis," in *Proceedings of the 4th Annual Serbian-Hungarian Joint Symposium on Intelligent Systems (SISY '06)*, pp. 275–283, Subotica, Serbia, September 2006.

[13] A. Jovanovic and A. Perovic, "Brain computer interfaces, some technical remarks," *International Journal for Bioelectromagnetism*, vol. 9, no. 3, pp. 91–102, 2007.

[14] D. Protic and M. Milosavljevic, "NNARX model of speech signal generating system: test error subject to modeling mode selection," in *Proceedings of the 25th International Conference on Microelectronics (ICM '06)*, pp. 685–688, Belgrade, Serbia, May 2006.

[15] M. Grierson, "Composing with brainwaves: minimal trial P300b recognition as an indication of subjective preference for the control of a musical instrument," in *Proceedings of International Cryogenic Materials Conference (ICMC '08)*, Seoul, Korea, July 2008.

[16] W. Klonowski, "From conformons to human brains: an informal overview of nonlinear dynamics and its applications in biomedicine," *Nonlinear Biomedical Physics*, vol. 1, article 5, pp. 1–19, 2007.

[17] K. Dobosz and W. Duch, "Fuzzy symbolic dynamics for neurodynamical systems," in *Proceedings of the 18th International Conference on Artificial Neural Networks (ICANN '08)*, vol. 5164 of *Lecture Notes in Computer Science*, pp. 471–478, Prague, Czech Republic, September 2008.

[18] J. K. Kroger, L. Elliott, T. N. Wong, J. Lakey, H. Dang, and J. George, "Detecting mental commands in high-frequency EEG: faster brain-machine interfaces," in *Proceedings of the Biomedical Engineering Society Annual Meeting*, Chicago, Ill, USA, October 2006.

[19] C. Watkins, J. Kroger, N. Kwong, L. Elliott, and J. George, "Exploring high-frequency EEG as a faster medium of brain-machine communication," in *Proceedings of the Institute of Biological Engineering Annual Meeting*, Tucson, Ariz, USA, March 2006.

[20] M. Kallenberg, "Auditory selective attention as a method for a brain computer interface," 2006, http://www.nici.kun.nl/mmm/papers/MK_Auditory_BCI.pdf.

[21] N. Birbaumer, A. Kübler, N. Ghanayim, et al., "The thought translation device (TTD) for completely paralyzed patients,"

IEEE Transactions on Rehabilitation Engineering, vol. 8, no. 2, pp. 190–193, 2000.

[22] A. Materka and M. Byczuk, "Alternate half-field stimulation technique for SSVEP-based brain-computer interfaces," *Electronics Letters*, vol. 42, no. 6, pp. 321–322, 2006.

[23] L. Astolfi, F. Cincotti, C. Babiloni, et al., "Estimation of the cortical connectivity by high-resolution EEG and structural equation modeling: simulations and application to finger tapping data," *IEEE Transactions on Biomedical Engineering*, vol. 52, no. 5, pp. 757–768, 2005.

[24] L. Liu, K. Arfanakis, and A. Ioannides, "Visual field influences functional connectivity pattern in a face affect recognition task," *International Journal of Bioelectromagnetism*, vol. 9, no. 4, pp. 245–248, 2007.

Hindawi Publishing Corporation
Computational Intelligence and Neuroscience
Volume 2009, Article ID 549419, 16 pages
doi:10.1155/2009/549419

Research Article

A Framework Combining Delta Event-Related Oscillations (EROs) and Synchronisation Effects (ERD/ERS) to Study Emotional Processing

Manousos A. Klados,[1] Christos Frantzidis,[1] Ana B. Vivas,[2] Christos Papadelis,[1] Chrysa Lithari,[1] Costas Pappas,[1] and Panagiotis D. Bamidis[1]

[1] *Laboratory of Medical Informatics, School of Medicine, Aristotle University of Thessaloniki, P.O. Box 323, 54124 Thessaloniki, Greece*
[2] *Department of Psychology, City College, Affiliated Institution of the University of Sheffield, 54624 Thessaloniki, Greece*

Correspondence should be addressed to Panagiotis D. Bamidis, bamidis@med.auth.gr

Received 21 March 2009; Revised 21 March 2009; Accepted 29 April 2009

Recommended by Laura Astolfi

Event-Related Potentials (ERPs) or Event-Related Oscillations (EROs) have been widely used to study emotional processing, mainly on the theta and gamma frequency bands. However, the role of the slow (delta) waves has been largely ignored. The aim of this study is to provide a framework that combines EROs with Event-Related Desynchronization (ERD)/Event-Related Synchronization (ERS), and peak amplitude analysis of delta activity, evoked by the passive viewing of emotionally evocative pictures. Results showed that this kind of approach is sensitive to the effects of gender, valence, and arousal, as well as, the study of interhemispherical disparity, as the two-brain hemispheres interplay roles in the detailed discrimination of gender. Valence effects are recovered in both the central electrodes as well as in the hemisphere interactions. These findings suggest that the temporal patterns of delta activity and the alterations of delta energy may contribute to the study of emotional processing. Finally the results depict the improved sensitivity of the proposed framework in comparison to the traditional ERP techniques, thereby delineating the need for further development of new methodologies to study slow brain frequencies.

1. Introduction

During the past few years many studies have attempted to investigate the role of neuronal mechanisms involved in emotional processing [1]. Most of those studies employed Event-Related Potentials (ERPs) and focused on the detection of time-locked changes in the activity of large pools of neurons [2]. This approach has been mostly preferred because induced cerebral activity demonstrates an almost fixed time-delay to the stimulus onset, and it superimposes to the normal ongoing brain signals, which are regarded as additive noise. In these studies, typically a sufficiently large number of epochs with the same stimulus type are averaged in order to enhance the signal-to-noise (SNR) ratio. Consequently, this type of analysis aims at enhancing certain ERP components. However, this model can only roughly approximate reality, since it cannot deal with robust dynamical changes that occur in the human brain [3].

It is known that EEG activity is generated by sets of circuits [4]. The neuronal cells involved in these circuits are synchronized upon the appearance of a novel stimulus. Therefore, their activity is coupled and overall EEG coherency is enhanced. Thus, the system's complexity is reduced since it becomes more ordered. This results in the generation of rhythmic oscillations in various frequency bands which are superimposed on each other to form the compound event-related potential [5]. So, the analysis of ERP waves and their oscillations may promote our biophysical understanding of the brain functional networks and the investigation of both the global and the local characteristics of human brain

activity. For instance, it is known [6], that there are particular events, which are time-locked to the event, but not phase-locked, and have an inhibitory effect to the alpha rhythm [7]. Consequently, the underlying cognitive processes cannot be thoroughly revealed using linear methods. Due to this limitation, frequency analyses are more appropriate, as long as, we assume that certain events affect specific bands of the ongoing EEG activity. This would result on the synchronization or desynchronization of underlying neurons exactly after the event (Event-Related Synchronization (ERS) or Desynchronization (ERD)) [7, 8]. The aforementioned reactions are time-locked to the event and concern specific brain waves. This type of spectral analysis is employed since selectively distributed oscillatory networks in the various frequency ranges control in an integrative way brain functions at every sensory and cognitive level. Cognitive processing of emotional visual stimuli involves several complex functions such as sensory processing, attention, decision making, and memory. Despite the potential interest of using such methodologies to emotionally evocative stimuli, research with these types of analyses employing the International Affective Picture System (IAPS) [9] is scarce.

A few such studies have indeed shown that brain rhythms are associated with several cognitive processes. For instance, an increase in theta activity has been associated with initial learning improvement, which is typically followed by a decrease that reflects habituation processes [10]. A more relevant study, it has been shown that the amygdala produces theta activity in response to emotionally evocative stimuli [11]; whereas detection of unpleasant stimuli has been associated with theta synchronization in the hippocampus, which appears to be lateralized to the right hemisphere [12]. Moreover, slow waves, contribute to the detection of salient-infrequent-stimuli, and consequently, they contribute to the P300 response [13, 14]. Taken all together, these findings suggest that slow cerebral oscillations are suitable to study the cognitive processes related to emotions.

Moreover, in the last few years, there is growing interest in investigating the neuronal mechanisms involved in the processing of emotionally evocative pictures [15, 16] using IAPS. IAPS pictures are rated in terms of valence and arousal. According to [17] emotional processing is mediated by two brain systems; the appetitive and the defensive. These two systems have evolved in order to assure the physical survival. The property "valence" refers to the direction of behavioral activation according to the motivational system induced by the stimulus. The property "arousal" represents the activation level elicited by the emotionally evocative stimulus [18]. The defense system is mainly active in unpleasant situations ranging from threat to melancholy and it is associated with "fight-or-flight" responses. On the other hand, the presence of pleasant situations like sustenance, procreation and nurturance activates the appetitive system. Therefore, the valence dimension refers to the system that is activated, while the arousal dimension refers to the intensity of this activation [19].

A few studies have investigated oscillatory modulation with visual emotional stimuli from the IAPS. In one of these studies [20], they investigated spectral responses in the gamma range by means of wavelet transforms, and found early effects (80 ms after stimulus onset) of the activity around 30 Hz which discriminated unpleasant stimuli from pleasant ones. Moreover, there was a later increase (480–550 ms poststimulus) in higher frequencies which appeared to be a reliable indicator of arousal. Theta activity has also been related to emotional stimuli, as early synchronization of theta activity has been reported, together with an interaction between valence and hemisphere for the anterior temporal regions [21]. In another study, it was found that theta ERS covaried with the stimulus intensity. Furthermore, the increase in theta activity was most pronounced over left anterior regions, and bilaterally over posterior regions [22]. Finally, the same study also reported that desynchronization of the medium alpha range was associated with attentional resources. The synchronization of the upper alpha in anterior cortical areas was also attributed to a greater cognitive involvement during processing of emotionally arousing stimuli [22]. To sum up, gamma, theta and alpha activities seem to be related with different aspects of the processing of emotional stimuli.

However, to our knowledge, there is limited literature about delta wave activity and whether it is modulated during the emotional processing of complex visual scenes, like IAPS pictures, or not. This is in fact surprising, since there is some evidence which suggests that this wave may also play a role in processing of emotional stimuli. For instance, a research has reported a relationship between the P300 component and the delta frequency component [23]. Also, it is generally agreed, that the P300 is associated with unexpected or motivationally relevant stimuli [10]. For instance, emotional stimuli elicit a more pronounced P300 response than neutral ones [16]. Furthermore, studies have shown an increase of the activity in the delta frequency band during sexual arousal [24]. Another study [25] has indicated higher coherence of slow waves in central and posterior regions of the right hemisphere during sexual arousal induced by imagery. A summary of the studies that have been conducted with delta wave activity to investigate cognitive and emotional processes in healthy adults, and brain abnormalities in neurological disorders is shown in Table 1. It is important to notice that most of these studies used the linked earlobes montage, and the number of electrodes varied from 7 to 62.

The aim of the present study is to investigate the feasibility of using event-related delta oscillations to study brain processing triggered by visually complex emotional stimuli. Based on previous research, we hypothesize that delta wave activity, particularly in posterior brain areas, is mainly associated with arousal, whereas valence effects on delta activity will be mostly observed in anterior brain areas. Furthermore, and since our ERP studies have reported gender differences with the same stimuli [17], we also aim to check the replication of such findings in delta wave activity. That is, we suspect increased delta activity for females as compared to males, particularly for unpleasant stimuli. Furthermore, this piece of work aims at the investigation of laterality differences by extending the delta oscillations framework with the inclusion of delta synchronization analysis in terms of ERS/ERD. In addition, as the studying

Table 1: Summary of studies conducted with delta wave activity in healthy adults and patients with neurological disorders, which includes the montage method and the number of electrodes as well.

Authors	Journal	Aim of the study	Montage	Number of electrodes
Yener et al. [26]	European Journal of Neurology (2008)	Detection of subtle abnormalities of cognitive processes	Linked earlobes	13
Başar et al. [27]	Brain Research (2008)	Brain oscillations evoked by the face of a loved person	Linked earlobes	14
Harmony et al. [28]	International Journal of Physiology (1996)	EEG delta activity during difficult mental tasks and analysis of short term memory	Linked earlobes	19
Aftanas et al. [29]	Neuroscience and Behavioral Physiology (2006)	Analysis of evoked EEG synchronization and desynchronization in all frequencies bands in response to sequential presentation of IAPS pictures	Nose	62
Schürmann et al. [30]	Neuroscience Letters (1995)	A new metric for analyzing single trials ERPs based on visual P300 delta responses	Linked earlobes	7
Moretti et al. [31]	Clinical Neurophysiology (2004)	Individual analysis of EEG frequency and band power in mild Alzheimer disease	Linked earlobes	19

of delta wave activity was found to be more sensitive to arousal modulations of emotional stimuli than classic ERP peak studies [32], and it is linked with decision-making and salience feature detection properties [27], it is important to examine whether we obtain stronger valence effects of delta wave activity than with the classic ERP approach. In other words, we aim to compare herein effect sizes for both ERP [17] and delta wave analyses (the present study). Finally, a side methodological aim is to compare the different montage methods for spatial filtering. Although, most of the studies summarized above (Table 1) have employed the linked earlobes montage, only a few studies have actually compared the effectiveness of this method in relation to other methods such as the Common Average Reference (CAR) and (large) Laplacian (LAP).

So, in the remaining of this paper, necessary background knowledge regarding the EROS extraction methodology, the artifact rejection approach and the ERD/ERS computation scheme are provided in Section 2. The results derived from the statistical analysis, which was performed on the average signals of each subject and for each emotional category are presented in Section 3. Finally, the contribution of the proposed framework to the estimation of the slow wave activity during emotional processing is discussed in Section 4.

2. Materials and Methods

2.1. Subjects. Twenty eight healthy adults (14 males and 14 females) participated in the experiment (mean age of males 28.2 ± 7.5, mean age of females 27.1 ± 5.2). All subjects had normal or corrected to normal vision. Each participant signed an informed consent form prior to his/her participation and completed a short questionnaire. All participants were paid for their participation. An approval from the Ethical Committee of the Medical School of the Aristotle University of Thessaloniki, Greece, was granted for this study.

2.2. Stimuli. The participants passively viewed 160 emotional pictures, selected from the IAPS. The pictures were grouped in 4 conditions based on their valence and arousal ratings. The conditions were pleasant pictures with high arousal ratings (HVHA), pleasant pictures with low arousal ratings (HVLA), unpleasant pictures (Low Valence) with high arousal ratings (LVHA), and unpleasant pictures with low arousal ratings (LVLA). More details about valence and arousal ratings for each condition specific to gender are shown in Table 2. The experimental conditions were manipulated between blocks, thus there were four blocks of 40 photographs each.

2.3. Electrophysiological Recordings. During the presentation of each emotional block multichannel, Electroenchaphalogram (EEG) and Electrooculogram (EOG) were recorded with 500 Hz sampling frequency. Nineteen EEG electrodes were placed according to the 10–20 International System at sites Fp1, Fp2, F3, F4, F7, F8, Fz, C3, C4, Cz, T3, T4, T5, T6, P3, P4, Pz, O1, O2 with electrode resistance lower than 20 kΩ. Two EOG electrodes were placed above and below the left eye and another two were placed at the outer canthi of each eye. Two bipolar signals were calculated from these four electrodes, namely vertical EOG (VEOG) and horizontal EOG (HEOG) and used for effective EOG artifact rejection.

Three different montages (Linked Mastoids, Common Average Reference and large Laplacian montage) (Figure 1)

Table 2: Mean and standard deviation as a function of valence and arousal for the pictures used in the study.

Picture group	Males				Females			
	Valence		Arousal		Valence		Arousal	
	mean	SD	mean	SD	mean	SD	mean	SD
HVHA	7.41	1.51	6.59	1.98	7.1	1.7	6.0.	2.26
HVLA	6.65	1.54	3.91	2.15	6.94	1.55	3.85	2.26
LVHA	3.12	1.58	5.93	2.15	2.0	1.37	6.64	2.15
LVLA	3.9	1.53	3.91	2.04	3.6	1.54	4.16	2.1

have been compared for optimal representation of cerebral responses. According to the linked mastoids montage, electrodes with odd indices were referenced to left mastoid and electrodes with even indices were referenced to right mastoid. Central electrodes (Fz, Cz, Pz) were referenced to the half of the sum of left and right mastoids. The Common Average Reference (CAR) which was computed according to the next formula:

$$V_i^{\mathrm{CAR}} = V_i - \frac{\sum_{j=1}^{n} V_j}{n}, \tag{1}$$

where j is the number of electrodes and V_i is the potential of ith electrode. As for the third montage, the large Laplacian reference (LAP) has been employed, since the number of electrodes is restrictive for the small Laplacian reference. The following formula has been used for the calculation of the LAP:

$$V_i^{\mathrm{LAP}} = V_i - \sum_{j \in S_i}^{n} g_{ij} V_j, \tag{2}$$

where

$$g_{ij} = \frac{1/d_{ij}}{\sum_{j \in S_i} \left(1/d_{ij}\right)}, \tag{3}$$

S_i is the set of electrodes surrounding the ith electrode, and d_{ij} is the distance between electrodes i and j (where j is a member of S_i). The aforementioned distance is 3 cm for the small Laplacian montage, in contrast to large one, where the distance of two neighbor electrodes is 6 cm [33]. Linked mastoids were more effective in normalizing the data (see Section 3.1) as compared to the other methods, so it was further used for the purposes of this study. More detailed results are mentioned in Section 3.

2.4. Experimental Procedure. Participants were asked to sit on a comfortable armchair in front of a computer screen placed at 80 cm distance from their eye horizontal level. The experiment started with a 30-second recording, during which, participants were asked to keep their eyes open and look at the blank screen. This recording was followed by another one where participants were asked to keep their eyes closed. These recordings were taken to serve as baseline values. The experimental protocol was comprised of stimuli in the form of IAPS pictures, forming blocks of forty randomly selected pictures according to their arousal and valence ratings (Table 2). The order of the blocks was counterbalanced across participants. Each single epoch had 0.5 seconds prestimulus showing a white cross in the center of the screen and 2 seconds poststimulus period (1 second picture duration followed by 1 second of the white cross). At the end of the procedure the initial 30-second recordings, with eyes open and then closed, were repeated.

2.5. Event-Related Desynchronizations (ERD)/Event-Related Synchronization (ERS). Sensory, motor, cognitive and emotional processing can affect the ongoing EEG by decreasing (ERD) or increasing (ERS) the synchrony of underlying neurons, so cerebral activity can be quantified using the ERD/ERS method which is described in [7]. ERD/ERS depict the percentage of band power changes during a test interval compared to a reference interval in a specific frequency band. There are a lot of different methods used today for quantification of ERD/ERS, which are summarized in [7]. The band power method [8] has been selected for the purpose of this study. According to this method each EEG signal for each channel was band-pass filtered in the delta frequency band (0.5–4 Hz), squared in order to calculate the delta band power, epoched and averaged over trials for each subject and for each emotion block. Finally in order to obtain the percentage of event-related changes in delta band power the following formula was used:

$$\mathrm{ERD(or\ ERS)\%} = \frac{R - A}{R} \cdot 100\%, \tag{4}$$

where R is the power of delta band in the reference interval (here 500 ms prestimulus) and A is the delta band power for the test intervals after the event (here 0–500 ms, 500–1000 ms, 1000–1500 ms, 1500–2000 ms after picture onset). For a more detailed description of this method see [10]. According to the aforementioned formula positive values ($R > A$) indicate that the test interval's band power is lower compared to the reference, which means that delta oscillations decrease their synchrony (desynchronize), and, therefore, ERD is obtained for positive values. Negative values ($A > R$) indicate neuronal synchrony in a similar way and they are obtained for ERS.

2.6. Artifact Rejection. We have used the Least Mean Square (LMS) method, as it was proved to have better a performance among other widely used techniques for artifact rejection, based on Blind Source Separation (BSS) or regression methodology [34]. According to the LMS adaptive filtering

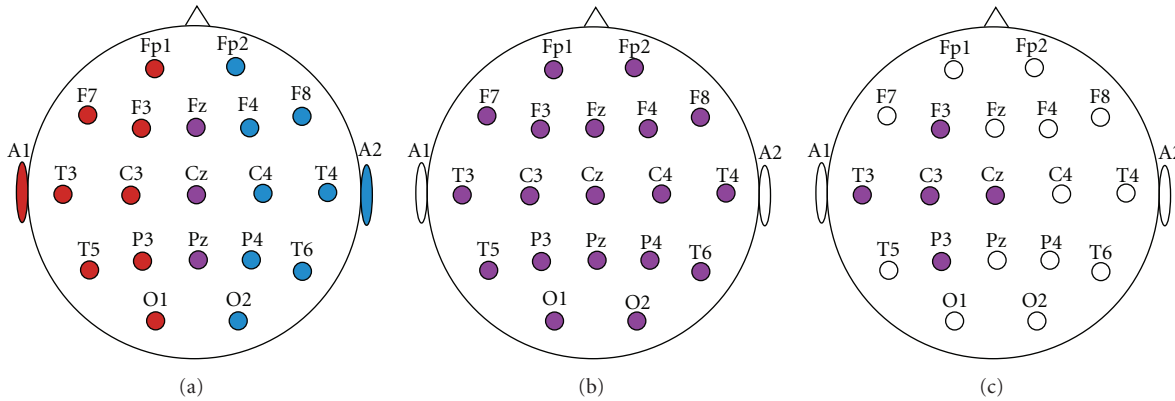

Figure 1: Illustration of the three different montage electrodes referencing methods. (a) Linked Mastoids Montage; left sites are referenced to the A1 while right site are referenced to A2, and the central sites are referenced to the half of the sum of A1 and A2. (b) C.A.R.; each site is referenced to the average of all electrode sites. (c) Large Laplacian; each site is referenced to the weighted average of their one-step neighbors.

procedure, the goal is to adjust the filter coefficients $\hat{w}(n)$ and make them approach the optimal filter coefficients $w(n)$ as close as possible (Figure 2). The underlying idea of the LMS algorithm is to use a steepest descent algorithm to find the coefficients $\hat{w}(n)$ which minimize the objective function,

$$F(n) = E\left\{|e(n)|^2\right\}, \tag{5}$$

where $e(n)$ is the error from the block diagram (Figure 2) and $E\{\cdots\}$ denotes the expected value. After the application of the steepest descent algorithm we have

$$\nabla F(n) = 2E\{\nabla e(n)e(n)\}, \tag{6}$$

where ∇ denotes the gradient operator. For

$$\mathrm{EOG}(n) = \left[\mathrm{EOG}(n), \mathrm{EOG}(n-1), \ldots, \mathrm{EOG}(n-p+1)\right]^T, \tag{7}$$

where p is the order of the adaptive filter, and $\nabla e(n) = -\mathrm{EOG}(n)$ we have

$$\nabla F(n) = -2E\{\mathrm{EOG}(n)e(n)\}. \tag{8}$$

$\nabla F(n)$ is a vector orientated to the steepest ascent of the objective function, so we have to take the opposite direction of $\nabla F(n)$ for the minimization of $\nabla F(n)$. Thus we have the following equation:

$$\begin{aligned} \hat{w}(n+1) &= \hat{w}(n) - \mu\nabla F(n) \\ &= \hat{w}(n) + 2\mu E\{\mathrm{EOG}(n)e(n)\}, \end{aligned} \tag{9}$$

where μ is the step size. Note that in most systems the expectation function $E\{\mathrm{EOG}(n)e(n)\}$ has to be approximated, and this can be achieved with the following estimator:

$$\hat{E}\{\mathrm{EOG}(n)e(n)\} = \frac{1}{N}\sum_{i=0}^{N-1}\mathrm{EOG}(n-i)e(n-i), \tag{10}$$

where N is the number of samples used for the estimation. For $N = 1$ we have

$$\hat{E}\{\mathrm{EOG}(n)e(n)\} = \mathrm{EOG}(n)e(n), \tag{11}$$

so the update algorithm is

$$\hat{w}(n+1) = \hat{w}(n) + 2\mu\,\mathrm{EOG}(n)e(n). \tag{12}$$

2.7. EEG Processing. A band pass filter (0.5–40 Hz) and a notch filter at 50 Hz were applied to raw EEG signals. EOG signals were also notch filtered at 50 Hz for main line noise extraction but were band pass filtered in a different frequency band at 0.5–13 Hz. The artifacts originated from ocular activity were rejected offline with the use of the LMS adaptive filter algorithm. To obtain delta oscillations the EEG data were band-pass filtered in delta band (0.5–4 Hz) using Kaiser filter. After that, each EEG signal was epoched into 40 trials with duration of 2.5 seconds each (fixed length of 500 ms prestimulus and 2 seconds after picture onset) and averaged over these epochs to perform Event-Related Oscillation (ERO) analysis. Finally for each average signal, the ERD/ERS was calculated.

2.8. ERD/ERS Data Reduction. ERD/ERS values were averaged into 2-electrode clusters according to their hemisphere (Left Hemisphere: Fp1, F3, F7, C3, T3, P3, T5, O1; Right Hemisphere Fp2, F4, F8, C4, T4, P4, T6, O2) thereby facilitating the investigation of possible brain asymmetries.

2.9. Statistical Analysis. In order to investigate the evoked differences of delta oscillations to emotional stimuli, ERD/ERS mean values were submitted to a mixed $2 \times 2 \times 4 \times 2 \times 2$ ANOVA with gender (male and female) as the between subject factor, and hemisphere (left and right), time intervals (0–500 ms, 500–1000 ms, 1000–1500 ms, and 1500–2000 ms), valence (pleasant and unpleasant) and arousal (high and low) as the within subject factors. Also $2 \times 2 \times 2$ ANOVAs with gender as the between subject factor and valence and arousal as the within subject factors were conducted on the delta activity EROs of the six characteristic peaks (200–300, 300–400, 400–500, 600–800, 1100–1250, 1200–1500 ms after picture onset).

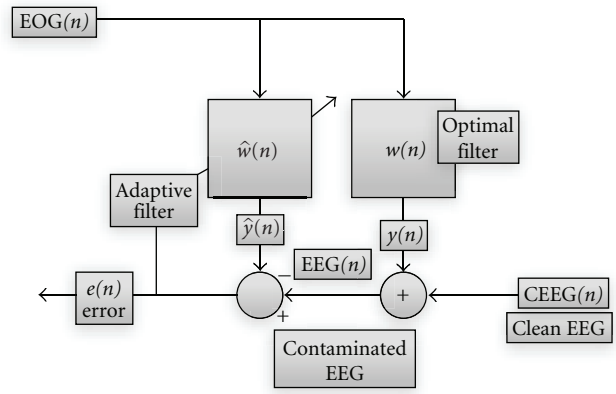

Figure 2: A block diagram of an adaptive filter. It is obvious that $\mathrm{EEG}(n) = w(n)\mathrm{EOG}(n) + \mathrm{CEEG}(n)$. Adaption filtering is trying to adjust $\hat{w}(n)$ as close as possible to $w(n)$, so our goal is to approach clean EEG as much as possible. $e(n) = \mathrm{EEG}(n) - \hat{w}(n)\mathrm{EOG}(n)$. It stands that $e(n) \to 0$ when $\hat{w}(n) \to w(n)$.

3. Results

As we mentioned above, the linked mastoids reference was more effective in normalizing the data as compared to the other two methods. In general, results showed that females had a stronger response to emotional stimuli as compared to males, in addition high arousal pictures provoke greater delta responses than the trials with low arousal pictures. Also delta responses provoked by unpleasant pictures were greater compared to the pleasant pictures. Finally, significant differences concerning the valence dimension were observed in the greater centro-frontal area, while the arousal was more discernible in the centro-parietal region.

3.1. Montage. As mentioned earlier, three different montages have been compared with regards to their effect in the ERD/ERS indices. Figure 3 illustrates delta waveform examples of the three montage methods. All reference techniques have similar overall features in terms of main peak responses. Otherwise the great scaling difference among the Large Laplacian montage and the rest methods is noticeable.

The results pointed out that the CAR and LAP approaches were not effective in normalizing the data; actually both montages increased greatly the mean square error (MSE) relative to the linked mastoids reference. For instance, the main effect of time interval was significant for all three methods, but the MSE was considerably increased for the CAR ($F(3,78) = 22.70$, MSE = 2467660, $P < .0001$) and LAP ($F(3,78) = 43.78$, MSE = 442632.50, $P < .0001$) methods in contrast to Linked Mastoids ($F(3,78) = 19.57$, MSE = 1800.80, $P < .0001$). We also conducted the Kolmogorov-Smirnov test to check for normality, and found that data were not normalised with the CAR and LAP methods for many of the experimental conditions. This was not the case for the linked mastoid method, where all $P > .05$.

3.2. EROs. The averaged delta oscillatory activity from all the epoch segments was extracted for all the participants. The grand average waveform corresponding to the mean activity of all participants is visualized for each central electrode (Figure 4). The analysis presented herein is focused on the three central electrodes in order to study the differences among the four emotional categories and possible gender effects. Laterality issues are beyond the scope of the current EROs analysis.

The average delta activity contains six major peaks which are identified in the same temporal window for each block category. The selection of these windows was made in order to analyze early, late and very late cortical effects. The analysis is structured in a way to report only the significant results for each temporal window.

3.2.1. Positive Peak 200–300 ms. There was a significant arousal by gender interaction ($F(1,26) = 5.824$, $P = .023$) on the central electrode (Cz). Planned t-test revealed significant differences between the low arousal ($1.0766\,\mu$V) and the high arousal ($-0.0938\,\mu$V) conditions only for the female group ($t(13) = -2.643$, $P = .020$). No other effect reached statistical significance, $P > .05$.

3.2.2. Negative Peak 300–400 ms. Results revealed significant main effects of valence ($F(1,26) = 4.378$, $P = .046$) and gender ($F(1,26) = 7.136$, $P = .013$) on the centro-frontal area. More specifically, unpleasant stimuli elicited greater responses than pleasant ones (-7.588 and $-8.177\,\mu$V, resp.), and females produced greater responses relative to males (-6.469 and $-9.297\,\mu$V, resp.). On the central electrode (Cz), there was a marginally significant main effect of gender ($F(1,26) = 4.01$, $P = .056$), that is, females showed stronger responses ($-6.495\,\mu$V) than males ($-4.212\,\mu$V).

3.2.3. Positive Peak 400–500 ms. Results on the central electrode exhibited a highly significant main effect of arousal ($F(1,26) = 17.209$, $P < .001$); the delta activity was stronger for the high arousal condition ($0.686\,\mu$V) relative to the low arousal ($-0.455\,\mu$V) condition during this temporal window. Similarly, for the parietal electrode only the main effect of arousal reached statistical significance ($F(1,26) =$

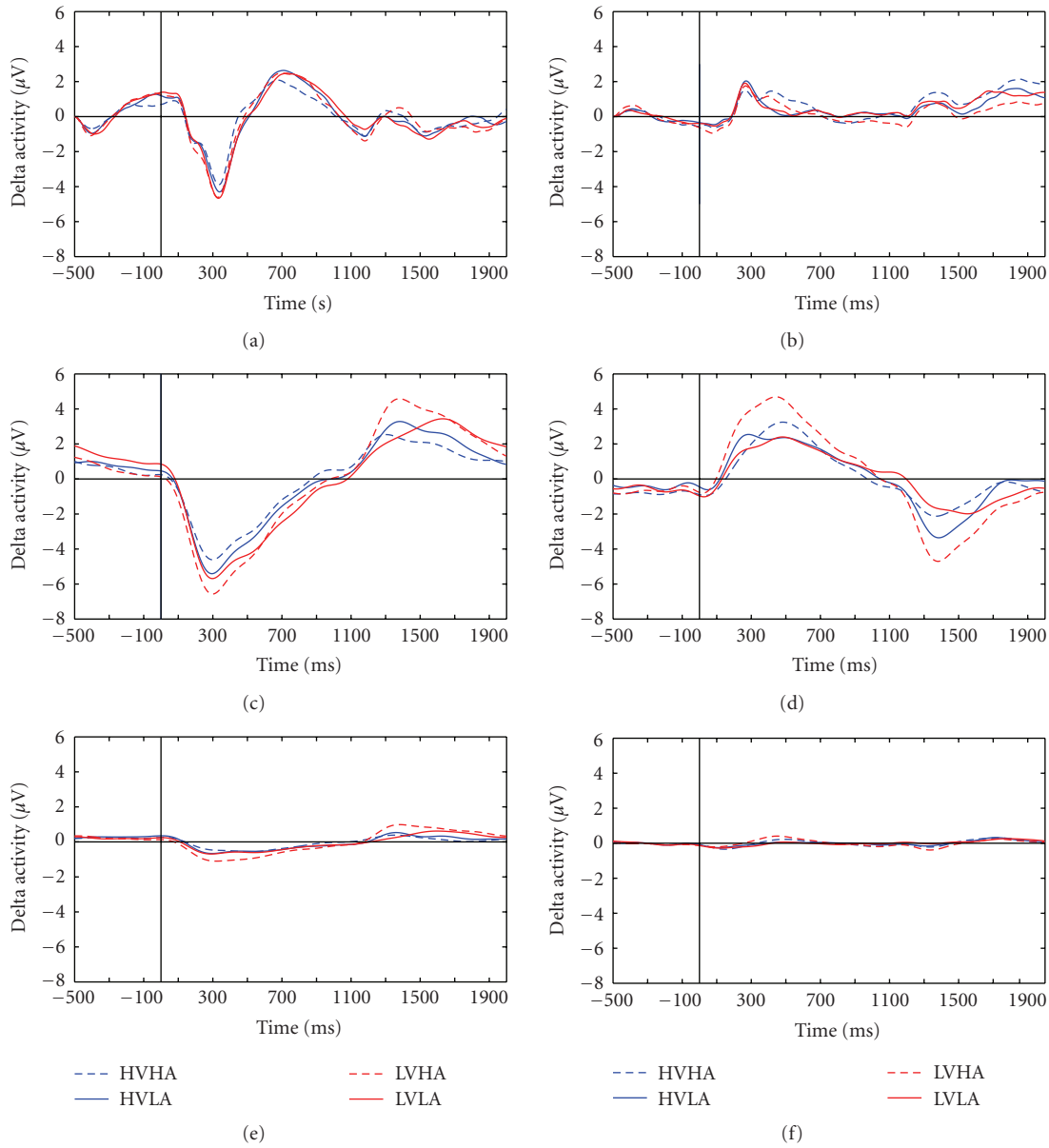

Figure 3: Comparison of different montage methods (Linked Mastoids-top-, Common Average Reference-middle- and Large Laplacian-bottom-) on the basis of delta activity waveform. Left: averaged delta oscillation waveform across all subjects and over all trials for Fz electrodes for all emotional stages separately. Right: delta oscillations in Pz, respectively.

68.511, $P < .0001$), with high arousal condition eliciting much stronger responses than the low arousal condition (2.0043 and 0.8763 μV, resp.).

3.2.4. Positive Peak 600–800 ms. Only the valence by gender interaction reached statistical significance ($F(1, 26) = 5.398$, $P = .028$) on the frontal electrode. Planned t-tests showed significant differences between males (1.59) and females (2.69) ($t(26) = -3.069$, $P = .005$) only for the unpleasant pictures, however there were no differences between male and female groups for the pleasant pictures, $P > .05$. In addition, there were significant differences between pleasant and unpleasant pictures (2.0742 and 1.5091 μV, resp.) ($t(13) = 2.641$, $P = .02$) only for the male group.

Table 3 summarizes the statistical analysis for both ERP [17] and delta wave methodologies, which were performed on the same data. As it can be seen the proposed framework appears to be more sensitive to arousal effects of the emotional stimuli. The proposed framework revealed Gender and Arousal by Gender effects in Fz with higher F-values, which means better sensitivity/specificity. Also the valence and the arousal effects in Cz and Pz respectively are superimposed by the use of the proposed framework analysis. At the current delta activity framework revealed more statistical significant effects in contrast to traditional ERP analysis (see Table 3).

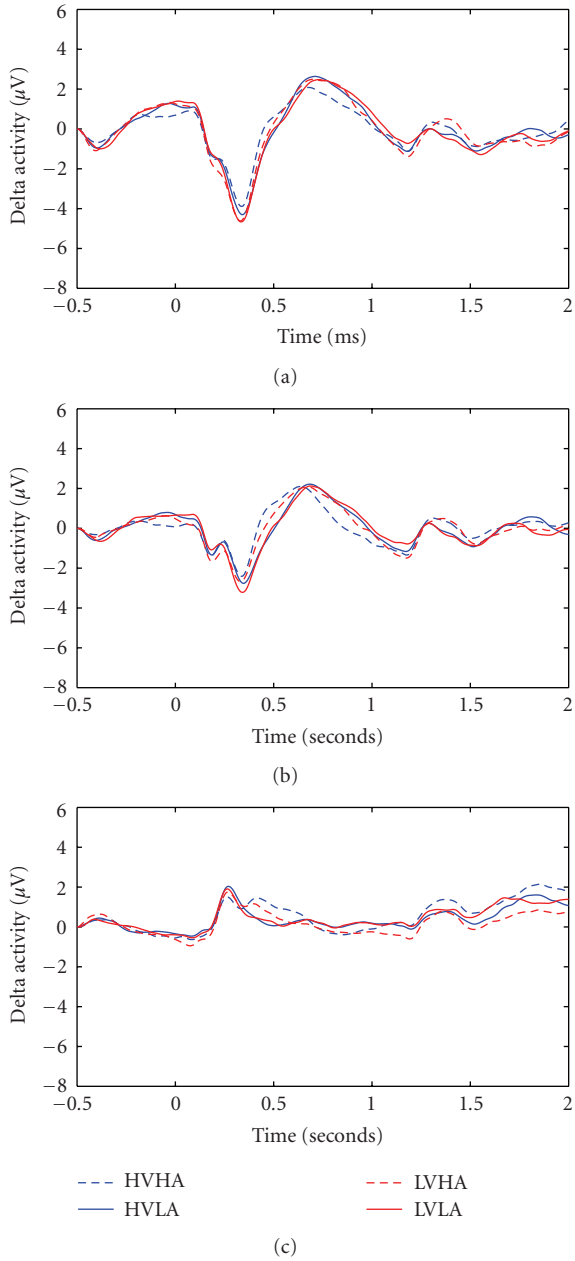

FIGURE 4: Illustration of delta oscillation over central electrodes (Fz-top-, Cz-middle- and Pz-bottom-). Averaged waveform across all the subjects for all emotional are used.

3.3. ERD/ERS. All ERD/ERS mean values for delta oscillations are negative, so it can safely be deduced that delta oscillations are synchronized after emotional stimuli. It has to be noted that lower ERS values (from an algebraic point of view) denote higher increases of delta band powers.

Results showed a significant main effect of time ($F(3,78) = 19.57$, $P < .0001$). Scheffe posthoc comparisons showed significant differences between the first interval (-40.083) and the three remaining intervals (mean ERS value equal to -19.9565, -18.98 and -10.4989, resp., all P-values <.0001). No other comparisons reached statistical significance, $P > .05$. That is, delta oscillations increased their band power after the stimulus onset (0–500 ms), dropped significantly in the second interval (500–1000 ms) and remained almost stable in the next two intervals (1000–1500, 1500–2000). Also, the main effect of arousal was significant ($F(1,26) = 4.99$, $P = 0.034$). High arousal stimuli ($-25{,}474$) produced greater synchronization of delta wave than low arousal pictures ($-19{,}285$). In addition, the following 2-way interactions were significant: gender by time interaction ($F(3,78) = 3.74$, $P = .014$), and valence by arousal ($F(1.26) = 4.55$, $P = .043$). The gender by time interaction, evident only right after stimulus onset (0–500 ms interval), was due to a stronger response for female participants (-50%) than for male participants (-30%). Most importantly, these interactions were further modulated by a significant 5-way interaction, gender by hemisphere by time by valence by arousal interaction, ($F(3,78) = 3.01$, $P = .035$).

In order to analyze further the 5-way interaction, we conducted two separate ANOVAs for each gender group with hemisphere, time, valence and arousal as the within subject factors (Figures 8–11).

3.4. Males. For the male group, results showed a significant main effect of time intervals ($F(3,39) = 4.83$, $P = .006$). Scheffe posthoc comparisons exhibited significant differences only between the first (-30.3349) and the last interval (-12.3907), $P = .008$. Also, the main effect of arousal was highly significant ($F(1,13) = 5.63$, $P = .034$). That is, trials with high arousal pictures (-25.1821) provoke greater synchronization of delta rhythm as compared to trials with low arousal (-15.8206) pictures.

Also, the following interactions were significant in the male group: hemisphere by valence, ($F(1,13) = 4.62$, $P = .05$) (Figure 9), and hemisphere by time by valence by arousal, ($F(3,39) = 2.61$, $P = .065$) (marginal). The hemisphere by valence interaction was due to significant differences between the left (-15.25) and right (-23.31) hemisphere for the unpleasant pictures, ($t(13) = 2.11$, $P = .05$); whereas no differences were found between the two hemisphere conditions for the pleasant pictures, $P > .05$.

Finally, in order to analyze the 4-way interaction, we conducted four separate ANOVAs for each time interval with hemisphere, valence and arousal as the within subject factors.

3.4.1. Interval 1 (0–500 ms). The analyses for the time interval of 0–500 ms revealed a significant main effect of hemisphere, ($F(1,13) = 5.53$, $P = .035$). Mean ERS value for left hemisphere was -26.6563, whereas right hemisphere's ERS was -34.0134. No other effect or interaction reached statistical significance, $P > .05$.

3.4.2. Interval 2 (500–1000 ms). In the second interval, 500–1000 ms, there was a significant main effect of arousal, ($F(1,13) = 4.98$, $P = .043$). That is, there was a greater synchronization of delta activity for the high arousal pictures (-27.4742) than for the low arousal pictures (-16.1314).

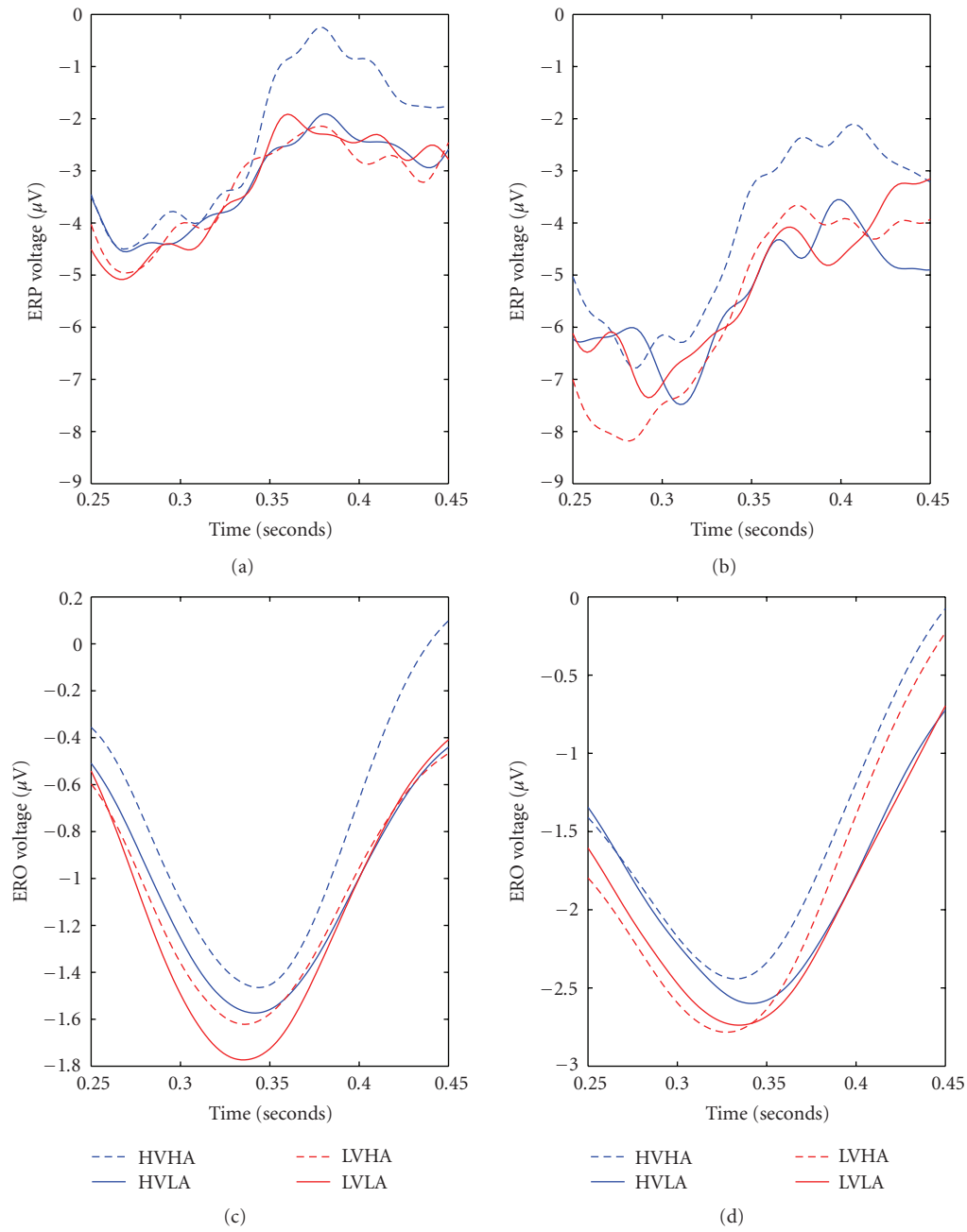

Figure 5: ERPs versus EROs findings for Fz electrode during the P300 response. Averaged waveforms across all subjects (males (left) females (right)) for all emotional stages. Top are depict ERPs while EROs are depicted in two bottom subfigures. All are in the Fz site between 250–450 ms.

3.4.3. Interval 3 (1000–1500 ms). In the third interval, 1000–1500 ms, there was a significant main effect of arousal as well, ($F(1, 13) = 9.07$, $P = .01$). As it was observed before, there was a greater synchronization of delta activity for the high arousal pictures (−23.2588) than for low arousal pictures (−11.6904). In this third interval there was also a significant hemisphere by valence interaction ($F(1, 13) = 8.31$, $P = .013$) (Figure 10). That is, whereas synchronization of delta rhythm was greater for the pleasant picture (−18.34) than for the unpleasant pictures (−14.38) in the left hemisphere, the opposite pattern was observed for the right hemisphere (−14.57 versus −22.61).

3.4.4. Interval 4 (1500–2000 ms). Finally, in the analyses of the fourth interval, 1500–2000 ms, none of the main effects or their interaction reached statistical significance, $P > .05$.

3.5. Females. The analyses for the female group revealed a significant main effect of time interval as well ($F(3, 39) =$

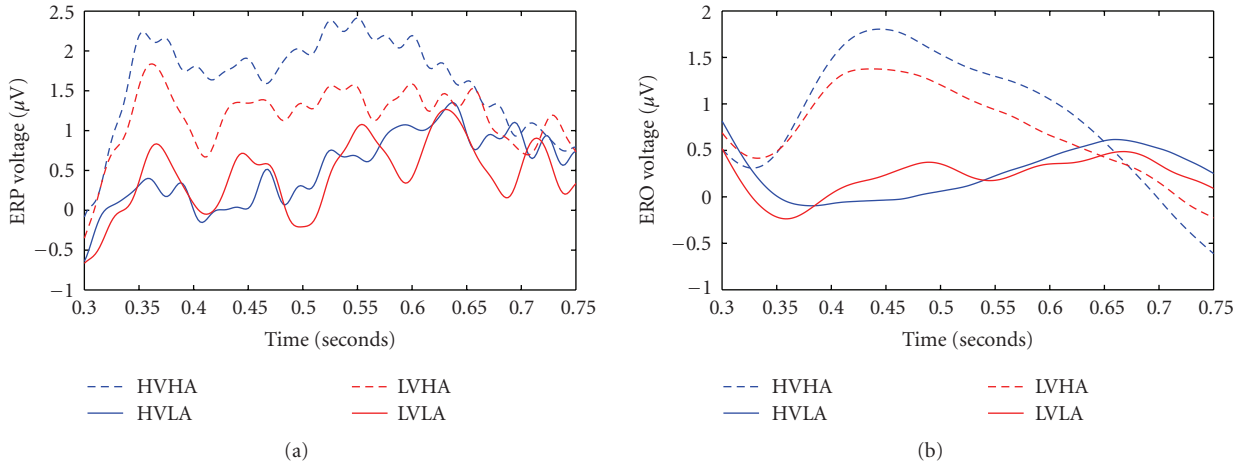

Figure 6: ERPs versus EROs findings for Pz electrode in the 300–750 ms time interval. Averaged waveforms across all the subjects for all emotional stages. ERPs are depicted in (a) while EROS are illustrated in (b).

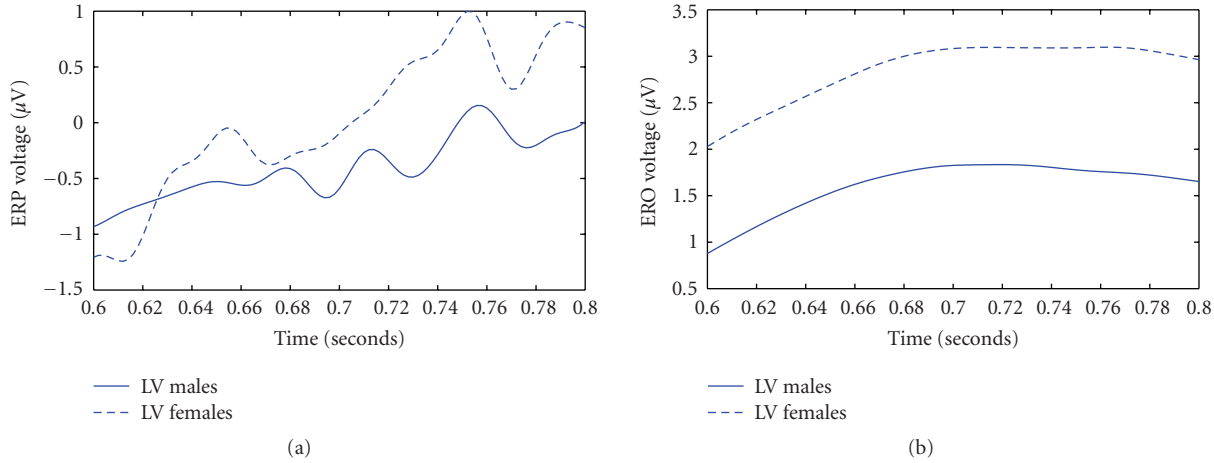

Figure 7: ERPs versus EROs findings for Fz electrode in the 600–800 ms time interval. Averaged waveforms over the gender (solid line: Males, dashed line: Females) for the low valence category. ERPs are depicted in (a) while EROS are illustrated in (b).

15.69, $P < .0001$). Scheffe posthoc comparisons showed significant differences in the mean ERS value between the first interval (−49.8315) and other three intervals (−18.1076, −20.4854, −8.6071, resp.; $P < .0001$). Furthermore, the interaction time by valence reached statistical significance ($F(3, 39) = 4.27$, $P = .012$). To analyze this interaction we conducted two separate ANOVAs for each valence condition with time as the within subject factors. Results showed a significant main effect of time for both pleasant and unpleasant conditions (($F(3, 81) = 14.683$, $P < .0001$) and ($F(3, 81) = 15.829$, $P < .0001$), resp.). Scheffe posthoc comparisons revealed significant differences between the first and the other three intervals for both the pleasant, (−37.501, −19.094, −21.668, and −11.442; $P < .0001$), and the unpleasant condition, (−42.665, −19.094, −21.668 and −9.555, resp.; $P < .0001$). However the interaction was due to a greater difference between the first and the second interval for the unpleasant pictures relative to the pleasant ones.

4. Discussion

The major methodological aim of this paper was to investigate the feasibility of using a combination of event-related delta oscillations and delta synchronization analysis in terms of ERS/ERD in order to study emotional brain processing triggered by visually complex emotional stimuli. We have provided evidence herein that this kind of analysis is probably more sensitive to study not only arousal but also valence modulations of emotional stimuli than classic ERP peak studies. To provide such evidence, we compared effect sizes for both ERP and delta wave analyses. The resulted improved sensitivity of the proposed framework is given in both quantitative and qualitative terms, that is, on one hand, by the statistical analysis for both ERP and delta wave methodologies as depicted in Table 3; moreover, the differences between the two methodologies are qualitatively illustrated by Figures 5–7. According to Figure 6, the arousal modulation of the posterior areas is more intense when

Table 3: Summary of F values for significant effects with the ERP methodology (reported in [17]) and the delta wave methodology. Notice that both methodologies were performed on the same data, but the EROs methodology has a better sensitivity/specificity.

EROs			ERPs		
Fz	Cz	Pz	Fz	Cz	Pz
Valence by gender ($F = 5.398$)	Valence ($F = 4.378$)	Arousal ($F = 68.51$)	Valence ($F = 9.18$)	Valence ($F = 4.23$)	Arousal ($F = 13.4$)
Valence by arousal by gender ($F = 5.439$)	Arousal by gender ($F = 5.824$)		Arousal by gender ($F = 4.96$)		
Gender ($F = 7.136$)			Gender ($F = 6.64$)		
Arousal by gender ($F = 13.519$)					

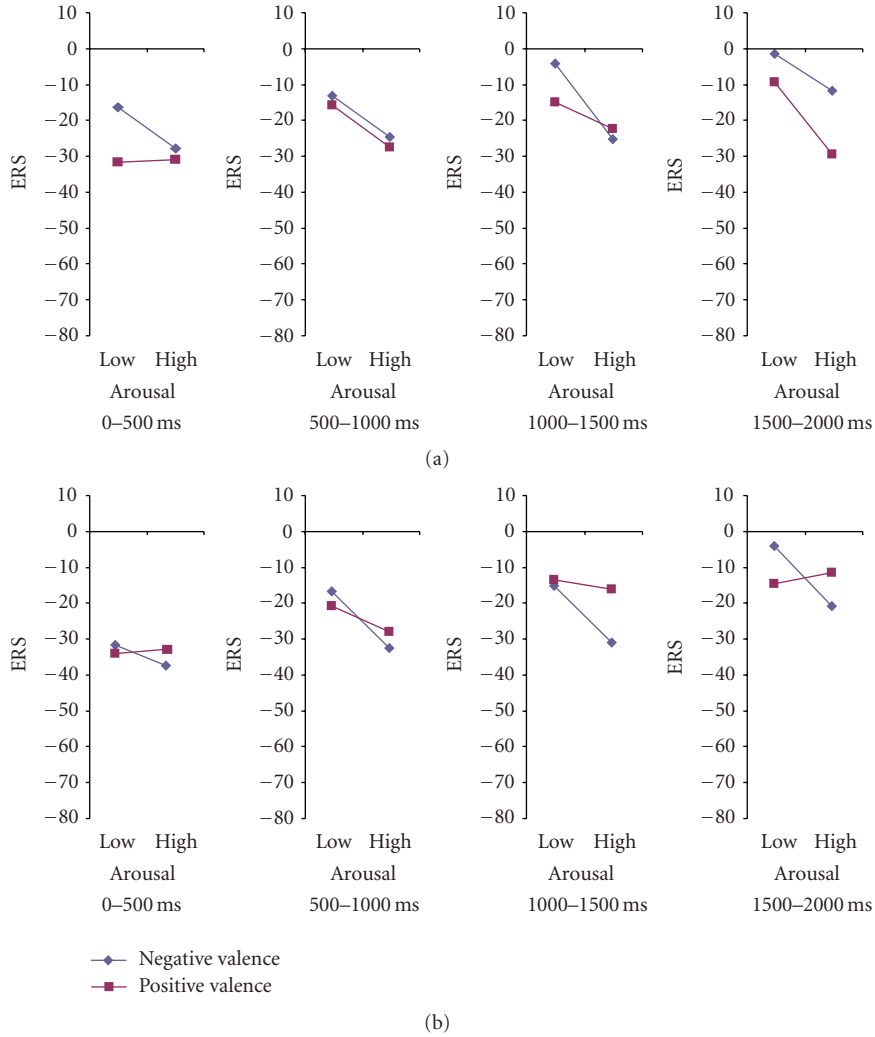

Figure 8: Five-way interactions of ERS index according to valence and arousal dimensions for males in (a) left and (b) right hemisphere.

adopting delta oscillatory methodology in contrast to traditional ERP analysis. Similarly, the proposed framework is more sensitive in revealing the gender effect and valence modulation of the anterior areas as depicted in Figure 7. Finally, Figures 5 and 6 highlights the gender by valence and the gender by arousal interactions which also occur in the frontal lobe.

4.1. ERD/ERS. Delta oscillations are categorized among the brain's natural oscillations, which generally provide basic

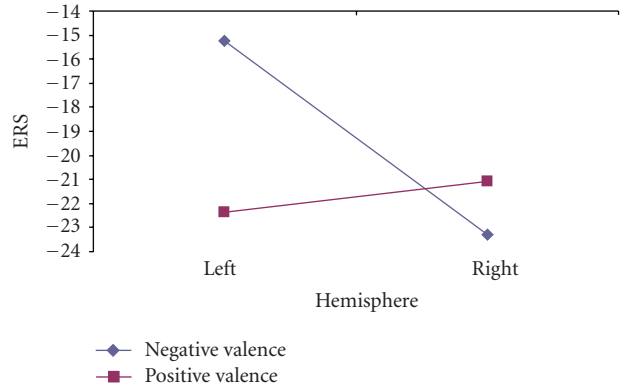

Figure 9: ERS dependence on the stimuli's valence. Note the laterality differences for males.

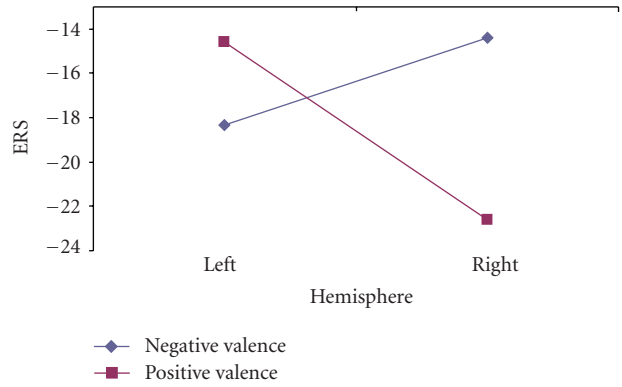

Figure 10: Valence by hemisphere interactions for males in third test interval.

links to cognitive functions by integrative control at all levels [4]. According to [35], delta responses are evoked in the entire scalp of the human brain by sensory stimulation. The activity in this frequency band is related to signal matching, decision making and surprise [36]. Our results concerning this type of analysis indicate the important role of the delta activity as a marker of emotional processing. As already commented above, this type of analysis is more sensitive than the classic ERP peak approach; this is also supported by the fact that interactions like the valence by arousal interaction according to the subject's gender are revealed by the framework proposed here. Specifically, female participants exhibited stronger responses than males, particularly right after stimulus onset. Also, in general, high arousing and unpleasant pictures provoked stronger responses. In addition, the effects of valence and arousal in delta oscillations were modulated by gender. As expected, when an ERD/ERS analysis has been conducted, hemispheric differences have been found for the aforementioned effects in the male group. In a previous study [37] authors remark the contribution of delta waves in emotional modulation by visual inspection of emotional face expressions. The results presented in this paper demonstrate the participation of delta oscillations in emotional processing, in agreement with what has been shown in that study [37].

The main findings for the ERD/ERS analyses were the following: high arousal pictures provoked greater ERS responses of delta oscillations than low arousal pictures, which is in line with previous literature [10, 22], and this was mostly the case for the males participants. Moreover, females showed a greater ERS response as compared to males not only right after stimulus onset (0–500 ms interval), but also during the whole trial. Both males and females showed an effect of valence on ERD/ERS responses. Though, this effect interacted with hemisphere in males. On the other hand, in females, regardless of hemisphere, unpleasant pictures provoked a greater ERS values relative to pleasant pictures, whereas in males this was the case only for the right hemisphere. In the left hemisphere of the male group, ERS exhibited greater values for the pleasant pictures relative to the unpleasant. The prevalence of the right hemisphere in the emotional processing was also supported by a stronger initial (0–500 ms interval) synchronization in the right hemisphere relative to the left hemisphere.

Finally, results showed that the time course of these effects differed for males and females. Females showed a significant effect of the emotional valence of the stimulus only right after onset, whereas the effect of valence on ERS appeared much later (in the 1000–1500 ms interval) in males. The effect of arousal on ERS response was observed relatively soon (500–1000 ms after stimulus onset) in males. These findings suggest that there is a slower synchronization of delta oscillations in response to emotional stimuli for males as compared to females.

The initial stronger and faster response of females to emotional stimuli, as shown in the ERS analyses, replicate previous findings [38, 39], that have shown gender differences in cognitive tasks. Thus, it is generally agreed that male's performance is better on spatial tasks, whereas females perform better on emotion-related tasks [40–42]. These results suggest that this difference may not only be due to cultural influences but may also reflect gender differences concerning information processing in the brain. There were also gender differences in arousal. While males showed greater ERS values for HA pictures relative to LA pictures, there was not a significant effect of arousal for females.

As it is expected, ERS analyses were sensitive to brain asymmetry in emotional processing as well. Clearly, the results summarized above, support the dominance of the right hemisphere in emotional processing but only for males. In females, the emotional response was not lateralized. It is known that specific cognitive processes are lateralized either to the left or right hemisphere in males [43]. In contrast, cognitive processes are not so strongly lateralized in females, possibly because of the anatomical differences in the corpus callosum; it has been reported that women have a larger callosal size, which would enhance inter-hemispheric transfer, and would result in stronger bilateral processing as compared to males [43]. This may explain why we found brain asymmetry effects on ERS responses in males but not in females. Our finding regarding right hemisphere prevalence in emotional processing, particularly for unpleasant-threatening stimuli, is also in line with already published literature (see [44] for a review). On the other

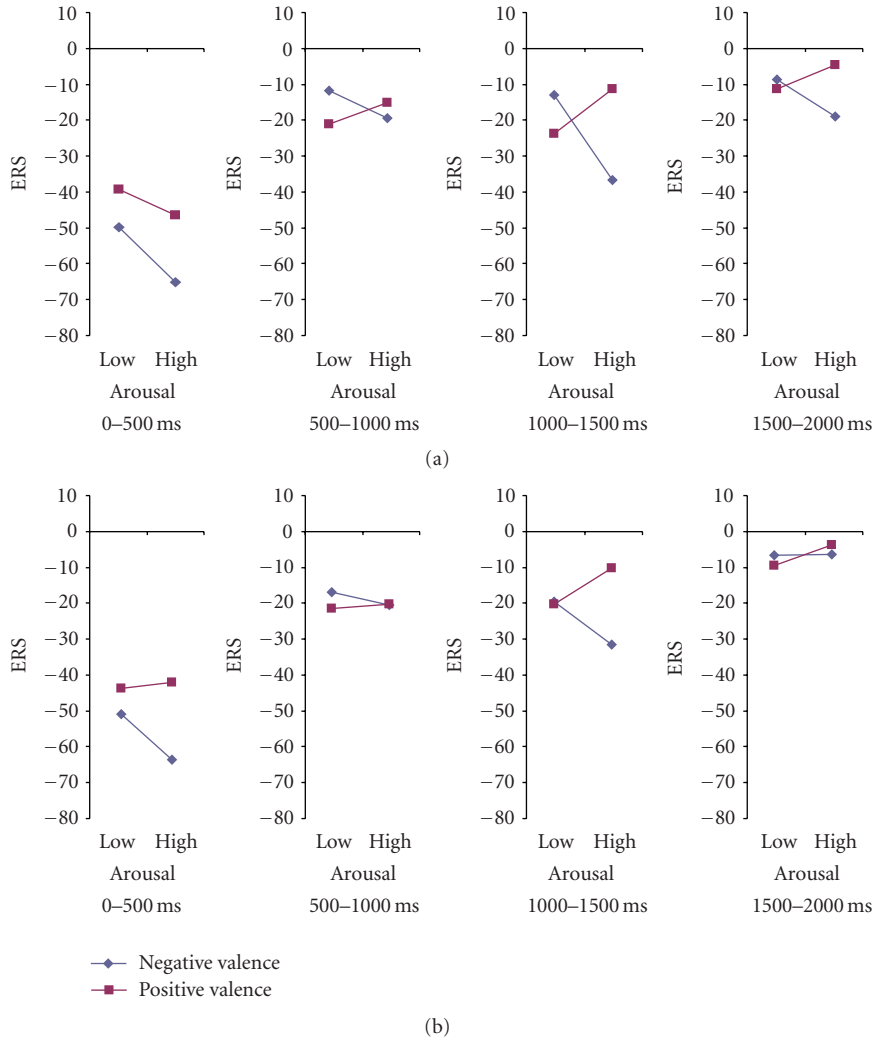

Figure 11: Modulation of ERS index according to valence and arousal dimensions for females in (a) left and (b) right hemisphere.

hand, our results show that the left hemisphere appears to be dominant for the processing of pleasant-positive-stimuli. As Davidson has shown [45–47], the LH is associated with more positive emotions in contrast to the RH, which is more involved in negative stimuli [48].

4.2. EROs. The most consistent finding was that female participants exhibited in general greater responses than male participants, and this finding was true for early and late components. The literature about gender differences in emotional processing is limited and focuses mainly on brain asymmetries employing event-related potentials. For instance, a recent study [49] investigated memory processing of faces that were classified as neutral, friendly and unfriendly. The ERP analysis demonstrated larger amplitudes in female participants relative to male participants. These differences were present during both early processing, as indicated by N300 and N400 components and late processing which lasted until the P600. Thus, the present study generalizes this finding to complex emotional stimuli, using a different measure of brain activity. In the present study, gender differences were stronger at the early negative peaks (N300, N400). Also, in agreement with this study [49], we observed later gender effects by positive deflections approximately 600–800 ms and 1200–1500 after stimulus onset. A more recent study [50] used simple light stimulation in order to investigate gender differences during the various frequency bands of the human EEG. The results showed that the delta response amplitudes for women were significantly higher than for men over occipital, parietal, central and temporal electrode locations. Consequently, the specific frequency band has a key role in the investigation of gender differences in the processing of emotionally stimuli. At last, gender differences in emotional processing can be explained in terms of differences in phyletic memory [51]. This memory has genetic origin and is based on the evolution theory.

The second main finding was that event-related delta oscillations were also modulated by the valence of the

stimulus. In general, unpleasant pictures provoked greater responses than pleasant pictures did, although this effect was sometimes modulated by gender. Also, these effects were stronger and most consistent at the frontal electrodes (e.g., N300–400, P600–800, and N1100–1200 components). This finding agrees with previous work [52] that has shown that areas in the frontal cortex are activated by the valence dimension of the emotional stimuli. There is also converging evidence from neuropsychological studies, which supports a deficit in the processing of pleasant stimuli after damage to the left dorsolateral area [53], whereas bilateral lesions of the ventromedial prefrontal cortex are associated with inability to anticipate the rewarding consequences of an action [54]. Neuroimaging studies with healthy adults have also reported [55] activation in the right frontal region during withdrawal-related negative affective states. However, despite the great amount of studies investigating the laterality of emotional processing in the frontal cortex, the function of the medial frontal cortical structure has not been studied so thoroughly. The present study suggests that the analysis of temporal changes occurring in this area reveals an effect of the emotional valence of the stimulus during the early processing (N300–400 component), since the activation of the defense system (unpleasant pictures) elicits greater delta activity in comparison to the activation of the appetitive system (pleasant pictures).

Finally, the results suggested that the positive peak that occurred almost 350 ms after stimulus onset mainly on parietal locations resulted in a strong arousal effect. Arousal effects on delta oscillations were also found for later positive (P400–500 and P1200–1500) and negative components (N1100–N1200). A substantial portion of P300 variation appears to be caused by fluctuations in the arousal state of the participants [56]. A more recent study using IAPS pictures, demonstrated that the emotional stimuli elicit a more positive wave in the P300 area than neutral stimuli. Further evidence is provided by studies that showed enhanced P300 responses to alcohol and smoking-related cues in alcoholics and smokers respectively [57, 58]. On the other hand, time-frequency analysis of task-related and rare stimuli yielded a later delta coefficient with a parietal predominance [59]. These findings are further supported by findings that suggest the contribution of delta activity to P3b expression [60]. Furthermore, a more technical study [61] demonstrated that P3b components have a more centro-parietal distribution. Indeed the results reported above mention a main effect of arousal 450 ms after stimulus onset. However, the latency of this response is delayed in comparison to the ERP occurrence and it also follows the parietal delta response.

The results of this piece of work provide some evidence towards the confirmation of the authors' hypothesis, that human emotional state and its associated brain processing related to and affects delta frequency activity. However, the relatively small number of electrodes used in the experimental recordings pertains to certain limitations [4, 37], since the spreading effect of the low conductivity skull cannot convey on detailed information of the scalp distributed potentials. So, there is a need for further research in this field with more accurate recordings, which will disclose effectively the scalp distributed phenomena occurred by emotional visual stimuli. It is also expected that the full intraband comparison will delineate the human brain emotional processing characteristics in a more comprehensive way. Nevertheless, the results presented here regarding the affection of delta oscillations by emotional stimuli cannot be overlooked.

In conclusion, to the best of our knowledge, this is the first study concerning the relation of delta oscillations (in terms of peak amplitude analysis and synchronization effects) and emotional processing triggered by visual stimuli from the IAPS collection. The results obtained here denote the important role of emotional processing in delta wave modulation. However, further research is needed in order to extend the interaction of two emotional dimensions (valence and arousal) with the subject's gender and their effect on other bands and characteristic oscillations.

References

[1] P. Vuilleumier, "How brains beware: neural mechanisms of emotional attention," *Trends in Cognitive Sciences*, vol. 9, no. 12, pp. 585–594, 2005.

[2] C. Neuper and G. Pfurtscheller, "Event-related dynamics of cortical rhythms: frequency-specific features and functional correlates," *International Journal of Psychophysiology*, vol. 43, no. 1, pp. 41–58, 2001.

[3] S. Makeig, S. Debener, J. Onton, and A. Delorme, "Mining event-related brain dynamics," *Trends in Cognitive Sciences*, vol. 8, no. 5, pp. 204–210, 2004.

[4] E. Başar, C. Başar-Eroglu, S. Karakaş, and M. Schürmann, "Gamma, alpha, delta, and theta oscillations govern cognitive processes," *International Journal of Psychophysiology*, vol. 39, no. 2-3, pp. 241–248, 2001.

[5] J. Yordanova, V. Kolev, and E. Başar, "Oscillatory brain responses: changes with development and aging," in *Brain Function and Oscillations. I. Brain Oscillations: Principles and Approaches*, E. Başar, Ed., pp. 239–251, Springer, Berlin, Germany, 1998.

[6] H. Berger, "UÈ ber das Elektrenkephalogramm des Menschen II," *Journal of Comparative Neurology and Psychology*, vol. 40, pp. 160–179, 1930.

[7] G. Pfurtscheller and F. H. Lopes da Silva, "Event-related EEG/MEG synchronization and desynchronization: basic principles," *Clinical Neurophysiology*, vol. 110, no. 11, pp. 1842–1857, 1999.

[8] G. Pfurtscheller and A. Aranibar, "Event related cortical desynchronization detected by power measurements of scalp EEG," *Electroencephalography and Clinical Neurophysiology*, vol. 42, no. 6, pp. 817–826, 1977.

[9] P. J. Lang, M. M. Bradley, and B. N. Cuthbert, "International Affective Picture System (IAPS): Technical Manual and Affective Ratings," NIMH Center for the Study of Emotion and Attention, 1997.

[10] G. G. Knyazev, "Motivation, emotion, and their inhibitory control mirrored in brain oscillations," *Neuroscience and Biobehavioral Reviews*, vol. 31, no. 3, pp. 377–395, 2007.

[11] D. Paré, "Role of the basolateral amygdala in memory consolidation," *Progress in Neurobiology*, vol. 70, no. 5, pp. 409–420, 2003.

[12] N. Nishitani, "Dynamics of cognitive processing in the human hippocampus by neuromagnetic and neurochemical assessments," *NeuroImage*, vol. 20, no. 1, pp. 561–571, 2003.

[13] E. Başar, *Brain Function and Oscillations. I. Brain Oscillations: Principles and Approaches*, Springer, Berlin, Germany, 1998.

[14] E. Başar, *Brain Function and Oscillations. II. Integrative Brain Function. Neurophysiology and Cognitive Processes*, Springer, Berlin, Germany, 1999.

[15] C. Amrhein, A. Muhlberger, P. Pauli, and G. Wiedemann, "Modulation of event-related brain potentials during affective picture processing: a complement to startle reflex and skin conductance response?" *International Journal of Psychophysiology*, vol. 54, no. 3, pp. 231–240, 2004.

[16] B. N. Cuthbert, H. T. Schupp, M. M. Bradley, N. Birbaumer, and P. J. Lang, "Brain potentials in affective picture processing: covariation with autonomic arousal and affective report," *Biological Psychology*, vol. 52, no. 2, pp. 95–111, 2000.

[17] C. Lithari, C. Frantzidis, C. Papadelis, et al., "Are females more sensitive to emotional stimuli? A neurophysiological study across arousal and valence dimensions," *Brain Topography*, under review.

[18] R. D. Lane, P. M.-L. Chua, and R. J. Dolan, "Common effects of emotional valence, arousal and attention on neural activation during visual processing of pictures," *Neuropsychologia*, vol. 37, no. 9, pp. 989–997, 1999.

[19] M. M. Bradley, M. Codispoti, B. N. Cuthbert, and P. J. Lang, "Emotion and motivation I: defensive and appetitive reactions in picture processing," *Emotion*, vol. 1, no. 3, pp. 276–298, 2001.

[20] A. Keil, M. M. Müller, T. Gruber, C. Wienbruch, M. Stolarova, and T. Elbert, "Effects of emotional arousal in the cerebral hemispheres: a study of oscillatory brain activity and event-related potentials," *Clinical Neurophysiology*, vol. 112, no. 11, pp. 2057–2068, 2001.

[21] L. I. Aftanas, A. A. Varlamov, S. V. Pavlov, V. P. Makhnev, and N. V. Reva, "Affective picture processing: event-related synchronization within individually defined human theta band is modulated by valence dimension," *Neuroscience Letters*, vol. 303, no. 2, pp. 115–118, 2001.

[22] L. I. Aftanas, A. A. Varlamov, S. V. Pavlov, V. P. Makhnev, and N. V. Reva, "Time-dependent cortical asymmetries induced by emotional arousal: EEG analysis of event-related synchronization and desynchronization in individually defined frequency bands," *International Journal of Psychophysiology*, vol. 44, no. 1, pp. 67–82, 2002.

[23] T. Demiralp and E. Başar, "Theta rhythmicities following expected visual and auditory targets," *International Journal of Psychophysiology*, vol. 13, no. 2, pp. 147–160, 1992.

[24] R. G. Heath, "Pleasure and brain activity in man. Deep and surface electroencephalograms during orgasm," *Journal of Nervous and Mental Disease*, vol. 154, no. 1, pp. 3–18, 1972.

[25] D. M. Tucker and S. L. Dawson, "Asymmetric EEG changes as method actors generated emotions," *Biological Psychology*, vol. 19, no. 1, pp. 63–75, 1984.

[26] G. Yener, B. Güntekin, and E. Başar, "Event-related delta oscillatory responses of Alzheimer patients," *European Journal of Neurology*, vol. 15, no. 6, pp. 540–547, 2008.

[27] E. Başar, C. Schmiedt-Fehr, A. Öniz, and C. Başar-Eroğlu, "Brain oscillations evoked by the face of a loved person," *Brain Research*, vol. 1214, pp. 105–115, 2008.

[28] T. Harmony, T. Fernandez, J. Silva, et al., "EEG delta activity: an indicator of attention to internal processing during performance of mental tasks," *International Journal of Psychophysiology*, vol. 24, no. 1-2, pp. 161–171, 1996.

[29] L. I. Aftanas, L. N. Savotina, V. P. Makhnev, and N. V. Reva, "Analysis of evoked EEG synchronization and desynchronization during perception of emotiogenic stimuli: association with autonomic activation processes," *Neuroscience and Behavioral Physiology*, vol. 35, no. 9, pp. 951–957, 2005.

[30] M. Schürmann, C. Başar-Eroglu, V. Kolev, and E. Başar, "A new metric for analyzing single-trial event-related potentials (ERPs): application to human visual P300 delta response," *Neuroscience Letters*, vol. 197, no. 3, pp. 167–170, 1995.

[31] D. V. Moretti, C. Babiloni, G. Binetti, et al., "Individual analysis of EEG frequency and band power in mild Alzheimer's disease," *Clinical Neurophysiology*, vol. 115, no. 2, pp. 299–308, 2004.

[32] C. A. Frantzidis, C. Lithari, A. Vivas, et al., "Towards emotion aware computing: a study of arousal modulation with multichannel event-related potentials, delta oscillatory activity and skin conductivity responses," in *Proceedings of the 8th IEEE International Conference on BioInformatics and BioEngineering (BIBE '08)*, 2008.

[33] D. J. McFarland, L. M. McCane, S. V. David, and J. R. Wolpaw, "Spatial filter selection for EEG-based communication," *Electroencephalography and Clinical Neurophysiology*, vol. 103, no. 3, pp. 386–394, 1997.

[34] M. A. Klados, C. Papadelis, C. Lythari, and P. D. Bamidis, "The removal of ocular artifacts from EEG signals: a comparison of performances for different methods," in *Proceedings of the 4th European Conference of the International Federation for Medical and Biological Engineering (ECIFMBE '08)*, IFMBE Proceedings 22, pp. 1259–1263, Antwerp, Belgium, November 2008.

[35] E. Başar, C. Başar-Eroglu, S. Karakas, and M. Schürmann, "Oscillatory brain theory: a new trend in neuroscience: the role of oscillatory processes in sensory and cognitive functions," *IEEE Engineering in Medicine and Biology Magazine*, vol. 18, no. 3, pp. 56–66, 1999.

[36] C. Başar-Eroglu, E. Başar, T. Demiralp, and M. Schürmann, "P300-response: possible psychophysiological correlates in delta and theta frequency channels. A review," *International Journal of Psychophysiology*, vol. 13, no. 2, pp. 161–179, 1992.

[37] M. Balconi and U. Pozzoli, "Event-related oscillations (ERO) and event-related potentials (ERP) in emotional face recognition," *International Journal of Neuroscience*, vol. 118, no. 10, pp. 1412–1424, 2008.

[38] J. Wrase, S. Klein, S. M. Gruesser, et al., "Gender differences in the processing of standardized emotional visual stimuli in humans: a functional magnetic resonance imaging study," *Neuroscience Letters*, vol. 348, no. 1–4, pp. 41–45, 2003.

[39] M. Lewis, J. M. Haviland-Jones, and L. Feldman Barrett, *Handbook of Emotions*, Guilford Press, New York, NY, USA, 2008.

[40] N. Jaušovec and K. Jaušovec, "Spatial rotation and recognizing emotions: gender related differences in brain activity," *Intelligence*, vol. 36, no. 5, pp. 383–393, 2008.

[41] M. Grossman and W. Wood, "Sex differences in intensity of emotional experience: a social role interpretation," *Journal of Personality and Social Psychology*, vol. 65, no. 5, pp. 1010–1022, 1993.

[42] A. M. Kring and A. H. Gordon, "Sex differences in emotion: expression, experience, and physiology," *Journal of Personality and Social Psychology*, vol. 74, no. 3, pp. 686–703, 1998.

[43] C. Davatzikos and S. M. Resnick, "Sex differences in anatomic measures of interhemispheric connectivity: correlations with cognition in women but not men," *Cerebral Cortex*, vol. 8, no. 7, pp. 635–640, 1998.

[44] H. A. Demaree, D. E. Everhart, E. A. Youngstrom, and D. W. Harrison, "Brain lateralization of emotional processing:

historical roots and a future incorporating "dominance"," *Behavioral and Cognitive Neuroscience Reviews*, vol. 4, no. 1, pp. 3–20, 2005.

[45] R. J. Davidson, "Emotion and affective style: hemispheric substrate," *Psychological Science*, vol. 3, pp. 39–43, 1992.

[46] R. J. Davidson, "Cerebral asymmetry, emotion and affective style," in *Brain Asymmetry*, R. J. Davidson and K. Hugdahl, Eds., pp. 361–387, MIT Press, Boston, Mass, USA, 1995.

[47] R. J. Davidson, "Anterior electrophysiological asymmetries, emotion, and depression: conceptual and methodological conundrums," *Psychophysiology*, vol. 35, pp. 607–614, 1998.

[48] D. C. Hammond, "Neurofeedback treatment of depression and anxiety," *Journal of Adult Development*, vol. 12, no. 2-3, pp. 131–137, 2005.

[49] F. Guillem and M. Mograss, "Gender differences in memory processing: evidence from event-related potentials to faces," *Brain and Cognition*, vol. 57, no. 1, pp. 84–92, 2005.

[50] B. Güntekin and E. Başar, "Brain oscillations are highly influenced by gender differences," *International Journal of Psychophysiology*, vol. 65, no. 3, pp. 294–299, 2007.

[51] J. M. Fuster, *Memory in the Cerebral Cortex: An Empirical Approach to Neural Networks in the Human and Nonhuman Primate*, MIT Press, Cambridge, Mass, USA, 1995.

[52] R. J. Davidson and W. Irwin, "The functional neuroanatomy of emotion and affective style," *Trends in Cognitive Sciences*, vol. 3, no. 1, pp. 11–21, 1999.

[53] G. Gianotti, "Emotional behaviour and hemispheric side of lesion," *Cortex*, pp. 41–55, 1972.

[54] A. Bechara, A. R. Damasio, H. Damasio, and S. W. Anderson, "Insensitivity to future consequences following damage to human prefrontal cortex," *Cognition*, vol. 50, no. 1–3, pp. 7–15, 1994.

[55] R. J. Davidson, P. Ekman, C. D. Saron, J. A. Senulis, and W. V. Friesen, "Approach-withdrawal and cerebral asymmetry: emotional expression and brain physiology," *Journal of Personality and Social Psychology*, vol. 58, no. 2, pp. 330–341, 1990.

[56] J. Polich and A. Kok, "Cognitive and biological determinants of P300: an integrative review," *Biological Psychology*, vol. 41, no. 2, pp. 103–146, 1995.

[57] C. Hermann, S. Ziegler, N. Birbaumer, and H. Flor, "Pavlovian aversive and appetitive odor conditioning in humans: subjective, peripheral, and electrocortical changes," *Experimental Brain Research*, vol. 132, no. 2, pp. 203–215, 2000.

[58] C. A. Warren and B. E. McDonough, "Event-related brain potentials as indicators of smoking cue-reactivity," *Clinical Neurophysiology*, vol. 110, no. 9, pp. 1570–1584, 1999.

[59] V. Kolev, T. Demiralp, J. Yordanova, A. Ademoglu, and U. Isoglu-Alkac, "Time-frequency analysis reveals multiple functional components during oddball P300," *NeuroReport*, vol. 8, no. 8, pp. 2061–2065, 1997.

[60] T. Demiralp, J. Yordanova, V. Kolev, A. Ademoglu, M. Devrim, and V. J. Samar, "Time-frequency analysis of single-sweep event-related potentials by means of fast wavelet transform," *Brain and Language*, vol. 66, no. 1, pp. 129–145, 1999.

[61] M. Jing, S. Sanei, and A. Sumich, "An automatic detection and localization of P300 sub-components using ICA," in *Proceedings of the IEEE International Workshop on Biomedical Circuits and Systems (BioCAS '04)*, pp. S3.6-1–S3.6-4, Singapore, December 2004.

Hindawi Publishing Corporation
Computational Intelligence and Neuroscience
Volume 2009, Article ID 409624, 5 pages
doi:10.1155/2009/409624

Research Article

Information Infrastructure for Cooperative Research in Neuroscience

P. J. Durka,[1] G. J. Blinowski,[2] H. Klekowicz,[1] U. Malinowska,[1] R. Kuś,[1] and K. J. Blinowska[1]

[1] *Department of Biomedical Physics, Warsaw University, Hoza 69 street, 00 681 Warszawa, Poland*
[2] *Institute of Computer Science, Warsaw University of Technology, Nowowiejska 15/19 street, 00 665 Warszawa, Poland*

Correspondence should be addressed to P. J. Durka, piotr-j.durka@fuw.edu.pl

Received 4 November 2008; Revised 10 March 2009; Accepted 29 April 2009

Recommended by Fabio Babiloni

The paper describes a framework for efficient sharing of knowledge between research groups, which have been working for several years without flaws. The obstacles in cooperation are connected primarily with the lack of platforms for effective exchange of experimental data, models, and algorithms. The solution to these problems is proposed by construction of the platform (EEG.pl) with the semantic aware search scheme between portals. The above approach implanted in the international cooperative projects like NEUROMATH may bring the significant progress in designing efficient methods for neuroscience research.

1. Introduction

Nowadays, publications alone are not enough to coherently increase our knowledge of the mathematical methods applied in neuroscience. To foster the progress on that field, the efficient mechanisms of sharing the experience of scientific teams are needed. The NEUROMATH is an action in which the scientists are called to harmonize their efforts in order to offer a comprehensive approach to the problem of the estimation of brain activity and connectivity for sensory and cognitive behavioral tasks. For solving this problem, the optimal mathematical methods has to be designed and tested on the large databases, which require efficient mechanisms for sharing resources. The problem of an efficient application of internet databases for sharing computational resources was approached, for example, in [1] where the practical barriers to progress on that field were identified.

This paper proposes working solutions to these issues, implemented and working for several years in the EEG.pl portal with the semantic-aware search scheme for interconnecting portals. The structure and layout of EEG.pl (except for the interportal search), at least of the part dedicated to sharing software, can be found in the recently started Software Center of the International Neuroinformatics Coordination Facility (http://software.incf.org/). When adopted within the NEUROMATH framework, these solutions will foster the cooperation between the groups and consolidate their efforts to the aim of designing the optimal methods for estimation of brain activity and connectivity.

2. EEG.pl Open Repository

EEG.pl is a portal dedicated to sharing software, models, and data related to EEG and local field potentials. It is open to anybody interested in making relevant items freely available or downloading resources shared by others. Only submission of material requires free registration; browsing and downloading is available to anybody. The invitation on the first page states:

> *EEG.pl is an open repository for software, publications and datasets related to the analysis of brain potentials: electroencephalogram (EEG), local field potentials (LFPs) and event related potentials (ERP), created to foster and facilitate Reproducible Research in these fields.*
>
> *You can freely search the content of this and other thematic vortals linked via the Interneuro initiative. As a registered user you can submit your article, data or model. Registration and submissions are free. You can also comment and respond to comments on any of the published items.*

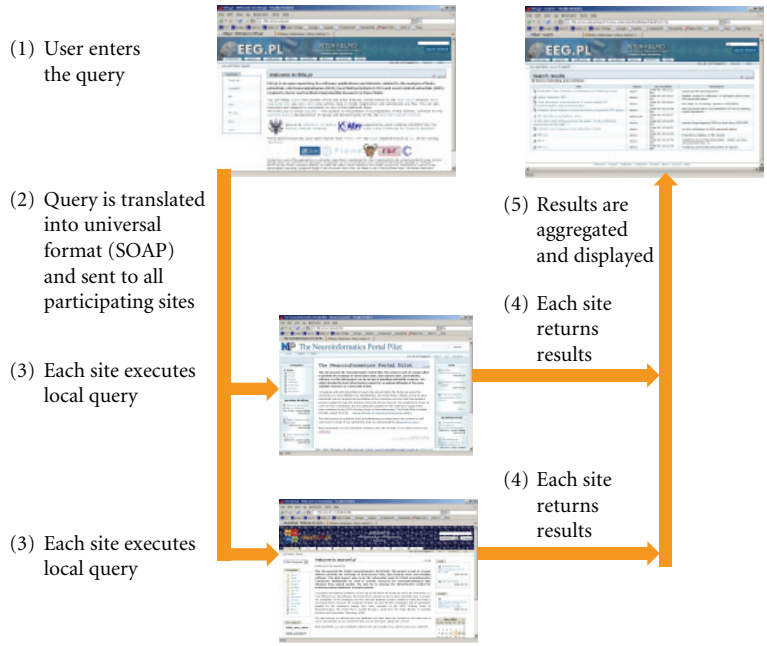

Figure 1: Information flow during the distributed search according to the InterNeuro scheme.

There are also Disclaimers: *none of the organizations or individuals supporting or maintaining this site is responsible for the content provided by users and any damage which may result from its application. In particular, we do not provide any virus scanning for the binaries available as "software". We do not peer-review submitted material, just retain the right to reject irrelevant or low quality submissions. We believe in opinions of the Neuroscience Community, expressed hereby in the comments which users can attach to any of the published items. We believe that these comments provide most objective evaluation*.

During over five years of experience in running this service, we learned two major lessons.

(1) The software framework and chosen solutions are stable and caused no problems while retaining large amount of flexibility to both the administrator and the users.

(2) EEG.pl is not the only resource of this kind, and the response of the community was not as widespread as expected.

The latter issue calls into attention the issue of interoperability with other portals. This can be achieved within the "Interneuro" framework, described in http://www.eeg.pl/documents/about_connections. Below we briefly recall the ideas underlying the semantic-aware search, which is the key feature in this scheme.

3. Semantic Aware Search

Semantic-aware search—contrary to the search provided by typical Internet-wide search engines like Google—indexes not only simple keyword data but also the *meaning* of the data. In case of books, that metainformation would include the author, creator, title, major keywords, and references. In general, the choice of metainformation is not trivial. Fortunately standards exist which regulate naming and scope of metainformation attributes. One of the most popular standards in this field is the Dublin Core (DC) standard. The DC specification is developed and maintained by "The Dublin Core Metadata Initiative" (DCMI), an "open forum engaged in the development of interoperable online metadata standards that support a broad range of purposes and business models." The full specification of the DC standard may be found in [2]. Here we will summarize only the most important elements of the DC metadata.

Type "The nature or genre of the content of the resource"—this may be a text (paper, article, preprint); a software item (i.e., a description of a freeware or commercial software piece); a dataset (i.e., an experiment collected time series in a well know format).

Title "A name given to the resource", for example, in case of a paper—its title.

Identifier "An unambiguous reference to the resource within a given context"; the identifier does not have to have a sensible meaning to a human being; "it is simply a unique token identifying the resource", for example, a URL.

Creator "An entity primarily responsible for making the content of the resource"—that is, a person, an organization, or a service.

Description "An account of the content of the resource"—abstract, table of contents, reference, and so forth.

```
<?xml version="1.0"?>
<SOAP-ENV:Envelope xmlns:SOAP-
ENV="http://schemas.xmlsoap.org/soap/envelope/" ...>
  <SOAP-ENV:Body>
    <NeuroQuery>
      <QueryTypexsi:type="xsd:string">Software </QueryType>
      <FullTextQuery xsi:type="xsd:string">
        some pattern here
      </FullTextQuery>
      <search xsi:type="SOAP-ENC:Array"
       SOAP-ENC:arrayType="ns1:searchcrit[3]">
        <item>
          <pname>DC:creator</pname>
          <pvalue>regexp</pvalue>
        </item>
        <item>
          <pname>DC:title</pname>
          <pvalue>regexp</pvalue>
        </item>
        <item>...</item>
      </search>
      <searchlogic xsi:type="xsd:string"> AND </searchlogic>

      <datebeg xsi:type="xsd:string"> 2002-01-01</datebeg>
      <dateend xsi:type="xsd:string"> 2002-01-01</dateend>
    </NeuroQuery>
  </SOAP-ENV:Body>
</SOAP-ENV:Envelope>
```

Indicates the DC object type: Software ; Dataset ; etc.
This component is for "full-text" search
The third component specifies universal "by-DC-attribute" search

and so on for other DC attributes

either AND or OR

Date conditions further limit the search scope

Figure 2: SOAP query.

```
<?xml version="1.0"?>
<SOAP-ENV:Envelope xmlns:SOAP-
ENV="http://schemas.xmlsoap.org/soap/envelope/"
       ...>

<SOAP-ENV:Body>
       <NeuroQueryResponse>
              <statusxsi:type="xsd:int">0
       </status>
              <resultsxsi:type="SOAP-ENC:Array"
               SOAP-ENC:arrayType="ns1:res[3]">
                     <item
       rdf:about="http://www.eeg.pl/somepaper">
                      <title>A fine paper
                        on EEG</title>
                       <dc:date>2003-06-23</dc:date>
                       <dc:title>Analysis of EEG
                        signas</dc:title>
                       <dc:description>some info
                        here</dc:description>
                     ...
                     </item>
               ...
              </results>
       </NeuroQueryResponse>
</SOAP-ENV:Body>
</SOAP-ENV:Envelope>
```

General status, e.g. 0 - OK, <0 - error
because more than one record may be returned an SOAP array is used here
First result tuple

More attributes here

More result tuples

Figure 3: RDF response to the query from Figure 2.

Subject "The topic of the content of the resource"—keywords, key phrases, and classification codes that describe the resource.

DC defines also a handful of other attributes, like time and date information, information about the publisher, more data about the content itself, and so forth. Sophisticated distributed search mechanism is around it. With metainformation standardized, there is no longer an issue of"what to search for?", only an issue of "how to search?" (technically) remains.

For the low-level implementation of queries we have adopted the SOAP/RDF XML [3] based standards for

describing queries, and results. As a consequence, the HTTP protocol [4] is used for transporting the query and the response over the network.

The search service is build around the distributed P2P paradigm: each portal is both a client and a server, that is, is able to formulate and send the queries as well as listen for search requests and to answer them. The rationale for using SOAP/RDF/XML is the following.

(i) SOAP/XML is portable and both platform, and system independent.

(ii) SOAP/XML and SOAP over http are *defacto* standards for building distributed applications.

(iii) SOAP is simple—there is no heavyweight software required to generate and parse it.

(iv) There is a multitude of XML parsers and tools available (both commercial and open-source), so building software compatible with our format should not be a technical problem.

The process of executing a distributed query, illustrated also on Figure 1, is executed as follows.

(1) User enters the query: he/she connects to one of the cooperating sites (e.g., http://eeg.pl), chooses "advanced search", enters the search phrase(s), marks the "external search" check box, and clicks the search button.

(2) Query is translated into universal format (SOAP/XML) and sent to all participating sites.

(3) Each site executes local query.

(4) Each site returns results.

(5) Results are aggregated and displayed to the user.

The format of queries and returned results is based upon (Simple Object Access Protocol SOAP) [3]—a stateless, message exchange paradigm based on XML. In simpler terms, SOAP is a mechanism similar to (Remote Procedure Call RPC) based on open standards: the remote object access (or a "procedure call") is express purely in XML notation; the same applies to returned results. A SOAP message consists of an outermost envelope, an optional header, and body. From the logical point of view the body consists of a remote objects' (or procedures') identifier and parameters. The SOAP standard describes how parameters should be represented, serialized, and encoded. SOAP defines both a method for encoding simple types (strings, integers, etc.) as well as complex types such as arrays and structures. In case of the remote search employed in Interneuro a relatively simple query is used: only string type parameters representing DC attributes are passed—see Figure 2.

The result is generated and recorded as an RDF serialized (encoded) in SOAP response—see Figure 3. RDF stands for Resource Description Framework [3], a language for representing information about resources in the World Wide Web. RDF, similarly to SOAP, is based on XML. It is particularly intended for representing metadata about web resources, such as the title, author, and modification date of a web page. RDF is intended for situations in which information needs to be processed by applications, rather than being only displayed for people. RDF provides a common framework for expressing this information so it can be exchanged between applications without loss of meaning.

Implementation of the EEG.pl portal is based on the Zope/CMS/Plone (http://plone.org/) free application server/content management/portal engine. Although Zope/Plone provides some mechanisms for distributed communication between different sites (RPC-over-XML) it currently lacks SOAP/RDF support as such. We have used ZOPE's template mechanisms and programming capabilities to develop a distributed search component. The software is written in Python (a default development language for ZOPE, in which the whole system is actually written) and freely available as ZOPE package (technically ZOPE "product"). These software components are freely available from http://eeg.pl.

4. Conclusion

We presented a working solution to some of the problems encountered in the integration of the efforts of scientific teams, such as the participants of the NEUROMATH action. Proposed approach answers the need of a computational platform for sharing resources.

EEG.pl portal and the semantic-aware search scheme provide a solution to the major problem of information noise, which sometimes overweight advantages of the Internet in scientific communication. Our solution lies in between the two extrema of the absolute centralization and a complete decentralization. Disadvantages of one central repository of information are obvious, but, on the other hand, Semantic Web and superintelligent software agents, creating structure from the chaos, are still more of buzzwords than reality. We propose a humble compromise. As presented, relevant information can be gathered in specialized repositories of possibly well-defined scope. Owing to this specialization, these relatively small services can assure the quality and proper annotation of resources. Seamless integration of these small repositories into a significant knowledge base can be effectuated by the connection paradigm presented in this paper. More technical details and a complete software implementation of this solution are freely available from http://eeg.pl.

Acknowledgments

This work was supported partly by Polish super-intelligent funds for science 2006–2009. This work was supported also by the COST Action BM0601 "NeuroMath" and Grant of Polish Ministry of Science and Higher Education (Decision no. 119/N-COST/2008/0). Neither the COST Office nor any person acting on its behalf is responsible for the use which might be made of the information contained in this publication. The COST Office is not responsible for the external websites referred to in this publication. The authors thank Raphael Ritz for early discussions and sharing his ideas on the semantic-aware search.

References

[1] K. J. Blinowska and P. J. Durka, "Efficient application of internet databases for new signal processing methods," *Clinical EEG and Neuroscience*, vol. 36, no. 2, pp. 123–130, 2005.

[2] A. Powell, M. Nilsson, A. Naeve, P. Johnston, and T. Baker, "DCMI Abstract Model," June 2007, http://dublincore.org/documents/abstract-model.

[3] M. Gudgin, M. Hadley, N. Mendelsohn, et al., Eds., "SOAP Version 1.2 Part 1: Messaging Framework, W3C Recommendation," April 2007, http://www.w3.org/TR/soap12-part1.

[4] R. Fielding, J. Gettys, J. Mogul, et al., "Hypertext Transfer Protocol—HTTP/1.1," Network Working Group Request for Comments: 2616, June 1999, http://www.w3.org/Protocols/rfc2616/rfc2616.html.

Hindawi Publishing Corporation
Computational Intelligence and Neuroscience
Volume 2009, Article ID 989824, 7 pages
doi:10.1155/2009/989824

Review Article

Signatures of Depression in Non-Stationary Biometric Time Series

Milka Culic,[1] Biljana Gjoneska,[2] Hiie Hinrikus,[3] Magnus Jändel,[4] Wlodzimierz Klonowski,[5] Hans Liljenström,[6] Nada Pop-Jordanova,[7] Dan Psatta,[8] Dietrich von Rosen,[6] and Björn Wahlund[9]

[1] *Department of Neurobiology Institute for Biological Research, University of Belgrade, 11000 Belgrade, Serbia*
[2] *Division of Bioinformatics, Macedonian Academy of Sciences and Arts, 1000 Skopje, Macedonia*
[3] *Department of Biomedical Engineering, Technomedicum of the Tallinn University of Technology, 19086 Tallinn, Estonia*
[4] *The Swedish Defence Research Agency, SE-16490 Stockholm, Sweden*
[5] *Lab of Biosignal Analysis Fundamentals, Institute of Biocybernetics and Biomedical Engineering, Polish Academy of Sciences, 00901 Warsaw, Poland*
[6] *Department of Energy and Technology, Swedish University of Agricultural Sciences, SE-75007 Uppsala, Sweden*
[7] *Pediatric Clinic, Faculty of Medicine, University of Skopje, 1000 Skopje, Macedonia*
[8] *Institute of Neurology and Psychiatry in Bucharest, 75622 Bucharest, Romania*
[9] *Department of Clinical Neuroscience, Division of Psychiatry, Karolinska Instititute, SE-17177 Stockholm, Sweden*

Correspondence should be addressed to Dietrich von Rosen, dietrich.von.rosen@et.slu.se

Received 30 October 2008; Revised 19 March 2009; Accepted 29 April 2009

Recommended by Laura Astolfi

This paper is based on a discussion that was held during a special session on models of mental disorders, at the NeuroMath meeting in Stockholm, Sweden, in September 2008. At this occasion, scientists from different countries and different fields of research presented their research and discussed open questions with regard to analyses and models of mental disorders, in particular depression. The content of this paper emerged from these discussions and in the presentation we briefly link biomarkers (hormones), bio-signals (EEG) and biomaps (brain-maps via EEG) to depression and its treatments, via linear statistical models as well as nonlinear dynamic models. Some examples involving EEG-data are presented.

1. Introduction

When studying mental disorders researchers have primarily focused on gathering data, that is, the approach is basically empirical. In recent years, this has often been performed with advanced technical equipment. On the other hand, analysis of data often consists of rather elementary statistics, where comparisons are performed through testing hypotheses. There is also a growing literature on dynamics and non-linear modelling, in particular for EEG data, but very rarely it is distinguished *between* individual and *within* individual variation. To some extent, technology is far ahead of analytic tools and explanatory theories. The research mainly relies on the following well known paradigm: (i) make a model of the phenomenon under study; (ii) collect data by an experiment or sample survey; (iii) test the model using data; (iv) refine the model and restart. The weak point is of course the knowledge about the model. Einstein once rather drastically pointed out: "A theory can be proved by an experiment but no path leads from the experiment to the birth of a theory."

This paper is unique in so far that many researcher from many disciplines have met and discussed depression from different perspectives. The paper delivers a lot of bricks, but no house is built. In fact, an architect is missing. The aim of the paper is to share our experiences of a multidisciplinary view where hopefully empirically oriented researchers, as well as those who are more deductive can find new perspectives in modelling depression. Indeed, the project is a novel approach to help to uncover a serious mental decease, which would be hard to carry out within commonly structured academic institutions.

Problems in Classifying and Modelling Major Depression. The use of the current classification schemas, including DSM-IV, undoubtedly contributes to the difficulties in finding genes and biological variables for psychiatric disorders. They are based on clusters of symptoms and characteristics of clinical courses that do not necessarily describe homogenous disorders, and rather reflect common final pathways of different pathophysiological processes [1].

Moreover, biological variables and behaviours may not be associated on a simplistic, one-to-one basis; the true relationship between, for example, a gene and a behaviour, is probably more akin to the sensitive dependence on initial conditions in chaos theory. For example, there is presumably no gene for 'language'. Instead, there is a number of genes that pattern the embryonic brain in such a way as to facilitate and allow the physiological processes necessary for language acquisition. In a similar manner, no gene has been found to singularly code for a human psychiatric condition. To understand the pathogenesis and neurobiology of depression multidisciplinary research is necessary.

A strategy to overcome the methodological difficulties mentioned above is the proposal of putative endophenotypes. The term "endophenotype" was described as an internal phenotype (i.e., not obvious to the unaided eye) that fills the gap between available descriptors and between the gene and the elusive disease process [2], and therefore may help to resolve questions about etiological models. Modelling Major Depression must be based on the state of art of knowledge of which psychopathological characteristics that are biologically and clinically meaningful and can be assessed quantitatively.

The endophenotypes may be defined at two levels, (a) the key components of major depression, that is, kern symptoms and stress sensitivity and (b) biological endophenotypes Not surprisingly, studies on the biological basis of depression have found stronger associations between specific biological dysfunctions and certain components of major depression symptoms, such as cognitive deficits, rumination, psychomotor retardation, anhedonia, and lowered mood have been associated with specific focal abnormalities of regional cerebral blood flow (CBF; [3, 4]). Thus, biological variables strongly related to key components are defined as biological endophenotypes.

The key components of major depression are: (1) Depressed Mood (Mood Bias Toward Negative Emotions), (2) Anhedonia (Impaired Reward Function), (3) Impaired Learning and Memory, (4) Neurovegetative Signs, (5) Diurnal Variation, (6) Impaired Executive Cognitive Function (Response Speed), (7) Psychomotor Change (Retardation, Agitation), (8) Increased Stress Sensitivity (Gender Specific).

The biological endophenotypes are: (1) REM Sleep, (2) Abnormalities in Brain Structure and Function (Functional imaging, Structural imaging, Receptor pharmacology, Serotonin, Dopamine, and Norepinephrine), (3) HPA Axis and CRH, (4) Intracellular Signalling Molecules (Neurotrophic factors, Ubiquitous signalling cascades).

In this paper we describe some potential biological endophenotypes, such as circadian rhythms, EEG findings and animal models. It is obvious that there is no simple model for depression, rather many complex models based on various scales from a micro-, meso- and macro perspective.

Finding appropriate models for mental disorders is the ultimate goal and we believe that for this purpose relevant inter-/multi-disciplinary knowledge is necessary. In this paper, we will briefly mention some advanced linear statistical models, which are useful when studying circadian rhythms (Sections 2 and 3), some ideas about complexity in signals (EEG data, Sections 4 and 5), and we also consider animal models (Section 7), which are important in generating models for humans. Moreover, four different examples which comprise EEG data are presented (Sections 6, 8, and 9).

2. Circadian Rhythms, Melatonin, and Bright Light Therapy

Circadian rhythms control, among other things, appetite, energy, mood and sleep. The study of these rhythms dates back to the 19th century. From about 1980 one began to study changes in physical strength, aerobic capacity, blood pressure, mental alertness, and secretion of neurotransmitters and hormones. Depression was then studied in relation to the disruption of biological clocks. In Seasonal Affective Disorder (SAD) the mood is closely connected with circadian rhythm disorder. Moreover, it seems that the Suprachiasmatic Nucleus (SCN), which may be viewed as a master clock of the body, has difficulties to follow the changes in the day and night cycle. A support for this hypothesis is the production of the hormone melatonin and its relation so SAD. Melatonin is produced by pinealocytes in the pineal gland, which is under the influence of SCN and is suppressed by daylight.

More than 20 years ago, depression was studied in relation to various hormones, in particular melatonin. Melatonin peak level was found lowered in acutely ill depressed patients, who also had hypercortisolemia and an abnormal dexamethasone suppression test in comparison to healthy subjects. The melatonin peak levels remained low when these patients were re-examined during remission, whereas the changes in the hypothalamatic-pictiutary-adrent-cortex axis disappeared (see Wetterberg et al. [5], Beck-Friis et al. [6]). Therefore, melatonin levels may be viewed as biomarkers for depression.

During the 1980s, Bright Light Therapy (BLT) was introduced with a clear therapeutic effect on approximately 85% of the patients with SAD, as well as on patients with bipolar disorder. Most studies support that BLT normalizes circadian rhythms, that is, the phase and the melatonin level (amplitude) may vary between individuals, as well as states of physiological conditions and disorders (cf. [7, 8]).

It is important to have appropriate designs of experiments, strong statistical/mathematical tools, and specialized knowledge concerning the hormones under investigation. For example, the effect of age, gender, body weight/height on the melatonin level is important to take into account. Initially, circadian melatonin rhythms were analysed with ordinary regression analysis and trigonometric functions.

Studies were often designed so that around 10 serum measurements per individual were taken over the day and night cycle. Usually between 10 and 50 individuals from different diagnostic groups, including a control group, were studied with an aim to compare the treatment groups with respect to the hormone profile over the day and night cycle. The main problem is that melatonin is not stable in serum, since it is rhythmically released within relatively short time intervals. With a sampling strategy of about 10 measurements over 24 hours the release of melatonin is impossible to capture and the variation will be built in as a measurement error.

3. Statistical Repeated Measurements Models for the Analysis of Circadian Rhythms: An Example of Linear Models Analysis

Since there are often repeated measurements on individuals in depression studies one has to apply some of the repeated measurements tools that nowadays are available, and not use standard regression methods. The difficulty lays in finding an appropriate model for the covariance structure within individuals. A conservative approach is to assume an arbitrary covariance matrix and if melatonin sampling has taken place at the same time points for all individuals we may apply the classical Growth Curve model due to Potthoff and Roy [9] or generalized Growth Curve models (cf. Kollo and von Rosen [10, Chapter 4]). Otherwise, we may rely on mixed linear models analysis (cf. Fitzmaurice et al. [11]) with random parameters, which is suitable for analyzing short time series. However, this approach usually gives only asymptotic correct results.

Nowadays, for example, melatonin is often sampled via an inserted indwelling intravenous catheter and samples are collected every, say, 15 minutes. This calls for more advanced methods than the suggested analyses above, which are extensions of classical multivariate variance analysis. New methods have to be developed in order to estimate melatonin profiles and to perform rigorous significance tests. Of course, one can always create summary statistics, but it is challenging to make use of the full sampling resolution. In the future, we will probably see more of high-dimensional statistical analysis or stochastic process approaches.

4. Techniques for Identifying Depression from EEG

An even more advanced method than to model high-resolution hormone samples is to study bio-signals, such as EEG and sometimes EEG in addition to hormones, in particular when assessing BLT. The information from EEG is of a completely different type than, for example, serum melatonin concentration, and it is important to study these often nonstationary time series.

As behavioural alterations are based on neurophysiology, behaviour should be studied in association with brain activity correlates—single neuronal discharges, local field potentials and EEG/ECoG. In other words, the behavioural changes in food intake, sleep patterns, work habits and general motor activity are quite conspicuous in depression, in humans as well as in animals, and may be quantified with changes in EEG. Moreover, antidepressant treatments (drug therapy, moderate physical exercise, electroconvulsive shock) reverse more or less the EEG changes found in human depression, or in certain animal models of depression. In this way, brain lateralization effects of depression are electrophysiologically evident. The brain-rate parameter may serve as an effective integral indicator of these changes (Pop-Jordanova and Pop-Jordanov, [12]). Neuronal models and other approaches for electroencephalographically identifying/quantifying depression may act complementarily. In order to refine the treatment procedure, we may suggest more specified electrocortical stimulations in an animal model, and various analyses in complexity of acquired electrical brain signals by multichannel chronic recording techniques with telemetry technology (Culic, [13]).

5. EEG Signals and Complexity Measures: An Example of Non-Linear Analysis

In EEG signals, the classical statistical approach of interpreting measurement errors as generators of uncertainty is not valid. For EEG, most of the noise seems due to model error, which cannot be considered to be random. We have not seen any EEG model where residuals are completely randomly distributed around a fitted model. This may be due to dependence structures but it is not clear how to estimate this dependency in non-stationary series. Therefore, it is reasonable that when studying EEG completely different tools than classical statistical ones are advantageous. For example, non-linear dynamic models may play an important role. Moreover, the number of used electrodes is important. With many electrodes we can analyze spatio-temporal models, that is, brain-maps. Below, a non-linear method of complexity analysis is presented. For references to other non-linear methods for studying complex EEG signals, see Freeman [14] and Perlovsky and Kozma, [15].

Methods that assess signal complexity, like fractal and symbolic methods, may be suitable. For example EEG-signal complexity measured by Higuchi's fractal dimension in time domain, $D_f(t)$, is proposed in assessing BLT for treatment of SAD (cf. Klonowski [16]). $D_f(t)$ is calculated for EEG-signal on each electrode on the scalp and then a spatio-temporal map of complexity measured by fractal dimension can be made. The term 'fractal dimension' may have different meanings, so it is necessary to emphasize that $D_f(t)$ measures local complexity of the curve representing the given signal—a simple curve has always a dimension equal to 1, while a plane has a dimension equal to 2, so local complexity of a curve on a plane may be characterized by a number between 1 and 2, with 2 corresponding to pure noise (the curve "filling up" the whole plane). For assessing signal complexity using Higuchi's D_f in time domain it is not important if the signal is "really" chaotic (which makes the curve that represents the

signal showing fractal properties), and neither deterministic nor random.

6. Example 1: An Example Where Complexity is Studied

To illustrate a non-linear analysis technique, the EEG from 10 patients suffering of SAD and treated with BLT, was analyzed. The data were collected before and 2 weeks after BLT was applied. It was demonstrated that in patients suffering of SAD, the mean D_f of the EEG-signal was smaller than in healthy subjects—BLT increased the mean value of D_f in those suffering of SAD (cf. Klonowski et al. [17]). For every patient epochs with a duration of approximate 20 seconds length, starting about 5 seconds before eyes-opening and ending about 5 seconds after eyes-closing were analyzed. When an eyes-opening event occurred, the fractal dimension of the EEG-signal (based on windows of 100 observations) increased from 1.1–1.3 to 1.5-1.6 in the occipital channels and even to 1.8 in the frontal channels. This increase is denoted by Δ_o. When the eyes remained open, the fractal dimension diminished, and rose again when an eyes-closing event occurred; when the eyes remained closed, it diminished again. This decrease is denoted by Δ_c.

The open-/closed-eyes fractal dimension ratio (FD-ratio), that is, Δ_o/Δ_c was investigated. For a clinical assessment of the patients the Hamilton Depression Rating Scale (HDRS), [18] was used It was observed that in EEG of healthy subjects the *FD-ratio* was close to 1, while for patients with high HDRS the *FD*-ratio differed from 1.0. For SAD patients the *FD-ratio* was compared with HDRS before and after BLT. For those patients for whom HDRS diminished after BLT the *FD*-ratio "normalized"—it became closer to 1.0.

In the material mentioned above, there was a focus on possible BLT effects on the EEG. One of the main problems of studying depression is that patient groups are very inhomogeneous with a strong individual component of response. Besides this, there are covariables such as age, gender and body height/weight which influence the measured response. Moreover, patients may have used medicines which even after wash-out periods may have an effect on the results.

As a complement, one can consider ADHD children. They constitute an interesting group, since they usually have not undergone pharmacological treatment, and therefore could be used as a control group (Zorcec et al. [19]). However, in order to propose initial theories, the best is probably to start with animal models.

7. Animal Models for Developing Antidepressive Treatment: A Short Introduction

The overall goal is to understand the interplay between structural, chemical, and electrical signals in the brain, which gives rise to a depressed behaviour in humans. In particular, studies of animal models of depression may be important for performing screening tests to discover and develop new antidepressant drugs. Moreover, animal models are used to simulate and elucidate neurobiological aspects of depressive illness—to induce anhedonia as a core symptom of depression, or to a particular subtype of depression, and to examine mechanisms of depressive syndromes and of various acute and chronic antidepressive treatments (Mitchell and Redfern [20]; Harro [21]; Sarbadhikari and Sankar [22]; Willner [23, 24]; Porsolt et al. [25]). For instance, disruption of neurochemistry of the noradrenergic *locus coeruleus* (LC) is at least one aspect of the pathophysiology of major depression (Klimek et al. [26]). The mutual role of LC and cerebellum is also bringing new information about motor and non-motor cerebellar processing (Culic et al. [27]). The fitness of an animal model depends on the similarity with the human disorder with respect to symptomatology, etiology, biochemistry, electrophysiology and response to antidepressive treatment. It is of vital importance to fully recognize the limitations of such models.

Certain behavioural or physiological responses, which are supposed to be important for depression, are measured in animal assay models. Examples of assay models are: muricide, potentiation of yohimbine lethality or amphetamine-induced hyperactivity, antagonism of apomorphine-induced hypothermia, preferential reduction of kindled seizures initiated from the amygdale, and facilitation of circadian rhythm readjustment. Such models focus on the predictive value for screening of new drugs and other treatments, without trying to create a human disorder in the animal. On the other hand, homologous animal models place less emphasis on correlative approaches and rely more on construct and face validity. They are based on resemblance to symptoms of human depression although some symptoms can never be mimicked in animals. Homologous examples include: forced swim test, tail suspension test, electrolytic lesioning of the dorsomedial amygdala, exhaustion stress, and chronic mild/variable stress-induced anhedonia.

8. Example 2: An Example with Experimental Neurosis in Cats

That EEG correlates of motivation and short term memory (STM) in cats during an approach-avoidance delayed differentiation task were studied several decades ago (Psatta [28, 29]). The preparatory (cue) stimuli were tone and intermittent light stimulation (ILS), the delay of ten seconds, and reinforcement was either food or pain. Under these conditions, motivation changed from one trial to another. EEG activity varying with motivation during the delayed period was statistically confirmed. Changes occurred only in the amygdaloidal and the hypothalamic nuclei. Changes significantly related to STM (either prolonged desynchronization or ILS memory traces during the delay period) occurred only in the cortical cognitive areas (Ectosylvius medius or Marginalis posterior in cats). The electrical activity in the Hippocampus had complex relationships. A prolonged theta activity in the Dorsal Hippocampus (DH) accompanied by

fast activity in the Ventral Hippocampus (VH) occurred when STM was successful, attention sustained and the motor response delayed. Occurrence of theta activity in VH systematically accompanied the motor response. It was concluded that hippocampus exerts a complex sensory-motor integration. DH intervenes in the sensory processing of information, by closing the thalamic gates. Any fast activity (even short) in DH was accompanied by the loss of STM correlates (weak, fast stimulations of DH also blocked STM). VH exerts an inhibitory motor control on the frontal cortex (by uncial fibers).

Depression occurred in five out of 13 investigated animals, when the approach-avoidance conflict induced manifestations of experimental neurosis (Psatta [30, 31]). The most characteristic electrical change in these animals was the constant occurrence of a mid-amplitude very fast rhythm in both DH and VH. Thus depression was attributed to the exaggerated inhibitory control of hippocampus induced by the emotional conflict imposed. The experiment permitted an exploration of the adrenergic/cholinergic ratio contribution to the deviated behaviour. Administration of small doses of Reserpine, reducing the cerebral amount of free catecholamines, induced a reoccurrence of the theta rhythm in the hippocampus and of the coordinated motor responses. Further administration resulted in change in the appearance of higher amplitude fast rhythms in the hippocampus and of exhaustion type of depression.

It was concluded that there is an optimal monoamine level (a narrow window) for which hippocampus acts normally. Administration of Nialamide after Reserpine restored first theta activity and eventually the original aspect of mid amplitude fast rhythms in the hippocampus (the anxious type of depression). A choline-estherase inhibitor (eserine) in small doses restored in the depressed animals both the DH theta activity and the EEG correlates of STM (the memory traces). In higher doses, Eserine induced instead an extreme agitation of those animals (on a high level cholinergic/adrenergic equilibrium). Atropine after Reserpine induced a release of motor behaviour, but no signs of performing STM. These experiments reveal the difficulty of controlling depression by psychotropic drugs administration. It is also outlined the difficult extrapolation of these results in animals to experimentation in humans in whom subcortical EEG investigation is not possible.

In order to replicate the described experiment, the authors tried the effects of Go-NoGo STM performances in humans (using auditory click cue stimuli and slightly delayed motor finger responses). They considered that the rolandic reaction evidenced by EEG Spectral Reaction Mapping was the equivalent of the cognitive cortical areas response encountered in animals, whereas the N220/P300 components of the Auditory Reponses evoked by the click stimuli, are the equivalent of the fast and slow rhytms occuring in the Hippocampus in animals. N220 is larger in NoGo, P300 is deeper in Go situations. Both these EEG manifestations disappear in case of Temporal Lobe Epilepsy (and Neurosis), and are enhanced in case of Frontal Lobe Epilepsy (Psatta and Matei, [32, 33]).

9. Example 3: Exposure Experiments

Finally, we mention two different exposure treatment/experiments which also indicate that EEG is appropriate to study when investigating mental disorders.

Electroconvulsive therapy (ECT) is a treatment in which seizures are electrically induced in anesthetized patients for therapeutic purposes. ECT is most often used as a treatment for severe major depression, where patients have not responded to other treatments. Seizures may be monitored by EEG, electrocardiogram (ECG) and electromyogram (EMG). The course can be summarized as three events of distinct and sequential phase patterns. The first event contains high-voltage "sharp waves and spikes," the second rhythmical "slow-waves" and the third event an abrupt and well-defined ending.

Most ECT studies have investigated the physiological mechanism of action in relation to clinical response [34]. A typical study runs as follows: subjects with unilateral electrode placement according to the d'Elia method [35] receive bi-directional pulse ECT; ECT is routinely administrated three times a week for a period of 2–4 weeks; each time EEG is recorded it covers the above mentioned three distinct phases. Studies consist often of about 30 patients who are followed 5–9 times. This results in a huge data set with a possibility to test several interesting hypothesis, for example "can one subgroup depressive disorder with the aid of seizure data?" Moreover, one problem with ECT is that it is not known what happens in the brain during or after treatment. In order to test various hypotheses of ECT effects (e.g., on neural network connectivity by stimulation of nerve sprouting or nerve deletion), computational models of cortical neural networks may be useful (Gu et al. [36–38]).

Microwave exposure is a method in which the electromagnetic radiation at field power densities is much lower than used in ECT is applied for treatment of mental disorders. For example, mood improvement in patients with bipolar depressive disorder has been reported at the field power density within clinical magnetic resonance system limits [39]. Exposure to 450 MHz microwave radiation modulated at 1000 Hz frequency at the field power density 0.9 mW/cm^2 has been shown to cause short-term alteration in mood of major depressive disorder [40]. The experiments were carried out on a group of depressive patients (18 females) and a control group of healthy volunteers (18 females) exposed by microwave radiation during 30 minutes. Subjects with nonpsychotic major depressive disorder are defined by ICD-10 criteria and determined by the 17-item HDRS score (as in Example 1). The average HDRS score for the group was 21 (s.d. 3.3). All the subjects passed two experimental procedures—with exposure and sham. As a subjective criteria of microwave effect, the Brief Affect Scale (BAS) and Visual Analogue Scale (VAS) before and after each exposure and sham procedure were used. The resting 9 channel EEG was recorded during the experiment.

As a measure for evaluation of the mood improvement the spectral asymmetry index (SASI) as a combination of the EEG beta and theta power was selected [41]. The BAS revealed a minor improvement (11 subjects) in subjective

mood score after exposure and VAS test revealed significant change between scores before (average 33.3) and after (average 40.2) treatment for exposed subjects and no significant change for sham exposed subjects.

The EEG analysis detected objective effects of the treatment. The calculated SASI values were positive for depressive and negative for healthy subjects. Correlation between HDRS score and SASI values was 0.67. Exposure to microwave during 30 minutes reduced SASI values for depressive patients: average SASI value was 0.16 for exposed and 0.19 for sham exposed recordings. The analysis revealed statistically significant differences between exposed and sham exposed patients. These preliminary results are promising and the SASI method of EEG analysis for mood evaluation as well as microwave exposure for treatment of mental disorders need further investigations. Variations between individuals and within individuals should be investigated and experiments on different groups should be performed.

10. Concluding Remarks

In this paper we have focused on the neural understanding of depression. The aim is to find a link between physiology and mental disorders. There are several indications for such links, for example between hormone levels and SAD. Also EEG analysis reveals connections with SAD. In the future, we hope to have found models that would manifest connections between depression and bio-markers, bio-signals, and bio-maps, such as hormone levels, EEG, fMRI, and so forth. To achieve this goal statistical/mathematical theory has to be developed together with experimental designs. In particular, we have to learn how to take into account *between* and *within* subject variations in spatio-temporal, parametric or semi-parametric models.

Acknowledgments

This work was supported also by the COST Action BM0601 "NeuroMath." Neither the COST Office nor any person acting on its behalf is responsible for the use which might be made of the information contained in this publication. The COST Office is not responsible for the external websites referred to in this publication. W. Klonowski acknowledges support of the Polish Ministry of Science and Higher Education through the Grant 142/COS/2006/01. M. Culic acknowledges the Serbian Ministry of Science and Technological Development (Project no. 14021).

References

[1] D. Charney, D. Barlow, K. Botteron, et al., "Neuroscience research agenda to guide development of a sychophysiologically based classification system," in *A Research Agenda for DSM-IV*, D. Kupfer, M. First, and D. Regier, Eds., pp. 31–83, American Psychoatric Association, Washington, DC, USA, 2002.

[2] I. I. Gottesman and J. Shields, "Genetic theorizing and schizophrenia," *British Journal of Psychiatry*, vol. 122, no. 566, pp. 15–30, 1973.

[3] W. C. Drevets, "Neuroimaging studies of mood disorders," *Biological Psychiatry*, vol. 48, no. 8, pp. 813–829, 2000.

[4] H. S. Mayberg, M. Liotti, S. K. Brannan, et al., "Reciprocal limbic-cortical function and negative mood: converging PET findings in depression and normal sadness," *American Journal of Psychiatry*, vol. 156, no. 5, pp. 675–682, 1999.

[5] L. Wetterberg, J. Beck-Friis, B. F. Kjellman, and J. G. Ljunggren, "Circadian rhythms in melatonin and cortisol secretion in depression," *Advances in Biochemical Psychopharmacology*, vol. 39, pp. 197–205, 1984.

[6] J. Beck-Friis, J.-G. Ljunggren, M. Thorén, D. von Rosen, B. Kjellman, and L. Wetterberg, "Melatonin, cortisol and ACTH in patients with major depressive disorder and healthy humans with special reference to the outcome of the dexamethasone suppression test," *Psychoneuroendocrinology*, vol. 10, no. 2, pp. 173–186, 1985.

[7] B. L. Parry, C. J. Meliska, D. L. Sorenson, et al., "Plasma melatonin circadian rhythm disturbances during pregnancy and postpartum in depressed women and women with personal or family histories of depression," *American Journal of Psychiatry*, vol. 165, no. 12, pp. 1551–1558, 2008.

[8] A. J. Lewy, "Melatonin and human chronobiology," *Cold Spring Harbor Symposia on Quantitative Biology*, vol. 72, pp. 623–636, 2007.

[9] R. F. Potthoff and S. N. Roy, "A generalized multivariate analysis of variance model useful especially for growth curve problems," *Biometrika*, vol. 51, pp. 313–326, 1964.

[10] T. Kollo and D. von Rosen, *Advanced Multivariate Statistics with Matrices*, vol. 579 of *Mathematics and Its Applications*, Springer, Dordrecht, The Netherlands, 2005.

[11] G. Fitzmaurice, N. Laird, and J. Ware, *Applied Longitudinal Analysis*, John Wiley & Sons, New York, NY, USA, 2004.

[12] N. Pop-Jordanova and J. Pop-Jordanov, "Spectrum-weighted EEG frequency ("brain-rate") as a quantitative indicator of mental arousal," *Prilozi*, vol. 26, no. 2, pp. 35–42, 2005.

[13] M. Culic, "Electrophysiological approaches for studying the brain dynamics," in *Proceedings of the Workshop on Fractal Analysis of Biosignals and Our Perspective*, University of Beograd, Beograd, Serbia, 2007.

[14] W. Freeman, *Neurodynamics: An Exploration in Mesoscopic Brain Dynamics*, Springer, New York, NY, USA, 2000.

[15] L. I. Perlovsky and R. Kozma, Eds., *Neurodynamics of Cognition and Consciousness*, Springer, New York, NY, USA, 2007.

[16] W. Klonowski, "From conformons to human brains: an informal overview of nonlinear dynamics and its applications in biomedicine," *Nonlinear Biomedical Physics*, vol. 1, article 5, 2007.

[17] W. Klonowski, R. Stepien, E. Olejarczyk, W. Jernajczyk, K. Niedzielska, and A. Karlinski, "Chaotic quantifiers of EEG-signal for assessing photo- and chemo-therapy," *Medical and Biological Engineering and Computing*, vol. 37, supplement 2, pp. 436–437, 1999.

[18] M. Hamilton, "A rating scale for depression," *Journal of Neurology, Neurosurgery & Psychiatry*, vol. 23, pp. 56–62, 1960.

[19] T. Zorcec, N. Pop-Jordanova, A. Mueller, and B. Gjoneska, "The role of QEEG in comprehensive classification of ADHD children," in *Proceedings of the Neuromath Workshop*, pp. 42–43, Jena, Germany, April 2008.

[20] P. J. Mitchell and P. H. Redfern, "Animal models of depressive illness: the importance of chronic drug treatment," *Current Pharmaceutical Design*, vol. 11, no. 2, pp. 171–203, 2005.

[21] J. Harro, "Animal models for better antidepressants: can pathogenic approaches make a difference," *Preclinica*, vol. 2, pp. 402–407, 2004.

[22] S. Sarbadhikari and K. Sankar, "Automated techniques for identifying depression from EEG," in *Handbook of Computational Methods in Biomaterials, Biotechnology and Biomedical Systems*, C. T. Leondes, Ed., vol. 4, chapter 3, pp. 51–81, Kluwer Academic Publishers, Norwell, Mass, USA, 2002.

[23] P. Willner, "The validity of animal models of depression," *Psychopharmacology*, vol. 83, no. 1, pp. 1–16, 1984.

[24] P. Willner, "Chronic mild stress (CMS) revisited: consistency and behavioural-neurobiological concordance in the effects of CMS," *Neuropsychobiology*, vol. 52, no. 2, pp. 90–110, 2005.

[25] R. D. Porsolt, M. Le Pichon, and M. Jalfre, "Depression: a new animal model sensitive to antidepressant treatments," *Nature*, vol. 266, no. 5604, pp. 730–732, 1977.

[26] V. Klimek, C. Stockmeir, J. Overholser, et al., "Reduced levels of norepinephrine transporters in the Locus Coeruleus in major depression," *Journal of Neuroscience*, vol. 17, no. 21, pp. 8451–8458, 1997.

[27] M. Culic, J. Saponjić, B. Jankovic, A. Kalauzi, and A. Jovanovic, "Slow oscillations of the purkinje cell firing rate induced by electrical stimulation of the Locus Coeruleus in rats," *Neurophysiology*, vol. 33, no. 1, pp. 48–52, 2001.

[28] D. M. Psatta, "EEG patterns of motivation in cats during approach-avoidance successive differentiation," *Revue Roumaine de Neurologie*, vol. 9, no. 4, pp. 229–248, 1972.

[29] D. M. Psatta, "EEG patterns of short-term memory in cats during approach-avoidance successive differentiation," *Revue Roumaine de Neurologie*, vol. 9, no. 4, pp. 249–263, 1972.

[30] D. M. Psatta, "Limbic electrical activity alterations during experimental neurosis in adult cats," *Revue Roumaine de Neurologie et Psychiatrie*, vol. 14, no. 3, pp. 225–233, 1976.

[31] D. M. Psatta, "The effects of some drugs (eserine, atropine, reserpine, niamid) upon the EEG manifestations of experimental neurosis in adult cats," *Revue Roumaine de Neurologie et Psychiatrie*, vol. 14, no. 4, pp. 283–293, 1976.

[32] D. M. Psatta and M. Matei, "Investigation of P300 in various forms of epilepsy," *Revue Roumaine de Neurologie et Psychiatrie*, vol. 33, no. 3-4, pp. 183–202, 1995.

[33] D. Psatta and M. Matei, "EEG mapping during auditory oddball stimulation. A comparison with P300 scalp distribution in normal controls and epileptic patients," *Revue Roumaine de Neurologie et Psychiatrie*, vol. 34, pp. 35–53, 1996.

[34] B. Wahlund and D. von Rosen, "ECT of major depressed patients in relation to biological and clinical variables: a brief overview," *Neuropsychopharmacology*, vol. 28, pp. S21–S26, 2003.

[35] G. d'Elia and C. Perris, "Comparison of electroconvulsive therapy with unilateral and bilateral stimulation," *Acta Psychiatrica Scandinavica*, vol. 215, pp. 9–29, 1970.

[36] Y. Gu, G. Halnes, H. Liljenström, and B. Wahlund, "A cortical network model for clinical EEG data analysis," *Neurocomputing*, vol. 58-60, pp. 1187–1196, 2004.

[37] Y. Gu, B. Wahlund, H. Liljenström, D. von Rosen, and H. Liang, "Analysis of phase shifts in clinical EEG evoked by ECT," *Neurocomputing*, vol. 65-66, pp. 475–483, 2005.

[38] Y. Gu, G. Halnes, H. Liljenström, D. von Rosen, B. Wahlund, and H. Liang, "Modelling ECT effects by connectivity changes in cortical neural networks," *Neurocomputing*, vol. 69, no. 10–12, pp. 1341–1347, 2006.

[39] M. Rohan, A. Parow, A. L. Stoll, et al., "Low-field magnetic stimulation in bipolar depression using an MRI-based stimulator," *American Journal of Psychiatry*, vol. 161, no. 1, pp. 93–98, 2004.

[40] M. Bachmann, H. Hinrikus, K. Aadamsoo, et al., "Modulated microwave effects on individuals with depressive disorder," *Environmentalist*, vol. 27, no. 4, pp. 505–510, 2007.

[41] H. Hinrikus, M. Bachmann, J. Lass, et al., "Method and device for determining depressive disorders by measuring bioelectromagnetic signals of the brain," Patent Application US12/196335 22.08, 2008.